

Response of the Patagonian Glaciers to Present and Future Atmospheric Changes

Claudio Andrés Bravo Lechuga

Submitted in accordance with the requirements for the degree of
Doctor of Philosophy

The University of Leeds
School of Geography

November, 2020

The candidate confirms that the work submitted is his/her own, except where work which has formed part of jointly-authored publications has been included. The contribution of the candidate and the other authors to this work has been explicitly indicated below. The candidate confirms that appropriate credit has been given within the thesis where reference has been made to the work of others.

The work in Chapter three of the thesis has appeared in publication as follows:

Bravo C., D. Quincey, A. Ross, A. Rivera, B. Brock, E. Miles and A. Silva (2019). Air temperature characteristics, distribution and impact on modeled ablation for the South Patagonia Icefield. *Journal of Geophysical Research: Atmospheres* 124(2), 907–925. doi: org/10.1029/2018JD028857.

C. Bravo designed the study, analysed the data and prepared the paper. E. Miles discussed the results and contributed to the writing. D.J. Quincey, A.N. Ross, A. Rivera, B. Brock and E. Miles oversaw the research and reviewed the manuscript. C. Bravo, A. Silva and A. Rivera participated in the field campaigns preparing logistic and installing and configuring the Automatic Weather Stations. All authors discussed the results and reviewed the manuscript.

The work in Chapter four of the thesis has appeared in publication as follows:

Bravo C., D. Bozkurt, Á. Gonzalez-Reyes, D.J. Quincey, A.N. Ross, D. Farías-Barahona and M. Rojas (2019). Assessing snow accumulation patterns and changes on the Patagonian Icefields. *Front. Environ. Sci.* 7:30. doi: 10.3389/fenvs.2019.00030

C. Bravo, D.J. Quincey, and A.N. Ross designed the study. C. Bravo analysed the data and prepared the first draft of the paper. D. Bozkurt performed the RegCM4.6 simulations in addition to data processing and contributed to the writing. Á. Gonzalez-Reyes and C. Bravo performed the statistical analysis and analysed the results. D. Farías-Barahona compiled and analysed glaciological data. D.J. Quincey, A.N. Ross, and M. Rojas oversaw the research and reviewed the manuscript. All authors discussed the results and reviewed the manuscript.

The work presented in Chapter five of this thesis is in preparation for resubmission to *Journal of Glaciology*.

Bravo C., A.N. Ross, D.J. Quincey, S. Cisternas and A. Rivera (In preparation). Drivers of surface ablation on the Southern Patagonian Icefield. *Journal of Glaciology*.

C. Bravo designed the study, analysed the data, prepare figures and wrote the manuscript. S. Cisternas performed the albedo estimations using remote sensing technics and contributed to the writing. D.J. Quincey, A.N. Ross, and A. Rivera oversaw the research, and reviewed and commented on the manuscript. C. Bravo, S. Cisternas and A. Rivera participated in the field campaigns preparing logistic and installing and configuring the Automatic Weather Stations. All authors discussed the results and reviewed the manuscript.

The work presented in Chapter six of this thesis is in preparation for submission to *Scientific Reports*.

Bravo C., D. Bozkurt, A.N. Ross and D.J. Quincey (In preparation). Projected increases in surface melt and ice loss for the Northern and Southern Patagonian Icefields. Target Journal: *Scientific Reports*.

C. Bravo designed the study, analysed the data, prepare figures and wrote of the Manuscript. D. Bozkurt performed the RegCM4.6 simulations, contributed to the writing, discussed the results and reviewed the manuscript. D.J. Quincey and A.N. Ross, collaborated with the design and oversaw the research and reviewed the manuscript.

Copyright Declaration

This copy has been supplied on the understanding that it is copyright material and that no quotation from the thesis may be published without proper acknowledgement.

Assertion of moral rights:

The right of Claudio Andrés Bravo Lechuga to be identified as Author of this work has been asserted by him in accordance with the Copyright, Designs and Patents Act 1988.

Acknowledgements

This work was funded by the National Agency for Research and Development (ANID), Scholarship Program, Doctorado Becas Chile, 2016 – 72170022.

During these years, several persons and institutions support me and made it possible to finish this thesis. I am really gratefully to all of them. I am hugely indebted to my supervisors, Duncan J. Quincey and Andrew N. Ross, their constant support, patience and advice were fundamental to improve my research, but in parallel, I appreciate the independence they gave me to conduct this research, this way it felt like a very enjoyable scientific collaboration experience. I appreciate all the time that you gave me during the last four years and I do really hope to continue the collaboration in the incoming years.

Ben Brock, Andrés Rivera, Evan Miles, David Farias-Barahona, Deniz Bozkurt, Álvaro González-Reyes, Maisa Rojas, Alejandro Silva and Sebastián Cisternas, researchers that collaborated in my PhD project are thanked for their scientific inputs, advice and precious time dedicated to read, review and discuss my results. Thanks to the support given by the School of Geography, its cleaning, administrative and academic teams. Special thanks to Jonathan Carrivick, Mark Smith (School of Geography) and Piers Forster (School of Earth and Environment), panel members in the RSG meetings. Their recommendations and feedbacks helped to improve this work. I want to thanks to Jacqui Manton for always answer my questions and support me throughout the years as PhD researcher. Also, thanks to my colleagues, PhD researchers of the School of Geography, with whom I shared this path.

My gratitude is extended to the River Basin and Processes Management cluster to be an opportunity to listen and learn about other researches and in conjunction with Leeds for Life provided funding to attend to scientific meetings. Thanks to Centro de Estudios Científicos (CECs), Chile, for the continuous supports along these years.

I want to take this opportunity to express my huge thanks to my friends in Chile and especially to my family, my parents-in-law, Margarita and Miguel, my sister Carol and my brother Rodrigo, and my parents Estrella and Raúl, despite the distance, all of you were always accompanying us along these years. Lastly, the greatest grateful is to my wife Nataly, my life partner, and to my son Oliver, my hero. This would not have been possible without you both, with your continuous patience, happiness and love; always essential in my life.

Abstract

Patagonia (40°S-55°S) includes two large icefields, the Northern and Southern Patagonian Icefields (NPI and SPI). Most of the glaciers within these icefields are shrinking rapidly, raising concerns about their contribution to sea-level rise and the local to regional impacts of glacier shrinking in the face of ongoing climatic change. Empirically based studies that characterize the fundamental glacier conditions are scarce in this region. Consequently, our understanding of how the glaciers are responding to changes in climate, and what the key controls are, is limited. The aim of this project was to describe, estimate and analyse key meteorological and glaciological characteristics using nine months of meteorological observations, gridded-climate products and glacier modelling in a multi-scale approach.

In the north of the SPI and between October 2015 and June 2016, humid and warm on-glacier conditions prevailed to the west of the main topographic divide, whereas dry and cold conditions prevailed to the east. Air temperature lapse rates were steeper in the east ($-0.0072^{\circ}\text{C m}^{-1}$) compared to the west ($-0.0055^{\circ}\text{C m}^{-1}$). Modelled energy balance fluxes revealed that the controls of ablation differ along the west-east transect, although sensible heat and net shortwave radiation fluxes provided the main sources throughout. Melt was high on both sides of the divide, but at comparable elevations, it was greater on the western side. At glacier-wide scale, this disparity is amplified by the accumulation-area ratio, leading to the west having more melt (8.2. m w.e) than the east (2.1 m w.e.).

At the Icefield scale, surface mass balance (SMB) modelling (1976-2050), forced only by climate data, revealed that the NPI is currently losing mass while the SPI is not. Ice mass loss previously detected in the SPI is attributed to frontal ablation of calving glaciers. Glaciers in balance, however, are restricted to areas where snow accumulation has increased during the period 2000–2015. Projections until 2050 suggest a mean reduction in SMB of between 1.5 and 1.9 m w.e. in the NPI and between 1.1 and 1.5 m w.e in the SPI. SMB decrease is associated with melt increase due to projected air temperature increase. SMB is still projected to be positive in the SPI, however, assuming equal frontal ablation of the recent past, both Icefields will continue losing mass and contributing to sea-level rise. Additionally, an increase in meltwater availability could act as positive feedback by affecting ice dynamics and inducing greater frontal ablation for calving glaciers. This multi-scale assessment has increased our knowledge of the meteorological and glaciological characteristics of Patagonian glaciers, and quantified the response of these glaciers to atmospheric changes.

Table of Contents

| | |
|---|------------|
| Acknowledgements | iv |
| Abstract | v |
| Table of Contents | vi |
| List of Tables | x |
| List of Figures | xii |
| List of Abbreviations | xx |
| Chapter 1 | |
| Introduction | 1 |
| 1.1 Introduction | 1 |
| 1.2 Glacier response to atmospheric changes | 3 |
| 1.3 Mass balance measurements, modelling and meteorological observations on the Patagonian Icefields..... | 4 |
| 1.4 Aims and Objectives | 9 |
| 1.5 Study Area | 10 |
| 1.5.1 Patagonia climate | 10 |
| 1.5.2 Climate change in Patagonia..... | 11 |
| 1.5.3 Patagonian Icefields | 12 |
| 1.5.4 Glaciers in the northern sector of the Southern Patagonian Icefield..... | 13 |
| Chapter 2 | |
| Methods Summary | 17 |
| 2.1 Overview | 17 |
| 2.2 Automatic Weather Stations (Chapters 3, 4 and 5) | 18 |
| 2.3 Regional Climate Model and re-analysis (Chapter 4, 5 and 6).... | 19 |
| 2.4 Analysis of meteorological observations and spatial distribution (Chapter 3 and 5)..... | 20 |
| 2.5 Glaciological modelling (Chapter 4, 5, 6 and 7)..... | 21 |
| 2.6 Long-term surface mass balance (Chapter 4, 5 and 6) | 22 |
| Chapter 3 | |
| Air Temperature Characteristics, Distribution, and Impact on Modeled Ablation for the South Patagonia Icefield | 23 |
| 3.1 Abstract..... | 24 |
| 3.2 Introduction | 24 |
| 3.3 Materials and Methods..... | 27 |
| 3.3.1 Study Area and Observations..... | 27 |

| | |
|--|----|
| 3.3.2 Lapse Rates | 31 |
| 3.3.3 Air Temperature Distribution..... | 31 |
| 3.3.4 Melt and Ablation Models | 33 |
| 3.4 Results | 34 |
| 3.4.1 Characterization of the Observed Air Temperature | 34 |
| 3.4.2 LRs at Glacier Scale..... | 36 |
| 3.4.3 Air Temperature Distribution..... | 39 |
| 3.4.4 Ablation Estimates..... | 41 |
| 3.5 Discussion..... | 44 |
| 3.5.1 Uncertainties | 44 |
| 3.5.2 LRs and Air Temperature Spatial Patterns..... | 45 |
| 3.5.3 Glacier Cooling Effect..... | 48 |
| 3.5.4 Ablation Impacts..... | 49 |
| 3.6 Conclusions..... | 50 |
| 3.7 References..... | 52 |

Chapter 4

| | |
|--|-----------|
| Assessing Snow Accumulation Patterns and Changes on the Patagonian Icefields..... | 60 |
| 4.1 Abstract..... | 61 |
| 4.2 Introduction | 61 |
| 4.3 Materials and Methods..... | 64 |
| 4.3.1 Study Area..... | 64 |
| 4.3.2 Observations | 66 |
| 4.3.3 Data Compilation..... | 67 |
| 4.3.4 Regional Climate Model (RegCM4.6)..... | 67 |
| 4.3.5 Phase Partitioning Methods (PPMs)..... | 69 |
| 4.3.6 Trend Analysis..... | 71 |
| 4.4 Results | 71 |
| 4.4.1 Inter-comparison of PPMs..... | 71 |
| 4.4.2 Seasonal Trends 1980–2015 | 75 |
| 4.4.3 Comparisons with Measured data | 77 |
| 4.4.3.1 UDG Observations | 77 |
| 4.4.3.2 Previous Snow Accumulation Estimations and Comparisons..... | 78 |
| 4.5 Discussion..... | 82 |
| 4.5.1 Performance of the RegCM4.6 Model and PPMs Parametrization | 82 |

| | |
|--|----|
| 4.5.2 Snow Accumulation Changes 1980–2015..... | 84 |
| 4.5.3 Implications for Glacier Mass Balance..... | 86 |
| 4.6 Conclusions..... | 89 |
| 4.7 References..... | 91 |

Chapter 5

Drivers of surface ablation on the Southern Patagonian Icefield 101

| | |
|---|-----|
| 5.1 Abstract..... | 102 |
| 5.2 Introduction | 102 |
| 5.3 Materials and Methods..... | 105 |
| 5.3.1 Energy balance model..... | 105 |
| 5.3.2 Automatic Weather Stations (AWSs)..... | 106 |
| 5.3.3 Distribution of meteorological variables | 107 |
| 5.3.4 Extended ablation time series to hydrological years 1982/82-2018/19 | 110 |
| 5.4 Results | 111 |
| 5.4.1 Meteorological conditions | 111 |
| 5.4.2 Energy balance fluxes and ablation..... | 113 |
| 5.4.3 Extended ablation time series and mass balance | 120 |
| 5.5 Discussion..... | 122 |
| 5.5.1 Energy balance fluxes: Uncertainties and comparison with previous works..... | 122 |
| 5.5.2 Drivers of ablation | 125 |
| 5.5.3 Long-term ablation and surface mass balance..... | 127 |
| 5.6 Conclusions..... | 129 |
| 5.7 References..... | 131 |

Chapter 6

Projected increases in surface melt and ice loss for the Northern and Southern Patagonian Icefields 140

| | |
|--|-----|
| 6.1 Abstract..... | 141 |
| 6.2 Introduction | 141 |
| 6.3 Results | 145 |
| 6.3.1 Historical SMB..... | 145 |
| 6.3.2 Equilibrium-Line Altitudes | 146 |
| 6.3.3 Projected changes in SMB and ELAs..... | 147 |
| 6.3.4 Annual time series and trends in accumulation, melt and sublimation | 150 |
| 6.3.5 Ice loss and contribution to sea-level rise..... | 151 |

| | | | |
|---|--|-----|------------|
| 6.4 | Discussion..... | 152 | |
| 6.5 | Conclusions..... | 155 | |
| 6.6 | Data and methods..... | 156 | |
| 6.6.1 | RegCM4.6 simulations | 156 | |
| 6.6.2 | Energy balance modelling | 157 | |
| 6.6.3 | Snow accumulation | 158 | |
| 6.6.4 | Ice loss estimation and contribution to sea-level rise | 158 | |
| 6.7 | References..... | 159 | |
| Chapter 7 | | | |
| Discussion and Conclusions | | | 164 |
| 7.1 | West-east ablation spatial differences..... | 164 | |
| 7.2 | West-east accumulation spatial differences | 169 | |
| 7.3 | Implications for glacier modelling | 171 | |
| 7.4 | Surface mass balance feedbacks | 172 | |
| 7.5 | Future Work | 173 | |
| 7.6 | Conclusions..... | 174 | |
| List of References (Chapters 1, 2 and 7) | | | 177 |
| Appendix | | | |
| Supplementary Information..... | | | 189 |
| A.1 | Chapter 3. Air Temperature Characteristics, Distribution and Impact on Modeled Ablation for the South Patagonia Icefield ... | 189 | |
| A.2 | Chapter 4. Assessing Snow Accumulation Patterns and Changes on the Patagonian Icefields..... | 193 | |
| A.3 | Chapter 5. Drivers of surface ablation on the Southern Patagonian Icefield..... | 204 | |
| A.4 | Chapter 6. Projected increases in surface melt will drive future changes in the Patagonian Icefields..... | 212 | |

List of Tables

| | |
|--|-----|
| Table 1.1 Compilation of previous energy balance fluxes estimation in Patagonia at point-scale and distributed. | 7 |
| Table 1.2 Area estimate of the glaciers of the study area by different inventories. | 14 |
| Table 1.3 Area change estimates for the glaciers of the study area. | 15 |
| Table 1.4 Geodetic mass balance for the glaciers in the northern sector of the SPI. Units are m w.e. | 16 |
| Table 3.1 Details of the location, period of measurements and sensor characteristics of the five AWSs and the three GBL stations. The name of each AWS is the official name given by the DGA (www.dga.cl). | 30 |
| Table 3.2 Mean seasonal lapse rate at hourly time step for each season. Spring is October to December, summer is January to March and fall April to June. Number of cases are indicated by n and number of thermal inversions episodes (abbreviation t.i.) in brackets. The table include data from multi-linear regression of air temperature observations against elevation where parenthesis indicate the R^2 relationship. Also data obtained between each pair of AWS is shown (stepwise). | 38 |
| Table 4.1 Details of the two UDGs at the GBL stations. | 67 |
| Table 4.2 Annual mean and standard deviation 1980-2015 of the snow accumulation values by zone and PPM. | 74 |
| Table 4.3 Comparison of previous snow accumulation estimates using ice core data with the snow accumulation obtained in this work. Note that periods for each comparison are different. | 80 |
| Table 5.1 Locations and details of the sensors for each AWS. n/a are not available measurements. | 107 |
| Table 5.2 Methods, assumptions and approach references used to distribute the meteorological data over the glaciers on the SPI. | 110 |
| Table 6.1 Comparison of the ELA per sub-zone obtained in this work with those obtained by observations of the end of summer snowline using satellite images ^{3-5,39-41} and by SMB modelling ^{23,25} . Previous values are the mean of several glaciers observed. Number of glaciers are variable depending availability in the references. The lower limit in this work was obtained using a higher glacier cooling effect and the upper limit was obtained using lower glacier cooling. In bold are the closest ELA values of this work comparing with the previous observations and estimations. | 147 |

| | |
|---|-----|
| Table 6.2 Range of difference in the mean long-term ELA per sub-zone between historical period and each RCP scenario. ELA was obtained as the long-term mean of the elevation where the SMB reach 0 m w.e. The range of difference at each scenario is given by the runs using -1°C and -3°C of cooling effect as meteorological observations suggests ¹⁸ . Following Table 6.1, bold values denote values that most closely approach actual conditions observed in SPI in terms of glacier cooling effect and ELA. | 149 |
| Supplementary Table 3.1 Correlation (Pearson r) matrix of the hourly time series of air temperature for the five AWS and three snow sensor. Time series of GBL3 with GBL1 and GBL2 do not coincide. All the values are significant ($p < 0.01$). | 192 |
| Supplementary Table 3.2. Comparison of the observed and estimated melt at GBL1 and GBL2 locations. Estimated melt is using the DDM. | 192 |
| Supplementary Table 4.1 Mean and standard deviation (inter-annual variability) of the snow accumulation values by season, zone and PPM in the period 1980-2015. | 202 |
| Supplementary Table 4.2 Maximum and minimum values of the mean snow accumulation values (1980-2015) by season, zone and PPMs. | 203 |
| Supplementary Table 5.1 Fixed surface roughness for albedo range depending on the surface type. | 207 |
| Supplementary Table 6.1 Comparison of geodetic mass balance and modelled surface mass balance estimated in this work in the NPI. For those period started in 2000/01, we used values of the historical period until 2004 and then to complete the comparison period, we used the values for each scenario. | 213 |
| Supplementary Table 6.2 Comparison of geodetic mass balance and modelled surface mass balance estimated in this work in the SPI. For those period started in 2000/01, we used values of the historical period until 2004 and then to complete the comparison period, we used the values for each scenario. | 213 |

List of Figures

| | |
|--|----|
| Figure 1.1. Location of the Patagonian Icefields in southern South America. Inset corresponds to regional context of the location in South America. Base maps were taken from ESRI and red rectangle correspond to the zone showed in Figure 2.2..... | 13 |
| Figure 1.2 Glaciers in the northern sector of the SPI. a) Calving front of the O'Higgins Glacier, b) Calving front of Chico Glacier and c) View to the west from the plateau at the location of HSNO (Figure 1.4). Photos by the Author..... | 14 |
| Figure 1.3 Different stages of the calving event at the front of O'Higgins Glacier in the austral autumn of 2017. The blue line indicates the position of the intact glacier terminus. Images obtained from www.planet.com..... | 16 |
| Figure 2.1 Schematic representation of the steps taken in the present research. | 17 |
| Figure 2.2 Location of the AWSs (orange triangles) and ultrasonic depth gauges (GBL1, GBL2, and GBL3, red circles) on the plateau of the SPI. Glacier outlines in green and contour lines in blue every 200 m. The satellite image is a Landsat 8 OLI from 1 April 2014. | 19 |
| Figure 2.3 AWS installed in the surrounding (GT and GO) and on the plateau (HSNO, HSG, HSO) of the SPI. Photos by Claudio Bravo (HSNO, HSO), Alejandro Silva (GT, HSG) and Jonathan Oberreuter (GO)..... | 19 |
| Figure 3.1 (a) Spatial configuration of the AWSs (red triangles) and ultrasonic depth gauges (GBL1, GBL2, and GBL3). Glacier contours (blue lines) are from De Angelis (2014). Purple line is the profile in (b). The satellite image is a Landsat from 8 April 2014. Contour lines are 400 m spaced. (b) Longitudinal profile of the elevations of AWS and sonic ranges. Bedrock topography is derived from thickness observed data from Gourlet et al. (2016, black line) and thickness modelled data from Carrivick et al. (2016, green line). Dashed black line represents the ice divide. SRTM = Shuttle Radar Topography Mission; AWS = automatic weather station..... | 29 |
| Figure 3.2 (a) Time series of the mean daily temperature of the five automatic weather stations (AWSs) and the three snow sensors. Sensors are located 2 m above the ground, except GBL1 located at 1.2 m. Gray shadows correspond to the minimum and maximum values in each day. The order from top to bottom is from west to east. Note that y axis is different between plots. (b) Hourly mean for each AWSs for the period 25 October 2015 to 15 February 2016 and (c) hourly mean for each AWSs for the period 10 October 2016 to 30 June 2016. | 36 |

Figure 3.3 (a–f) Monthly boxplot of the lapse rates (LRs) estimated for each pair of automatic weather station. Upper and lower box limits are the 75% and 25% quartiles, the red horizontal line is the median, the filled green circle is the mean, and crosses are outlying values. As a reference, the environmental lapse rate and the dry adiabatic lapse rate are indicated. For (e) note the different y axis scale (dashed lines correspond to the range in all other panels). The gray line corresponds to zero lapse rate. (a) GT-HSNO; (b) HSNO-HSG; (c) West, GT-HSNO-HSG; (d) GO-HSO; (e) HSO-HSG; and (f) East, GO-HSO-HSG. 38

Figure 3.4 Scatterplot of the observed air temperature and the estimated air temperature using the variable lapse rate method. Locations are (a) GBL1, (b) GBL2, and (c) GBL3. Colored according to the relative humidity observed at HSG. Black line is the best fit, and the dashed line is the one-to-one relation. GBL = glacier boundary layer. 39

Figure 3.5 Mean air temperature for each method to distribute the air temperature on both sides of the South Patagonia Icefield. Color bar units are in degrees Celsius. Elevation contour lines interval 200 m. The top row shows the west side, and the bottom row shows the east side. ELR = environmental lapse rate; MLR = mean observed lapse rate; VLR = variable lapse rate..... 41

Figure 3.6 Melt differences between each of the methods used to distribute the air temperature using a range of DDF in a simple degree-day model. Upper panels correspond to the west side, and lower panels correspond to the east side. Note that at east side the lowest elevation is 250 m above sea level. ELR = environmental lapse rate; MLR = mean observed lapse rate; VLR = variable lapse rate; DDF = degree-day factor..... 43

Figure 3.7 Results of the point-scale energy balance: (a) Estimated mean energy fluxes using different air temperature distributions schemes. (b) Observed radiation fluxes. (c) Estimated cumulative melt and sublimation and observed ablation at GBL1 and GBL2 locations. Shadowed area corresponds to the range of snow densities observed at both locations. (a)–(c) On the west side at the location of HSNO. (d)–(f) On the east side at the location of HSO. Note that in (c) and (f) sublimation is on different scales. VLR = variable lapse rate; GBL = glacier boundary layer; SWR = shortwave radiation; LWR = longwave radiation. 44

Figure 4.1 (A) Regional climatic setting over the Patagonian region. Colors correspond to the predominant Köppen-Geiger climate classification for Patagonia (Beck et al., 2018) and the red rectangle corresponds to the study area. (B) SRTM topography at 1 km resolution of the study area and locations of some glaciers mentioned in the text, and (C) localization of the observations (Ultrasonic Depth Gauges) used in this work. The satellite image was acquired by Landsat 8 (OLI) on the 8 April 2014. 64

| | |
|---|-----|
| Figure 4.2 1980–2015 annual mean value of snow accumulation (mm w.e.) for each PPM. (A) 2C, (B) WE, (C) SC, and (D) DI method. Icefield contours in black were obtained from RGI consortium (2017) and edited using a Landsat 8 image (OLI) of the 8 April 2014. Coastlines are in gray..... | 73 |
| Figure 4.3 1980–2015 maximum mean value of snowfall for each PPMs. | 74 |
| Figure 4.4 Annual cycle of snow accumulation for the sub-regions of both Patagonia Icefields. (A) 2C, (B) WE, (C) SC, (D) DI..... | 75 |
| Figure 4.5 Seasonal trends 1980–2015 in mm w.e. yr ⁻¹ for three Phase Partitioning Methods. Points indicate statistically significant trend ($p < 0.05$). (A) Summer, (B) Autumn, (C) Winter and, (D) Spring. Icefield contours are in black and coastlines in gray. | 76 |
| Figure 4.6 Seasonal time series and trends of the snow accumulation for six sub-regions of the study area using the DI method. (A) Summer, (B) Autumn, (C) Winter and, (D) Spring. The legend also indicates the annual trend. | 77 |
| Figure 4.7 Comparison of accumulated snowfall using four PPMs and observations at (A) GBL1 and (B) GBL2. The correlation coefficient (r) values of each method are calculated in comparing with the observations..... | 78 |
| Figure 4.8 Comparison of annual snow accumulation using the four PPMs and estimates from Weidemann et al. (2018). (A) Distributed mean at Grey Glacier, and (B) distributed mean at Tyndall Glacier. | 81 |
| Figure 4.9 Observed elevation changes in the period 2000–2014/2015 for both icefields vs. the accumulation-area ratio (AAR). The color represents the snow accumulation trends by glaciers using the 2C as PPM. Terminus type is also indicated depending the color of the contour for each symbol, triangle for the SPI, and circle for the NPI (see legend). Note that the x-axis is broken. Due to space issues some glaciers names are not indicated. | 88 |
| Figure 5.1 (a) Southern South America, NPI and SPI are the Northern and Southern Patagonian Icefields, respectively. (b) Southern Patagonian Icefield overlying a hillshade map of the region obtained from SRTM. (c) Study area and locations of the observational network in a Landsat 8 OLI acquired the 1 of April 2014. Symbols are Automatic Weather Stations (triangles) and on-glacier air temperature sensors (GBL, red circles). Image coordinates are UTM18-S, WGS-1984..... | 105 |
| Figure 5.2 Boxplot summaries of the hourly observed meteorological variables in the SPI during the period October 2015 to June 2016. Data used in the incoming shortwave radiation boxplots (e) correspond to daytime hours..... | 112 |

| | |
|---|-----|
| Figure 5.3 Spatially distributed mean values of the meteorological variables. Numbers shown in each variable map represent mean glacier-wide values for each side of the Icefield. White lines are the glacier divide and black lines are contour lines at an interval of 200 m. Coordinates are in m, UTM18-S, WGS-1984. | 113 |
| Figure 5.4 Comparative forcing of the cloud factor on the incoming shortwave and longwave radiation observed at HSNO (a) and HSO (c). Panels (b) and (d) show histograms of the cloud factor estimated at the same AWSs. TOA is top of atmosphere. | 115 |
| Figure 5.5 Distributed mean values of the energy balance fluxes estimated over the period October 2015 – June 2016. Values are the mean glacier-wide for each flux. White lines are the glacier divide and black lines are contour lines at an interval of 200 m. Coordinates are in m, UTM18-S, WGS-1984. | 117 |
| Figure 5.6 Mean values of the energy balance fluxes per elevation range and margin of the SPI during the period between October 2015 and June 2016, (a) West and (b) East. For reference, hypsometric curves (grey continuous line) estimated using the TanDEM-X with the accumulated area in the bottom axis are showed and the mean elevation of the isotherm 0°C (segmented line). | 118 |
| Figure 5.7 Total modelled melt and sublimation over the whole period. (a) West, melt and sublimation vs elevation. The colour of each melt point denotes the albedo used in the EB model and the grey line is the glacier hypsometry with the area (upper axis) per 100 m bin. (b) Map of the total melt, (c) Map of the total sublimation and (d) same as (a) but for the eastern margin glaciers. | 120 |
| Figure 5.8 Extended time series of ablation (a), accumulation (b) and surface mass balance (c) calculated with data from re-analysis ERA5-Land and regional model RegCMv4 in the case of the accumulation. Error bars show the uncertainties in the estimations. These data are representative of the 2014 glacier area. | 122 |
| Figure 6.1 Location of the NPI and SPI in Southern South America (a). Details of the NPI (b) and the SPI (c). Colour shading is the topography from SRTM and blue tones are lakes and fjords. In the NPI the main glaciers per each sub-zone are: San Rafael and San Quintin (NW), Exploradores, Soler and Nef (NE), Steffen and Acodado (SW) and Colonia, Pared Norte and Pared Sur (SE). In the SPI: Jorge Montt, Témpano, Bernardo, Occidental and Greve (NW), O’Higgins and Chico (NE), Pio XI, HPS12, HPS13, Europa and Guilardi (CW), Viedma and Upsala(CE), Calvo, Asia and Amalia (SW) and Perito Moreno, Grey and Tyndall (SE). | 144 |

| | |
|---|-----|
| Figure 6.2 Time series of the modelled surface annual mass balance. (a) NPI and (b) SPI. Colour shadow represent the uncertainties in the modelled SMB for the historical period and the two scenarios. This is mainly due to the parametrization of the glacier cooling effect and the method used for the phase partitioning in the total precipitation to define the surface snow accumulation. Green coloured bars indicate previously derived geodetic mass balances and their error range previously estimated in NPI ^{3,4,6,8-12} and in the SPI ^{3,5,7,9-12} . Trends with the 95% confidence interval are shown. Significant trends are also indicated when $p < 0.05$ | 146 |
| Figure 6.3 Surface mass balance differences per sub-zone (Figure 6.1) and elevation range in both Icefields. The differences were derived by comparing long-term SMBs between the historical period and each RCP scenario. | 149 |
| Figure 6.4 Annual values (hydrological years 1976/77-2049/50) and linear trends of the SMB components in m w.e. in NPI and SPI for the historical period and the two pathway scenarios. (a),(c) and (e) are accumulation, melt and sublimation in the NPI and (b),(d) and (f) are accumulation, melt and sublimation in the SPI. Trends with the 95% confidence interval are shown. Significant trends are also indicated when $p < 0.05$. Trends in melt for RCP2.6 are significant where estimated between 1976 and 2050, reaching 0.027 ± 0.012 m w.e. in NPI and 0.0204 ± 0.009 m w.e. in SPI. | 151 |
| Figure 6.5 Cumulative ice loss estimated for both Icefields combined between 2012 and 2050 (a) and total equivalent sea-level contribution to year 2050 (b). For comparison purposes, data from GlacierMIP ⁴³ is showed (grey area). GlacierMIP ice mass loss corresponds to all the models runs under scenarios RCP2.6 and 8.5 computed for the Southern Andes RGI region. Ice mass loss estimations by Abdel-Jaber et al. ¹² and Foresta et al. ⁹ for the four first years (2012-2016) are also shown. Inset, corresponds to a detailed view of this period. | 152 |
| Figure 6.6 Spatially distributed melt trends over the Patagonian Icefields estimated with the EBM. Trends are from hydrological year 1976/77 to 2049/50, following after 2005 the pathway scenario RCP2.6 (a) and the pathway scenario RCP8.5 (b). Black lines are the glacier basins and grey lines are coast lines. All the grid points are significant ($p < 0.05$). | 155 |
| Figure 7.1 Profile of the mean melt (a) and sublimation (b) per 100 m elevation bin, obtained for the northern glaciers of the SPI during the period between October 2015 and June 2016. | 165 |

Figure 7.2 Semi-quantitative schematic representation of the meteorological and glaciological conditions along the west-east transect on the northern SPI during the period between October 2015 and June 2016. Mean values were obtained per 100 m elevation bin, for the northern glaciers of the SPI. Panel (a) shows the relative humidity and the location of the AWS. Panel (b) shows the wind speed. Arrows represent the predominant observed wind direction. Panel (c) is the surface and air temperature. Mean air temperature lapse rates at each margin are indicated. Panel (d) shows the energy fluxes obtained with the energy balance modelling. Panel (e) is the modelled albedo. SGM corresponds to the surface area where the supra-glacial moraine influence albedo. Panel (f) is the melt and sublimation. Panel (g) is the hypsometry, showing the accumulated area versus elevation. The red area corresponds to the zone under predominant melt and the green area is a qualitative representation of the glacier cooling effect. EOSS corresponds to the end-of-summer snowline observed with a satellite image acquired on 12th March 2016 and the ELA is the mean value of several previous studies. The grey area corresponds to those elevations of the Icefields where the meteorological variables were extrapolated based on the lower elevations observations..... 166

Figure 7.3 Comparison between glacier-wide mean air temperature and glacier-wide mean melt using a Distributed-Degree Day model. Each point represents the mean values for ELR, MLR, VLR, VLRBias and SM10 (Chapter 3) and the lines the regression using a Degree-Day Factor (DDF) of 8.5 mm w.e. °C⁻¹ d⁻¹. Shadow area represents the boundary of the linear regression of the melt using a DDF between 10 mm w.e. °C⁻¹ d⁻¹ (upper limit) and 3.5 mm w.e. °C⁻¹ d⁻¹ (lower limit)..... 167

Figure 7.4 Relationship between geodetic mass balance and AAR for glaciers in the NPI (a) and in the SPI (b). Symbols indicated the front characteristic of each glacier. Glaciers of the western side of the NPI are Acodado, Andree, Benito, Fraenkel, Gualas, HPN1, Reichert, San Quintin, San Rafael, Strindberg and Steffen. Glaciers of the eastern side of the NPI are Arco, Cachet, Cachet Norte, Colonia, Cristal, Fiero, Hyades, Leones, Mocho, Nef, Soler, U-4, U-5, U-6, U-7, Exploradores, Grosse, Pared Norte and Pared Sur. Glaciers of the western side of the SPI are Amalia, Asia, Bernardo, Calvo, Europa, Greve, Guilardi HPS8, HPS9, HPS10, HPS12, HPS13, HPS15, HPS19, HPS28, HPS29, HPS31, HPS34, HPS38, HPS41, Jorge Montt, Occidental, Ofhidro, Penguin, Pio XI and Témpano. Glaciers of the eastern side of the SPI are Agassiz, Ameghino, Balmaceda, Bravo, Chico, Frias, Grey, Dickson, Lucia, Mayo, Mellizo Sur, O'Higgins, Onelli, Oriental, Pascua, Perito Moreno, Pingo, Spegazzini, Tyndall, Upsala and Viedma..... 169

| | |
|--|-----|
| Figure 7.5 Profile of the differences of the total snow accumulation per 100 m elevation bin, obtained for the northern glaciers of the SPI during the period between October 2015 and March 2016 using ERA5-Land reanalysis..... | 171 |
| Supplementary Figure 3.1 Estimated distance flow path length (upper).Below, parameters used by Shea and Moore (2010) and Shaw et al. (2017) to distribute the air temperature. Also as comparison purposes, the parameters observed at GBL1, GBL2 and GBL3 are included. The flow pat length is defined as “the average flow distance to a given point starting from an upslope limit or ridge” (Carturan et al., 2015). In our estimation we first define the ridges. As shows in Figure, not all the ice divide was considered as a ridge. The ice divide between east and west was considered and also those ridge with a higher slope (e.g. Pirámide and Chico glaciers in the east, Unnamed and HPS8 in the west). The northern ice divide of Témpano glacier was not considered as this area is almost flat and is difficult to define the exact point of the ice divide. The same situation was assumed between the ice divide of Témpano-Occidental and Occidental-Greve. After we define the “ridge” zone we calculate the distance using the SRTM DEM and the “Path Distance” tool in ArcMap® 10.4. | 190 |
| Supplementary Figure 3.2. Mean monthly air temperature compared with elevation for all the AWS and GBL (black line) and mean monthly lapse rate for different spatial configurations (color line). Light grey, grey and dark grey lines are the mean daily air temperatures at the west, east and on-glacier, respectively..... | 191 |
| Supplementary Figure 3.3 Relation between observed relative humidity and wind speed in the tongues of each side in the South Patagonia Icefield..... | 191 |
| Supplementary Figure 4.1 a) RegCM4.6 topography at 10 km resolution, b) and c) comparative hypsometric curves of the icefields using 1 km SRTM topographic data and data from a). | 193 |
| Supplementary Figure 4.2 1980-2015 annual mean value of accumulation type for DI PPM. a) sleet and b) snow plus sleet. Red line corresponds to the Icefields limits and glaciers. | 194 |
| Supplementary Figure 4.3 Seasonal trends 1980-2015 in mm w.e. yr-1 for three PPMs using Sen’s slope method. (a) Summer, (b) Autumn, (c) Winter and (d) Spring. Statistically significant trend ($p < 0.1$ and $p < 0.05$) are also shown. Icefields contours in black..... | 198 |
| Supplementary Figure 4.4 Boxplot of the ERA-Interim zonal wind for a region covering the Icefields for calendar years 2001 to 2005 at two pressure levels of 700 hPa and 850 hPa..... | 199 |
| Supplementary Figure 4.5 (a) Spatial distribution of 36-year (1980-2015) mean annual, DJF and JJA average of 850hPa zonal wind speed (m/s) from ERA-Interim and RegCM4. (b) 36-year (1980-2015) mean annual cycle of 850hPa zonal wind speed (m/s) from ERA-Interim and RegCM4 for a region covering the Icefields..... | 200 |

| | |
|--|-----|
| Supplementary Figure 4.6 Seasonal trends 1980-2015 for the near surface air temperature obtained from RegCM4.6. Colorbar in in °C yr-1. Note that each season show a different scale in the trends. Icefields limits in white and coastlines in black..... | 201 |
| Supplementary Figure 5.1 Bulk atmospheric transmissivity on the west side of the Southern Patagonian Icefield..... | 204 |
| Supplementary Figure 5.2 Comparison of the observed albedo using Landsat-8 satellite images (a) and modelled albedo using Oerlemans and Knapp (1998) approach (b). Albedo values on supraglacial moraine is prescribed..... | 209 |
| Supplementary Figure 6.1 . Annual air temperature anomalies over NPI (a) and SPI (b) for both scenarios (RCP2.6 and 8.5) estimated with respect to the mean of the historical period (1976-2004). | 212 |

List of Abbreviations

| | | |
|---------|---|--|
| AAR | - | Accumulation-Area Ratio |
| AWS | - | Automatic Weather Station |
| ELA | - | Equilibrium-Line Altitude |
| ELR | - | Environmental Lapse Rate |
| GBL | - | Glacier Boundary Layer air temperature station |
| LR | - | Air temperature lapse rate |
| NPI | - | Northern Patagonia Icefield |
| PPM | - | Phase Partitioning Method |
| SM10 | - | Shea and Moore (2010) air temperature distribution |
| SMB | - | Surface Mass Balance |
| SPI | - | Southern Patagonia Icefield |
| SRTM | - | Shuttle Radar Topography Mission |
| UDG | - | Ultrasonic Depth Gauges |
| VLR | - | Variable Lapse Rate |
| VLRbias | - | Variable Lapse Rate bias corrected |

Chapter 1 Introduction

1.1 Introduction

Glaciers are important indicators of climate change (Mackintosh et al., 2017) and have shown almost ubiquitous negative mass changes between 1961 and 2016 (Zemp et al., 2019). In western South America, the Andes extend 8000 km from north to south, and comprise more than 31000 km² of glacierized area (Braun et al., 2019). Between 2006 and 2016, glaciers in this region showed more negative specific mass changes than any other region in the world (Zemp et al., 2019). These glaciers are located under a great variety of topographic and climatic conditions, resulting in numerous mountain glaciers, rock glaciers, ice-caps and ice-fields, located in tropical, dry and wet climate conditions, and spanning elevations from sea level to over 6000 m a.s.l. (Dusallant et al., 2019; Masiokas et al., 2020).

In southern South America lies Patagonia (40° S – 55° S), a region with a remarkable concentration of ice masses. Here, inventory work has characterised mountain glaciers (e.g. Falaschi et al., 2013; Casassa et al. 2002, 2014; Masiokas et al., 2015; Barcaza et al., 2017; Meier et al., 2018; Zalazar et al., 2020), ice-caps (e.g. Schneider et al., 2007a) and three ice-fields: Northern Patagonian Icefield (NPI, e.g. Aniya, 1988; Rivera et al., 2007), Southern Patagonian Icefield (SPI, e.g. Casassa et al., 2014) and Cordillera Darwin (CD, e.g. Bown et al., 2014). It has been widely recognized that glaciers in Patagonia are shrinking rapidly (Davies and Glasser, 2012; White and Copland, 2015; Malz et al., 2018; Foresta et al., 2018; Abdel-Jaber et al., 2019; Dusallant et al., 2018, 2019), being the Andean sub-region with the greatest rates of glacier surface lowering (Braun et al., 2019). Despite their notoriety, empirically-based studies that characterize the fundamental glacier conditions are scarce in this region. Consequently, our understanding of how the glaciers are responding to changes in climate, and what the key controls are, is limited (Pellicciotti et al., 2014).

The main reason for this dearth of empirical data is associated with the sparsity of in-situ long-term meteorological observations, especially on the plateaus of the Icefields, where extreme weather conditions prevail throughout most of the year. High uncertainty therefore exists in previous modelling efforts, as no on-glacier observations have been available to validate the driving meteorological variables (e.g. Schaefer et al., 2013, 2015; Lenaerts et al., 2014; Mernild et al. 2016).

Air temperatures are projected to continue to rise over coming decades across the Andes (Huss et al., 2017; Pabón-Caicedo et al., 2020). Additionally, the frequency of extreme events that dramatically accelerate the ice loss as the strong El Niño event around 2016 (Li et al., 2019) are projected to increase in the future (Wang et al., 2017), impacting the inter-annual variability of the precipitation in this region. As a consequence, glaciers in Patagonia are likely to increase in ablation and/or reduce accumulation, inducing high thinning and negative mass balances, as has been observed in past decades (e.g. Rignot et al., 2003; Braun et al., 2019; Dusaillant et al., 2019). This ice volume loss has led to a changing landscape in Patagonia. In addition to the rapidly receding glacier tongues (Lopez et al., 2010; Rivera et al., 2012; Davies and Glasser, 2012; White and Copland, 2015), other consequences have been described and analysed at different spatial scales: an increase in both area and number of glacial lakes (Loriaux et al., 2013, Wilson et al., 2018, Shugar et al., 2020), an increase in landslide occurrence and glacial-lake outburst flood (GLOFs) events (Dusaillant et al., 2010, Wilson et al., 2018, Iribarren-Anacona et al., 2015), an increase in debris-covered area over ice surfaces (Glasser et al., 2016), and impacts on aquatic ecosystem and sediment dynamics (Gutierrez et al. 2015; Quiroga et al., 2016).

The improve of the understanding of the mechanisms controlling surface mass balance has also societal implications in terms of water resources. An increase demand on water resources for irrigation, domestic consumption and industrial activities has been recognized in southern South America and glacier meltwater are recognized as one of the main supplies (Immerzeel et al., 2020). This can be particularly critical in the basins in the Atlantic coast that depends on the rivers feeder by glacier meltwater and where a medium to high water risk has been determined (Schoolmeester et al., 2018).

In summary, appropriate knowledge of the processes and meteorological controls on the surface mass balance, its components and spatial differences are necessary to increase the confidence in models that simulate the behaviour of the glaciers in Patagonia. In attempting to fill this knowledge gap, this thesis focuses on 1) characterising the meteorological conditions and controls on the surface ablation and accumulation at both sides of Patagonian Icefields, 2) assessing how Patagonian glaciers respond to atmospheric forcing changes and its spatial variability and 3) quantifying changes in glaciological parameters due to projected scenarios of climate change.

1.2 Glacier response to atmospheric changes

Glaciers are strongly coupled to the atmosphere, which importantly defines the inputs and outputs of the glacier system and its response. Glacier response depends primarily on the regional climate setting as well as on the local climate characteristics (Cuffey and Paterson, 2010). For instance, high-precipitation (e.g. maritime) glaciers are more sensitive to air temperature fluctuations than glaciers located in dry environments (e.g. continental types). Due to the relatively large mass turnover in maritime environments, small changes in air temperature can cause large changes in accumulation (Mackintosh et al., 2017). However, sensitivity depends on the time scale of analysis, as changes in the Southern Westerly Winds with associated changes in precipitation have driven glacial advances in the past over southern South America (Davies et al., 2020).

The exchange in mass over a glacier surface, i.e. the surface mass balance (SMB), defines the glacier-wide mass gain or loss (Cuffey and Paterson, 2010). The glacier mass balance quantifies the relationship between accumulation and ablation during a hydrological year. In Patagonia, where the glaciers can be considered temperate (Masiokas et al., 2020), accumulation is associated with snowfall from low-pressure systems as well as orographic processes. In turn, ablation is controlled by the surface energy balance, which defines melt as the primary ablation mechanism. Overall, shortwave radiation is the primary energy source for melt, but interannual variability in mass balance depends mainly on air temperature (Mackintosh et al., 2017).

An important issue to note is that glaciers located in different climatic settings can respond with great diversity to the same climate perturbation (Sagredo and Lowell, 2012). In Patagonia, winter and summer precipitation and summer temperatures are the most important determinants of the mass balance and the position relative to the coast is also relevant (Cook et al. 2003). According to Cook et al. (2003), on the western side of the icefields, the high precipitation rates dominate the surface mass balance, while on the eastern side, ablation mechanisms were deemed more important. In particular, glaciers to the east showed enhanced sensitivity to air temperature, wind speed and humidity. On the other hand, it has also been stated that glaciers in a wetter environment (i.e. those to the west of the icefields), are sensitive to temperature fluctuations because ablation is dominated by melt (Sagredo et al., 2012). Patagonian glaciers are generally in the elevation range of the 0°C isotherm, meaning that changes in temperature cause a 'double effect'. First, less or more energy is available for melt. Secondly, a small decrease in air temperature below 0°C

during the accumulation season alters the partitioning between rain and snow, thus impacting on a glacier's net mass balance (Rodbell et al. 2009).

In terms of changes to the Equilibrium-Line Altitude (ELA), the amount of precipitation required to compensate its rise within a forcing of 1°C is ~33%, which means that future precipitation changes in Patagonia could also play an important role in the mass balance (Sagredo et al., 2014). Unfortunately, the works of Sagredo and Lowell (2012) and Sagredo et al. (2014) did not include a comparative analysis of the sensitivities of glaciers located between the west and east margins over the Patagonian Icefields, concentrating their analysis within the latitudinal gradient that defines the climate regions where glaciers exists. There remains, therefore, considerable uncertainty on exactly what the controls are on glaciers to either side of the topographic divide, and their relative importance.

1.3 Mass balance measurements, modelling and meteorological observations on the Patagonian Icefields

Field-based mass balance measurements and on-glacier meteorological observations are lacking for both Patagonian Icefields, primarily because of the extreme weather conditions. Nevertheless, valuable data exists dating back to the 1980s, thanks to the periodic field campaigns of Japanese research teams, focussing first on the NPI, and subsequently the SPI. The results of each campaign were published in the Bulletin of Glaciological Research (<https://web.seppyo.org/bgr-en>), which compiled reports describing the meteorological observations as well as some estimations of surface mass balance and energy balance fluxes (e.g. Ohata et al., 1985a and 1985b; Fukami and Naruse, 1987; Kondo and Inoue, 1988; Koizumi and Naruse, 1992; Takeuchi et al., 1995, 1996). These publications were invaluable for providing the long-term context in which the analysis of this thesis sits.

There are some additional early observations available for the SPI, mostly concentrated along the eastern margin due to its relatively easy access. Observations exist on the Perito Moreno Glacier (Takeuchi et al., 1999; Stuefer et al, 2007; Rott et al., 1998), Upsala Glacier (Naruse et al., 1997), Tyndall Glacier (Koizumi and Naruse, 1992; Takeuchi et al., 1999) and Chico Glacier (Rivera, 2004). Though temporally limited (mostly to single ablation seasons) the observations have been used to calculate melt, using degree-day models. For instance, at Chico Glacier, Rivera (2004) estimated the surface mass balance using the glaciological method. Ablation towards the terminus of the glacier (~250 m a.s.l.) reached a mean value of 16.1 m w.e. yr⁻¹ for the period 1994/95 to 2001/02, decreasing almost linearly up to 1500

m a.s.l. where the ablation reached 4 m w.e. yr⁻¹. At higher elevations, the ablation reduced more gradually. Three stakes located at 1445, 1577 and 1833 m a.s.l., were used to estimate the accumulation (Rivera, 2004). The values reached 9.63±1.36 m w.e. yr⁻¹ at the highest stake and 4.07±0.54 m w.e. yr⁻¹ at the lower stake. These distributions indicate an exponential relationship between precipitation and elevation.

Further accumulation estimations have been derived from ice core analysis. Schwikowski et al. (2013) estimated a mean annual accumulation of 5.8 m w.e. in the accumulation zone of Pio XI Glacier (~2600 m asl) within a range of 3.4-7.1 m w.e. These values are somewhat subdued compared to other (modelled and observed) datasets, and suggest that even at the flat plateau of the Pío XI site, the influence of snowdrift and wind erosion cannot be excluded.

In the NPI, Koppes et al. (2011) used a combination of the sparse observations and climate re-analysis data to estimate the mass balance of the San Rafael Glacier between 1950 and 2005. A compilation of these works, their results and an analysis of the degree-day factor approach was presented and discussed by Fernandez and Mark (2016).

Modelling efforts have largely focussed on estimating the energy balance fluxes (see Table 1.1 for a summary). These studies are also limited in number, and undermined to an extent by a lack of calibration/validation data, but they provide the historical context for the calculations presented in subsequent chapters. In particular, and as described above, Ohata et al. (1985a,b), Kobayashi and Sato (1985), and Kondo and Inoue (1988) used field data to drive analyses of the energy fluxes and their spatial variability, comparing those estimated for San Rafael Glacier (46.7°S) to the west of the NPI, with those derived for Soler Glacier (46.9°S) on the eastern side of the NPI. The key finding was that the Soler Glacier presented favourable conditions for strong föhn events increasing the turbulent exchange when compared to the San Rafael Glacier, and that overall, net shortwave radiation was the main source for melt followed by the sensible heat flux. Konya and Matsumoto (2010) focussed specifically on energy fluxes in Exploradores Glacier in the NPI and under different weather conditions, finding that during cloudy/rainy days the turbulent fluxes exceed those on clear-sky days, during which stability and weak winds prevail. As might be expected, net radiation was also larger on clear-sky days. Besides the short period, these findings underline the importance of the turbulent fluxes and melt under cloud cover, conditions that tend to prevail over the glaciers of Patagonia.

In the SPI, Takeuchi et al. (1995) similarly characterized the energy balance of the Perito Moreno (50.5°S) and Tyndall (51.3°S) glaciers during the summers of 1993 and 1994. Although the measurements were for relatively short periods of time (15-18 days), they confirmed the importance of both net radiation and sensible heat fluxes, and revealed that latent heat flux was the most variable among the studied glaciers. At long time-scales, the importance of net shortwave radiation and sensible heat flux was also confirmed by Weidemann et al. (2018) for Tyndall and Grey (51°S) glaciers. The energy balance fluxes were analysed at wide-glacier scales being the net shortwave radiation the most important contributor for melt followed by sensible heat flux.

Only recently has there been published work that analysed the energy fluxes supported by in-situ meteorological observations (Schaefer et al., 2020). One of the aims of this work was to analyse the differences in the point-scale fluxes estimated on glaciers located from Central Chile to Patagonia. In accordance with previous studies in Patagonia (Exploradores and Tyndall glaciers, Table 1.1) the turbulent fluxes were shown to be an important source of energy. The contribution of Schaefer et al., (2020) represents a major step forward in understanding of the energy fluxes, their control on surface melt and their latitudinal differences due to different climate settings in the Andes.

Table 1.1 Compilation of previous energy balance fluxes estimation in Patagonia at point-scale and distributed.

| Reference | Glacier/ Elevation | Period | Sensible heat flux [W m ⁻²] | Latent heat flux [W m ⁻²] | Net shortwave radiation [W m ⁻²] | Net longwave radiation [W m ⁻²] |
|--|------------------------------|---------------------------------|---|---|---|--|
| Point-scale, AWS | | | | | | |
| NPI | | | | | | |
| Ohata et al. (1985a,b) | San Rafael 104 m a.s.l. | 29 Dec. 1983-1 Jan. 1984 | 103 | 41 | 110 | 25 |
| Kobayashi and Saito (1985) | Soler 400 m a.s.l. | 15-29 Dec. 1983 | 138 | 82 | 181 | -100 |
| Fukami and Naruse (1987) | Soler 378 m a.s.l. | 1-5 Nov. 1985 | 64 | -9 | 86 | -24 |
| | | 25-29 Nov. 1985 | 88 | -4 | 191 | -25 |
| Kondo and Inoue (1988) | San Rafael 1045 m a.s.l. | 19-23, 30 Jan-1 Feb. 1986 | 52 | 29 | 54 | - |
| Konya and Matsumoto (2010) | Exploradores 200 m a.s.l. | 27 Dec. 2006-3 Jan. 2007* | 50 | 27 | 127*** | |
| | | 3-7 Jan. 2007** | 19 | 8 | 169*** | |
| Schaefer et al.(2020)*** | Exploradores 191 m a.s.l. | 1 Jan. - 31 Mar. 2015 | 65/51/64 | 38/32/46 | 143/141/129 | -2/-18/-10 |
| SPI | | | | | | |
| Takeuchi et al. (1995,1999) | Moreno 330 m a.s.l. | 12-27 Nov. 1993 | 126 | -9 | 138*** | |
| | Tyndall 700 m a.s.l. | 9-17 Dec.1993 | 111 | 19 | 136*** | |
| Schaefer et al.(2020)**** | Tyndall 608 m a.s.l. | 1 Jan. - 31 Mar. 2015 | 65/52/70 | 9/5/9 | 94/92/132 | -14/-30/-22 |
| | | 1 Jan. - 31 Mar. 2016 | 76/55/75 | 9/5/8 | 110/109/135 | -13/-29/-21 |
| Gran Campo Nevado | | | | | | |
| Schneider et al. (2007) | Lengua 450 m a.s.l. | 22 Feb.-13 Apr. 2000 | 86 | 12 | 57*** | |
| Glacier-wide, observations and reanalysis climate data | | | | | | |
| SPI | | | | | | |
| Weidemann et al. (2018) | Grey | 2000-2016 | 11 | -9 | 39 | -9 |
| | Tyndall | | 16 | -7 | 45 | -18 |
| Monte Sarmiento | | | | | | |
| Weidemann et al. (2020) | Schiaparelli | 2000-2016 | 32 | -10 | 26 | -5 |
| * Cloudy days / ** Clear days | | | | | | |
| *** Net radiation | | | | | | |
| **** Schaefer et al. (2020) estimated the EB fluxes using three models | | | | | | |

Further modelling has attempted to quantify surface mass balance using downscaled re-analysis and global circulation model (GCM) data to drive glacier-wide simulations.

Slightly negative to near-zero SMB conditions have generally been modelled for the NPI, but with a positive trend in recent years (Schaefer et al., 2013; Lenaerts et al., 2014; Mernild et al., 2016). However, projected (future) surface mass balances suggest that accelerating negative mass balance will prevail until the end of the century (Schaefer et al., 2013). On the contrary, in the SPI (e.g. Lenaerts et al., 2014; Schaefer et al., 2015; Mernild et al., 2016), surface mass balance has been shown to be increasingly positive over recent decades, although subdued to an extent by increases in calving losses (Schaefer et al., 2015).

At the Icefield scale, the control on surface mass balance strongly depends on the extreme orographic precipitation due to the narrow Andes barrier, as the modelling results of Lenaerts et al. (2014) suggest. This topographic high separates the west, with a wet climate, from the east, with less precipitation, as well as stronger near-surface winds and colder winters. The maximum amount of simulated annual precipitation was extremely high, reaching 10 m w.e. yr⁻¹ on the plateau (and even 30 m w.e. yr⁻¹ in the southern part of the SPI).

The west-to-east climatic and meteorological differences at the Icefield scale have been also observed by remote sensing studies. These studies have characterized the glacier surfaces and given insights into meteorological conditions, their spatial heterogeneity, and the spatial patterns of ablation/accumulation processes. For instance, the earlier onset of melt on western-facing glaciers has been described (Monahan and Ramage, 2010), partly explaining the disparity in total melt between each side of the divide. The snow facies classification of De Angelis et al. (2007) in the SPI also showed that along the western margin there were large areas of slush, as well as a greater degree of snow metamorphism associated with melt-freeze episodes, suggesting relatively warmer conditions.

While all of the investigations discussed here give important information about recently observed and future predicted glacier response, and how this will vary through space and time, limitations still exist in our understanding of the meteorological controls. Specifically, our gap is related in how the spatial differences in the meteorological conditions driven by the orographic effect impacts the ablation rates.

The knowledge that we do have is built on three main methodologies. First, on-glacier meteorological observations have been used to calculate energy balance fluxes, albeit limited to the point-scale and to very short periods. In a second group, surface mass balance calculated at the scale of the Icefields has concentrated on quantifying and discussing changes in terms of air temperature and precipitation patterns and comparing these observations with geodetic mass balance. In a third group, a minority of studies have used a combination of on-glacier observations and modelling to estimate the surface mass balance and its controls.

This thesis builds on the limited number of studies comprising the lattermost group (e.g. Weidemann et al., 2018, 2020), using a combination of meteorological observations, gridded climate data and glaciological modelling. The distinctive data input to this thesis was the observations acquired by an Automatic Weather Station network installed in the SPI (CECs-DGA, 2016). These data were used to distribute the meteorological variables, recognizing and discussing their spatial differences, and to conduct a distributed energy balance allowing a spatial analysis of the energy fluxes that control ablation. Here, the focus is to assess if the glaciers located on either side of the SPI shows different sensitivities and ablation controls due to different meteorological conditions. In a second step and in combination with gridded-climate products and other secondary sources of data, these analyses are extended to both Icefields, focusing on inferring the past, present and future response of Patagonian glaciers through the quantification of the surface mass balance and its components. The focus here is to assess how these glaciers are responding to ongoing climate change and how differently these glaciers will respond to future climate change scenarios.

1.4 Aims and Objectives

Aim

The overall aim of this thesis is to integrate on-glacier observations, climate data and glacier modelling to produce detailed and robust estimations of Patagonian glacier response to current and future climate change.

Objectives

There are four objectives that will need to be met in order to satisfy this aim:

1. to characterize meteorological conditions based on observations acquired along a longitudinal profile across the northern part of the Southern Patagonian Icefield.

2. to identify the main meteorological drivers and surface controls on ablation along this longitudinal profile.
3. to quantify the role of accumulation and its uncertainty in the surface mass balance of the Patagonian Icefields.
4. to model the surface glacier mass balance response to future climate change on the Patagonian Icefields.

In order to achieve the main goal, this thesis is structured following each of the objectives. In order to address objective 1, chapter 3 is focused on the differences in the air temperature characteristics and how these differences are important in order to quantify the ablation at point and distributed scale. Part of objective 1 as well as objective 2 are addressed in chapter 5. Here, most of the meteorological variables necessary to feed an energy balance are spatially distributed, allowing a spatial analysis of the energy fluxes that control ablation. Both, chapters 3 and 5 are largely focused on meteorological observations. To address objective 3, through the use of a regional climate model, chapter 4 is focused on recognizing the spatial differences in the accumulation rates and trends along both Icefields and how these characteristics are related with the previously estimated elevational changes over both Icefields. Objective 4 is addressed in chapter 6, where the focus is on modelling the future response of both Icefields under two pathway scenarios using a regional climate model. Finally, in chapter 7 an integrated discussion of the key findings presented in each chapter is performed.

1.5 Study Area

1.5.1 Patagonia climate

In Patagonia, there are a small number of long-standing meteorological stations (Garreaud et al., 2013) that do not adequately represent the climatology and meteorological conditions of this zone, especially at higher elevations. Data from the Climate Research Unit (Sagredo and Lowell, 2012) and the western fjord zone (Puerto Eden; 49.1°S, 74.4°W) (Carrasco et al., 2002), show that this zone is characterized by a marked seasonal temperature variation, and spatially variable precipitation patterns. In particular, south of 49°S the precipitation is equally distributed throughout the year, with slight maxima in March and April (Sagredo and Lowell, 2012), yet to the north, there is a marked annual cycle.

The longitudinal distribution of precipitation is strongly influenced by the presence of the Andes topography, which although in Patagonia is relatively subdued, still generates an extreme gradient with humid western slopes and

arid eastern slopes. At the regional scale, precipitation and the 850 hPa zonal wind are correlated positively (negatively) in the western (eastern) sector of the Andes. The mechanical effect of the mountain chain forces air to ascend in the western sector leading to saturation, and hence precipitation, while air subsidence in the east inhibits rainfall and leads to much reduced annual totals (Garreaud et al., 2013; Lenaerts et al., 2014). Between 42° and 52°S typical totals can reach 10000 mm yr⁻¹ to the west, and 300-400 mm yr⁻¹ to the east (Garreaud et al., 2013), with this zone overall being one of the best examples of orographic precipitation and shadow effect (Smith and Evans, 2007).

Precipitation changes and interannual variability strongly impact the surface mass balance of Patagonian glaciers, considering that snow is the main process of mass accumulation at these latitudes. Interannual precipitation variability responds to hemispheric scale patterns such as the Southern Annular Mode (SAM) or Antarctic Oscillation (AAO), El Niño Southern Oscillation (ENSO) and the Interdecadal Pacific Oscillation (IPO) (Garreaud et al., 2013). For instance, precipitation variability in northern Patagonia is driven largely by the different phases of ENSO events (Quintana and Aceituno, 2013), and Garreaud et al. (2013) find a strong correlation between summer precipitation and SAM.

In particular, the SAM in this zone has a significant impact on precipitation (and also on temperatures) where positive (negative) SAM are associated with higher (lower) temperatures (Gillet et al., 2006) and to a weakening (intensification) of the westerlies (Hall and Visbeck, 2002) which generates a decrease (increase) in precipitation in the study area. The SAM has shown a trend to positive values during the second half of the 20th century (Marshall, 2003) affecting the climatological characteristics, and in particular the strength of summer precipitation.

1.5.2 Climate change in Patagonia

It is generally accepted that air temperature in Chile has increased in recent decades. Although, in the Chilean Lake District region (38° - 42°S), located in the northern border of Patagonia, surface temperatures show a cooling in the second half of the 20th century; yet, in the middle to upper troposphere, radiosonde data from Puerto Montt (41.5°S) show a warming trend between 0.019°C a⁻¹ to 0.031°C a⁻¹ (Bown and Rivera, 2007). In southern Patagonia, warming of ~0.5°C in the last 40 years was detected by Rasmussen et al. (2007) using NCEP-NCAR reanalysis at 850 hPa level and Braun et al. (2019)

also detected generalized regional warming in Patagonia using ERA-Interim reanalysis.

Precipitation patterns are heterogeneous through space and time. Between 37° and 43°S, a downward trend in annual precipitation was detected from 1950. This trend was interrupted by a positive trend in the mid-70s, registered by all available stations, except between 40°S and 43°S. A negative trend then intensified in the last part of the 20th century (Quintana & Aceituno, 2012). According to Garreaud et al. (2013), a tendency for weaker westerlies has been detected at mid-latitudes (~45°S), while around 60°S an increase in westerlies prevails. This tendency in the westerlies accounts for a decrease of 300-800 mm dec⁻¹ over the north-central Patagonia and an increase of ~200 mm dec⁻¹ further south (50°S) (Garreaud et al., 2013). In terms of precipitation phase (solid vs liquid), the warming detected over the Patagonian Icefields had caused an estimated decrease in the amount of solid precipitation of 5% between 1960 and 1999 (Rasmussen et al., 2007).

1.5.3 Patagonian Icefields

The study area includes two large temperate ice masses: the Northern Patagonian and Southern Patagonian Icefields (NPI and SPI, Figure 1.1). The NPI extends from 46.5° to 47.5°S (Figure 1.1), stretching almost 120 km north–south. It covers an area of ~3675 km² in 2016 (Meier et al., 2018) extending from sea level to elevations above 4000 m a.s.l. at the summit of Mount San Valentin. It has a mean altitude of 1340 m a.s.l. (Davies and Glasser, 2012) and is composed of 38 glaciers larger than 0.5 km² (Dusallant et al., 2018). Between 1870 and 2011, it has been estimated that the total area reduced by 14.2% (Davies and Glasser, 2012).

The SPI spreads over 400 km between the latitudes 48.3°S and 51.5°S (Figure 1.1b), covering an area of 12232 km² in 2016 (Meier et al., 2018). The SPI includes a total of 48 main glacier basins, ending mainly in fjords on the western side and in lakes on the eastern side (Aniya et al., 1996). These glaciers are joined in the accumulation zone (“plateau”) with a measured thickness of more than 700 m (Rivera and Casassa, 2002) and a maximum estimate of ice thickness around ~1250 m (Gourlet et al., 2016). Between 1870 and 2011, the areal reduction was estimated to be 11.1% (Davies and Glasser, 2012).

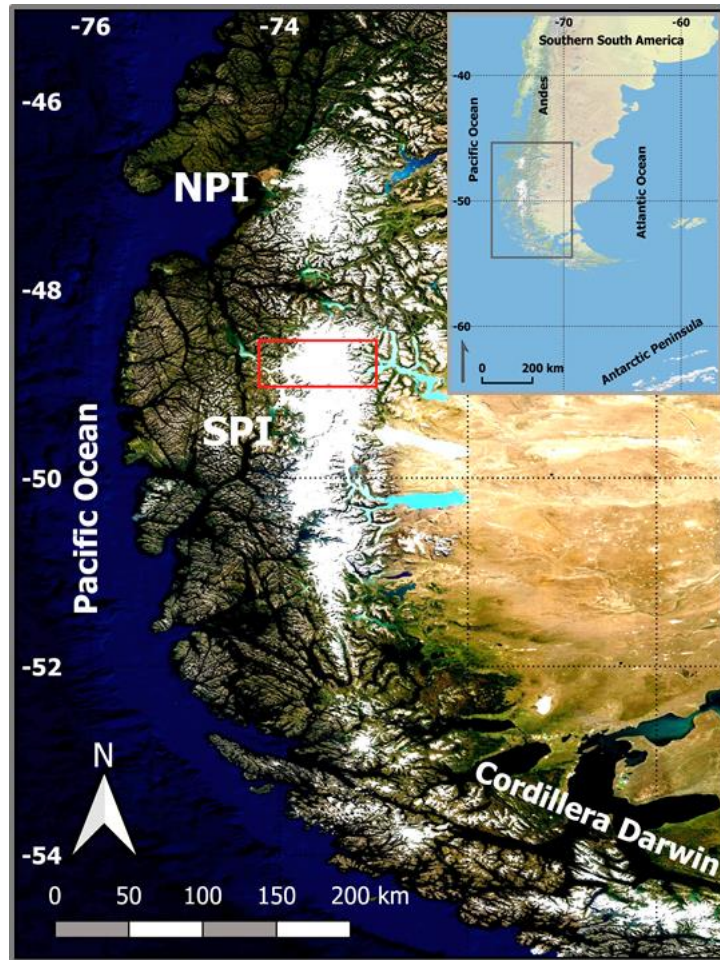


Figure 1.1. Location of the Patagonian Icefields in southern South America. Inset corresponds to regional context of the location in South America. Base maps were taken from ESRI and red rectangle correspond to the zone showed in Figure 2.2.

1.5.4 Glaciers in the northern sector of the Southern Patagonian Icefield

The analysis contained within this thesis is largely based on meteorological observations acquired by a network of five Automatic Weather Stations (AWS) concentrated in the northern section of the SPI. Given their locations, it was assumed that AWSs installed on the western side are representative of glaciers Témpano, Occidental, Greve, HPS8, HPS9 and one unnamed glacier (Figure 1.2). AWSs installed on the east side are deemed to be representative of glaciers O'Higgins, Pirámide and Chico (Figure 1.2).

The glaciers in the study zone show a great variety of size (Table 1.2). O'Higgins Glacier is the third largest glacier in all the SPI after Pio XI and Viedma glaciers. The smaller glaciers are HPS8 on the west side and Pirámide on the east side. All these glaciers terminate in lakes on the east side (O'Higgins and Chico glaciers, Figure 1.2) while in the west, glaciers

terminate in both lakes (Témpano, Greve and Occidental glaciers) and fjords (a portion of Témpano Glacier front).

Table 1.2 Area estimate of the glaciers of the study area by different inventories.

| Year and reference | Area [km ²] | | | | |
|-----------------------------|-------------------------|------------|-----------|------------------|------------------|
| | West side | | | East side | |
| | Témpano | Occidental | Greve | O'Higgins | Chico |
| 1986 (Aniya et al., 1996)* | 332 (333) | 244 (245) | 438 (439) | 893-747(902-754) | 306-243(320-255) |
| 2001 (DeAngelis, 2014) | 334±4.7 | 235±3.8 | 428±4.3 | 762±6.9 | 239±4.3 |
| 1986 (Casassa et al., 2014) | 292.6 | 182.2 | 519.2 | 797.9 | 202.6 |
| 2000 (Casassa et al., 2014) | 285.5 | 176 | 496.4 | 790.5 | 197.9 |

* Total area are listed without bedrock exposure; however, for additional information, those including bedrock exposure are also indicate in parentheses.

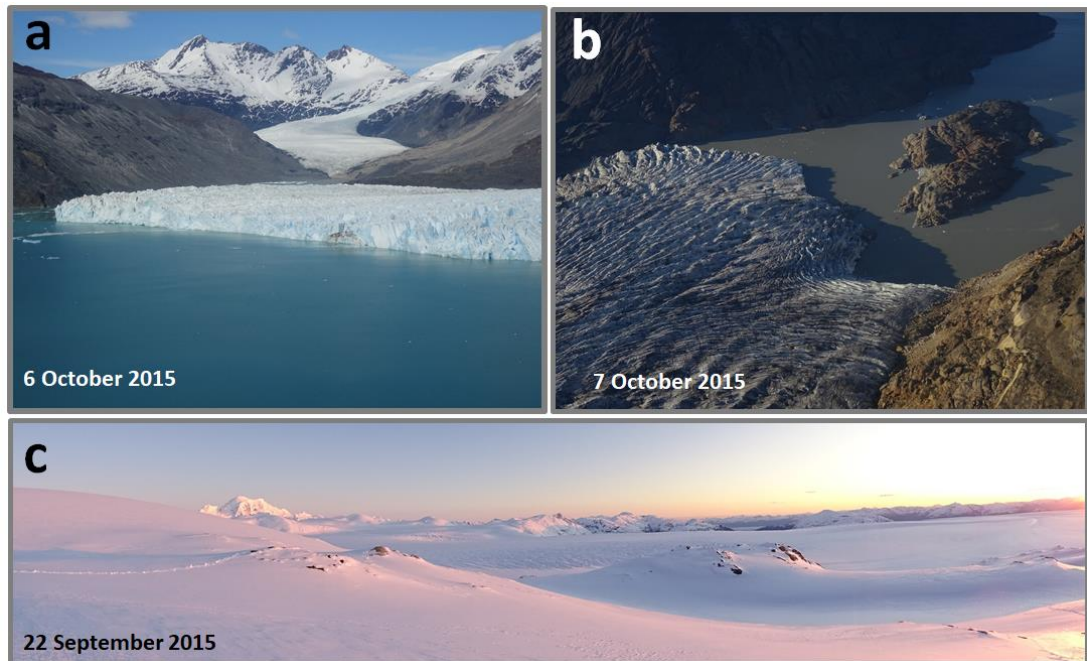


Figure 1.2 Glaciers in the northern sector of the SPI. a) Calving front of the O'Higgins Glacier, b) Calving front of Chico Glacier and c) View to the west from the plateau at the location of HSNO (Figure 1.4). Photos by the Author.

Area change analyses (Table 1.3) show an overall loss estimated for the last decades in the glaciers in the northern zone of the SPI. At long time-scales, Davies and Glasser (2012) estimated that O'Higgins Glacier lost 10.9% of its area between 1870 and 2011. Most of this loss occurred between 1870 and 1986, the period of the fastest recession. Recently, between years 2016 and 2017, O'Higgins Glacier experienced a strong frontal retreat. This retreat was

due to continuous calving events, concentrated during most of the 2017 austral autumn (Figure 1.3). Consequently, a total frontal area loss of 2.03 km² was estimated between July 2016 and July 2017 (www.glaciologia.cl).

On the western side, Greve, Témpano and Occidental glaciers are also losing mass (Table 1.3). At long time-scales, these glaciers experienced their fastest retreat between 1986 and 2011, with Occidental Glacier showing the largest retreat between 2001 and 2011 with a linear frontal retreat estimated in 216 m yr⁻¹ (Davies and Glasser, 2012).

Despite the ice loss generalized in this zone of the SPI (Table 1.3), the periods of fastest recession for these glaciers are not homogeneous, revealing the diverse response of these glaciers to climate change in conjunction with other factors.

Table 1.3 Area change estimates for the glaciers of the study area.

| Period of change and reference | Area Change [km ²] | | | | |
|--|--------------------------------|------------|------------|-----------|-----------|
| | West side | | | East side | |
| | Témpano | Occidental | Greve | O'Higgins | Chico |
| 1984/85/86-2000/01/02 (White and Copland, 2015) | -7.3 | -7.5 | -18.6 | -5.6 | -2.6 |
| 2000/01/02-2009/10 (White and Copland, 2015) | -3.8 | -8.1 | -8.4 | -2.2 | -1.6 |
| 1976/79-2009/10 (White and Copland, 2015) | -20.6 | -23.0 | -32.2 | -15.0 | -6.3 |
| 1986-2000 (Casassa et al., 2014) | -7.2±10.7 | -6.2±9.0 | -22.8±14.1 | -7.4±33.3 | -4.7±16.4 |
| 1944/45-1986/87 (Aniya et al., 1997) | -11.5 | -2.1 | -33.3 | -49.6 | -1.6 |

Both Patagonian Icefields have been the focus of geodetic mass balance studies leading to estimated volume changes for a large number of these glaciers. Prior to 2000, Rignot et al. (2003) showed an increase in volume losses towards the end of the century, with peak values recorded over Témpano and Occidental glaciers between 1995-2000 (Table 1.4). In contrast, thinning at O'Higgins Glacier (to the east) was just 1.4±0.2 m w.e. yr⁻¹ between 1975 and 2000 and 2.8±0.8 m w.e. yr⁻¹ between 1995 and 2000 (Table 1.4).

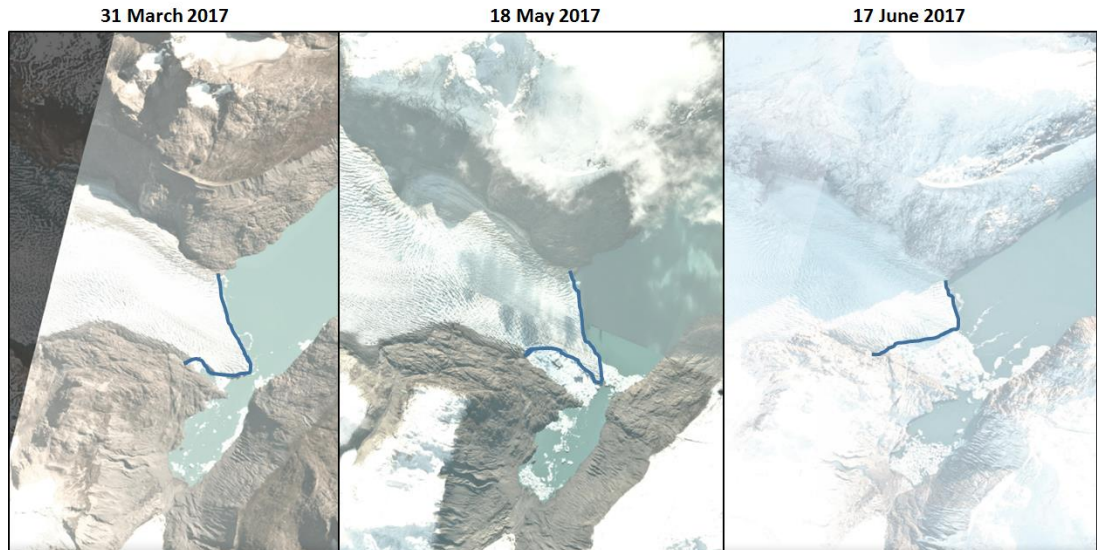


Figure 1.3 Different stages of the calving event at the front of O'Higgins Glacier in the austral autumn of 2017. The blue line indicates the position of the intact glacier terminus. Images obtained from www.planet.com.

More recently, a range of new studies have attempted to quantify mass losses for the region using the geodetic approach (Table 1.4). They are uniform in their assessment of region-wide negative mass balances, with peak values again detected over Occidental and Témpano glaciers and with thinning higher on glaciers to the west side of the divide, compared to those in the east.

Table 1.4 Geodetic mass balance for the glaciers in the northern sector of the SPI. Units are m w.e.

| | Rignot et al. (2003) | Rignot et al. (2003) | Willis et al. (2012) | Willis et al. (2012) | Malz et al. (2018) | Abdel-Jaber et al. (2019) | Abdel-Jaber et al. (2019) | Dusaillant et al. (2019) |
|-------------|----------------------|----------------------|----------------------|----------------------|--------------------|---------------------------|---------------------------|--------------------------|
| WEST | 1975-2000 | 1995-2000 | 2000-2012 Abl. | 2000-2012 Acc. | 2000-2016 | 2000-2012 | 2012-2016 | 2000-2018 |
| Occidental | -1.98±0.22 | -5.61±0.87 | -3.21±0.96 | -1.67±1.35 | -1.43 | -2.41±0.05 | -2.59±0.17 | -2.35±0.28 |
| Témpano | -1.98±0.22 | -5.61±0.87 | -3.64±0.89 | -1.67±1.02 | -1.43 | -1.67±0.04 | -1.97±0.17 | -1.63±0.25 |
| Greve | -1.24±0.19 | -3.47±0.87 | -3.51±1.04 | -0.93±1.68 | -1.43 | -1.68±0.04 | -1.81±0.17 | -1.53±0.27 |
| EAST | | | | | | | | |
| O'Higgins | -1.37±0.18 | -2.75±0.87 | -2.34±1.15 | -1.22±1.18 | -0.93 | -1.05±0.03 | -1.00±0.14 | -0.63±0.11 |
| Chico | -0.50±0.21 | -1.22±0.76 | -2.47±0.50 | -0.76±0.58 | -0.89 | -1.03±0.03 | -1.37±0.10 | -0.99±0.10 |

Chapter 2 Methods Summary

2.1 Overview

The analysis in this thesis spans two spatial scales. First, the focus is on a suite of nine glaciers in the northern sector of the SPI, but concentrating the analyses of results in the three main glaciers of the west (Greve, Témpano and Occidental) and the two main glaciers of the east (O'Higgins and Chico). The analysis is strongly based on a longitudinal profile of AWS observations (details in section 2.2). Second, the analysis is upscaled to a spatial extent that encompasses both the NPI and the SPI, with gridded climate products being the main inputs. These analyses interact throughout, with parameters and assumptions made at the scale of the Icefield taken (or estimated) from point-based observations, and inputs from the gridded products compared, validated and corrected using the point-scale observations. In parallel, data from gridded products were used to estimate non-observed variables necessary for the distributed energy balance model in the northern sector of the SPI, such as rates of accumulation, which in turn were used to derive albedo. Figure 2.1 presents the key steps followed in this work and the connection between datasets and the results of this thesis. Additionally, data from previous works were used to discuss the findings and infer some potential feedbacks.

The details of the methods and physical approaches used to distribute, estimate and quantify meteorological and glaciological variables, are presented in each individual Chapter. The following sections therefore focus on a description of the data used as well as the general approaches to estimate meteorological and glaciological variables.

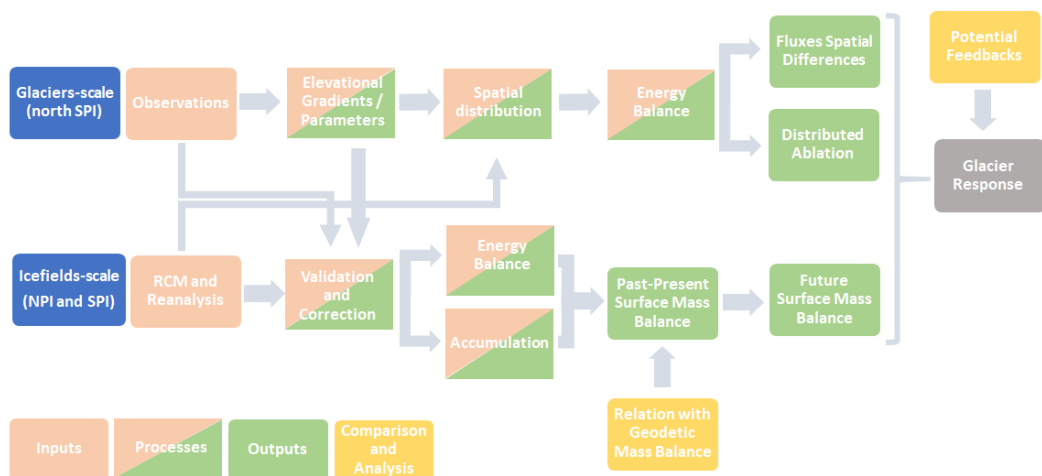


Figure 2.1 Schematic representation of the steps taken in the present research.

2.2 Automatic Weather Stations (Chapters 3, 4 and 5)

In the context of a project of the Chilean government, through the Chilean Water Cadastre (DGA, Spanish acronym) and executed by the Centre for Scientific Studies (CECs, Spanish acronym), a network of five full weather stations and three on-glacier temperature sensors and ultrasonic depth-gauges were installed on the glaciers of the northern sector of the SPI (Figure 2.2; CECs-DGA, 2016). This project aimed to characterize the glaciological conditions in the northern sector of the SPI. Several field campaigns during 2014, 2015 and 2016 were conducted (prior to the commencement of this PhD study). These field campaigns included radar and LIDAR measurements, snow pits, installations of shelters on nunataks along the plateau of the SPI (at same locations of the AWS), bathymetry measurements and pro-glacial lake level measurements (CECS-DGA, 2016). The author of this thesis participated in two of the field campaigns (2014 and 2015) being part of the team that configured and installed the three AWSs located on the plateau (HSNO, HSG, HSO, Figure 2.2).

The meteorological network consists of five AWSs (Tables 3.1 and 5.1 for details). Three were located on nunataks on the plateau and two were located close to the fronts of glaciers O'Higgins (GO) and Témpano (GT) (Figure 2.3). On the plateau, both AWSs were installed on Greve Glacier at different elevations (HSNO and HSG) and one on O'Higgins Glacier (HSO) (Figure 2.3). Since October 2015, each station recorded a full set of meteorological variables including air temperature, humidity, wind speed and direction, incoming shortwave and longwave radiation and atmospheric pressure. The time step of the recorded data was 15 minutes. Although some of these AWSs had data available for previous years (GT, GO and HSG), the analysis was concentrated on the period between October 2015 and June 2016, where all five AWSs obtained simultaneous observations.

Additionally, three on-glacier air temperature and ultrasonic depth gauges (UDG) were installed (Tables 3.1 and 5.1). These stations were called GBL1-3 (Figure 2.2). These data were used to validate air temperatures estimated with the different methods (Chapter 3) and to compare the accumulation and ablation estimations (Chapters 4 and 5 respectively).

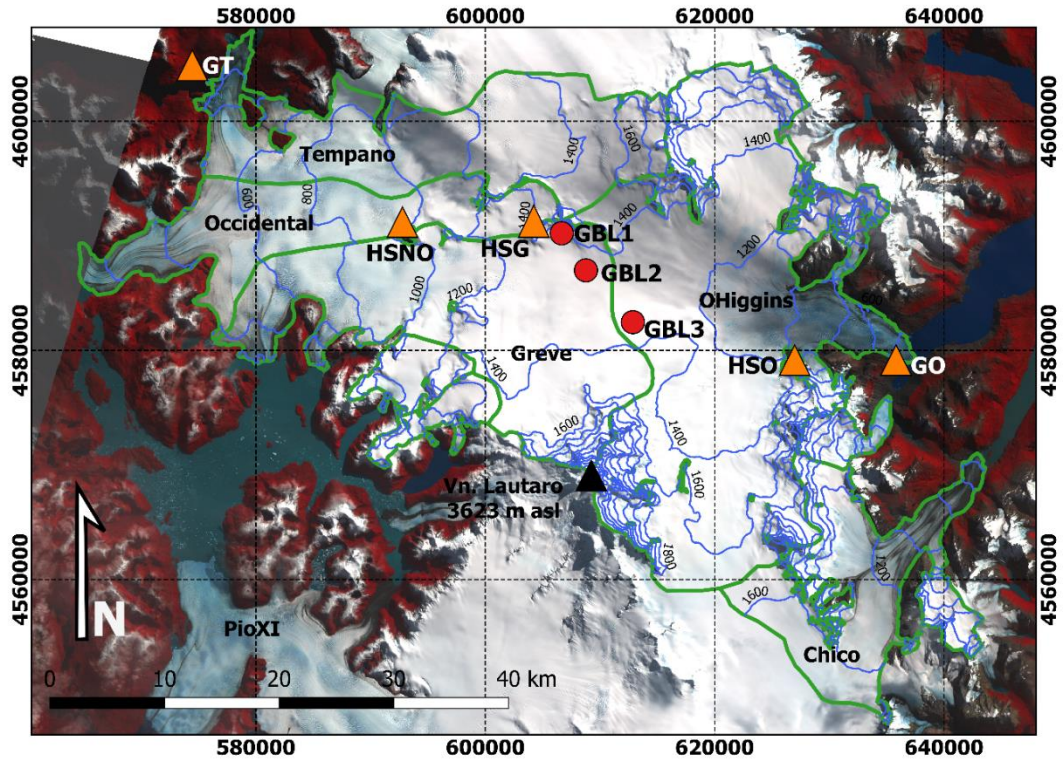


Figure 2.2 Location of the AWSs (orange triangles) and ultrasonic depth gauges (GBL1, GBL2, and GBL3, red circles) on the plateau of the SPI. Glacier outlines in green and contour lines in blue every 200 m. The satellite image is a Landsat 8 OLI from 1 April 2014.



Figure 2.3 AWS installed in the surrounding (GT and GO) and on the plateau (HSNO, HSG, HSO) of the SPI. Photos by Claudio Bravo (HSNO, HSO), Alejandro Silva (GT, HSG) and Jonathan Oberreuter (GO).

2.3 Regional Climate Model and re-analysis (Chapter 4, 5 and 6)

For the broader-scale Icefield analysis, gridded products were used. A Regional Climate Model (RCM) was used to assess the snow accumulation pattern and changes on both Patagonia Icefields in the period between 1980 and 2015 (Chapter 4) as well as to feed an energy and mass balance to estimate the past and future surface mass balance of the Patagonia Icefields (1976-2050, Chapter 6). The RCM chosen was the RegCM4.6 (Bozkurt et al.,

2019). This simulation has a resolution of 10 km. For the period 1980-2015, the initial and boundary conditions were provided by ERA-Interim (Bozkurt et al., 2019). In this case, the output used in the analysis was the total precipitation (Chapter 4). For the surface mass balance simulation of the historical period (1976-2005) and the scenarios RCP2.6 and 8.5 (2006-2050) (Chapter 6) RegCM4.6 was used to downscale lateral boundary conditions derived from MPI-ESM-MR Earth System Model (Giorgetta et al., 2013) on a nested domain centred over Chile at 10-km spatial resolution (Bozkurt et al., 2019). In this case, the variables used were daily mean near-surface temperature, total precipitation, wind speed, surface pressure, near-surface relative humidity, incoming shortwave and longwave radiation.

Additionally, in order to estimate the ablation and the surface mass balance in the glaciers of the northern sector of the SPI (Chapter 5), the ERA5-Land reanalysis product was used (9 km, CS3, 2019). The variables used were 2 m air temperature, 2 m dewpoint temperature (as a proxy to surface temperature), surface pressure, 10 m u and v wind components, incoming shortwave, longwave radiation and total precipitation.

2.4 Analysis of meteorological observations and spatial distribution (Chapter 3 and 5)

As a first step, the AWSs observations were used to characterize the meteorological conditions and their spatial variability. Air temperature lapse rates were calculated using regression with all the available AWS at each side as well as using a stepwise approach. From these, fields of distributed air temperature were obtained. These fields were compared with on-glacier air temperatures where available and estimation of the glacier cooling effect was derived and discussed. Following this same approach, the rest of the meteorological variables were spatially distributed using different methods depending on the variable. Considering the spatial configuration of the AWSs, most of the variables were distributed using elevation gradients, a common approach in modelling frameworks for many disciplines, but perhaps more scarce within glaciological applications (Mölg et al., 2020). The main inputs were i) Digital Elevation Models (DEM), which in this case were SRTM (90 m) and TanDEM-X (12 m), both re-scaled to 200 m resolution, and ii) glacier outlines acquired from De Angelis (2014) and corrected, especially in the frontal zone of each glacier, to the conditions close to the dates of the observed data (October 2015 to June 2016).

Use of the AWS network in this way facilitated a clear analysis of the meteorological differences between the west and east margins of the Icefield, and how this exerts control on the regional glacier response.

2.5 Glaciological modelling (Chapter 4, 5, 6 and 7)

In order to estimate glacier response to any observed spatial differences in the meteorological conditions, the surface mass balance and its individual components were quantified, at both glacier- and regional-scales. Here, and using the meteorological observations in the northern sector of the SPI, the focus was on the ablation component.

To evaluate the efficacy of different air temperature distribution approaches, in a first step a classic degree-day modelling was applied. A second step was to model the surface energy balance using the meteorological observations and their spatially distributed fields as input. Distributed fields for temperature and precipitation were available from the earlier analyses (above). Turbulent and radiative fluxes were estimated. In both cases, meteorological observations were the main input, but distribution steps were complemented with modelling approaches and gridded climate products. The method for the calculation of the turbulent fluxes was the bulk approach (Cuffey and Paterson, 2010). For radiative fluxes, the potential shortwave radiation was spatially estimated using solar geometry and a DEM and was corrected using observed incoming shortwave radiation at each side of the SPI. The correction factor was obtained from the ratio between the potential and the observed incoming shortwave radiation and the variability inherent in this approach is mainly associated with the cloud conditions. To estimate the reflected shortwave radiation (and hence the albedo), the model of Oerlemans and Knapp (1998) was used. This is based on the age of the snow. Therefore the main inputs were the precipitation field obtained from the gridded climate products and the air temperature (to define if the precipitation was rain or snow).

Incoming longwave radiation was calculated using the distributed air temperature assuming the atmosphere as a blackbody with an emissivity. The atmospheric emissivity was obtained from the observations. The emitted longwave radiation was calculated from the temperature of the ice/snow surface. This variable was not observed along the study period so the approach used here was based on previous studies (e.g. Ayala et al., 2017).

Another important variable associated with the turbulent fluxes is the surface roughness (Quincey et al., 2017; Smith et al., 2016). This variable was not

observed or measured, so a relationship with albedo was used. Finally, to close the energy balance equation, the energy released by rainfall was calculated using the approach of Hock and Holmgren (2005). The gridded precipitation and the air temperatures were used to differentiate between solid and liquid precipitation.

Additionally, accumulation estimates were used to define some of the variables necessary for completing the energy balance. Here, the key input was the gridded climate products, and several methods were tested to define the ratio of snow and rain. These methods were all within the realm of what is known as precipitation Phase Partitioning Method (PPM) and are discussed in more detail in Chapter 4 at the scale of both Patagonian Icefields. The UDGs installed on-glacier (Section 4.3.1) were used to compare the accumulation rates of the different methods. However, due to the harsh weather conditions, the measurements obtained from GBL stations were limited to shorter periods.

2.6 Long-term surface mass balance (Chapter 4, 5 and 6)

Using the RegCM4.6 and ERA5-Land reanalysis (Section 2.3), extended time series of ablation and accumulation were estimated. To evaluate different sources of data, ERA5-Land reanalysis was used for assessing the glaciers of the northern sector of the SPI while RegCM4.6 was used at the scale of both Patagonian Icefields. In both cases, to estimate the ablation, the same energy balance was used, while the accumulation was estimated using the PPMs. Corrections to the inputs from the gridded data set were applied for variables that showed systematic differences when compared to the field-based observations acquired over the coincident nine months. An additional parameterisation to account for glacier cooling was also introduced based on the findings from the analysis of the meteorological observations (Chapter 3).

Chapter 3
Air Temperature Characteristics, Distribution, and Impact
on Modeled Ablation for the South Patagonia Icefield

Claudio Bravo, Duncan J. Quincey, Andrew N. Ross, Andrés Rivera, Ben Brock, Evan Miles, and Alejandro Silva

Manuscript published in Journal of Geophysical Research: Atmospheres
124(2), pp. 907-925

DOI: 10.1029/2018JD028857

3.1 Abstract

The glaciers of Patagonia are the largest in South America and are shrinking rapidly, raising concerns about their contribution to sea level rise in the face of ongoing climatic change. However, modeling studies forecasting future glacier recession are limited by the scarcity of measured on-glacier air temperatures and thus tend to use spatially and temporally constant lapse rates. This study presents 9 months of air temperature observations. The network consists of five automatic weather stations and three on-glacier air temperature sensors installed on the South Patagonia Icefield along a transect at 48°45'S. Observed lapse rates are, overall, steeper on the east (-0.0072 °C/m) compared to the west (-0.0055 °C/m) and vary between the lower section (tongue, ablation zone) and the upper section (plateau, accumulation zone) of the glaciers. Warmer off-glacier temperatures are found in the east compared to the west for similar elevations. However, on-glacier observations suggest that the glacier cooling effect is higher in the east compared to the west. Through application of distributed temperature-index and point-scale energy balance models we show that modelled ablation rates vary by up to 60%, depending on the air temperature extrapolation method applied, and that melt is overestimated and sublimation is underestimated if the glacier cooling effect is not included in the distributed air temperature data. These results can improve current and future modelling efforts of the energy and mass balance of the whole South Patagonia Icefield.

3.2 Introduction

On midlatitude glaciers, near-surface air temperature is the main control on energy exchange over a snow or ice surface (Petersen et al., 2013; Shaw et al., 2016) and for glaciological applications, it is used as input for melt calculations ranging from empirical temperature index (Hock, 2003) through to physically based energy balance models (Greuell & Genthon, 2003). The air temperature is used to calculate the incoming longwave radiation and the sensible heat and also where air temperature influences other variables such as moisture, which is used to calculate latent heat (Ebrahimi & Marshall, 2016). In terms of accumulation processes, the accurate distribution of air temperature over the glacier surface is essential for distinguishing areas where precipitation falls as rain or snow (Minder et al., 2010), and it also has a direct impact on snowpack metamorphism affecting snow redistribution (Carturan et al., 2015). Glacier mass balance models thus rely on accurate spatial distribution of the air temperature (Carturan et al., 2015).

Patagonia (40–55°S) contains the largest glacierized area in South America, but recent evidence shows that most of these glaciers are shrinking rapidly (Davies & Glasser, 2012; Foresta et al., 2018; Malz et al., 2018; Meier et al., 2018; White & Copland, 2015). This deglaciation is primarily a matter of concern for sea level rise (Foresta et al., 2018; Gardner et al., 2013; Rignot et al., 2003; Willis et al., 2012). However, very little is known about how glacial areal changes and mass balance processes are linked to changes in climate (Malz et al., 2018; Pellicciotti et al., 2014; Weidemann et al., 2018). Overall, these changes are generally attributed to temperature increase as the glaciers in Patagonia are strongly sensitive to temperature change (Malz et al., 2018; Masiokas et al., 2008). This is because ablation is dominated by melt (Sagredo & Lowell, 2012). Thus, an in-depth understanding of air temperature variability and on-glacier near-surface meteorology is needed to understand the current and future state of these glaciers.

Previous research has described the steep gradients of some meteorological variables on the east side of the Southern Andes, which is a relatively dry “rain shadow” leading to a foehn effect, while the windward west side experiences high precipitation and humidity and lower lapse rates (LRs; Lenaerts et al., 2014; Schneider et al., 2003; Smith & Evans, 2007). However, little attention has been given to the implications of these spatial contrasts for glacier mass balance and response to climate. Schneider et al. (2003) demonstrated a relationship between atmospheric circulation and glacier response, stating that wetter conditions caused by a change in circulation on one side lead to drier conditions on the other and vice versa. Despite its importance for glaciological applications, there are no empirical studies of the spatial and temporal variability of air temperature over the surface of both sides of the Patagonian Icefields, and hence, its significance to the climatic response of glaciers is unknown.

Vertical LRs are the most common method of distributing air temperature in modeling studies (Marshall et al., 2007; Petersen & Pellicciotti, 2011; Wheler et al., 2014) and are one of the parameters to which melt models are most sensitive (Heynen et al., 2013). However, due to the complex boundary layer meteorology of mountainous areas and the general lack of detailed on-glacier measurements (Hanna et al., 2017), constant and linear LRs are commonly used for glacier ablation estimations, rather than distributed air temperature fields for glacier ablation estimations (Ayala et al., 2015). This is a major simplification, as it has been widely recognized that air temperature LRs are spatially and temporally variable in mountainous regions (Petersen &

Pellicciotti, 2011), both on-glacier (Ayala et al., 2015; Hanna et al., 2017; Shaw et al., 2017) and off-glacier (Heynen et al., 2016; Shen et al., 2016). Many studies use off-glacier data that do not account for the variability of the air temperature associated with katabatic boundary layer flows and the damping and ice surface cooling effect observed over glacier surfaces (Ayala et al., 2015; Carturan et al., 2015; Petersen & Pellicciotti, 2011; Petersen et al., 2013; Shaw et al., 2016). The cooling effect occurs under positive atmospheric temperatures as the lowest layers of air are cooled by sensible heat exchange with the underlying ice. The magnitude of the cooling effect is defined as the difference between screen-level temperatures over a glacier compared to equivalent-altitude ambient temperatures. This cooling is not homogenous over a glacier surface and depends on the geometric characteristics (Carturan et al., 2015). Cold dense air flows down glacier as a katabatic flow whose temperature structure can be simplified by a balance between adiabatic warming and cooling by sensible heat exchange with the glacier (Greuell & Böhm, 1998). Due to this reason, on-glacier LRs are typically lower than the environmental lapse rates (ELRs; Shaw et al., 2017).

In Patagonia, a few reported LR exist, but most are based on off-glacier observations. Regarding on-glacier observations, Takeuchi et al. (1996) and Stuefer et al. (2007) both estimated a LR of -0.0080 °C/m at the lower end of Perito Moreno glacier on the eastern side of the South Patagonia Icefield (SPI), while Popovnin et al. (1999) reported an on-glacier LR for the small De Los Tres glacier, which is located outside the SPI. This study reported a mean LR over the glacier surface of -0.015 °C/m over the terminus area and noted frequent thermal inversions. Above 1,400 m above sea level (a.s.l.), the LR reduced to -0.0017 °C/m (Popovnin et al., 1999). While useful, these observations are limited by their short observation period of approximately 5 weeks, from 26 January to 4 March 1996.

Usually, mass balance modeling and temperature sensitivity analyses in Patagonia distribute the air temperature using the ELR (-0.0060 to -0.0065 °C/m; Barry, 2008) as a spatially and temporally constant value (Bravo et al., 2015; Kerr & Sugden, 1994; Schaefer et al., 2013; Schaefer et al., 2015). At best, studies use a monthly variable LR (Mernild et al., 2016, following Liston & Elder, 2006) and distribute the air temperature using climate data from regional and global models. Constant LR have also been used to extrapolate off-glacier meteorological data; for example, Rivera (2004) used a constant LR of -0.0060 °C/m to distribute the monthly air temperature over Chico

Glacier, and De Angelis (2014) used a constant LR of -0.0080 °C/m to distribute daily air temperature across all the SPI.

Historically, meteorological observation on the plateau of the SPI has been difficult, due to the harsh weather conditions and the extreme logistical challenges. In spite of these restrictions, a weather station network was installed in 2015 (CECs-DGA, 2016), providing 9 months of continuous temperature measurements for a longitudinal profile at around $48^{\circ}45'S$ enabling spatial and temporal patterns of air temperature to be investigated.

In this work, we present an analysis of the air temperature and the LRs observed in this first automatic weather station (AWS) network across the SPI. First, we describe the air temperature observations, concentrating on the spatial differences along the profile. Then, the vertical structure of the air temperature is analysed at the glacier scale, and comparison between on-glacier and off-glaciers air temperature conditions is conducted. Finally, the impacts on ablation processes are assessed, for which we use both a distributed degree-day model (DDM) and a point-based energy balance model to quantify the effects of different air temperature parametrizations on the modeled melt.

3.3 Materials and Methods

3.3.1 Study Area and Observations

The largest ice mass in Patagonia is the SPI which extends over 350 km between the latitudes $48^{\circ}20'S$ and $51^{\circ}30'S$, along the meridian $73^{\circ}30'W$, with an area of $\sim 13,000$ km² (De Angelis, 2014). The SPI comprises 48 main glacier basins, which end primarily in fjords on the western side and in lakes on the eastern side (Aniya et al., 1996). These glaciers are joined in the accumulation zone (“plateau”), with an average altitude of $\sim 1,500$ m a.s.l. The SPI is the second largest freshwater reservoir in the Southern Hemisphere, after Antarctica (Warren & Sugden, 1993).

In recent decades, the majority of the outlet glaciers in the SPI have been retreating (Davies & Glasser, 2012). Overall, White and Copland (2015) report a total area loss of 542 km² ($\sim 4\%$ of the SPI) between the end of the 1970s and 2008–2010. Nevertheless, the rates and trends are neither homogeneous nor synchronous (Sakakibara & Sugiyama, 2014) and include episodes of advance (e.g., Pio XI glacier, Wilson et al., 2016).

This work focuses on the northern sector of the SPI (Figure 3.1) using data from a series of five AWSs, installed on proglacial zones and nunataks, running west-east across the ice divide. We take the AWS installed on the

west side to be representative of glaciers Témpano (334 km²), Occidental (235 km²), Greve (428 km²), HPS8 (35 km²), and one unnamed glacier (41 km²). AWSs installed on the east side are representative of glaciers O'Higgins (762 km²), Pirámide (27 km²), and Chico (239 km²; Figure 1; De Angelis, 2014).

Each AWS recorded a full set of meteorological variables between October 2015 and June 2016, comprising air temperature, relative humidity, wind speed and direction, incoming shortwave and longwave radiation, and atmospheric pressure (Table 3.1). In addition, three ultrasonic depth gauges (UDGs) were installed directly on the glacier surface over the plateau. In the same structure, two air temperature sensors were also installed at an initial height of 2 and 4 m above ground level. We call these glacier boundary layer (GBL) air temperature stations (GBL1, GBL2, and GBL3 in Figure 3.1 and Table 3.1). We use these data to validate air temperature estimated with the different methods and to compare the ablation estimations. Unfortunately, the observations during three months (July, August, and September 2016) are not complete or are completely absent, probably due to the harsh weather conditions and logistical difficulties in recovering the data; hence, we discard these periods.

The environment at proglacial and nunatak sites is influenced by local warming from solar heated rocks, although a partial influence of the GBL at these locations is expected. Two AWS (GO and GT) are proglacial stations. GT is located in a valley at a distance of 2.5 km from one of the calving fronts of the Témpano glacier, separated from the glacier by a fjord and by a hill of ~350 m a.s.l. At the time of the measurements, GO was located approximately 0.5 km from the glacier terminus, separated from the ice by a small branch of the O'Higgins lake. Three AWS (HSNO, HSG, and HSO) are located on nunataks on the plateau. HSNO is located on a small nunatak (1.8 km² in area) on the Greve glacier. This AWS is located 100–150 m above the elevation of the tongue of the glacier, but a sector of the nunatak, east of the AWS, is still covered by ice. HSG is located on a narrow nunatak (1.6 km² in area). The relative height over the plateau of the location of HSG reaches 50–60 m of the west side of the nunatak and 10–15 m to the east side of the nunatak. HSO is also located on a nunatak (2.8 km² in area) close to the elevation of the equilibrium line altitude of the O'Higgins glacier. This AWS is located at a relative height over the glacier surface of 50 to 250 m.

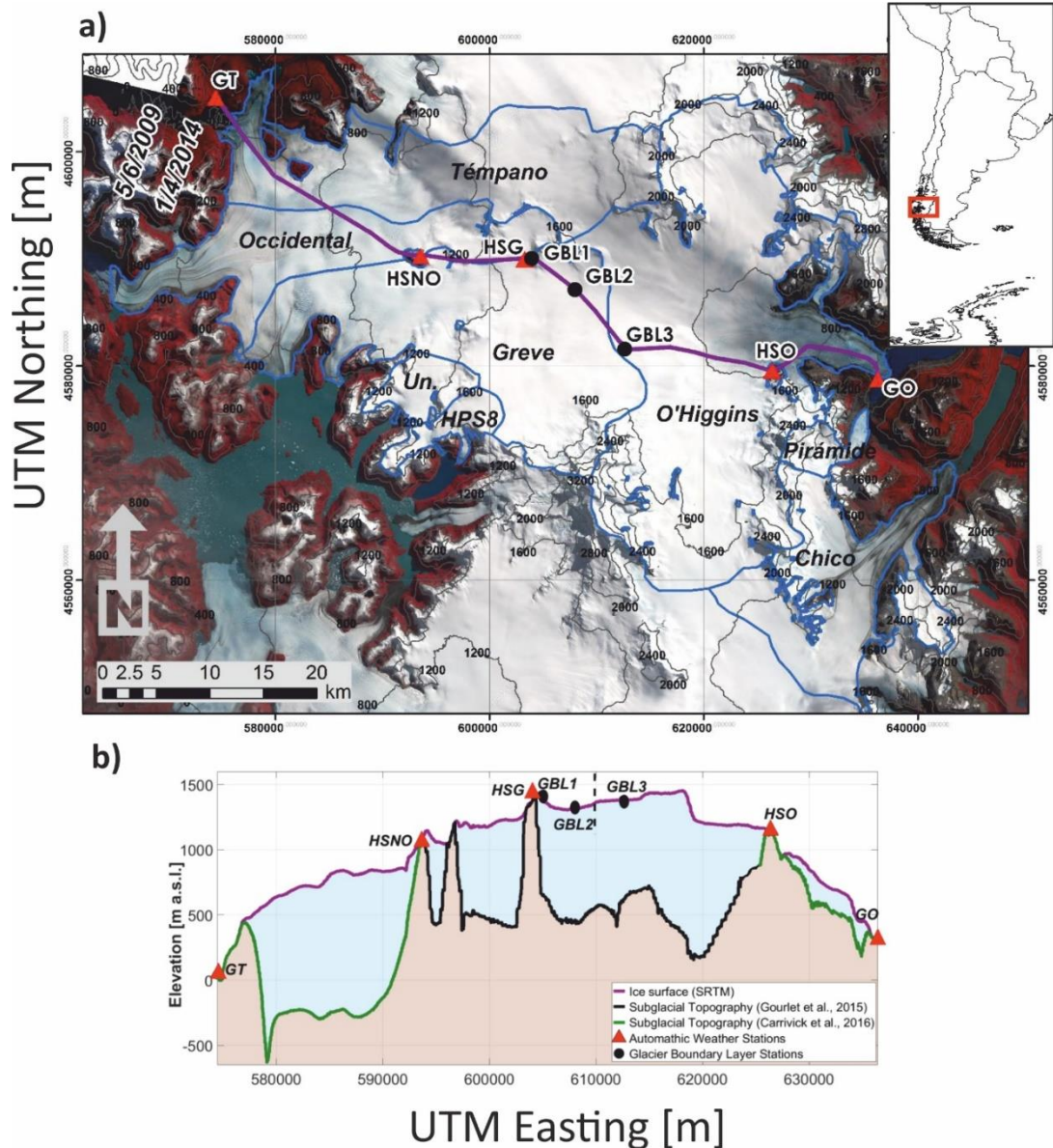


Figure 3.1 (a) Spatial configuration of the AWSs (red triangles) and ultrasonic depth gauges (GBL1, GBL2, and GBL3). Glacier contours (blue lines) are from De Angelis (2014). Purple line is the profile in (b). The satellite image is a Landsat from 8 April 2014. Contour lines are 400 m spaced. (b) Longitudinal profile of the elevations of AWS and sonic ranges. Bedrock topography is derived from thickness observed data from Gourlet et al. (2016, black line) and thickness modelled data from Carrivick et al. (2016, green line). Dashed black line represents the ice divide. SRTM = Shuttle Radar Topography Mission; AWS = automatic weather station.

Air temperature sensors were installed in a naturally ventilated radiation screen. Errors due to radiative heating of the sensors are likely to be minor due to the prevalence of strong winds over the icefield (Garreaud et al., 2013). Except for HSG all the stations have 100% of the observations during the periods indicated in Table 3.1. A gap of data was detected in HSG, between the hours 2100 and 2200, for the entire observation period. These gaps were

filled using linear interpolation. We take the measurements error to be that declared by the manufacturer (Table 3.1), and unfortunately, no intercomparison was possible as the AWS and GBL were installed at different dates. The air temperature sensors at 4 m were used to verify the observations at 2 m.

Table 3.1 Details of the location, period of measurements and sensor characteristics of the five AWSs and the three GBL stations. The name of each AWS is the official name given by the DGA (www.dga.cl).

| Location | | Automatic Weather Station | Acronym | Latitude / Longitude / [m a.s.l.] | Air temp. sensors | Error | Height [m] | Period |
|----------|-----------------|--|---------|------------------------------------|---------------------|--------------------|------------|--|
| West | Rock | Glaciar Témpano | GT | 48°42'09"S/ 73°59'17"W/ 50 | Young 41382VC | ±0.3°C at 23°C | 2 | 1 October 2015 -30 June 2016 |
| | Nunatak | Hielo Sur en Glaciar Greve, Nunatak Occidental | HSNO | 48°49'59"S/ 73°43'25"W/ 1040 | Rotronic HC2-S3 | ±0.1°C at 23°C | 2 | 1 October 2015 -30 June 2016 |
| | | Hielo Sur en Glaciar Greve | HSG | 48°49'55"S/ 73°34'53"W/ 1428 | Young 41382VC | ±0.3°C at 23°C | 2 | 1 October 2015 -30 June 2016 |
| | Glacier surface | Glacier Boundary Layer Station 1 | GBL1 | 48°50'02"S/ 73°34'51"W/ 1415 | Thermistor 107-L | ±0.2°C - ±0.5°C | 1.2 | 17 October 2015 -15 February 2016 |
| | | Glacier Boundary Layer Station 2 | GBL2 | 48°51'34"S/ 73°31'37"W/ 1294 | Thermistor 107-L | ±0.2°C - ±0.5°C | 2 | 25 October 2015 -31 March 2016 |
| | | Glacier Boundary Layer Station 3 | GBL3 | 48°54'30"S/ 73°27'47"W/ 1378 | Thermistor 109-L | ±0.1°C - ±0.5°C | 2 | 10 April 2016 -30 June 2016 |
| East | Nunatak | Hielo Sur en Glaciar O'Higgins | HSO | 48°55'28"S/ 73°16'26"W/ 1234 | Rotronic HC2-S3 | ±0.1°C at 23°C | 2 | 17 October 2015 -30 June 2016 |
| | Rock | Glaciar O'Higgins | GO | 48°55'47"S/ 73°08'21"W/ 310 | Young 41382VC | ±0.3°C at 23°C | 2 | 1 October 2015 -30 June 2016 |

3.3.2 Lapse Rates

We concentrate our analysis on the observed LRs between AWSs and their spatial and temporal differences. For calculation of LRs, it has been suggested that multiple measurements should be used, as this allows calculation of the strength of the relationship between air temperature and elevation (Heynen et al., 2016). We thus calculate the SPI LRs from the regression of all mean temperature values, and the measure of the strength of the elevation dependence is provided by the determination coefficients (R^2) of the linear regression. In addition, to establish the differences between the western and eastern sides of the icefield, stepwise air temperature LRs were estimated at hourly intervals.

As HSG is located 2.9 km from the glacier divide (Figure 3.1), the LRs for the west side were estimated between GT-HSNO and HSNO-HSG and on the east side between GO-HSO and HSO-HSG. The observed air temperatures at GBL1, GBL2, and GBL3 were used to assess how representative the different extrapolation methods are of temperatures within the glacier surface layer.

3.3.3 Air Temperature Distribution

Based on these observations, we apply five different extrapolation methods to simulate air temperature distribution, using air temperatures observed in HSNO for the west side and HSO for the east side as the primary input data sets. For all five methods, the hourly air temperature was distributed using the LP DAAC NASA Version 3 Shuttle Radar Topography Mission Digital Elevation Model (hereafter, SRTM DEM; National Aeronautics and Space Administration Jet Propulsion Laboratory, 2013) using the local UTM zone 18S. Considering the hypsometry of this zone and to maximize computational efficiency, we resampled the SRTM DEM to 200 m resolution.

First, air temperature was distributed using a constant LR of -0.0065 °C/m (Barry, 2008) corresponding to the ELR. This value is the most commonly used value in the literature for glaciological and hydrological modeling (e.g., Schaefer et al., 2015).

Second, the seasonal mean observed LRs (MLR) were used to characterize the spatial differences between east and west sides and also between the plateau and the tongue of the glaciers.

Third, stepwise observed and hourly variable LRs (VLR) were applied. This method includes both spatial and temporal variability. On the west side, we used the GT-HSNO LR between 0 and 1,040 m a.s.l. and the HSNO-HSG LR between 1,041 and 3,500 m a.s.l. (the highest point). On the east side, we used the GO-HSO LR between 250 m (approximately the elevation of the front of O'Higgins glacier) and 1,234 m a.s.l. and the HSO-HSG LR between 1,235 and 3,500 m a.s.l.

As the second and third methods use data from both proglacial and nunatak weather stations, they represent nonglacial surface temperatures rather than the GBL temperature. Hence, VLR corresponds to the variable atmospheric LR. For input to a glacier ablation model the air temperature using VLR must be adjusted for the GBL cooling effect. The fourth method therefore compared the VLR air temperatures with observations from on-glacier sensors (VLRBias). GBL2 is assumed to be representative of the west side and GBL3 of the east side. The adjustment of the air temperature (T_{vlra}) consists of a bias correction of the data using the following expression (Teutschbein & Seibert, 2012):

$$T_{vlra} = T_{vlr} + \mu_m(T_{obs}) - \mu_m(T_{vlr}) \quad (1)$$

where T_{vlr} is the air temperature estimated with the VLR method at the elevation of the GBL2 on the west side and of the GBL3 on the east side, and μ_m is the mean of the observed air temperature at GBL2 and GBL3 (T_{obs}) and of the T_{vlr} . This approach is the same as that adopted by Ragetti et al. (2014) and Ayala et al. (2016) for glaciers in central Chile. Considering that the time series of GBL2 and GBL3 are shorter (Table 3.1), it is assumed that the difference in the mean is constant along the period and is isotropic. This approach attempts to replicate data observed on-glacier rather than AWSs off-glacier alone. We only used data from GBL2 and GBL3, considering that the air temperature sensor in GBL1 was installed at 1.2 m.

Finally, the fifth method corresponds to the method of Shea and Moore (2010, SM10 hereafter), which was then applied to alpine glaciers by Carturan et al. (2015) and Shaw et al. (2017). The advantage of this method is that it uses off-glacier data to extrapolate the air temperature and is a function of the flowline distance, which is the average from a summit or ridge (Shaw et al., 2017). In our case, the distance was calculated using the SRTM DEM (Supplementary Figure 3.1 in the supporting information). The air temperature is estimated using a statistical model that accounts for the differences between ambient temperature and on-glacier temperature:

$$T_{sm10} = \begin{cases} T_1 + k_2 (T_{vtr} - T^*), & T_{vtr} \geq T^* \\ T_1 - k_1 (T^* - T_{vtr}), & T_{vtr} < T^* \end{cases} \quad (2)$$

T_{vtr} is representative of the free atmospheric air temperature. The k_1 and k_2 are parameters obtained from the slope of the linear piecewise regression, modeled as exponential functions of the flow distance. These parameters related the 2m air temperature with the free atmospheric temperature (Supplementary Figure 3.1) below and above the threshold T^* , which is defined as a function of the flow distance (D_f ; Carturan et al., 2015; Shaw et al., 2017):

$$T^* = \frac{C_1 D_f}{C_2 + D_f} \quad (3)$$

where C_1 and C_2 are 6.61 and 436.04, respectively, corresponding to fitted coefficients. T_1 is the air temperature threshold for katabatic effects and is calculated as $T^* \cdot k_1$.

The parameters used in this model are the same as those used by SM10 as the three on-glacier observation sites in this study are insufficient to define a new exponential curve. However, the resulting factors (k_1 and k_2) obtained are compared with those used by SM10 and Shaw et al. (2017). In the case of GBL1 and GBL2 the factors agree with the previous curves of k_1 and k_2 , but the GBL3 factors do not (Supplementary Figure 3.1).

Considering the distance of GBL3 to the nearest ridge, it is expected that the factors k_1 and k_2 reach values close to 1; however, we obtained values around ~ 0.5 (Supplementary Figure 3.1).

3.3.4 Melt and Ablation Models

Two models commonly used in the glaciological literature were applied to quantify the impact of air temperature distribution method on the melt and ablation over the SPI surface. First, a standard DDM (e.g., Hock, 2003, 2005) was used with an hourly time step for each air temperature distribution. We chose this model over an enhanced temperature index model (Pellicciotti et al., 2005), as the purpose is to identify the impacts of the air temperatures in the model rather than quantify the real melt of these glaciers. This basic model has been used to predict future response of glaciers worldwide in many recent works (e.g., Bliss et al., 2014; Davies et al., 2014; Radić et al., 2014), and so it is important to evaluate the corresponding parameters and assumptions used. In this model, the melt is assumed to increase linearly with air temperature above a given critical threshold assumed in this case to be at 0 °C. The only data requirement is air temperature and empirically calibrated

degree-day factors (DDFs) that are used to scale the air temperatures to melt rates (Tsai & Ruan, 2018). The DDFs account for the different properties of snow, firn, and ice (Mackay et al., 2018). As we do not have enough data to calibrate the DDFs, as, for example, stake measurements in the east side, we used a range of values between 3 and 10 mm w.e. $\cdot^{\circ}\text{C}^{-1}\cdot\text{day}^{-1}$ based on previous work (Hock, 2003, 2005).

The second model is an energy balance at the point scale where meteorological observations are available. Radiative fluxes (incoming shortwave and longwave radiation) and the meteorological inputs (wind speed, relative humidity, and atmospheric pressure) were taken from HSNO (west) and HSO (east) observations. Air temperature input is also variable depending on the method used for air distribution. As the air temperature distributions of the ELR, MLR, and VLR were extrapolated from the observations at HSNO and HSO, at this elevation the observed air temperature is the same as that obtained from these methods. Hence, energy balance was calculated using VLR, the VLRBias, and the SM10 air temperatures. Energy available for melt (W/m^2) was determined following Oerlemans (2001), assuming that the conductive heat flux and sensible heat brought to the surface by rain or snow are considered negligible. Indeed, recent work calculated 1 W/m^2 for sensible flux due to rain and 4 W/m^2 for ground heat flux (Weidemann et al., 2018) for two glaciers in the south of our study area. Surface temperature is assumed constant at 273.15 K (0 $^{\circ}\text{C}$). The heat fluxes were calculated using the bulk approach (Cuffey & Paterson, 2010), and stability corrections were applied to turbulent fluxes using the bulk Richardson number, which is used to describe the stability of the surface layer (Oke, 1987).

The complete set of equations used for the calculations of the turbulent fluxes is presented in Bravo et al. (2017) and references therein.

3.4 Results

3.4.1 Characterization of the Observed Air Temperature

The observed 2m daily and hourly mean of the air temperature for each station are shown in Figure 3.2. Lower air temperatures are recorded at the higher elevation AWS (HSG), and positive daily means at this high elevation site (1,428 m a.s.l.) are observed in summer months and even in fall where it is possible to see inversion episodes of the air temperature. Hence, higher values are observed on the plateau when compared with off-glacier values.

The off-glacier air temperature shows positive values throughout the observational period with higher mean values generally registered at GO despite being located at a higher elevation than GT. At similar elevations, air temperatures at GBL1 are lower than at HSG, except in February. We associate this difference with the cooling effect of the glacier surface (Carturan et al., 2015), as HSG is installed on the rock surface and GBL1 is on snow on the glacier surface. The daily mean amplitude is higher on the west at GT (~ 4.5 °C) compared with eastern AWS GO (~ 2 °C).

The diurnal temperature range is higher at the off-glacier AWS compared to on-glacier AWS (Figure 3.2), revealing the dampening effect of the ice surface. The hourly mean values show that the highest Pearson's correlation coefficients (r) are between plateau air temperatures (Supplementary Table 3.1) with $r > 0.88$ in almost all the cases. The r between off-glacier temperatures and plateau temperatures are in all cases < 0.52 . The r between the AWSs on the west side (GT and HSNO) is 0.44 and 0.47 between the eastern AWSs (GO and HSO). The correlation is higher if the time series are compared between October and March with 0.67 and 0.59, respectively. Large-scale climate anomalies during the austral fall (Garreaud, 2018) lead to a lower correlation between off-glacier AWS and on-glacier and nunataks AWS. The observations reveal that this circulation pattern increases the air temperature over the plateau more than over the off-glacier sites. Interestingly, r between both off-glacier (67 km distance) air temperatures is 0.77.

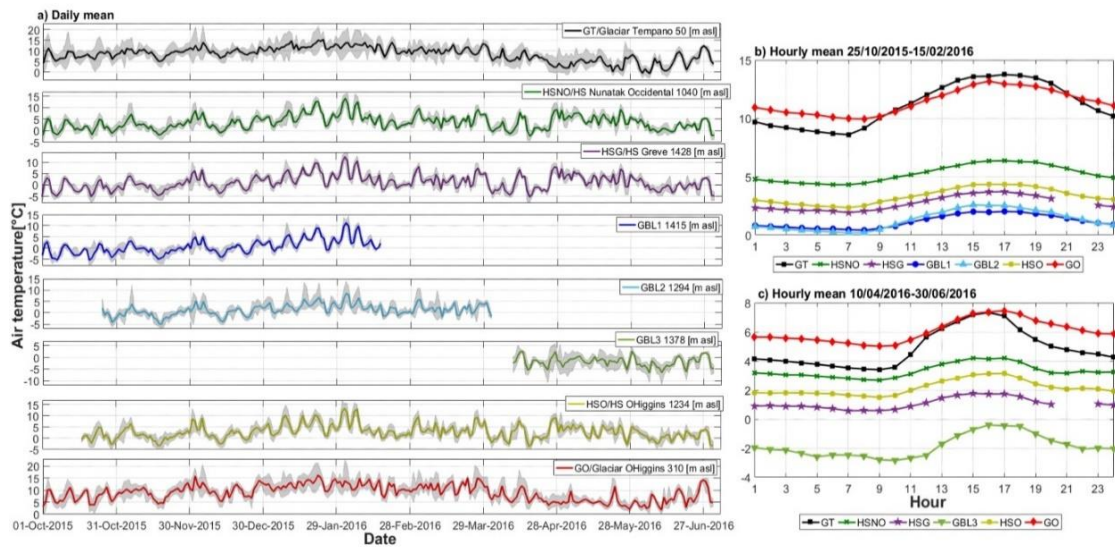


Figure 3.2 (a) Time series of the mean daily temperature of the five automatic weather stations (AWSs) and the three snow sensors. Sensors are located 2 m above the ground, except GBL1 located at 1.2 m. Gray shadows correspond to the minimum and maximum values in each day. The order from top to bottom is from west to east. Note that y axis is different between plots. (b) Hourly mean for each AWSs for the period 25 October 2015 to 15 February 2016 and (c) hourly mean for each AWSs for the period 10 October 2016 to 30 June 2016.

3.4.2 LRs at Glacier Scale

The comparison between monthly mean air temperature and the elevation of the AWS on the SPI (Table 3.2) shows that LRs are highly linear with coefficient of determination (R^2) values over 0.90 from October to March. In the fall months this correlation diminishes to values close to 0.61, and during May the R^2 value is very low (0.18) when using all AWSs, suggesting an important control other than elevation at this scale (Supplementary Figure 3.2). Spatially and temporally, the LRs estimated are steeper in the east compared to the west. Both sides show higher R^2 values (0.99) when considered separately, with the exception of fall (Table 3.2).

The stepwise hourly LRs show a range of values (Figure 3.3 and Table 3.2). The estimated hourly observed LR between each pair of AWS shows that on the west side, LRs are shallower (mean value -0.0055 °C/m) compared with the LRs observed on the east side (mean value -0.0072 °C/m). Mean values of LR on the west side (GT-HSNO and HSNO-HSG) are close to the ELR (-0.0065 °C/m). On the east side, the mean values are between the ELR and the dry adiabatic LR (-0.0098 °C/m). On the east side, the plateau LRs (HSO-HSG) are steeper than the tongue LRs (HSO-GO). On-glacier LRs (GBL1 and

GBL2) are shallower, with values in October, November, and December close to -0.0040 °C/m followed by predominantly thermal inversions episodes in January and February (Supplementary Figure 3.2).

In the west, GT-HSNO shows higher variability than the HSNO-HSG rate. In the latter case, the mean values and the median for each month are close to the ELR, while mean and median values for GT-HSNO show higher intermonthly variability. In the east, the difference between GO-HSO and HSO-HSG is less evident. In both cases, during the spring and summer months, the LRs are between the ELR and the dry adiabatic LR. LRs calculated for the HSO-HSG show a great number of steeper negative outlier values.

Thermal inversions are observed on both sides of the divide. Multisite regression and stepwise statistics show that these episodes are more frequent on the west side, especially during fall. The data in Table 3.2 show that the episodes of thermal inversion are not necessarily concordant between the lower and the higher part of the glaciers on each side. Interestingly, the time series for the east side shows that a plateau (HSO-HSG) thermal inversion could occur with decreasing temperatures on the tongue (GO-HSO) and vice versa. On the west side, it is also possible to identify episodes of thermal inversion on the tongue (GT-HSNO); meanwhile, the plateau (HSNO-HSG) shows a decrease in temperature with elevation. Therefore, a more complex structure in the air temperature LRs is detected. The lower R^2 values coincide with more frequent thermal inversion episodes, but an important difference is that the signal of the thermal inversion in the fall months, especially May, is not strong in the distribution of the LRs of HSNO-HSG.

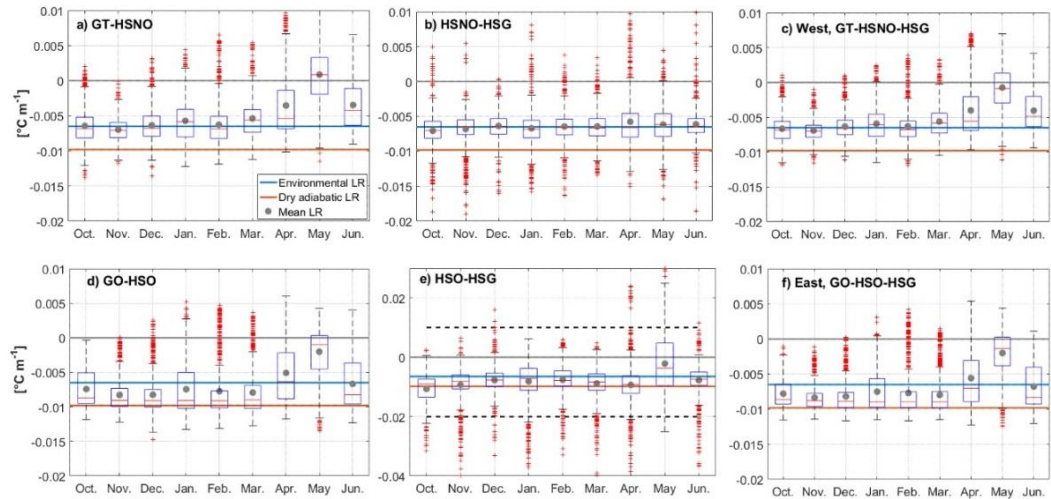


Figure 3.3 (a–f) Monthly boxplot of the lapse rates (LRs) estimated for each pair of automatic weather station. Upper and lower box limits are the 75% and 25% quartiles, the red horizontal line is the median, the filled green circle is the mean, and crosses are outlying values. As a reference, the environmental lapse rate and the dry adiabatic lapse rate are indicated. For (e) note the different y axis scale (dashed lines correspond to the range in all other panels). The gray line corresponds to zero lapse rate. (a) GT-HSNO; (b) HSNO-HSG; (c) West, GT-HSNO-HSG; (d) GO-HSO; (e) HSO-HSG; and (f) East, GO-HSO-HSG.

Table 3.2 Mean seasonal lapse rate at hourly time step for each season. Spring is October to December, summer is January to March and fall April to June. Number of cases are indicated by n and number of thermal inversions episodes (abbreviation t.i.) in brackets. The table include data from multi-linear regression of air temperature observations against elevation where parenthesis indicate the R^2 relationship. Also data obtained between each pair of AWS is shown (stepwise).

| | Multi-site linear regression | | | | | | Stepwise | | | | | | | |
|---------------|------------------------------|--|---------------|--|---------------|--|---------------|-------------------------------------|--------------|-------------------------------------|---------------|-------------------------------------|---------------|-------------------------------------|
| | All AWSs | | All AWSs West | | All AWSs East | | West | | HSNO-HSG | | East | | HSO-HSG | |
| | n (t.i.) | Lapse rate [°C m ⁻¹] (R ²) | n (t.i.) | Lapse rate [°C m ⁻¹] (R ²) | n (t.i.) | Lapse rate [°C m ⁻¹] (R ²) | n (t.i.) | Lapse rate [°C m ⁻¹] | n (t.i.) | Lapse rate [°C m ⁻¹] | n (t.i.) | Lapse rate [°C m ⁻¹] | n (t.i.) | Lapse rate [°C m ⁻¹] |
| Spring | 1672 (7) | -0.0074 (0.97) | 2024 (16) | -0.0066 (0.99) | 1672 (2) | -0.0081 (0.99) | 2208 (36) | -0.0066 | 2208 (17) | -0.0068 | 1824 (14) | -0.0080 | 1672 (46) | -0.0092 |
| Summer | 1998 (89) | -0.0069 (0.93) | 1971 (84) | -0.0059 (0.99) | 2002 (85) | -0.0077 (0.99) | 2180 (115) | -0.0058 | 2180 (47) | -0.0065 | 2184 (164) | -0.0077 | 2002 (75) | -0.0082 |
| Fall | 1993 (428) | -0.0028 (0.61) | 1993 (471) | -0.0029 (0.86) | 2002 (320) | -0.0048 (0.98) | 2175 (732) | -0.0020 | 2175 (77) | -0.0060 | 2184 (397) | -0.0046 | 2002 (341) | -0.0064 |

3.4.3 Air Temperature Distribution

A comparison of the observed air temperature (GBL) with air temperature extrapolated using the VLR method (Figure 3.4) shows an offset, especially at GBL1 (Figure 3.4a) and GBL2 (Figure 3.4b). This offset is associated with the cooling effect that off-glacier and nunatak air temperatures observations cannot account for.

The variability of the time series is almost the same, especially GBL1 and GBL2 where the correlation coefficients are 0.98 and 0.92, whereas in the location of GBL3 it is 0.54 (Figure 3.4c). Comparing these two time series reveals that spatial differences exist regarding the cooling effect. The observed on-glacier air temperature shows that the cooling effect on the west side reaches a mean value between 0.8 (GBL1) and 1.3 °C (GBL2), while on the east side it reaches 3.3 °C, with significantly more scatter (GBL3, Figure 3.4c). The strength of the glacier cooling effect could be also related to humid conditions on both sides. Figure 3.4 shows that under lower relative humidity values, the differences between VLR and the observed air temperatures are higher, and hence, the correlation is poor, especially at the GBL3 location (Figure 3.4c). We verified these data by comparing the observations from the same station at 4 m; the correlation coefficient is 0.95, and the mean difference is 0.6 °C. As the differences become more pronounced with lower values of relative humidity, and the east side is drier than the west side, we might expect to see greater differences in the east.

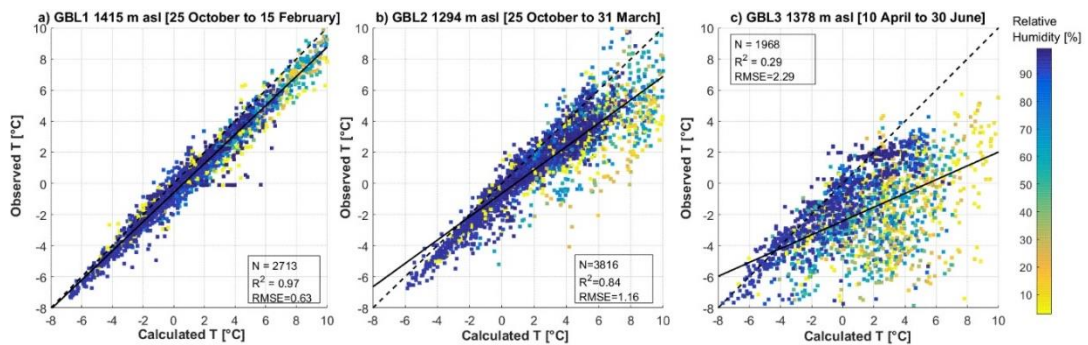


Figure 3.4 Scatterplot of the observed air temperature and the estimated air temperature using the variable lapse rate method. Locations are (a) GBL1, (b) GBL2, and (c) GBL3. Colored according to the relative humidity observed at HSG. Black line is the best fit, and the dashed line is the one-to-one relation. GBL = glacier boundary layer.

The mean values of the air temperature distribution for each of the methods are presented in Figure 3.5. At comparable elevations, warmer conditions are observed in the east using the ELR, MLR, and the VLR methods. The mean

air temperature calculated with the VLR and MLR is similar on both sides, implying a reduction of 0.5 to 0.6 °C relative to the ELR.

On the west side, ELR, VLR, and MLR showed similar values, except on the tongues of the glaciers, where ELR shows mean air temperature over 10 °C. The lowest mean air temperature is obtained with the SM10 method. SM10 shows a lower air temperature across all glacier surfaces, especially notable at the tongue of each of the glaciers. At the point scale, the comparison of the observed air temperature at GBL2 compared with the SM10 shows a mean difference of 0.6 °C. This represents a reduction of the difference with the other methods (ELR, MLR, and VLR) implying that SM10 captures some of the cooling effect of the glacier surface.

On the east side, the lowest mean air temperature is obtained with the VLRBias method. The SM10 just captures a small portion of the cooling effect as at the location of the GBL3, the mean difference with the observed data is only reduced by 0.1 °C compared with the difference using VLR. On both sides, some uncertainties exist in the magnitude of the real cooling effect using SM10 as we used the original parameters of SM10 and not newly calibrated parameters.

On the east side, the difference between ELR/MLR and VLR is smaller along the plateau and the tongues of the glaciers. However, at higher elevations, the VLR determines warmer conditions due to the thermal inversion episodes. The vertical extension of the thermal inversion is an uncertainty, considering that there are no observations over ~1,500 m a.s.l.; hence, the data at higher elevations must be taken with caution.

On both sides the VLRBias air temperature distribution shows colder conditions compared with the ELR, MLR, and the VLR. On the west side, the SM10 method gives higher cooling compared to VLRBias below 1,000 m a.s.l. and similar conditions in the range 1,000 to 1,500 m a.s.l. At higher elevations, SM10 shows warmer conditions than VLRBias. However, the area above 1,500 m a.s.l. is only ~10% of the total, which explains the generally colder conditions of SM10 compared to VLRBias on the west side (Figure 3.5). In the east, at the lower elevational range the SM10 presents colder conditions compared with VLRBias; this is a small portion of the total area of the glaciers as their fronts are located at ~250–300 m a.s.l.

Spatially, the differences between the west and east side depend on the method used for the air temperature distribution. The ELR method determines almost the same condition for each elevation range between west and east,

while the MLR and VLR method determine warm conditions on the east compared to the west in all the elevation ranges. The opposite is true using the VLRBias method with warmer conditions in the west up to ~2,000–2,500 m a.s.l. and then warmer conditions in the east due to the great number of thermal inversion episodes.

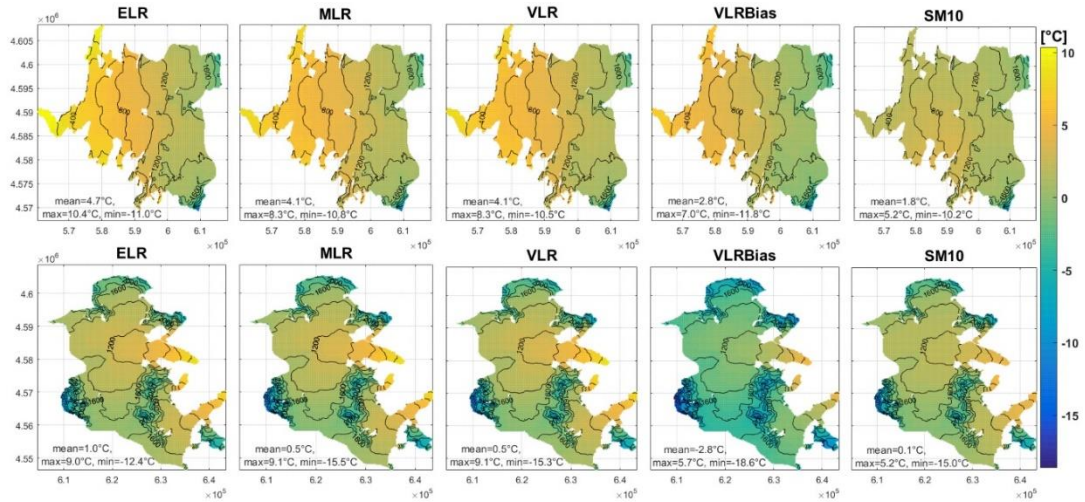


Figure 3.5 Mean air temperature for each method to distribute the air temperature on both sides of the South Patagonia Icefield. Color bar units are in degrees Celsius. Elevation contour lines interval 200 m. The top row shows the west side, and the bottom row shows the east side. ELR = environmental lapse rate; MLR = mean observed lapse rate; VLR = variable lapse rate.

3.4.4 Ablation Estimates

Hourly distributed degree-day modeling (DDM) shows the effects of the different air temperature distributions on estimating melt across the SPI during the period 1 October 2015 to 30 June 2016. For comparison, Figure 3.6 shows the differences in the melt between each of the methods used to distribute the air temperature. The differences are shown by elevation range and for a range of DDFs.

In the west, the larger differences between all the methods are concentrated at elevations below 1,000 m a.s.l. The ELR melt is highest for most of the elevation range, except the greatest elevations where all the other methods tend to be similar or higher melt rate. The highest melt differences are between ELR/MLR and SM10, reaching values between 7 and 14 m w.e. at the lower elevations. The VLR estimated greater melt than VLRBias, as expected; depending on the DDF used, this difference could reach more than 3 m w.e. in the tongue of the glacier (0 to 1,000 m a.s.l.). However, with the typical DDF used for ice (6 to 7 mm w.e.·°C⁻¹·day⁻¹), the difference is 1.5–2 m w.e. Interestingly, the differences between MLR and VLR are very low and

the differences between VLRBias and SM10 are also low except at the very lower elevations, suggesting that greater cooling effect in the tongue of the glacier is represented by SM10. At the locations of GBL1 and GBL2 and over 1,000 m a.s.l. the differences are close to 0 m w.e.

On the east side, the VLR modeled melt is higher than the ELR at higher elevations and similar at lower elevations. Higher differences are observed in the lower sector between ELR and SM10, between MLR and SM10, and between VLR and SM10, in all these cases with a maximum of 8 m w.e. assuming higher DDF. Differences between 4 and 6 m w.e. are observed for more typical DDF for ice (6 to 8 mm w.e. $\cdot^{\circ}\text{C}^{-1}\cdot\text{day}^{-1}$). The VLRBias-SM10 difference shows that the SM10 captures the cooling effect at the lower elevations, as the difference is close to 0 m w.e.

The results of the estimated melt using the five methods are compared with the observations of the ablation using UDGs at GBL1 and GBL2 locations (Supplementary Table 3.2). The observed air temperatures at these locations, following the same DDM approach, suggest that the DDF to replicate the observed melt is close to 8.5 mm w.e. $\cdot^{\circ}\text{C}^{-1}\cdot\text{day}^{-1}$, which compares well with values derived in other glaciated areas (Hock, 2003). On both sides, ELR, MLR, and VLR melt are higher than the observed; 0.4–0.5 m w.e. at GBL1 and 1.3 m w.e. at GBL2 location. VLRBias and SM10 melt rate are close to the observed values with an overestimation of 0.2–0.3 m w.e. at GBL2. This emphasizes that the inclusion of the cooling effect is necessary for melt estimations as this is a comparison with an independent source of data from the UDGs.

The results of the energy balance at point scale (Figure 3.7) show the spatial differences related to the meteorological conditions between the east side and the west side. Incoming shortwave radiation is higher in the east due to less humidity and cloud cover, and incoming longwave radiation is slightly higher in the west due to more persistent cloud cover. Turbulent fluxes are the smaller contributors to the energy balance on both sides and are the most sensitive fluxes to the changes in the air temperature distribution method.

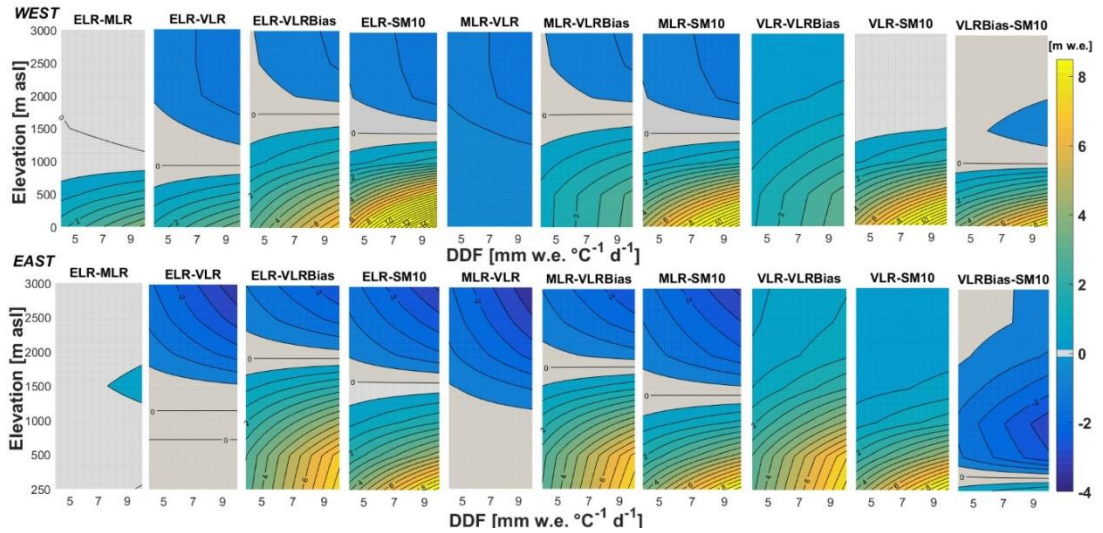


Figure 3.6 Melt differences between each of the methods used to distribute the air temperature using a range of DDF in a simple degree-day model. Upper panels correspond to the west side, and lower panels correspond to the east side. Note that at east side the lowest elevation is 250 m above sea level. ELR = environmental lapse rate; MLR = mean observed lapse rate; VLR = variable lapse rate; DDF = degree-day factor.

The sensitivity of the energy fluxes to three methods of air temperature distribution (VLR, VLRBias, and SM10) is shown in Figures 3.7a and 3.7b. In the west, the greatest change is observed in energy available for melt, as the 208 W/m^2 estimated by the VLR method reduces to 180 W/m^2 (VLRBias) and 157 W/m^2 (SM10). Refreezing values are similar. The mean latent heat changes from 45 W/m^2 (VLR) to 24 W/m^2 (VLRBias) and 19 W/m^2 (SM10), and the sensible heat changes from 68 W/m^2 (VLR) to 47 W/m^2 (VLRBias) and 43 W/m^2 (SM10). On the east side the changes in the turbulent fluxes are even higher; latent heat changes from 20 W/m^2 (VLR) to -76 W/m^2 (VLRBias) and 0 W/m^2 (SM10), and the sensible heat changes from 91 W/m^2 (VLR) to -24 W/m^2 (VLRBias) and 70 W/m^2 (SM10). The energy for melt also decreases from VLR to VLRBias but increases comparing VLRBias and SM10.

The ablation impacts associated with the different methods to distribute the air temperature to input the point-scale energy balance are shown in Figures 3.7c and 3.7f. The accumulated melt on the west side decreases from 7.4 m w.e. (VLR) to 5.9 m w.e. (VLRBias) and 5.4 m w.e. (SM10), while sublimation increases from 0.03 m w.e. (VLR) to 0.05 m w.e. (VLRBias) and 0.04 m w.e. (SM10). In any case, these sublimation values represent a very small fraction (less than 0.8%) of the total melt. On the east side the differences are more evident, the accumulated melt decreases from 8.2 m w.e. (VLR) to 3.0 m w.e. (VLRBias) and 6.6 m w.e. (SM10). The accumulated sublimation increases from 0.1 m w.e. (VLR and SM10) to 0.4 m w.e. (VLRBias). This means that in the east and using the VLRBias, sublimation

comprises 12% of the total ablation. On the west side, a qualitative comparison of the ablation is obtained from UDGs data at GBL1 and GBL2. As GBL1 and GBL2 are located at higher elevation it is expected that the ablation will be lower with respect to the HSN0 (1,040 m a.s.l.). Unfortunately, the UDG installed at GBL3 on the east side did not record data during the period of analysis. However, the UDG at GBL2 located at ~20 km from HSO represents an estimate, suggesting the VLRBias air temperature is closest to the observed ablation.

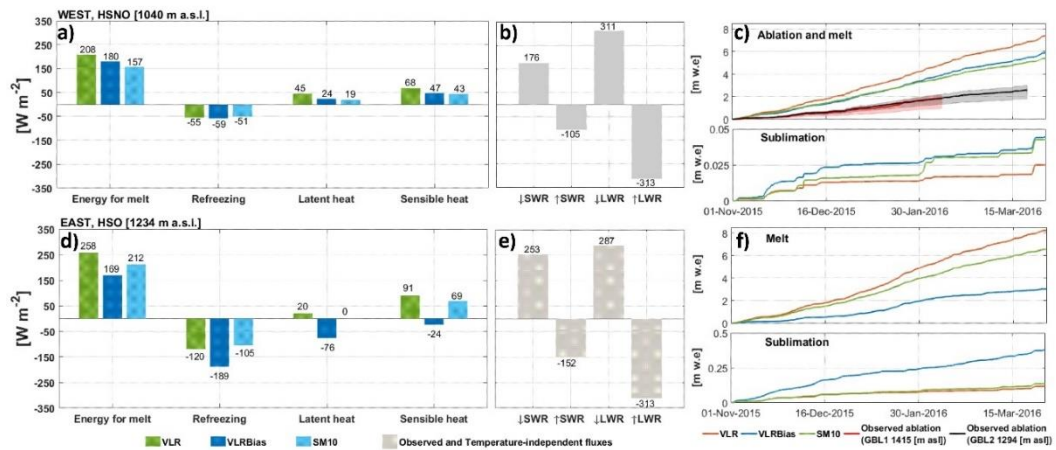


Figure 3.7 Results of the point-scale energy balance: (a) Estimated mean energy fluxes using different air temperature distributions schemes. (b) Observed radiation fluxes. (c) Estimated cumulative melt and sublimation and observed ablation at GBL1 and GBL2 locations. Shaded area corresponds to the range of snow densities observed at both locations. (a)–(c) On the west side at the location of HSN0. (d)–(f) On the east side at the location of HSO. Note that in (c) and (f) sublimation is on different scales. VLR = variable lapse rate; GBL = glacier boundary layer; SWR = shortwave radiation; LWR = longwave radiation.

3.5 Discussion

3.5.1 Uncertainties

In estimating LR from observations, it is important to recognize the influence that the number and position of stations may have on the derived values. For example, sites located at valleys bottoms, on mountain passes, and in positions elevated above glacier surfaces may not be representative of the wider terrain (Minder et al., 2010). In the current study, the correlation matrix of air temperatures revealed that GT and GO showed the weakest relationship. GT is located at the lower end of a small valley frequently affected by temperature inversion (Carturan et al., 2015). GO is located close to the front of the O'Higgins glacier but in an area also affected by the wind dynamics

of the valley of Pirámide glacier. Additionally, both AWSs are located close to water bodies, GT is close to a fjord and GO to a lake, and the boundary layer dynamics of these water bodies could also influence the air temperature at these locations. The great number of factors that potentially influence the air temperature observations indicates that corrections are necessary for using such data over glacier surfaces.

The reliability of on-glacier temperatures is crucial for the robustness of the VLRBias method. Our data show that GBL1 and GBL2 are well correlated with the observed air temperature at the nunataks (Supplementary Table 3.1) and hence could be representative of the on-glacier conditions on the plateau of the west side. However, at GBL3, there is a greater uncertainty considering the short time series and the large-scale climate anomalies during this period, which were characterized by the predominance of high sea level pressure in fall (April to May) 2016 that brought about unusual weather conditions (Garreaud, 2018). Overall, correlation coefficients are lower between all the time series during the April–June period, especially when comparing rock AWS with nunatak AWS, with values around 0.01. However, the correlations between nunatak AWSs (HSNO, HSG, and HSO) are still between 0.88 and 0.94, which means that conditions on the plateau seem to be influenced in the same direction. This gives confidence that the GBL3 data set, installed on the plateau, may reliably represent the long-term conditions on the east side of the SPI or at least is representative of the cooling effect under sunny and warm conditions. These conditions were predominant in fall 2016 due to large-scale climate anomalies (Garreaud, 2018). This is also supported by previous observations, as greater cooling effect has been observed under warm and sunny weather, while minimum values were observed during overcasts and unsettled weather (Carturan et al., 2015). However, the dispersion of the data still suggests that local conditions exist at this point, and hence, the conditions may not be representative of all the glacier area. Probably, this is the main reason that the correlation coefficient in GBL3 (~0.60) is not as high as GBL1 and GBL2, at least when compared to nunatak AWS (>0.90).

3.5.2 LRs and Air Temperature Spatial Patterns

Previous glacier mass balance modeling in the Patagonia region has not used spatial parametrization of LRs, but the results presented in this work demonstrate that clear spatial differences exist. Specifically, we show here that the observed LRs are low in the west relative to the east. Such differences across mountains are likely a common feature (e.g., the Cascade Mountains: Minder et al., 2010). At a smaller scale, there are also differences in the LRs

observed between the lower and upper regions of the icefield on both sides. Observed on-glacier LR_s are lower than off-glacier LR_s and the ELR, in agreement with findings for the Canadian Arctic (Gardner & Sharp, 2009; Marshall et al., 2007) but contrasting with steep LR_s observed over valley glaciers in the Central Andes of Chile (e.g., Bravo et al., 2017; Petersen & Pellicciotti, 2011).

Despite their common use in modeling studies, our results suggest that while the ELR, MLR, and VLR methods of temperature distribution do not represent the real on-glacier conditions, the VLR does appear to capture the on-glacier variability. Furthermore, the MLR captures the general spatial pattern and hence could also potentially be used.

For input to a glacier ablation model, including the glacier cooling effect in the air temperature distribution should theoretically give a more realistic estimate of the ablation. Considering that (i) observed on-glacier LR_s are difficult to obtain during longer periods, due to glacier surface characteristics (e.g., tilt of the structure by ice flux) and (ii) that the correlations between observed and estimated air temperature over the glacier surface are good (Figure 3.4), the glacier cooling effect could be represented by a bias correction (VLR_{Bias}, equation (2)) or by using the model of SM10, equation (3)). However, for both cases, further on-glacier data would be useful for calibrating the approach. In the first case, it is necessary to include spatial differences between the on-glacier and off-glacier air temperatures, due to cold spots and different lateral conditions with respect to the centerlines that have been observed over other glaciers (Shaw et al., 2017). In the second case, further observations are needed to calibrate the parameters of the statistical model of SM10, especially because the glaciers of the study area presents a longer fetch with respect to previous application on Alpine glaciers (e.g., Carturan et al., 2015; Shaw et al., 2017). An alternative to these corrections is the physically based model that was proposed to capture on-glacier air temperature conditions under katabatic flow events developed by Greuell and Böhm (1998), applied by Petersen et al. (2013), and its modified version previously used by Ayala et al. (2015) and Shaw et al. (2017).

The dominant control of LR_s depends of the size of the ice mass; Gardner et al. (2009) found that the free atmosphere air temperature is the main control of the LR_s rather than katabatic flow in icefields of the Canadian Arctic, but Petersen and Pellicciotti (2011) found that katabatic flow plays an important role in defining on-glacier air temperatures for a valley glacier. More in-depth analysis is therefore necessary to determine if katabatic flow plays an

important role in the SPI and hence assess the applicability of the Greuell and Böhm (1998) and SM10 models with greater confidence. The relationship between wind speed and LRs at the tongue of each side (LRs at GT-HSNO and GO-HSO, Supplementary Figure 3.3) seems to suggest a control from katabatic flow especially on the east side due to the larger temperature gradient between surface and off-glacier conditions. However, the wind speed could also be related to synoptic conditions on both sides and strong foehn winds in the east, as was previously suggested by Ohata et al. (1985) in the North Patagonia Icefield, thus preventing the development of near continuous katabatic flow. Independent of the physical explanation it is clear that at the tongues, wind speed also plays a role in defining the variability of the LRs.

The meteorological conditions clearly play an important role in defining the characteristics of the LRs on both sides of the northern sector of the SPI. Shen et al. (2016) indicated that the role of water vapor in the air is an essential driver of the spatial pattern of LRs. Gentle LRs are associated with moister atmospheric conditions, as rising air parcels cool more slowly in a humid environment than in a dry environment. Thus, the magnitude of temperature change with elevation is reduced. This mechanism can be revealed by the spatial variability of precipitation and humidity, which are higher on the western side than the eastern side as the meteorological observations and previous work indicates (Lenaerts et al., 2014; Schneider et al., 2003; Smith & Evans, 2007).

LR variability also depends on atmospheric circulation patterns. For example, the observed LRs in the area show episodes of thermal inversions, particularly in the fall months. These episodes respond to atmospheric circulation that favor the advection of warm air to the SPI (Garreaud, 2018). During these episodes, on the west side, negative LRs were observed on the plateau, while positive LRs were observed on the tongues. At the end of April, the air temperature at HSNO and HSG increased, reaching positive values during this period. Meanwhile, GT does not show this increase (Figure 3.2). This could indicate that the air temperature close to the glacier surface does not rise uniformly and the air temperature at higher elevation responds more linearly to a free-air temperature increase, as was previously suggested by Gardner et al. (2009).

It is generally accepted that at the regional scale, colder air temperatures prevail on the eastern side compared to the west side over both Patagonia Icefields (Garreaud et al., 2013; Villarroel et al., 2013), related to the topographic elevation differences between both flanks. However, at similar

elevations, the use of VLR and the off-glacier observations near the front of the glaciers (GT and GO) seems to describe warmer conditions in the east compared to the west but a steeper LR on the east, in apparent support of the results of Mernild et al. (2016).

3.5.3 Glacier Cooling Effect

On-glacier air temperature measurements reveal that the cooling effect associated with the glacier surface is higher in the east. Observed mean glacier cooling reaches a maximum of 3.3 °C relative to the VLR extrapolated between neighboring stations at the location of the GBL3 on the east side and under severe drought conditions in Patagonia (Garreaud, 2018). Similar magnitudes (3 to 4 °C) were previously observed at the Skagastøl Glacier (Norway) (Carturan et al., 2015) and in Juncal Norte glacier in central Chile (~33°S), where Ragettli et al. (2014) found a cooling effect of 2.9 °C. However, the values of the k_1 and k_2 parameters at GBL3 suggests a strong cooling effect besides being located close to the ridge (Supplementary Figure 3.1). The curves of SM10 and Shaw et al. (2017) suggest that the cooling effect at this point must be low. This discrepancy could be explained if the location of GBL3 is a cold spot. These special features require further investigation as the models cannot replicate (Shaw et al., 2017). Meanwhile, at GBL1 and GBL2, located on the west side, the cooling was between 0.8 and 1.3 °C. Although the one point of on-glacier validation and the extension of the GBL3 time series is insufficient to define the real cooling effect and its spatial differences, previous work suggests that the east side of the SPI is indeed cooler than the west. Monahan and Ramage (2010) used passive microwave observations to show that the melt-refreeze processes below 1,500 m a.s.l. start in July on the western part of the SPI, while in the east they start in September; sustained melt onset also tends to occur 25 to 35 days earlier on the west of the divide than in the east. De Angelis et al. (2007) showed larger areas of slush in the west compared to the east, as well as a greater degree of snow metamorphism associated with melt-freeze episodes in the west, suggesting warmer conditions.

The SM10 method also suggests slightly colder on-glacier conditions in the east compared to the west but limited to the elevation range between 1,000 and 2,000 m a.s.l., where 80% of the glacier area is concentrated. At the other elevation ranges, SM10 shows warmer on-glacier conditions in the east. This spatial variability reinforces the need for more distributed and longer term on-glacier observations.

3.5.4 Ablation Impacts

There is an evident impact in the reduction of the melt using a DDM with the VLRBias and SM10 air temperature data set compared to the DDM using the ELR, MLR, and VLR air temperatures. At point scale, these differences are higher in the east reaching values between 4 and 6 m w.e. for DDFs between 6 and 9 mm w.e. $\cdot^{\circ}\text{C}^{-1}\cdot\text{day}^{-1}$ at 500 m a.s.l. Assuming the mean annual melt of $\sim 10\text{--}12$ m w.e. for the tongue of O'Higgins glacier, estimated by Mernild et al. (2016), the difference between the methods represents between 33% and 60% of the melt at point scale. At the distributed scale, the mean melt in the period 1979/1980 and 2013/2014 estimated by Mernild et al. (2016) reached a mean value of 8.1 m w.e. on the west side (Greve, Témpano, and Occidental glaciers) and 6.3 m w.e. on the east side (O'Higgins and Chico glaciers). Although there are some restrictions in comparing these data (mean of 30 years) and the results of the current study (one particular season and an estimated DDF of 8.5 mm w.e. $\cdot^{\circ}\text{C}^{-1}\cdot\text{day}^{-1}$), it appears that in the east, the melt determined by Mernild et al. (2016) is too high even compared with the melt obtained from the ELR and MLR (5.6 and 5.9 m w.e.), while in the west the value obtained by Mernild et al. (2016) is close to our VLRBias estimation.

Overall, the use of the constant ELR, MLR, and VLR appears to overestimate the melt calculated by a DDM. However, MLR and VLR describe the variability of the on-glacier air temperature and hence could be used, after a correction, to estimate the melt. As the MLR represents the general spatial conditions (east-west; tongue-plateau), it should be noted that the MLR does not capture thermal inversion episodes and could underestimate the melt/ablation at higher elevations. The use of VLR has been highlighted as an important issue in glaciology applications (Marshall et al., 2007; Petersen & Pellicciotti, 2011).

The point-scale energy balance showed that the energy available decreases from VLR to VLRBias and SM10; hence, the melt decreases, notably on the east side. The energy balance results highlight that the most important impacts on the energy balance are related to the change in the sign of the turbulent fluxes using the VLRBias compared to the VLR as input to the energy balance model on the east side. The sublimation here, after a change in the sign of the mean latent heat, reaches 12% of the total ablation at 1,234 m a.s.l. This percentage could be even larger at higher elevations on the east side. Overall, the sublimation is considered a small percentage of the total ablation with values in the order of 0.1 m w.e. for the glaciers of the study area (Mernild et al., 2016). However, if the cooling effect is as high as the data from GBL3 suggest, the sublimation on the east side could be higher, and hence,

attention must be given to this ablation component when modelling future climate response.

Although the data in the current study are not conclusive, it does appear that spatially variable cooling effects must be considered as an important control on the differential response of the glaciers in this region, which has previously been attributed to the hypsometric characteristics and calving dynamics (e.g., De Angelis, 2014; Minowa et al., 2015; Rivera et al., 2012).

3.6 Conclusions

This work presents air temperature variations across the SPI along an east-west transect at approximately 48°45'S. We analyzed 9 months of observations from a network of five complete series of AWSs installed close to glacier fronts and on nunataks, supplemented by three air temperature sensors installed directly over the glacier surface. By analyzing these time series of observed air temperature and distributed values modeled with the observed LRs, including a bias correction over glacier surfaces, we identified spatial variability in the air temperature structure between the east and the west sides of the icefield. This work represents the first robust assessment of air temperature variability on the SPI. The main findings are as follows:

1. There is considerable spatial and temporal variability in LRs. Observed LRs are, overall, steeper in the east (-0.0072 °C/m) compared to the west (-0.0055 °C/m), and also differences and even contrasting behavior in the LRs exist between the lower sections (tongue of glacier, ablation zone) and upper sections (plateau, accumulation zone) on each side of the SPI. In the west, the mean LR at the tongue (GT-HSNO) reached -0.0045 °C/m, while at the plateau (HSNO-HSG) it reached -0.0064 °C/m. In the east, mean LR reached -0.0066 °C/m at the tongue (GO-HSO) and -0.0078 °C/m at the plateau (HSO-HSG).
2. Off-glacier temperature measurements are not representative for calculating on-glacier LRs. While off glacier LR accounts for the variability of the on-glacier air temperature, a bias exists in comparing the estimated and the observed air temperature time series. Applying a bias correction and/or the model of SM10, we find that on-glacier conditions are warmer on the west side compared to the east. The methods to distribute air temperature could reach differences of ~ 1 °C in the west and 3.3 °C in the east when comparing mean values. At the local scale, differences reach values higher than 10 °C especially on the tongues at each side. Certainly, more on-glacier

measurements are needed to account for this effect at the scale of the entire icefield.

3. These two factors (1 and 2) have an impact on ablation estimates. Investigating the sensitivity of ablation to modeled air temperatures shows that important differences exist depending on the method used for air temperature distribution. Distributed temperature-index modeling and point-scale energy balance analysis reveal that melt could be overestimated and sublimation could be underestimated if the glacier cooling effect is not included in the distributed temperature data. These uncertainties can lead to large variations in the estimated ablation. Overall, on the east side, total melt without air temperature corrections (ELR, MLR, and VLR) decreases by 51–56% for bias-corrected air temperatures (VLRBias) and 13–22% for the model of SM10. On the west side, this decrease is 21–31% and 54–60%, respectively. At the local scale, the energy balance shows that in the east (HSO), a reduction of 59% exists in the total ablation between VLR and VLRBias and a reduction of 19% exists between VLR and SM10. In the west (HSNO) this reduction is 20% and 27%, respectively. The turbulent flux analysis also shows that with the greater glacier cooling effect on the east side, sublimation could reach 12% of the total ablation.

In view of these findings, the main implication is that using a single, constant LR value for both sides to distribute the air temperature is not representative. Considering the overall, strong correlation between air temperature time series, the use of VLR captures the on-glacier variability. Also, the use of MLR captures the general spatial different conditions and hence could be used. However, for both cases, including the glacier cooling effect in the air temperature distribution gives more reliable ablation estimations. The correction could be done by a bias corrections as was proposed here (VLRBias), using the model of SM10 or by testing the applicability of other models (e.g., Greuell & Böhm, 1998). The calculation of the surface mass balance in these glaciers and others could be improved considering the spatial differences in the observed LR and taking account of the cooling effect to distribute the air temperatures.

Acknowledgments

We acknowledge the DGA for providing their data for analysis (<http://www.dga.cl/Paginas/estaciones.aspx>). CECs provided all the logistical support in four field campaigns. A. Rivera was supported by FONDECYT 1171832 and CECs. C. Bravo acknowledges support from the CONICYT Becas-Chile PhD scholarship program. We would like to thank Federico

Cazorzi and the anonymous reviewers for their constructive and useful comments and recommendations.

3.7 References

Aniya, M., Sato, H., Naruse, R., Skvarca, P. and Casassa, G. (1996), The use of satellite and airborne imagery to inventory outlet glaciers of the Southern Patagonia Icefield, South America. *Photogrammetric Engineering and Remote Sensing*, 62(12), 1361–1369.

Ayala, A., Pellicciotti, F. & Shea, J.M. (2015), Modeling 2 m air temperatures over mountain glaciers: exploring the influence of katabatic cooling and external warming. *Journal of Geophysical Research: Atmospheres*, 120, 1–19.

Ayala, A., Pellicciotti, F., MacDonell, S., McPhee, J., Vivero, S., Campos, C. & Egli, P. (2016), Modelling the hydrological response of debris-free and debris-covered glaciers to present climatic conditions in the semiarid Andes of central Chile, *Hydrological Processes*, 30, 4036–4058, <https://doi.org/10.1002/hyp.10971>.

Barry, R.G. (2008), *Mountain Weather and Climate*, Cambridge: University Press Cambridge.

Bliss, A., Hock, R. & Radić, V. (2014), Global response of glacier runoff to twenty-first century climate change, *Journal of Geophysical Research: Earth Surface*, 119, 717–730, doi:10.1002/2013JF002931

Bravo, C., Rojas, M., Anderson, B.M, Mackintosh, A.N., Sagredo, E., & Moreno, P.I. (2015), Modelled glacier equilibrium line altitudes during the mid-Holocene in the southern mid-latitudes. *Climate of the Past*, 11, 1575 – 1586.

Bravo, C., Loriaux, T., Rivera, A., & Brock, B.W. (2017), Assessing glacier melt contribution to streamflow at Universidad Glacier, central Andes of Chile. *Hydrological and Earth System Science*, 21, 3249-3266.

Carrivick, J.L., Davies, B.J., James, W.H.M., Quincey, D.J., & Glasser, N.F. (2016), Distributed ice thickness and glacier volume in southern South America. *Global and Planetary Change*, 146, 122-132.

Carturan, L., Cazorzi, F., De Blasi, F. & Dalla Fontana, G. (2015), Air temperature variability over three glaciers in the Ortles–Cevedale (Italian Alps): effects of glacier fragmentation, comparison of calculation methods, and impacts on mass balance modeling. *The Cryosphere*, 9, 1129–1146.

CECs-DGA (2016), Línea de base glaciológica del sector norte de Campo de Hielo Sur: Glaciares Jorge Montt, Témpano y O'Higgins. SIT N° 404, DGA, Technical Report in Spanish.

Cuffey, K. M. & Paterson, W. S. B. (2010), *The Physics of Glaciers*, 4th ed., Oxford: Elsevier.

Davies, B.J., Golledge, N.R., Glasser, N.F., Carrivick, J.L., Ligtenberg, S.R., Barrand, N.E., Van Den Broeke, M.R., Hambrey, M.J. & Smellie, J.L. (2014), Modelled glacier response to centennial temperature and precipitation trends on the Antarctic Peninsula, *Nature Climate Change*, 4, 993-998, doi: 10.1038/nclimate2369

Davies, B.J., & Glasser, N.F. (2012), Accelerating shrinkage of Patagonian glaciers from the Little Ice Age (similar to AD 1870) to 2011. *Journal of Glaciology*, 58, 1063-1084.

De Angelis, H. (2014), Hypsometry and sensitivity of the mass balance to change in equilibrium-line altitude: the case of the Southern Patagonia Icefield. *Journal of Glaciology*, 60, 14 – 28.

De Angelis, H., Rau, F., & Skvarca, P. (2007), Snow zonation on Hielo Patagónico Sur, southern Patagonia, derived from Landsat 5 TM data. *Global and Planetary Change*, 59, 149–158.

Ebrahimi, S. & Marshall, S. J. (2016), Surface energy balance sensitivity to meteorological variability on Haig Glacier, Canadian Rocky Mountains. *The Cryosphere*, 10, 2799-2819.

Foresta, L., Gourmelen, N., Weissgerber, F., Nienow, P., Williams, J.J., Shepherd, A., Drinkwater, M.R. & Plummer, S. (2018), Heterogeneous and rapid ice loss over the Patagonian Ice Fields revealed by CryoSat-2 swath radar altimetry, *Remote Sensing of Environment*, 2018, 441-455, doi.org/10.1016/j.rse.2018.03.041.

Gardner, A. S., & Sharp, M.J. (2009), Sensitivity of net mass-balance estimates to near-surface temperature lapse rates when employing the degree-day method to estimate glacier melt. *Annals of Glaciology*, 50, 80–86.

Gardner, A. S., Sharp, M. J., Koerner, R. M., Labine, C., Boon, S., Marshall, S. J., Burgess D.O., & Lewis, D. (2009), Near-surface temperature lapse rates over arctic glaciers and their implications for temperature downscaling. *Journal of Climatology*, 22, 4281–4298. doi:10.1175/2009JCLI2845.1.

Gardner, A.S., Moholdt, G., Cogley, J.G., Wouters, B., Arendt, A.A., Wahr, J., Berthier, E., Hock, R., Pfeffer, W.T., Kaser, G., Ligtenberg, S.R.M., Bolch, T.,

- Sharp, M.J., Hagen, J.O., van den Broeke, M.R., Paul, F., (2013), A reconciled estimate of glacier contributions to sea level rise: 2003 to 2009. *Science* 340 (6134), 852–857, doi.org/10.1126/science.1234532.
- Garreaud, R. (2018), Record-breaking climate anomalies lead to severe drought and environmental disruption in Western Patagonia in 2016. *Climate Research*, 74, 217-229, doi.org/10.3354/cr01505.
- Garreaud, R., Lopez, P., Minvielle, M., & Rojas, M. (2013), Large-Scale control on the Patagonian Climate. *Journal of Climate*, 26, 215 – 230.
- Gourlet, P., Rignot, E., Rivera, A., & Casassa, G. (2016), Ice thickness of the northern half of the Patagonia Icefields of South America from high-resolution airborne gravity surveys. *Geophysical Research Letters*, 43, 241-249. doi:10.1002/2015GL066728.
- Greuell, W., & Böhm, R. (1998), 2m temperatures along melting midlatitude glaciers, and implications for the sensitivity of the mass balance to variations in temperature. *Journal of Glaciology*, 44(146), 9–20.
- Greuell W., & Genthon, C., (2003), Modelling land ice surface mass balance. In Bamber, J.L. and A.J. Payne, eds. *Mass balance of the cryosphere: observations and modelling of contemporary and future changes*. Cambridge, Cambridge University Press.
- Hanna, E., Mernild, S., Yde, J.C., & de Villiers, S. (2017), Surface air temperature fluctuations and lapse rates on Olivares Gamma glacier, Rio Olivares basin, Central Chile, from a novel meteorological sensor network. *Advances in Meteorology*, 2017, 1-15, doi:10.1155/2017/6581537.
- Heynen, M., Pellicciotti, F., & Carenzo, M. (2013), Parameter sensitivity of a distributed enhanced temperature-index melt model. *Annals of Glaciology*, 54(63), 311-321. doi:10.3189/2013AoG63A537
- Heynen, M., Miles, E., Ragettli, S., Buri, P., Immerzeel, W., & Pellicciotti, F. (2016), Air temperature variability in a high-elevation Himalayan catchment. *Annals of Glaciology*, 57 (71), 212–222.
- Hock, R. (2003), Temperature index melt modelling in mountain regions. *Journal of Hydrology*, 282, 104–115.
- Hock, R. (2005), Glacier melt: a review of processes and their modelling. *Progress in Physical Geography*, 29, 362–391.
- Kerr, A., & Sugden, D. (1994), The sensitivity of the southern Chilean snowline to climatic change. *Climatic Change*, 28, 255 – 272.

Lenaerts, J.T.M., van den Broeke, M.R., van Wessem, J.M., van de Berg, W.J., van Meijgaard, E., van Uft, L., & Schaefer, M. (2014), Extreme Precipitations and Climate Gradients in Patagonia Revealed by High-Resolution Regional Atmospheric Climate Modeling. *Journal of Climate*, 27, 4607-4621.

Liston G. E., & Elder K. (2006), A meteorological distribution system for high-resolution terrestrial modeling (MicroMet). *Journal of Hydrometeorology*, 7, 217–234. doi: 10.1175/JHM486.1

Mackay, J. D., Barrand, N. E., Hannah, D. M., Krause, S., Jackson, C. R., Everest, J., & Aðalgeirsdóttir, G. (2018), Glacio-hydrological melt and run-off modelling: application of a limits of acceptability framework for model comparison and selection. *The Cryosphere*, 12, 2175-2210, <https://doi.org/10.5194/tc-12-2175-2018>.

Malz, P., Meier, W., Casassa, G., Jaña, R., Skvarca, P., & Braun, M.H. (2018), Elevation and Mass Changes of the Southern Patagonia Icefield Derived from TanDEM-X and SRTM Data. *Remote Sensing*, 10(2), 188. doi:10.3390/rs10020188

Marshall, S. J., Sharp, M. J., Burgess, D. O., & Anslow, F. S. (2007), Near-surface temperature gradients on the Prince of Wales Icefield, Ellesmere Island, Canada: implications for regional downscaling of temperature. *International Journal of Climatology*, 27, 385–398.

Masiokas, M., Villalba, R., Luckman, B., Lascano, M., Delgado, S., & Stepanek, P. (2008), 20th-century glacier recession and regional hydroclimatic changes in northwestern Patagonia. *Global and Planetary Change*, 60, 85–100

Meier, W.J-H, Griesinger, J., Hochreuther, P. & Braun, M.H. (2018), An Updated Multi-Temporal Glacier Inventory for the Patagonian Andes With Changes Between the Little Ice Age and 2016. *Frontiers in Earth Science*, 6, doi: 10.3389/feart.2018.00062

Mernild, S. H., Liston, G. E., Hiemstra, C. A., & Wilson, R. (2016), The Andes Cordillera. Part III: Glacier Surface Mass Balance and Contribution to Sea Level Rise (1979–2014). *International Journal of Climatology*, 37, 3154–3174.

Minder, J.R., Mote, P.W., & Lundquist, J.D. (2010), Surface temperature gradients over complex terrain: lessons from the Cascade Mountains. *Journal of Geophysical Research*, 115, D14122. doi: 10.1029/2009JD013493.

Minowa, M., Sugiyama, S., Sakakibara, D., & Sawagaki, T. (2015), Contrasting glacier variations of Glaciar Perito Moreno and Glaciar Ameghino, Southern Patagonia Icefield. *Annals of Glaciology*, 56, 26–32.

Monahan, P. & Ramage, J. (2010), AMSR-E Melt Patterns on the Southern Patagonian Icefield. *Journal of Glaciology*, 56, 699-708.

National Aeronautics and Space Administration Jet Propulsion Laboratory (2013), NASA Shuttle Radar Topography Mission Global 3 arc second sub-sampled [Data set]. NASA EOSDIS Land Processes DAAC. doi: 10.5067/MEaSURES/SRTM/SRTMGL3S.003

Oerlemans, J. (2001), *Glaciers and Climate Change*, Rotterdam, Netherlands: A. A. Balkema.

Ohata T., Kobayashi, S., Enomoto, H., Kondo, H., Saito, T., & Nakajima, C. (1985), The east-west contrast in meteorological conditions and its effect on glacier ablation. *Bulletin of Glaciological Research*, 3, 52-53.

Oke, T. R. (1987), *Boundary Layer Climate*, 2nd ed., London: Methuen.

Pellicciotti, F., Brock, B., Strasser, U., Burlando, P., Funk, M., & Corripio, J. (2005), An enhanced temperature-index glacier melt model including the shortwave radiation balance: development and testing for Haut Glacier d'Arolla, Switzerland. *Journal of Glaciology*, 51(175), 573–587. doi.org/10.3189/172756505781829124

Pellicciotti, F., Ragetti, S., Carenzo, M., & McPhee, J. (2014), Changes of glaciers in the Andes of Chile and priorities for future work. *Science of the Total Environment*, 493, 1197-1210, doi.org/10.1016/j.scitotenv.2013.10.055

Petersen, L. & Pellicciotti, F. (2011), Spatial and temporal variability of air temperature on a melting glacier: atmospheric controls, extrapolation methods and their effect on melt modeling, Juncal Norte Glacier, Chile. *Journal of Geophysical Research*, 116, D23109. doi: 10.1029/2011JD015842

Petersen, L., Pellicciotti, F., Juszak, I., Carenzo, M. & Brock, B.W. (2013), Suitability of a constant air temperature lapse rate over an alpine glacier: testing the Greuell and Böhm model as an alternative. *Annals of Glaciology*, 54, 120–130.

Popovnin, V., Danilova, T., & D. Petrakov, D. (1999), A pioneer mass balance estimate for a Patagonian glacier: Glaciar De Los Tres, Argentina. *Global and Planetary Change*, 22: 255 – 267.

Radić, V., Bliss, A., Beedlow, A. C., Hock, R., Miles, E., & Cogley J.G. (2013), Regional and global projections of 21st century glacier mass changes in response to climate scenarios from global climate models, *Climate Dynamics*, 42, 37–58, doi:10.1007/s00382-013-1719-7.

Ragettli, S., Cortés, G., McPhee, J. & Pellicciotti F. (2014), An evaluation of approaches for modelling hydrological processes in high-elevation, glacierized Andean watersheds. *Hydrological Processes*, 28, 5674–5695, doi:10.1002/hyp.10055

Rignot, E., Rivera, A., & Casassa, G. (2003), Contribution of the Patagonia Icefields of South America to Sea Level Rise. *Science*, 302, 434-436, 2003.

Rivera, A. (2004), Mass balance investigations at Glaciar Chico, Southern Patagonia Icefield, Chile (Doctoral dissertation), University of Bristol, UK.

Rivera, A.; Corripio, J., Bravo, C. & Cisternas, S. (2012), Glaciar Jorge Montt (Chilean Patagonia) dynamics derived from photos obtained by fixed cameras and satellite image feature tracking. *Annals of Glaciology*, 53(60), 147-155.

Sagredo, E., & Lowell, T. (2012), Climatology of Andean glaciers: A framework to understand glacier response to climate change. *Global and Planetary Change*, 86 – 87, 101 – 109.

Sakakibara, D., & Sugiyama, S. (2014), Ice-front variations and speed changes of calving glaciers in the Southern Patagonia Icefield from 1984 to 2011. *Journal of Geophysical Research: Earth Surface*, 119, 2541–2554. doi:10.1002/2014JF003148

Schaefer, M., Machguth, H., Falvey, M., & Casassa, G. (2013), Modeling past and future surface mass balance of the Northern Patagonian Icefield. *Journal of Geophysical Research: Earth Surface*, 118, 571–588. doi:10.1002/jgrf.20038

Schaefer, M., Machguth, H., Falvey, M., Casassa, G., & Rignot, E. (2015), Quantifying mass balance processes on the Southern Patagonia Icefield. *The Cryosphere*, 9, 25–35.

Schneider, C., Glaser, M., Killian, R., Santana, A., Butorovic, N., & Casassa, G. (2003), Weather observations across the Southern Andes at 53°S. *Physical Geography*, 24, 97-119.

Shaw, T., Brock, B. W., Fyffe, C., Pellicciotti, F., Rutter, N. & Diotri, F. (2016), Air temperature distribution and energy-balance modelling of a debris-covered glacier, *Journal of Glaciology*, 62, 185–198.

- Shaw, T. E., Brock, B. W., Ayala, A., Rutter, N., & Pellicciotti, F. (2017), Centreline and cross-glacier air temperature variability on an Alpine glacier: Assessing temperature distribution methods and their influence on melt model calculations. *Journal of Glaciology*, 63(242), 973–88.
- Shea, J. M. & Moore, R. D. (2010), Prediction of spatially distributed regional-scale fields of air temperature and vapour pressure over mountain glaciers, *Journal of Geophysical Research*, 115, D23107. doi:10.1029/2010JD014351
- Shen, Y. J., Shen, Y., Goetz, J., & Brenning, A. (2016), Spatial-temporal variation of near-surface temperature lapse rates over the Tianshan Mountains, central Asia. *Journal of Geophysical Research: Atmospheres*, 121, 14006–14017. doi:10.1002/2016JD025711
- Smith, R., & Evans, J. (2007), Orographic precipitation and water vapor fractionation over the Southern Andes. *Journal of Hydrometeorology*, 8, 3 – 19.
- Stuefer, M., Rott, H., & Skvarca P. (2007), Glaciar Perito Moreno, Patagonia: climate sensitivities and glacier characteristics preceding the 2003/04 and 2005/06 damming events. *Journal of Glaciology*, 53(180), 3–16. doi: 10.3189/172756507781833848.
- Takeuchi, Y., Naruse R. & Skvarca, P. (1996), Annual air-temperature measurement and ablation estimate at Moreno Glacier, Patagonia, *Bulletin of Glacier Research*, 14, 23-28.
- Teutschbein, C., & Seibert, J. (2012), Bias Correction of Regional Climate Model Simulations for Hydrological Climate-Change Impact Studies: Review and Evaluation of Different Methods. *Journal of Hydrology*, 456-457, 11-29.
- Tsai, V., & Ruan, X. (2018). A simple physics-based improvement to the positive degree day model. *Journal of Glaciology*, 1-8. doi:10.1017/jog.2018.55
- Villarroel, C., Carrasco, J., Casassa, G., & Falvey, M. (2013), Modeling near-surface air temperature and precipitation using WRF with 5-km resolution in the Northern Patagonia Icefield: A pilot simulation. *International Journal of Geosciences*, 4, 1193–1199. doi:10.4236/ijg.2013.48113
- Warren, C., & Sugden, D. (1993), The Patagonian Icefields: A glaciological review. *Arctic and Alpine Research*, 25(4), 316-331.
- Weidemann, S.S., Sauter, T., Malz, P., Jaña, R., Arigony-Neto, J., Casassa, G., & Schneider, C. (2018), Glacier Mass Changes of Lake-Terminating Grey and Tyndall Glaciers at the Southern Patagonia Icefield Derived From

Geodetic Observations and Energy and Mass Balance Modeling. *Frontiers in Earth Science*, 6, doi: 10.3389/feart.2018.00081

Wheler, B. A., Macdougall, A. H., Petersen, E. I., & Kohfeld, K. E. (2014), Effects of temperature forcing provenance and extrapolation on the performance of an empirical glacier-melt model. *Arctic Antarctic and Alpine Research*, 46, 379–393.

White, A., & Copland, L. (2015), Decadal-scale variations in glacier area changes across the Southern Patagonian Icefield since the 1970s. *Arctic Antarctic and Alpine Research*, 47, 147–167, 2015.

Willis, M., Melkonian, A., Pritchard, M., & Rivera, A. (2012), Ice loss from the Southern Patagonian Ice Field, South America, between 2000 and 2012. *Geophysical Research Letters*, 39, L17501. doi:10.1029/2012gl053136

Wilson, R., Carrión, D., & Rivera, A. (2016), Detailed dynamic, geometric and supraglacial moraine data for Glaciar Pio XI, the only surge-type glacier of the Southern Patagonia Icefield. *Annals of Glaciology*, 57, 119-130.

Chapter 4
**Assessing Snow Accumulation Patterns and Changes on
the Patagonian Icefields**

Claudio Bravo, Deniz Bozkurt, Álvaro Gonzalez-Reyes, Duncan J. Quincey,
Andrew N. Ross, David Farías-Barahona and Maisa Rojas

Manuscript published in *Frontiers in Environmental Sciences* 7:30

DOI: [10.3389/fenvs.2019.00030](https://doi.org/10.3389/fenvs.2019.00030)

4.1 Abstract

Recent evidence shows that most Patagonian glaciers are receding rapidly. Due to the lack of in situ long-term meteorological observations, the understanding of how glaciers are responding to changes in climate over this region is extremely limited, and uncertainties exist in the glacier surface mass balance model parameterizations. This precludes a robust assessment of glacier response to current and projected climate change. An issue of central concern is the accurate estimation of precipitation phase. In this work, we have assessed spatial and temporal patterns in snow accumulation in both the North Patagonia Icefield (NPI) and South Patagonia Icefield (SPI). We used a regional climate model, RegCM4.6 and four Phase Partitioning Methods (PPM) in addition to short-term snow accumulation observations using ultrasonic depth gauges (UDG). Snow accumulation shows that rates are higher on the west side relative to the east side for both icefields. The values depend on the PPM used and reach a mean difference of 1,500 mm w.e., with some areas reaching differences higher than 3,500 mm w.e. These differences could lead to divergent mass balance estimations depending on the scheme used to define the snow accumulation. Good agreement is found in comparing UDG observations with modeled data on the plateau area of the SPI during a short time period; however, there are important differences between rates of snow accumulation determined in this work and previous estimations using ice core data at annual scale. Significant positive trends are mainly present in the autumn season on the west side of the SPI, while on the east side, significant negative trends in autumn were observed. Overall, for the rest of the area and during other seasons, no significant changes can be determined. In addition, glaciers with positive and stable elevation and frontal changes determined by previous works are related to areas where snow accumulation has increased during the period 2000–2015. This suggests that increases in snow accumulation are attenuating the response of some Patagonian glaciers to warming in a regional context of overall glacier retreat.

4.2 Introduction

Patagonia is the largest glaciated area in the Southern Hemisphere outside Antarctica. Patagonian glaciers show a strong sensitivity to climate variations and recent evidence shows that most of these glaciers are receding rapidly (Davies and Glasser, 2012; White and Copland, 2015; Meier et al., 2018). This deglaciation process is a matter of concern due to their observed and potential contribution to sea level rise (Rignot et al., 2003; Willis et al., 2012; Gardner et al., 2013). Despite this, only a few studies have focused on understanding

how glacier mass balance is responding to changes in climate over this important region of the Southern Hemisphere (Pellicciotti et al., 2014; Malz et al., 2018). The main reason for the lack of research studies over this region is associated with the scarcity of in situ long-term meteorological observations, especially on the plateau of both icefields, where extreme weather conditions prevail throughout the year.

Previous studies have focused on comparing surface elevation changes during recent decades derived from digital elevations model (DEMs) obtained from topographic and satellite data in both the North Patagonia Icefield (NPI) and the South Patagonia Icefield (SPI). Overall, these analyses show surface lowering in almost all the NPI, with some exceptions in the accumulation zones (Rivera et al., 2007; Dussailant et al., 2018; Foresta et al., 2018). Meanwhile, negative changes are concentrated in the northern sector of the SPI (Foresta et al., 2018; Malz et al., 2018), whereas the south-central sector shows near balance conditions and even positive changes in elevation (e.g., Pío XI Glacier; Malz et al., 2018). As might be expected, the highest negative trends are concentrated in the ablation zone of the glaciers. The heterogeneity in glacial elevation changes reveals a complex spatial structure of the glacier responses in this region. The overall observed negative changes in surface elevation contrast with surface mass balance models studies that largely illustrate positive trends on both the NPI and SPI (Schaefer et al., 2013, 2015; Mernild et al., 2016b; Weidemann et al., 2018). One explanation suggested for this discrepancy is increasing ice flow velocities associated with ice loss due to calving. Unfortunately, to date there are no empirically-based studies of the meteorological conditions over both sides of the Patagonian Icefields that can constrain the mass balance modeling studies. Due to the lack of observation based analyses, high uncertainties exist in the glacier surface mass balance model parameterizations precluding a complete validation of the simulated accumulation (Villarroel et al., 2013) as well as a robust assessment of the response of the glaciers to projected climate change.

Despite recent and past efforts, one of the main components of the glacier mass balance, the snowfall and hence the snow accumulation in Patagonia, remains poorly understood. Snow accumulation has been estimated at different scales from Global and Regional Climate Models (Schaefer et al., 2013, 2015; Lenaerts et al., 2014; Mernild et al., 2016a; Weidemann et al., 2018) to point scale estimates from stake observations (Rivera, 2004) and ice core data (Yamada, 1987; Matsuoka and Naruse, 1999; Shiraiwa et al., 2002; Schwikowski et al., 2013). Considering the spatial extent of both Patagonian

Icefields, ice cores and stake estimates are only representative of local conditions. Furthermore, the lack of observed accumulation data causes high uncertainties in the simulations regarding the glacier-wide amount of solid precipitation. For example, using a mass balance model for Tyndall and Grey glaciers on the SPI, Weidemann et al. (2018) showed that the accumulation values are significantly lower than those estimated by Mernild et al. (2016b). These discrepancies in the estimations are partially associated with atmospheric forcing fields and different precipitation schemes used in the mass balance models.

The accurate estimation of precipitation phase is an issue of central concern regarding the uncertainties of mass balance models. To calculate accumulation in Patagonia, the precipitation phase has been parameterized using air temperature as the input for typical Phase Partitioning Methods (PPMs) such as static threshold (e.g., Rivera, 2004; Koppes et al., 2011) and linear transition (e.g., Schaefer et al., 2013, 2015; Weidemann et al., 2018) methods. However, recent studies have shown that precipitation phase is not only a function of surface air temperature, but is also influenced by relative humidity, wind speed, stability of the atmosphere, and interaction between hydrometeors (Behrangi et al., 2018 and references therein). According to Harpold et al. (2017), the first step toward improved hydrological (and glaciological) modeling in areas with a mixed precipitation phase such as the NPI and SPI, is to educate the scientific community about current techniques and their limitations and to highlight the areas where research is most needed.

Given the general lack of data and analysis on accumulation estimates and thus associated uncertainties, as well as its relevance to understanding snow accumulation processes on the Patagonian Icefields, the main goal of this work is to analyze snow accumulation over the period 1980–2015 using a regional climate model simulation (RegCM4.6, at ~10 km spatial resolution) and short-term on-glacier accumulation observations. In the first section, we compare the results of four PPMs, three of them previously used in the region. In the second section, we analyze the seasonal trends in snow accumulation over the period 1980–2015. In the third section, we compare the datasets with the in-situ observations and previous estimates made in the scientific literature. Finally, the results are discussed in terms of the implications for glacier surface mass balance modeling and the observed glacier response.

4.3 Materials and Methods

4.3.1 Study Area

The study area includes the two largest temperate ice masses located in the Southern Hemisphere: the North Patagonia Icefield (NPI) and the South Patagonia Icefield (SPI) (Figure 4.1). The NPI extends from 46°30'S to 47°30'S (Figure 4.1B), stretching almost 125 km north–south. It covered an area of ~3,675 km² in 2016 (Meier et al., 2018) extending from sea level to elevations in excess of 4,000 m a.s.l. at the summit of Mount San Valentín. It is composed of 38 glaciers larger than 0.5 km² (Dussailant et al., 2018).

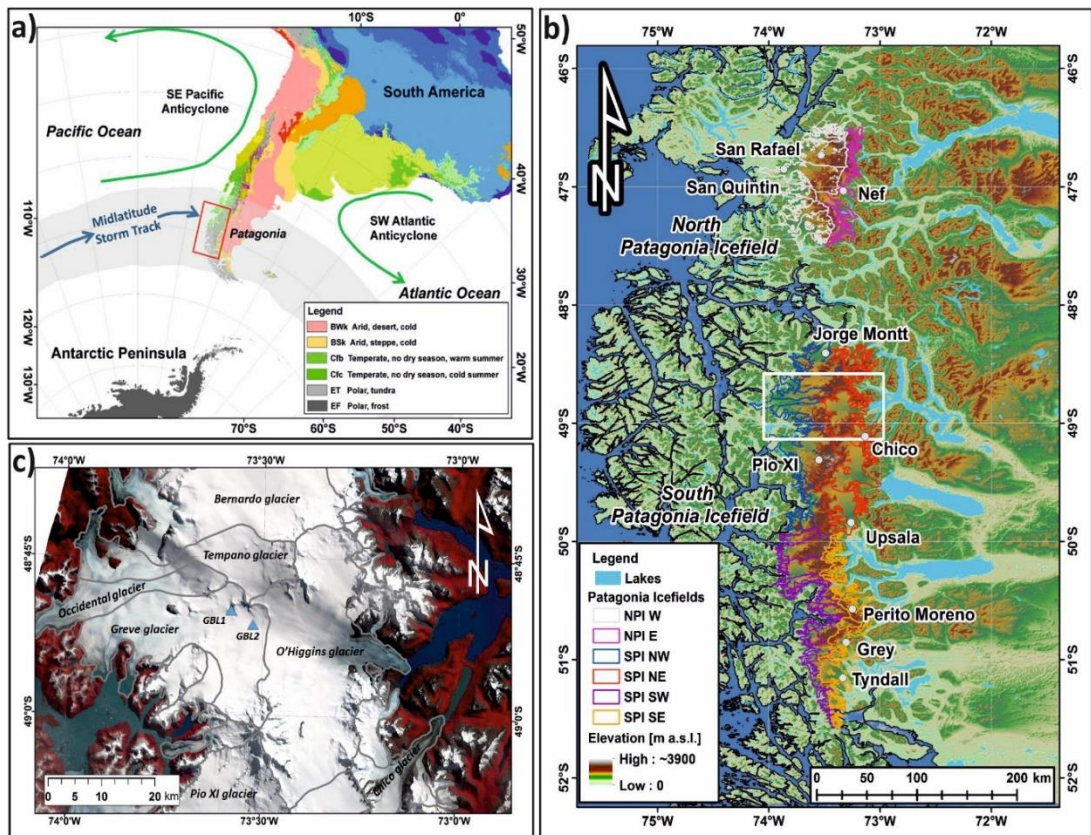


Figure 4.1 (A) Regional climatic setting over the Patagonian region. Colors correspond to the predominant Köppen-Geiger climate classification for Patagonia (Beck et al., 2018) and the red rectangle corresponds to the study area. (B) SRTM topography at 1 km resolution of the study area and locations of some glaciers mentioned in the text, and (C) localization of the observations (Ultrasonic Depth Gauges) used in this work. The satellite image was acquired by Landsat 8 (OLI) on the 8 April 2014.

The SPI spreads over 350 km between the latitudes 48°20'S and 51°30'S (Figure 4.1B), and is the most glaciated zone of the Andes, covering an area of 12,232 km² in 2016 (Meier et al., 2018). The SPI includes a total of 48 main glacier basins, ending mainly in fjords on the western side and in lakes on the eastern side (Aniya et al., 1996). These glaciers are joined in the accumulation

zone (“plateau”), with an average altitude of 1,600m a.s.l., and a measured thickness of more than 700 m (Rivera and Casassa, 2002) with a maximum estimate of ice thickness of ~1,250 m (Gourlet et al., 2016).

This zone is strongly influenced by frontal systems associated with mid-latitude cyclones forming over the South Pacific Ocean (Figure 4.1A). Given the complex terrain and extreme environment, there are a small number of meteorological stations (Garreaud et al., 2013) that only partially capture the climatology and meteorological conditions of this zone, especially at higher elevations. Data from the Climate Research Unit (CRU; Sagredo and Lowell, 2012) and from Puerto Eden weather station located in the fjord zone (49° 08'S, 74° 25'W, Carrasco et al., 2002), show that this zone is characterized by a seasonal variation in temperature with minimum values in the winter months (~3°C) and maximum values in summer (~11°C). South of 49°S, the precipitation is equally distributed throughout the year, with slightly maximum values in March and April (Sagredo and Lowell, 2012). However, given that Patagonian Icefields are in a transition zone, immediately to the north there is a marked annual cycle in the precipitation, with a winter maximum. At inter-annual scales, precipitation variability responds to hemispheric scale patterns associated with the Southern Annular Mode (SAM) and El Niño Southern Oscillation (ENSO), which determine the year-to-year variability of the precipitation. Multidecadal variations are related to the Inter-decadal Pacific Oscillation (IPO; Garreaud et al., 2013). The SAM mode presents a significant impact on regional climate, where positive SAM is associated with higher temperatures (Gillett et al., 2006), an intensification of the westerlies toward higher latitudes (Hall and Visbeck, 2002) and an increase in precipitation over the south of the study area. Negative SAM leads to opposite effects. This is particularly of interest since SAM has shown a positive trend during the second half of the 20th century (Marshall, 2003) and is associated with anthropogenic effects (Abram et al., 2014) that will potentially affect climatological trends in coming decades.

Although the southern Patagonian Andes is a relatively low elevation mountain belt, it has an influence on the longitudinal distribution of the precipitation in the region and generates an extreme climatic gradient, leading to very humid western slopes and dry eastern slopes (Schneider et al., 2003; Smith and Evans, 2007; Lenaerts et al., 2014). Garreaud et al. (2013) showed that the precipitation at regional scale is positively or negatively correlated with zonal wind component at 850 hPa, in the western or eastern sectors of the Andes, respectively, due to the mechanical effect of the mountain chain that

forces air to ascend in the western sector (windward side). On the other hand, these conditions favor downslope subsidence, and thus lead to arid conditions on the leeward side (Garreaud et al., 2013). Given these conditions, annual mean precipitation varies between 5,000 and 10,000 mm yr⁻¹ on the windward side, while it decreases to < ~300mm yr⁻¹ on the leeward side (Garreaud et al., 2013).

In addition to the precipitation characteristics, increases in air temperature are considered to have an impact on the mass balance (Cook et al., 2003), as these glaciers lie in the range of the 0°C isotherm. For instance, increases in air temperature may cause a compound effect; first, more energy becomes available for melting, and second, with a small increase in air temperature during the accumulation season, air temperature may rise above 0°C and alter the partitioning between rain and snow (Rasmussen et al., 2007). These changes eventually have an impact on the glacier's net mass balance. This indicates that the Patagonian glaciers are mainly sensitive to air temperature increase, since ablation is dominated by melt (Sagredo and Lowell, 2012). It is also stated that warming is the main cause for glacier retreat over the region (Masiokas et al., 2009). Between 43 and 49°S, a warming in the land surface temperature of 0.78°C/per decade in the period 2001–2016 was determined by Olivares-Contreras et al. (2018). In southern Patagonia (~50°S), warming of ~0.5°C in the last 40 years was detected by Rasmussen et al. (2007) using NCEP-NCAR reanalysis at 850 hPa level.

4.3.2 Observations

We used data obtained from two ultrasonic depth gauges (UDGs) (Figure 4.1C). These UDGs (model SR50) were installed directly on the glacier snow surface over the plateau (CECs-DGA, 2016). In the same structure, two air temperature sensors were also installed at an initial height of 2 and 4 m above ground level. Data obtained at 15 min time steps from these stations, referred to as Glacier Boundary Layer (GBL) air temperature stations (GBL1, GBL2 in Figure 4.1C and Table 4.1), are used to validate and compare snow accumulation against the estimated values obtained with the different PPMs (next sections). First, we separate the data between accumulation and ablation, before visually filtering the SR50 data to discard outlier values. Then, a moving average at hourly scale was applied in order to reduce the noise. Finally, the hourly data in meters was converted to mm w.e. using the method of estimation of density (ρ_s) of Hedstrom and Pomeroy (1998) based on air temperature (T_a) only:

$$\rho_s = 67.92 + 51.25 e^{(T_a/2.59)}. \quad (1)$$

Based on these results, we were able to estimate the daily accumulation.

Table 4.1 Details of the two UDGs at the GBL stations.

| Acronym | Latitude | Longitude | Elevation [m a.s.l.] | Period |
|---|------------|------------|----------------------|------------------------------------|
| Glacier Boundary Layer Station 1 (GBL1) | 48°50'02"S | 73°34'51"W | 1,415 | 17 October 2015 - 31 December 2015 |
| Glacier Boundary Layer Station 2 (GBL2) | 48°51'34"S | 73°31'37"W | 1,294 | 25 October 2015 - 31 December 2015 |

4.3.3 Data Compilation

We compiled snow accumulation estimates of the Patagonian Icefields from previous studies to compare with the snow accumulation estimations performed in this work. Some studies measured the ablation and accumulation using short-term direct observation through the use of stakes. There is a lack of long-term mass balance measurements using the glaciological method on the NPI and SPI. In view of this fact, we also considered ice core and modeling estimations in this study.

We also compiled glaciological data related to observed glacier changes mainly between 2000 and 2015 in both the NPI and SPI. In the current study, these data obtained at glacier scale are used to support our analysis of glacier response and its implications. The compilation corresponds to elevation changes in the SPI during the period 2000–2015 (Malz et al., 2018), elevation changes in the NPI during the period 2000–2014 (Braun et al., 2019), ice velocity in both Icefields (Mouginot and Rignot, 2015), frontal changes in the SPI (Sakakibara and Sugiyama, 2014), and estimation of the accumulation-area ratio (AAR) in the NPI (Rivera et al., 2007) and in the SPI (Malz et al., 2018). Finally, we compiled glacier characteristics from the Randolph Glacier Inventory 6.0 (RGI Consortium, 2017).

4.3.4 Regional Climate Model (RegCM4.6)

Regional Climate Model, version 4.6 (RegCM4.6) is a three-dimensional, primitive equation, hydrostatic regional climate model maintained by the International Center for Theoretical Physics (ICTP). RegCM4 was originally developed by Giorgi et al. (1993a,b) and its dynamical core is based on the hydrostatic version of the Penn State/NCAR mesoscale model MM5 (Grell et al., 1994). RegCM has been used in numerous regional climate model simulations, even over regions dominated by complex terrain features such

as the Atacama Desert (Bozkurt et al., 2016), the polar regions (Grassi et al., 2013; Bozkurt et al., 2018), and the European Alps (Giorgi et al., 2016). Multiple physical schemes are available in the model. RegCM4 simulations used in the present study are based on (1) the land surface model Biosphere-Atmosphere Transfer Scheme (BATS) of Dickinson et al. (1993); (2) the planetary boundary layer of Holtslag et al. (1990); (3) the radiative scheme of the NCAR Community Climate System Model Version 3 (CCSM3) (Kiehl et al., 1996); (4) the ocean flux parameterization of Zeng et al. (1998); and (5) the scheme of Pal et al. (2000) for representing resolvable precipitation. In terms of cumulus parameterization, there are several options for convective precipitation in the model; the Kuo-type scheme of Anthes (1977), the Grell scheme (Grell, 1993), the Emanuel scheme (Emanuel, 1991), and mixed schemes. Based on a couple of test simulations done with different convective schemes, the Grell scheme with a cumulus closure scheme of Fritsch and Chappell (Fritsch and Chappell, 1980) was applied in the simulations. A more detailed description of the model and physical parameterizations can be found in Giorgi et al. (2012).

The simulations were performed on two domains at 0.44° (~50 km) and 0.09° (~10 km) spatial resolutions and 23 vertical sigma levels with a one-way nesting approach. The topography of the icefields from 10 km simulations is given in Supplementary Figure 4.1. The mother domain has 192×202 grid cells covering all South America and the nested domain has 320×520 grid cells centered on Chile and southwest South America based on a Rotated Mercator projection. Initial and boundary conditions for the mother domain were provided by the European Center for Medium-Range Weather Forecasts (ECMWF, ERA-Interim) Reanalysis dataset at 6-h intervals with a grid spacing of 0.75° resolution. The nested domain was then forced by the 3D atmospheric outputs of the model domain at 6-h intervals. ERA-Interim sea surface temperature fields (6-h intervals, 0.75° resolution) were used as surface boundary conditions. The simulations were performed continuously from 1 January 1979 to 31 December 2015. The first year of simulations (1979) was selected as the spin-up period and, thus, was not considered in the analysis.

Ongoing work found that, overall, RegCM4 is capable of reproducing mean spatial fields of important large-scale features such as South Pacific Subtropical Anticyclone dry regime, westerlies over Patagonia and low-level moisture distribution along both sides of the Andes barrier. The same study also demonstrates that the simulations tend to have stronger westerlies over Patagonia and further suggest that 10-km simulation results exhibit a

reasonable representation of spatial and temporal variability of temperature and precipitation. For instance, high-resolution simulation results reproduce reasonably well the observed spatial pattern of frost days with a close estimate of the observed number of days over the Patagonian Icefields.

4.3.5 Phase Partitioning Methods (PPMs)

To calculate and assess the snow accumulation under different schemes, four methods were used to separate between snowfall and rain. The primary input is the 10-km total precipitation simulations from RegCM4.6, as our intention is to assess the snow accumulation under four PPMs, three of them previously used in the Patagonian Icefields. In addition, 10 km simulations from RegCM4.6 of near-surface air temperature, relative humidity (at 2 m), and atmospheric surface pressure were used. In all cases, we used daily model output. In all these methods, the required inputs are air temperature and total precipitation, while in the fourth method a broader range of meteorological inputs are needed.

The first method considers a threshold value in the air temperature to separate between rainfall and snowfall. The chosen threshold temperature is 2°C as this value was used in studies of the San Rafael Glacier in the NPI (Koppes et al., 2011) and the Chico Glacier in the SPI (Rivera, 2004). In this article, we refer to this method as 2C. This static temperature threshold is close to that used by the BATs scheme.

The second method was used by Weidemann et al. (2018) (WE, hereafter), where the fraction of solid precipitation (r) is estimated according to:

$$r = 0.5 * (-\tanh((T_a - 1) * 3) + 1). \quad (2)$$

In this equation, the proportion of solid precipitation to total precipitation is smoothly scaled between 100 and 0% within an air temperature range of 0–2°C, meaning that under 0°C the fraction of solid precipitation is 100%, while above the 2°C the fraction of solid precipitation is 0%. This method has been also applied to the Gran Campo Nevado Icefield in southernmost Patagonia (Möller et al., 2007; Weidemann et al., 2013).

The third method was used by Schaefer et al. (2013, 2015) in the NPI and SPI (SC, hereafter). The accumulation (q) is the fraction of the solid precipitation which is determined by the temperature (T_a) in the grid cell (I):

$$q(I) = \begin{cases} 0, & T_a(I) > 1.5^\circ\text{C} \\ \frac{1.5^\circ\text{C} - T_a(I)}{1^\circ\text{C}}, & 0.5^\circ\text{C} < T_a(I) < 1.5^\circ\text{C} \\ 1, & T_a(I) < 0.5^\circ\text{C}. \end{cases} \quad (3)$$

Finally, the fourth method corresponds to the parameterization proposed by Ding et al. (2014) (DI, hereafter). This scheme was constructed using climate data from China and only evaluated over China; however, evaluations for further regions are recommended (Ding et al., 2014). This scheme defines three types of precipitation (snow, sleet and rain) using minimum and maximum temperatures (T_{min} and T_{max}) and the wet-bulb temperature T_w [°C] as threshold:

$$type = \begin{cases} snow, & \text{if } T_w \leq T_{min}; \\ sleet, & \text{if } T_{min} < T_w < T_{max}; \\ rain, & \text{if } T_w \geq T_{max}. \end{cases} \quad (4)$$

$$T_{min} = \begin{cases} T_0 - \Delta S * \ln \left[\exp \left(\frac{\Delta T}{\Delta S} \right) - 2 * \exp \left(-\frac{\Delta T}{\Delta S} \right) \right], & \frac{\Delta T}{\Delta S} > 2 \\ T_0, & \frac{\Delta T}{\Delta S} \leq 2 \end{cases} \quad (5)$$

$$T_{max} = \begin{cases} 2 * T_0 - T_{min}, & \frac{\Delta T}{\Delta S} > 2 \\ T_0, & \frac{\Delta T}{\Delta S} \leq 2. \end{cases} \quad (6)$$

T_w is calculated using:

$$T_w = T_a - \frac{e_{sat}(T_a)(1-f)}{0.000643p_s + \frac{\partial e_{sat}}{\partial T_a}} \quad (7)$$

where $e_{sat}(T_a)$ is the saturated vapor pressure which is only a function of the air temperature and is calculated using the empirical equation of Bolton (1980), and p_s is the surface atmospheric pressure in hPa.

The three parameters (ΔT , ΔS , T_0) of this model depend not only on air temperature but also on other conditions such as relative humidity (f , ranges from 0 to 1) and the elevation of the point in km (Z):

$$\Delta T = 0.215 - 0.099 * f + 1.018 * f^2 \quad (8)$$

$$\Delta S = 2.374 - 1.634 * f \quad (9)$$

$$T_0 = -5.87 - 0.1042 * Z + 0.0885 * Z^2 + 16.06 * f - 9.614 * f^2. \quad (10)$$

ΔT is the difference between the temperature of the probability threshold for snow (or snow and sleet) and the temperature of the centralized probabilities curve. ΔS represents a temperature scale in which an increase in value leads to widening of the temperature range of snow/ratio transitions. T_0 is the temperature that approximately represents the center of T_w range in which snow/rain transitions happens. This method is dynamic as it is dual-threshold when $f > 78\%$ and single threshold method when $f \leq 78\%$. The complete parameterization scheme and explanation for precipitation type discrimination and data used can be found in Ding et al. (2014).

To analyze the spatial differences in the snow accumulation spatial patterns and annual cycle, we divide the study area into six zones, classifying the glaciers according to their location. The NPI is separated into west (NPI W; the San Rafael and San Quintin glaciers) and east (NPI E; the Nef, Colonia, Pared Norte, Soler, Leones, etc. glaciers) while the SPI is separated into four zones, SPI north-west (SPI NW, the Jorge Montt, Bernardo, Témpano, Occidental, Greve, and Pío XI glaciers), SPI north-east (SPI NE; the O'Higgins, Chico, and Viedma glaciers), SPI south-west (SPI SW; the HPS29, HPS31, HPS34, Asia, and Amalia glaciers) and SPI south-east (SPI SE; the Ameghino, Perito Moreno, Grey, and Tyndall glaciers).

4.3.6 Trend Analysis

In order to identify trends in annual and seasonal snow accumulation for the four PPM in the period 1980–2015, we used two methods—linear least-squares slopes and Sen's slope tests. The linear least-square slopes and the Sen's slope test allow to compute the magnitude of the trend. The slope of the snow accumulation at each season and at annual scale is regressed on time and hence used to quantify temporal trends. The Sen's slope test uses a linear model to estimate the slope of the trend choosing the median of the slopes, and the variance of the residuals should be constant in time (Salmi et al., 2002). We also estimate the statistical significance at 95% (p -value <0.05) using the Mann-Kendall test. The trend calculation is also applied to seasonal time series values of each zone [Figure 4.1 and defined in section Phase Partitioning Methods (PPMs)] and to individual glaciers in the period 2000–2015, in order to compare with the trends in the geodetic mass balance over the same period.

4.4 Results

4.4.1 Inter-comparison of PPMs

The spatial patterns in the distribution of annual snow accumulation are similar between the four PPM methods (Figure 4.2). All PPM methods driven by the data from RegCM4.6 show that the west sides of both Patagonian Icefields receive a higher amount of snowfall relative to the east side, indicating the capability of RegCM4.6 to capture the extreme orographic effect (Table 4.2 and Figure 4.2). Overall, in all the zones, the 2C method shows the highest amounts of snow accumulation, while the DI method shows the lowest values (Table 4.2). Interestingly, if we consider the sleet type as accumulation in the DI method, the total (snow plus sleet, Table 4.2 and Supplementary Figure 4.2) is of a similar magnitude to that of the 2C method. This suggests that the

air temperature threshold used in the 2C method is appropriate for estimating the total rain, if we compare with the DI method. The WE and SC method are of similar magnitude at annual and season scale (Figure 4.2, Table 4.2, Supplementary Table 4.2). The interannual variability (Table 4.2) and seasonal scale (Supplementary Table 4.1) is higher on the west side in both icefields. Finally, the sleet type precipitation (Supplementary Figure 4.2) shows a higher rate on the western side of both icefields, in line with the more humid conditions that would be expected at the windward side of the Andes.

A comparison of the maximum values of each PPM with respect to latitudinal variation of snow accumulation is given in Figure 4.3. Maximum values reach 14,000 mm w.e. in the 2C method, the DI model reaches 11,500 mm w.e., and the WE and SC methods are around 13,000 mm w.e. at the same latitude (Figure 4.3). This maximum accumulation point corresponds to the HPS15, HPS19, and Penguin glaciers in the SPI. Other areas with a high amount of accumulation are the accumulation zones of the Pío XI and HPS34 glaciers, with maximum values around 12,000 mm w.e. (2C method) and 9,000 mm w.e. (DI method). For the NPI, a similar amount of snow accumulation is estimated throughout the accumulation zones of the glaciers on the west side, with values between 4,000 and 7,500 mm w.e. The maximum value in the NPI depends on the PPM used (Figure 4.3). For instance, 2C shows a peak value (7,000 mm w.e.) in the accumulation zone of the San Quintin Glacier (~47°S) while the DI method shows maximum value on the San Rafael Glacier accumulation zone and on the Benito, HPN1, and Acodado glaciers (~5,000 mm w.e.).

The annual mean differences between the models that give the highest (2C) and lowest amounts of snow accumulation (DI) reach a mean value of 1,626 mm w.e. in NPI W, 373 mm w.e. in NPI E, 3,542 mm w.e. in SPI NW, 823 mm w.e. in SPI NE, 2,015 mm w.e. in SPI SW and 646 mm w.e. in SPI SE (Table 4.2). Details of the maximum and minimum amount of snow accumulation per zone and per season are given in Supplementary Table 4.2.

The mean annual cycle of snow accumulation for each PPM indicates that, overall, the minimum and maximum values exist in February and August, respectively (Figure 4.4). However, the annual cycles show some differences in the amplitude depending on the location. For instance, east side glaciers in all the zones exhibit snow accumulation equally distributed throughout the year, while west zones show a marked cycle in the snow accumulation. In the north-south direction, the east side zones show that the amplitude of the annual cycle is small in the SPI NE and SPI SE zones relative to the NPI E.

In summary, an overall spatial and temporal consistency exists between the four PPMs as all of them show consistently larger amounts of snow accumulation throughout the year on the west side zones of the icefields in comparison to those of the eastern zones. Also, similar annual cycles are simulated at each zone between the four PPMs. However, the absolute values in the snow accumulation simulated by the four PPMs differ widely in some cases.

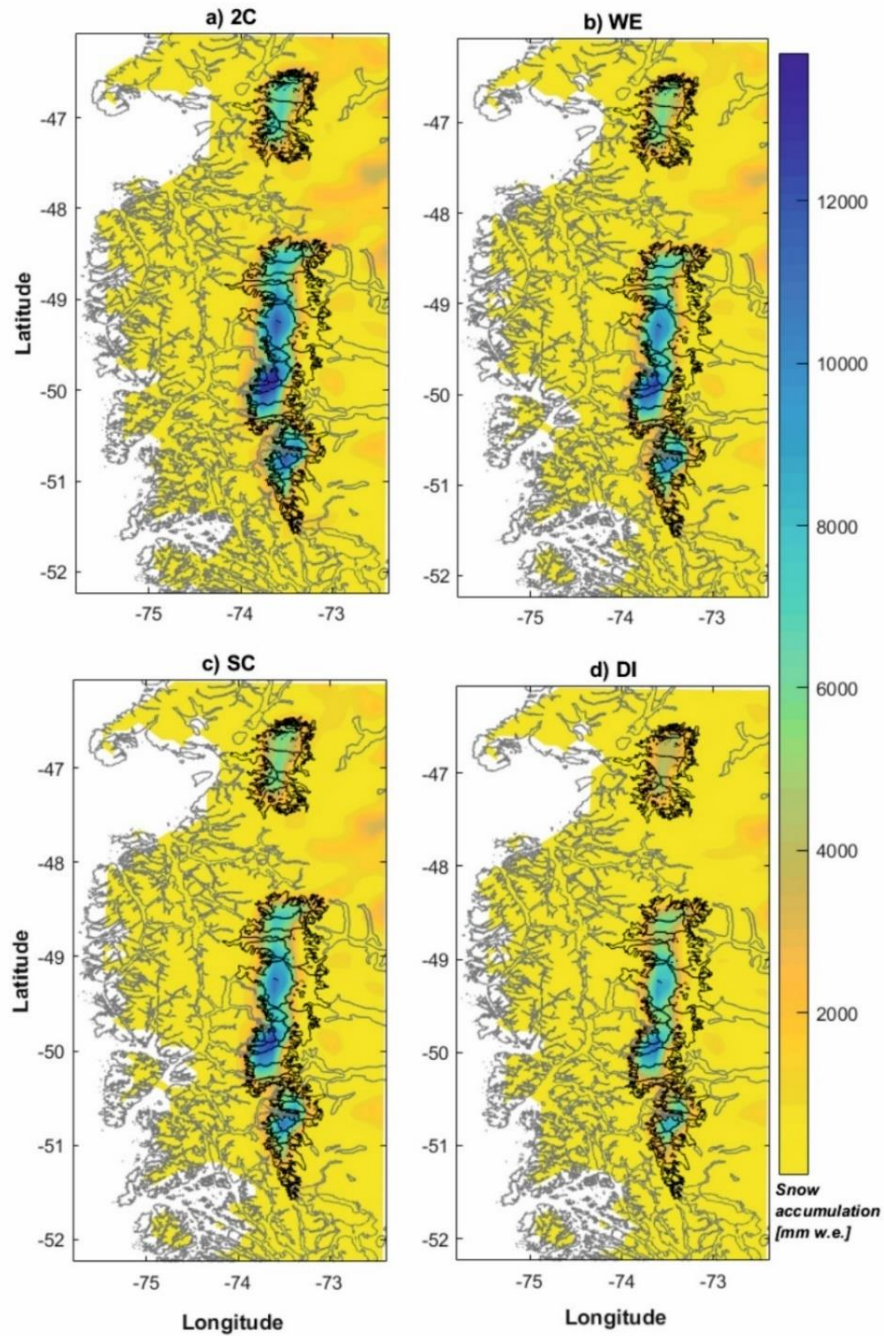


Figure 4.2 1980–2015 annual mean value of snow accumulation (mm w.e.) for each PPM. (A) 2C, (B) WE, (C) SC, and (D) DI method. Icefield contours in black were obtained from RGI consortium (2017) and edited using a Landsat 8 image (OLI) of the 8 April 2014. Coastlines are in gray.

Table 4.2 Annual mean and standard deviation 1980-2015 of the snow accumulation values by zone and PPM.

| Zone | PPM / RegCM4.6 [mm w.e.] | | | | | | | | | |
|--------|--------------------------|---------|-------|---------|-------|---------|-------|---------|-----------------|---------|
| | 2C | | WE | | SC | | DI | | DI (snow+sleet) | |
| | Mean | Std Dev | Mean | Std Dev | Mean | Std Dev | Mean | Std Dev | Mean | Std Dev |
| NPI W | 4,941 | 463 | 4,313 | 416 | 4,314 | 416 | 3,315 | 381 | 4,892 | 459 |
| NPI E | 1,084 | 107 | 913 | 98 | 914 | 99 | 710 | 92 | 1,084 | 107 |
| SPI NW | 8,010 | 908 | 6,500 | 796 | 6,500 | 796 | 4,467 | 641 | 7,883 | 891 |
| SPI NE | 4,186 | 381 | 3,873 | 358 | 3,874 | 358 | 3,363 | 326 | 4,166 | 380 |
| SPI SW | 5,471 | 532 | 4,680 | 492 | 4,680 | 491 | 3,455 | 436 | 5,408 | 527 |
| SPI SE | 3,033 | 226 | 2,801 | 215 | 2,801 | 216 | 2,388 | 201 | 3,027 | 224 |

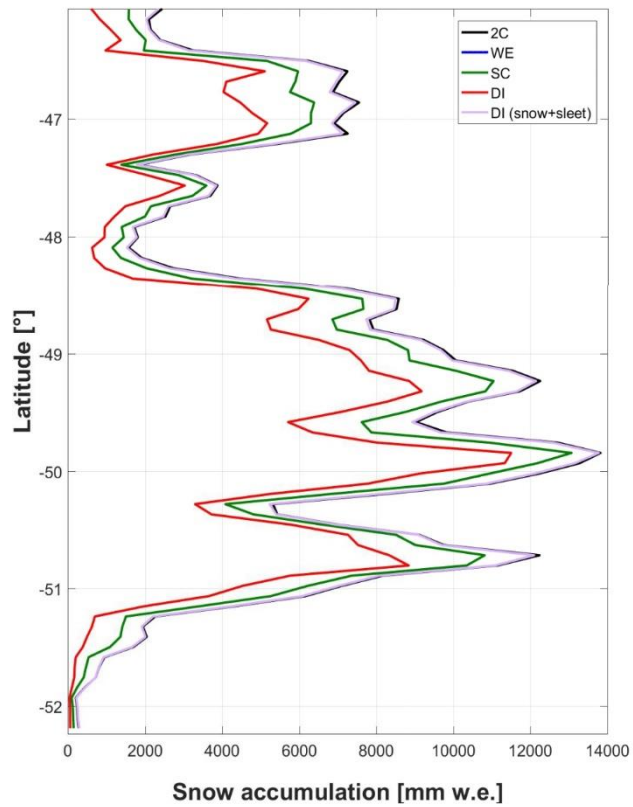


Figure 4.3 1980–2015 maximum mean value of snowfall for each PPMs.

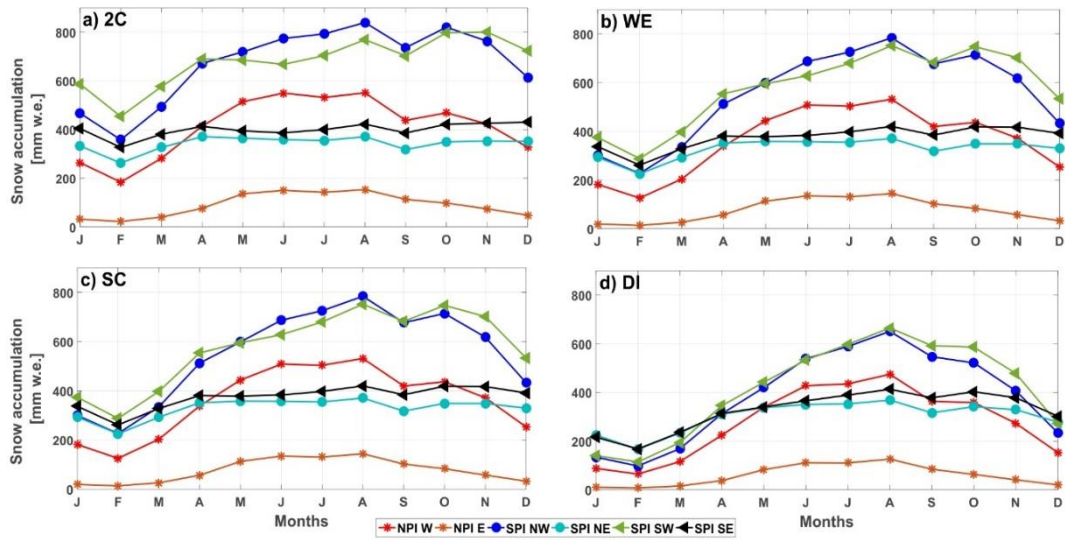


Figure 4.4 Annual cycle of snow accumulation for the sub-regions of both Patagonia Icefields. (A) 2C, (B) WE, (C) SC, (D) DI.

4.4.2 Seasonal Trends 1980–2015

We further analyzed the seasonal trends obtained by three of the four PPMs (2C, WE, and DI) as the WE and SC methods show almost identical values and inter-annual variability. Trends obtained using Sen's slope and linear least-square slopes are similar spatially and in magnitude, therefore in this section we analyzed the result of the least-square slope (Figure 4.5), while the results of the Sen's slope are shown in the Supplementary Figure 4.3.

Spatial heterogeneity exists in the trends, with some areas showing an increasing trend in snow accumulation while other areas show a decreasing trend or no change (Figure 4.5). Overall, throughout all the seasons, areas of no significant change correspond to terrain outside of both icefields. On the icefields, areas with increasing and decreasing trends in snow accumulation are concentrated on the plateau on the west and east sides of both icefields, respectively. Statistically significant positive trends are detected on the SPI in autumn. The location of these positive trends corresponds to the plateau or accumulation zones of the glaciers. On the other hand, in the ablation zones, especially those in the north-west section of the SPI (e.g., Témpano, Bernardo, Pío XI) there are no significant positive trends, and in some areas negative trends exist. In autumn, the significant negative trends are concentrated on the east side of the NPI and on the east side of the SPI in the zones of the O'Higgins, Chico, Upsala, Viedma, Ameghino, and Perito Moreno glaciers. In these areas, negative trends are also detected in spring but the values are not significant. In winter, a predominance of positive, although not significant, trends are determined on both icefields.

The time series of each zone are similar between the PPMs and [see section Phase Partitioning Methods (PPMs)] shows an important inter-annual variability. For instance, for the DI method in autumn (Figure 4.6), the generally positive trend was interrupted in 1997, with the snow accumulation values sharply dropping more than 500 mm w.e. for both icefields. Interestingly, the highest snow accumulation corresponds to the winter season of the same year, with values reaching around 3,000 mm w.e. in the west side of the SPI. Using 2C and WE methods, the winter 1998 values are close to 4,000 mm w.e. (not shown).

In summary, spatial and temporal differences exist in the snow accumulation trends. Spatially, positive trends are concentrated on the west side of both icefields throughout all seasons, while negative trends are concentrated in some areas on the east side of both icefields during autumn, winter and spring. However, in both cases significant trends are only present in the autumn season.

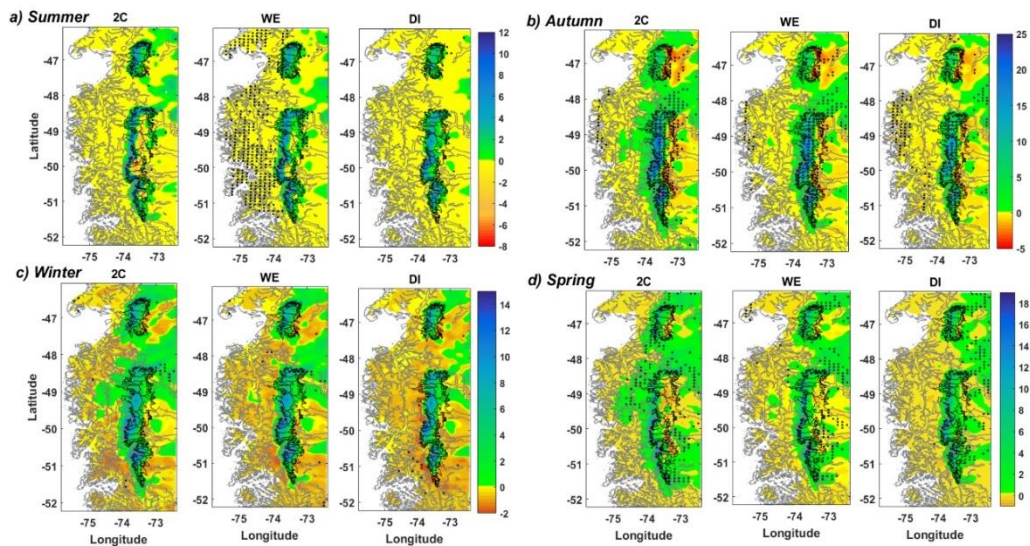


Figure 4.5 Seasonal trends 1980–2015 in mm w.e. yr⁻¹ for three Phase Partitioning Methods. Points indicate statistically significant trend ($p < 0.05$). (A) Summer, (B) Autumn, (C) Winter and, (D) Spring. Icefield contours are in black and coastlines in gray.

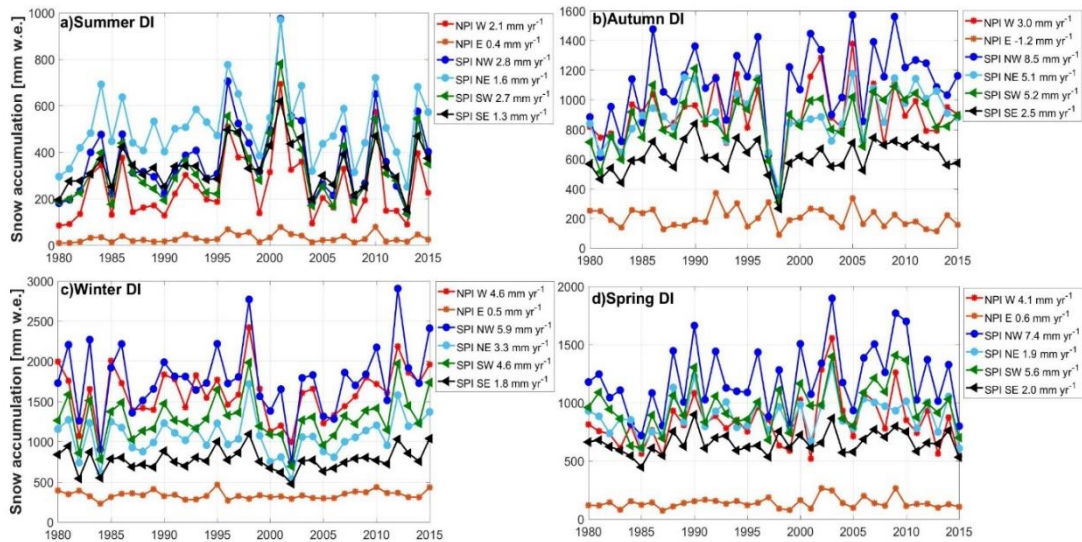


Figure 4.6 Seasonal time series and trends of the snow accumulation for six sub-regions of the study area using the DI method. (A) Summer, (B) Autumn, (C) Winter and, (D) Spring. The legend also indicates the annual trend.

4.4.3 Comparisons with Measured data

4.4.3.1 UDG Observations

We compared the estimated snow accumulations from the four PPMs, with the observations from the UDGs at locations GBL1 and GBL2 during the period October–December 2015 (Figure 4.7). Both stations are located at the same grid point of the RegCM4.6. Nevertheless, given that the elevation of this grid is 1,259 m a.s.l.; the grid characteristics are considered to be closer to the GBL2 (see Table 4.1). Regarding the GBL1, we used the grid point adjacent to the SW with an elevation of 1,492 m a.s.l., which is close to the real elevation of GBL1 (Table 4.1).

At GBL1, the PPMs show a total accumulation between 1,000 and 1,200 mm w.e. while the data from the UDG suggests an accumulation of 1,100 mm w.e. The observed accumulations during October and November are of a higher magnitude relative to the estimated values of PPMs. Daily correlation coefficients (r) between the different PPMs and the observations are very close to each other (0.62 to 0.64). At GBL2, PPMs show some differences in the accumulated values, ranging between 900 and 1,300 mm w.e. while the observations suggest 1,050 mm w.e. Similar to GBL1, the r values are in the order of 0.60 and 0.65, except the one for the DI method (0.49, Figure 4.7). In the same location, the r value is higher (0.60) if the sleet type is considered as accumulation. Although some uncertainties may exist in estimating the accumulation from the UDGs (e.g., filter used), estimated values of the four PPMs using RegCM4.6 data perform well-compared to those obtained from

the UDGs, especially at GBL1. The estimated values based on four PPMs are in the range of the observed values from the UDGs, but in terms of absolute values, the WE method is the most accurate at GBL1 (difference of 46 mm w.e.) while the SC method is the most accurate at GBL2 (difference of 135 mm w.e.). It is important to note that the regional climate models themselves may introduce uncertainty to the simulated variables associated with the physical configuration used in the model (e.g., radiation and cumulus schemes). Therefore, some inherent uncertainties may exist in the estimated values as well.

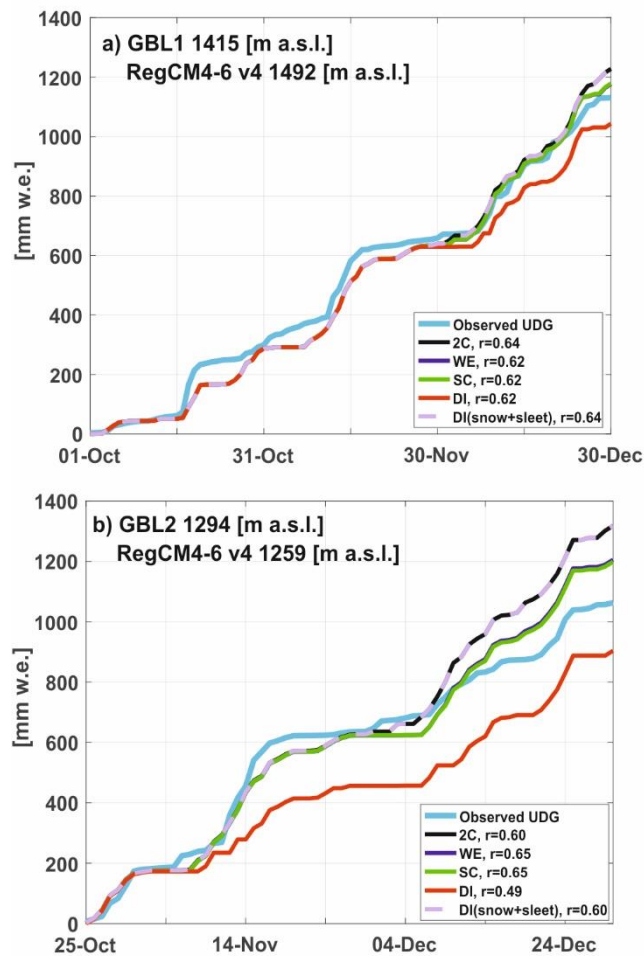


Figure 4.7 Comparison of accumulated snowfall using four PPMs and observations at (A) GBL1 and (B) GBL2. The correlation coefficient (r) values of each method are calculated in comparing with the observations.

4.4.3.2 Previous Snow Accumulation Estimations and Comparisons

Details of the location of ice cores collected on the Patagonian Icefields are given in Table 4.3. These data were analyzed in order to obtain snow accumulation rates across the NPI and SPI (Table 4.3). Ice core data estimates an accumulation of 5,600 mm w.e. at Nef Glacier in the NPI

(Matsuoka and Naruse, 1999), while the estimated values based on the RegCM4.6 data are in the range of 4,100 to 5,000 mm w.e. for the same glacier. On the other hand, at Tyndall Glacier located in the SPI, differences between the ice core and RegCM4.6 estimates are even larger, reaching (in the case of the DI method) a maximum difference of 11,400 mm w.e. in the period between summer 1998 and summer 1999. Other comparisons of ice core and RegCM4.6-based estimates are given in Table 4.3. In all cases, estimations using Tyndall Glacier ice core data are larger than those four PPMs using the RegCM4.6 data. The opposite relation is found when comparing the RegCM4.6-based snow accumulation values with those estimated by ice core data (Schwikowski et al., 2013) from the accumulation zone of the Pío XI Glacier (~2,600 m a.s.l.). For instance, this ice core data estimates a mean annual accumulation of 5,800 mm w.e. (with a range of 3,400–7,100 mm w.e.) between the years 2001 and 2005. These values are not as high as others have previously estimated for the SPI. At this point, the estimate based on RegCM4.6 data illustrates a higher amount of accumulation values with differences of ~4,500 mm in 2001 and < ~800 mm w.e. in 2002. Other studies estimate a mean accumulation of 1,200 mm w.e. yr⁻¹ in Perito Moreno Glacier of the SPI (50°38'S, 73°15'W, 2,680 m a.s.l., Aristarain and Delmas, 1993), which is lower than the annual rates of the current work.

In terms of modeling snow accumulation, a recent study by Weidemann et al. (2018) estimated the total mean precipitation for two glaciers of the SPI—the Tyndall and Grey glaciers. The precipitation distribution was modeled using an analytical orographic precipitation model at 1 km resolution, then the SC method was applied to obtain the amount of solid precipitation. The comparison of these results with those obtained in the current study for the same hydrological years is presented in Figures 4.8A,B. Overall, the inter-annual variability (2000–2015) between the time series of the two estimations is similar, yet there are some differences in the estimated snow accumulation values. At Grey Glacier, the annual accumulation estimated by Weidemann et al. (2018) is in the range of values determined by the four PPMs. In the first six hydrological years, snow accumulation estimates based on DI and SC-WE methods are close to those estimated by Weidemann et al. (2018). However, in the later hydrological years, the estimates of the 2C method give closer values to those in Weidemann et al. (2018). At Tyndall Glacier, the estimates from Weidemann et al. (2018) are in the range of those estimated by the four PPMs, mainly concentrated between the values estimated using the DI and SC-WE methods.

Table 4.3 Comparison of previous snow accumulation estimates using ice core data with the snow accumulation obtained in this work. Note that periods for each comparison are different.

| Reference | Location | Period | Accumulation [mm w.e.] | PPM / RegCM4.6 [mm w.e.] | | | |
|----------------------------|--|-------------------------------|---------------------------|--------------------------|-------|-------|-------|
| | | | | 2C | WE | SC | DI |
| Matsuoka and Naruse (1999) | Nef Glacier 46°56'S, 73°19'W 1500 m asl | 1996 | 5,600 | 5,000 | 4,900 | 4,900 | 4,100 |
| Shiraiwa et al. (2002) | Tyndall Glacier 50°59'S, 73°31' W 1756 m asl | Summer 1998- Summer 1999 | 17,800 | 9,000 | 8,100 | 8,100 | 6,400 |
| | | Summer 1999- Dec.1999 | 11,000 | 7,700 | 7,100 | 7,100 | 5,300 |
| Koshima et al. (2007) | Tyndall Glacier 50°59'S, 73°31' W 1756 m asl | Winter 1998 - Winter 1999 | 12,900 | 10,000 | 9,200 | 9,200 | 7,200 |
| | | Winter 1999 - Dec. 1999 | 5,100 | 4,100 | 4,000 | 4,000 | 3,300 |
| | | Fall 1998 - Fall 1999 | 14,700 | 9,000 | 8,100 | 8,100 | 6,200 |
| | | Fall 1999 - Dec. 1999 | 8,600 | 6,100 | 5,800 | 5,900 | 4,800 |
| (Schwikowski et al., 2013) | Pio XI Glacier 49°16' S, 73° 21' W 2600 m asl | 1 Feb. 2001 - 31 Jan. 2002 | 3,400 | 8,041 | 7,908 | 7,913 | 7,384 |
| | | 1 Feb. 2002 - 31 Jan. 2003 | 7,100 | 7,593 | 7,444 | 7,450 | 7,275 |
| | | 1 Feb. 2003 - 31 Jan. 2004 | 5,800 | 9,976 | 9,611 | 9,612 | 8,769 |
| | | 1 Feb. 2004 - 31 Jan. 2005 | 6,500 | 8,723 | 8,489 | 8,504 | 7,852 |
| | | 1 Feb. 2005 - 31 Jan. 2006 | 6,000 | 8,301 | 8,155 | 8,155 | 7,769 |

Previous observations of snow accumulation using stakes are limited to short and discrete periods, and to the ablation season. For example, Rivera (2004) used three stakes located at 1,445, 1,577, and 1,833 m a.s.l., and measured values of $9,630 \pm 1,360$ and $4,070 \pm 540$ mm yr⁻¹ at the highest and lower stakes, respectively. The RegCM4.6 based estimates give rates in the order of 1,000 to 3,000 mm w.e. The distributions of the observed snow

accumulation give an exponential relationship between precipitation and altitude, but if the precipitation is extrapolated to the higher altitudes of the Chico Glacier, the values reach $33,000 \text{ mm yr}^{-1}$, which seem to be unrealistic (Rivera, 2004) and approximately three times larger than the rates estimated in the current work. It is important to note that these observations were only collected over a period of 14 to 34 days and then extrapolated to annual values.

In summary, good agreement is found in comparing UDG observations with modeled data on the plateau area of the SPI during a short time period; however, there are important differences between rates of snow accumulation determined in this work and previous estimates using ice core and stake observation data at annual scale.

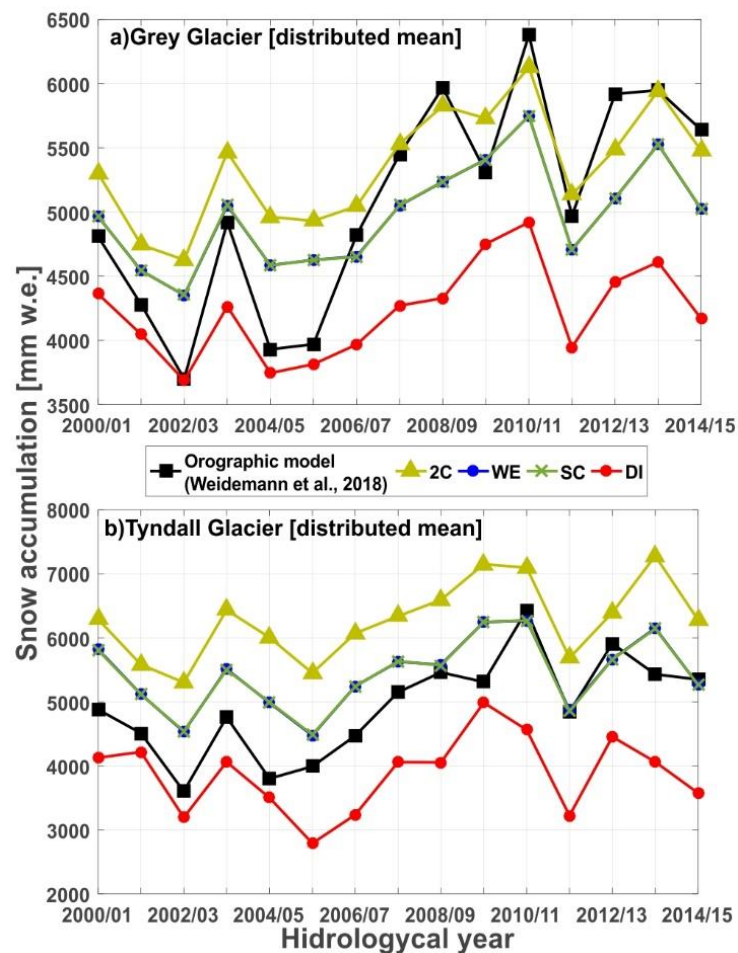


Figure 4.8 Comparison of annual snow accumulation using the four PPMs and estimates from Weidemann et al. (2018). (A) Distributed mean at Grey Glacier, and (B) distributed mean at Tyndall Glacier.

4.5 Discussion

4.5.1 Performance of the RegCM4.6 Model and PPMs Parametrization

Overall, at a regional scale the RegCM4.6 reproduces the main precipitation characteristics of the study area, which are dominated by extreme orographic effects. All four PPMs lead to higher amounts of snow accumulation on the west side relative to the east side. Other models have also shown similar features. For instance, Lenaerts et al. (2014) used a high-resolution regional atmospheric climate model over Patagonia (RACMO2, 1979–2012) to show extreme orographic precipitation due to the narrow Andes barrier separating the wet windward side from the dry leeward side. Specifically, in terms of spatial differences in snow accumulation, Mernild et al. (2016b) indicated that snow accumulation at the same elevation is higher at the west side relative to the east side. Another interesting point is that sleet is higher at the west side of both icefields than that at the east side, indicating more humid and warmer conditions observed on the west side, eventually allowing for the occurrence of the mixed phase precipitation. Remote sensing observations also suggest the influence of the humid conditions on the snow facies. For instance, De Angelis et al. (2007) determined a relatively higher area of advanced snow metamorphism on the west side compared to the east side of the SPI. Outside of the icefields, in the north-east of the NPI (upper Baker River Basin), Krogh et al. (2015) estimated that snowfall is 28.5% of the total precipitation at basin scale. This value is in the range of the fractions estimated for this region in our work (25–35%).

On the other hand, some notable differences exist when comparing the previous estimates mainly with ice core-derived accumulation with those calculated in our work. The causes of this disparity are unclear but could conceivably be associated with differences between the local conditions at the ice core site extraction vs. the spatial resolution of RegCM4.6. Furthermore, erroneous estimates from ice core data due to water melt percolation (Rivera, 2004) or a more general underestimation of snow accumulation by the RegCM4.6 can be considered for the discrepancies in estimation of snow accumulation. Regardless, these differences highlight that uncertainties in quantifying the snow accumulation still exist in this extreme environment.

Another explanation of the differences between measured and modeled snow accumulation may be wind transport of blowing snow particles at local scale. For example, the annual differences between the snow accumulation derived in our analysis and the data from Schaefer et al. (2015) as well as the snow

accumulation derived from Pío XI ice core (Table 4.3) suggest that even at a local point in the flat plateau of the Pío XI site, the influence of snow drift cannot totally be excluded. Coincidentally, the ERA-Interim zonal wind speed shows that the year of 2002, in which lower differences in snow accumulation exist (Table 4.3), had lower wind speed distribution at 700 and 850 hPa levels (Supplementary Figure 4.4). In contrast to this, the years of 2001 and 2003—with the largest differences in snow accumulation (Table 4.3)—had higher wind speeds at these same levels (Supplementary Figure 4.4). Given that RegCM4 is forced by ERA-Interim, the wind speed variability can be further amplified by the regional climate model itself. Indeed, RegCM4 gives a systematic overestimation of 850 hPa zonal wind speed over large parts of the Icefields (Supplementary Figure 4.5). These results illustrate the crucial role of local winds in controlling rates of snow accumulation, which is also indicated by Schwikowski et al. (2013) and Schaefer et al. (2015). In addition, Aristarain and Delmas (1993) also indicated the same mechanism to explain the low annual snow accumulation rate estimated in the accumulation zone of the Perito Moreno Glacier using an ice core. Thus, the derived net accumulation rates from these ice cores could represent lower limits in the snow accumulation.

In contrast, the estimated snow accumulation based on different PPMs using the RegCM4.6 data seems to agree with the observed snow accumulation, even at daily scale ($r = \sim 0.6$), during the October-December period of 2015. One reason is that UDG measurements are at 15 min time steps, capturing the actual snow accumulation. Therefore, UDGs are not affected by the effect of wind on the snow drift after the accumulation events. The location of the UDGs on the plateau, where gentle topography is present, is likely to reduce the differences between model and observation. On the other hand, the comparison of the hypsometric curve between the topography under 10 km and at 1 km resolutions (Supplementary Figure 4.1) shows important differences at elevations over $\sim 1,800$ m a.s.l., which correspond to around the 20% of the total area of both icefields. Therefore, the higher elevations are not represented by the topography used in the RegCM4.6 simulations, illustrating a limitation of the model, which could explain the differences between the snow accumulation determined by Weidemann et al. (2018) for the Tyndall and Grey glaciers, where a higher resolution model (1 km) was used. It is important to note that local precipitation amount and snow accumulation depend on the correct representation of topography (Lenaerts et al., 2014). Therefore, given that ~ 10 km grid resolution is not able to resolve always and exactly the complex topography in the region, the total amount of estimated

snow accumulation, especially in narrow glacier valleys (e.g., Chico and Nef glaciers), steep slopes and in the ice-rock transitions of both icefields, must be taken with caution. A robust statistical downscaling or bias correction method should therefore be applied if these data are to be used to drive mass balance estimations at glacier scale.

4.5.2 Snow Accumulation Changes 1980–2015

Previous modelling studies have also estimated an increase in snow accumulation over annual to decadal timescale. For example, Schaefer et al. (2013) simulated an increase of accumulation on the NPI, from 1990–2011 as compared to 1975–1990, and Mernild et al. (2016a) also estimated positive trends on the plateaus of both NPI and SPI during the period 1979–2014. These trends were detected at higher elevations above ~1,200 m a.s.l. and on the west side of the divide.

In contrast to the increased tendency of snow accumulation at higher elevations, observational-based studies focusing on the analysis of satellites images (e.g., MODIS, LANDSAT) show a reduction in snow cover area. For example, Pérez et al. (2018) estimated a non-significant decrease in snow cover over the Aysén River Catchment located north-east of our study area (45°–46°S). In the south of our study region, other studies suggested a reduction in snow cover area. For instance, further south, at Brunswick Peninsula (53°S), results show a significant decreasing trend of snow extent by 19% for the 1972–2016 period (Aguirre et al., 2018), while in Cordillera Darwin, Rojas-Zamorano et al. (2017) determined a decline of snow cover over the period from June 2005 to June 2016. It is important to note that the reduction in snow cover occurring at lower elevations is driven by its dependence on air temperature, at least at regional scale (Lopez et al., 2008). Therefore, an overall reduction in snow-covered area does not necessarily contradict the observed snow accumulation increase at the highest elevations. It should be noted, however, that the lack of long-term records of snow accumulation in this sector of the Andes makes it difficult to reach definitive results.

Previous studies show an increasing trend of the snow accumulation over the high latitudes in a warmer climate (e.g., Thomas et al., 2017; Medley and Thomas, 2019). These changes are mainly confined to regional scales and determined by thermodynamical (e.g., moisture-holding capacity of air) and dynamical (e.g., wind speed) responses under warmer climatic conditions. Indeed, the increase in snow accumulation determined in the current work occurs under a warming trend. The fields of the air temperature from the

RegCM4.6, which are used to calculate the snow accumulation, show positive trends, especially in autumn and winter (Supplementary Figure 4.6) when larger increases in snow accumulation are determined. However, rather than the regional scale, the positive trend in snow accumulation detected in this study and previous ones is limited to the local scale, mainly concentrated at elevations over ~1,000 m a.s.l on the west side of both icefields. Lower elevation terrain shows no trend and even a negative trend in snow accumulation on the eastern side of the icefields.

The spatial differences in snow accumulation trend could be associated with the location of the study area since it corresponds to the borders where a shift in the position of the zonal winds has been observed (Gupta and England, 2006). Indeed, an increase in the total precipitation of ~200 mm decade⁻¹ was observed south of 50°S for the period 1961–2000 (Garreaud et al., 2013). However, Garreaud et al. (2013) also indicated a negative trend in the west Andean flank lying north of 50°S and recently, Boisier et al. (2019) also indicated a negative trend in the total precipitation based on local observations during the period 1960–2016 on the eastern side of the NPI and in northern Patagonia. These regional differences are associated with spatial differences in the tendency of the westerlies, since weaker and stronger westerlies have been detected at mid-latitudes (~45°S) and around 60°S, respectively. This opposite trend in westerlies has been linked to the positive phase of the SAM. During this phase, a low pressure anomaly over Antarctica extends to ~55°S with an out of phase circumpolar positive anomaly centered at 45°S. This pressure difference is associated with a zonal geostrophic wind anomaly that is positive south of 45°S and negative to the north (Gupta and England, 2006). The positive phase of SAM has also been associated with warming sea surface temperatures in the western Pacific (Thomas et al., 2017). Hence, this is an area of transition where different temporal and spatial impacts are expected to exist. In fact, the positive trends in snow accumulation, especially in autumn and winter, tend to be larger toward the south (~50°S), suggesting some influence of the dominant positive phase of SAM in the last decades (Marshall, 2003).

Spatial differences in snow dynamics are also evident in snow persistence (fraction of time that snow is present on the ground). This area is a transition zone between a dominant decrease (north of 46°) and dominant increase (south of 50°S) of snow persistence (Hammond et al., 2018). In the west-east direction, SAM also influences the snow accumulation trends as the precipitation at the regional scale is positively or negatively correlated with a

zonal wind component of 850 hPa in the western or eastern sectors of the Andes, respectively, due to the mechanical effect of the Andes (Garreaud et al., 2013). This effect forces air masses to ascend in the western sector (windward), favoring conditions for saturation and hence the occurrence of precipitation; on the other hand, it results in subsidence and inhibition of the precipitation in the eastern sector (leeward) (Garreaud et al., 2013). Hence, an increase in the westerly winds and moisture content associated with a dominant positive phase of SAM as well as windward precipitation enhancement (and leeward inhibition) due to orographic effects could explain the snow accumulation increase over 1,000 m a.s.l. on the western side and the reduction on the east side in the context of climate warming (Rasmussen et al., 2007; Aguirre et al., 2018; Olivares-Contreras et al., 2018).

4.5.3 Implications for Glacier Mass Balance

The three methods previously used to define the snow accumulation in the icefields show some important differences in determining the absolute values. The difference in values between the 2C method and the WE-SC methods could reach as high as ~3,000 mm w.e. The differences are even higher when comparing the 2C method with the DI method. Therefore, the use of different schemes to derive the snow/rain ratio may lead surface mass balance modeling efforts to differ considerably (Weidemann et al., 2018). This could partly explain the differences between the positive modeling mass balance (e.g., Schaefer et al., 2013, 2015; Mernild et al., 2016b; Weidemann et al., 2018) and the negative geodetic mass balance (e.g., Dussailant et al., 2018; Malz et al., 2018) that have been documented in the literature.

Another issue to consider is if the sleet precipitation type should be considered as surface accumulation since the differences between the 2C and DI (snow plus sleet) methods are reduced considerably, especially on the western side of both icefields. Sleet is defined as a mixture of snow and rain and is associated with refreezing before reaching the ground, which forms an ice core surrounded by liquid water (Whiteman, 2000). Sleet particles are usually formed near the freezing point, where both rain and snow particles coexist (Ostrometzky et al., 2015). In this sense, it is probably valid that an undetermined percentage of sleet could be considered as surface accumulation (the ice core), while the liquid section percolates into the glacier and cannot therefore be considered as surface accumulation. It is beyond the aim of this work to define this percentage, but it seems that an accumulation in the range between the 2C and DI (snow plus sleet) and DI (snow) is a more realistic estimation. The SC and WE methods are in this range and are the

closest to the accumulation estimated with the UDG observations. Other types of accumulation have been described in this zone, such as rime accretion due to supercooled water droplets transport by the strong winds (Whiteman and Garibotti, 2013); nevertheless, quantification and implications for surface mass balance have not been studied in detail to date.

At long-term scale, the increase in snow accumulation during winter months has been discussed as the cause of glacier mass balance stability and even glacier expansion in the Karakoram region (the pattern that has been termed the Karakoram anomaly; Kapnick et al., 2014). To explore the long-term glacier response, we compare annual snow accumulation trends from this work and results from geodetic mass balance at glacier scale during the period 2000–2014/2015. Elevation change data for the SPI covers the period from 2000 to 2015 (Malz et al., 2018), whereas it covers the period from 2000 to 2014 for the NPI (Braun et al., 2019). Overall, at the glacier scale, elevation change data seem to suggest that the positive values correspond to the glaciers with accumulation area ratio (AAR) over 0.8 and classified as marine-terminating glaciers according to the Randolph Glacier Inventory (RGI 6.0; RGI Consortium, 2017). According to the data in this work, these glaciers also showed a larger annual positive trend in snow accumulation in the period 2000–2015 (Figure 4.9). Some exceptions exist such as Jorge Montt and HPS 12 glaciers, which besides being marine terminating glaciers, show mostly negative rates of elevation change (Malz et al., 2018). The other exception is the San Rafael Glacier which besides having a large AAR (0.85, Rivera et al., 2007) and being a marine-terminating glacier, shows a negative rate of elevation change, however the snow accumulation trend is less than those of glaciers located in the west side of the SPI. Glaciers with these characteristics (marine terminating, AAR over 0.8 and high positive snow accumulation trends) also showed positive or stable frontal position rates in the period 2000–2010/2011 (Sakakibara and Sugiyama, 2014). Furthermore, they also indicate the highest observed ice velocity in the period 1984–2014 (Mouginot and Rignot, 2015).

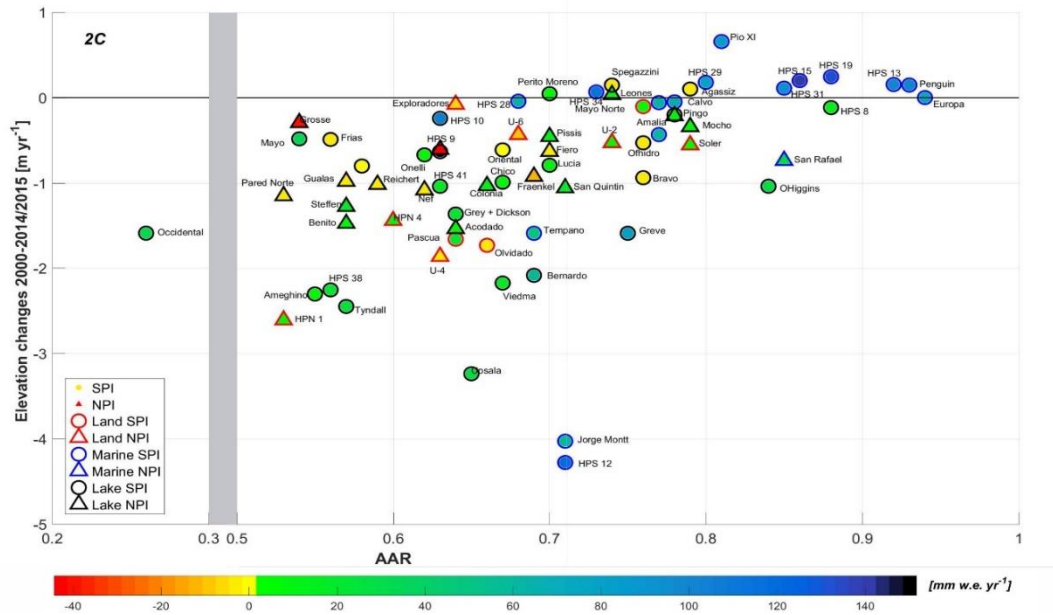


Figure 4.9 Observed elevation changes in the period 2000–2014/2015 for both icefields vs. the accumulation-area ratio (AAR). The color represents the snow accumulation trends by glaciers using the 2C as PPM. Terminus type is also indicated depending the color of the contour for each symbol, triangle for the SPI, and circle for the NPI (see legend). Note that the x-axis is broken. Due to space issues some glaciers names are not indicated.

Although previous studies suggest that elevation changes are dominated by ice dynamics (Mouginot and Rignot, 2015), the data in our work suggest a climate forcing in glaciers where positive elevation changes and stable/positive frontal changes were observed. The Pío XI Glacier, for example, is known for its large cumulative advance since 1945 (Wilson et al., 2016), and it has a large AAR (~0.8; Rivera and Casassa, 1999) as well as one of the highest rates of snow accumulation (and with a positive trend) according to our observations. Most of the other glaciers, where positive elevation changes have been observed, also show significant positive trends in snow accumulation. The exceptions of the Jorge Montt and HPS12 glaciers with positive snow accumulation trends and negative surface elevation changes, may then be explained by ice dynamics (Mouginot and Rignot, 2015), in which ice thinning is a result of the drawdown of the plateaus rather than a decrease in snow accumulation. Other observed processes in the icefields such as an increase in supraglacial debris-cover area (Glasser et al., 2016) or in glacial lake area (Loriaux and Casassa, 2013) could also play a role in the surface glacier mass balance of these glaciers through different feedback mechanisms, and they must be considered in elucidating the present and future evolution of these glaciers.

4.6 Conclusions

In this work, we have assessed both spatial and temporal patterns in snow accumulation in both the North Patagonia Icefield and the South Patagonia Icefield. We used a regional climate model, RegCM4.6, short-term snow accumulation observations using ultrasonic depth gauges (UDG) and previous snow accumulation estimations derived from ice core data, stake observations and modeling approaches. Snow accumulation derived using the RegCM4.6 and the four Phase Partitioning Methods (PPMs) replicated the snow accumulation gradient that is expected to exist in this area. Snow accumulation rates are higher on the west side relative to the east side for both icefields. A maximum amount of snow accumulation is determined at around 50°S on the west side of the SPI. The values depend on the PPM used and reach a maximum mean difference of 1,504 mm w.e. between 2C and DI methods, with some areas reaching differences higher than 3,500 mm w.e. These differences could lead to divergent mass balance estimations, depending on the scheme used, so we suggest that future works should adopt a multi-scheme parameterization to define the snow accumulation.

There are important differences between rates of snow accumulation determined in this work and previous estimations using ice core data at an annual scale. These differences could be related to the scale disparity between the datasets, with each grid point of the model representing an area of ~100 km², while ice core data are derived at the point-scale. Wind transport, with areas where erosion is dominant (e.g., Pío XI glacier ice core site), and areas where the deposition is dominant (e.g., Tyndall glacier ice core site), also seem to be reasonable explanations for these differences. However, good agreement is found when comparing UDG observations with modeled data in the plateau area of the SPI over a short time period.

Snow accumulation trends are mostly positive on the plateau on the west side of both icefields. In the SPI, significant positive trends are mainly present in the autumn season. For the rest of the area, and during other seasons, no significant changes can be determined, except on the east side between 48.5° and 50.5°S, where zones with significant negative trends in autumn were observed. Over annual timescales, glaciers previously observed to be exhibiting positive and stable elevation and frontal changes coincide with areas that show snow accumulation increases according to this study. This suggests that the increase in snow accumulation attenuates the response of the glaciers in a context of overall glacier retreat due to climate warming in Patagonia. The interplay with other factors such as the glacier terminus type

and accumulation-area ratio also seems to explain some of the glacier response (e.g. De Angelis, 2014), as for example the glacier advance observed in the Pío XI glacier.

Robustly validated climate model data therefore appear to be useful for exploring the relationship and spatial differences in glacier response to present and future climate change, especially in Patagonia where meltwater makes a strong contribution to sea level rise and where only a limited number of observational in situ efforts exist.

Data Availability

The datasets generated for this study are available on request to the corresponding author.

Author Contributions

CB, DJQ, and ANR designed the study. CB analyzed the data and prepared the first draft of the paper. DB performed the RegCM4.6 simulations in addition to data processing and contributed to the writing. ÁG-R and CB performed the statistical analysis and analyzed the results. DF-B compiled and analyzed glaciological data. DJQ, ANR, and MR oversaw the research, and reviewed the manuscript. All authors discussed the results and reviewed the manuscript.

Conflict of Interest Statement

The authors declare that the research was conducted in the absence of any commercial or financial relationships that could be construed as a potential conflict of interest.

Acknowledgments

We acknowledge the Dirección General de Aguas de Chile (DGA) for providing their data for analysis. The Centro de Estudios Científicos (CECs) installed the GBL stations and provided all the metadata of these stations. CB and DF-B acknowledge support from the National Committee of Sciences and Technology (CONICYT) Programa Becas de Doctorado en el Extranjero, Beca Chile for the doctoral scholarship. ÁG-R acknowledges CONICYT Doctorado Nacional 2016-21160642 for the doctoral scholarship.

Supplementary Material

The Supplementary Material for this article can be found online at: <https://www.frontiersin.org/articles/10.3389/fenvs.2019.00030/full#supplementary-material>

4.7 References

- Abram, N. J., Mulvaney, R., Vimeux, F., Phipps, S. J., Turner, J., and England, M. H. (2014). Evolution of the southern annular mode during the past millennium. *Nat. Clim. Change* 7, 564–569. doi: 10.1038/nclimate2235
- Aguirre, F., Carrasco, J., Sauter, T., Schneider, C. H., Gaete, K., Garín, E., et al. (2018). Snow cover change as a climate indicator in Brunswick Peninsula, Patagonia. *Front. Earth Sci.* 6:8. doi: 10.3389/feart.2018.00130
- Aniya, M., Sato, H., Naruse, R., Skvarca, P., and Casassa, G. (1996). The use of satellite and airborne imagery to inventory outlet glaciers of the Southern Patagonia Icefield, South America. *Photogramm. Eng. Rem. S.* 62, 1361–1369.
- Anthes, R. A. (1977). A cumulus parameterization scheme utilizing a one-dimensional cloud model. *Mon. Wea. Rev.* 105, 270–286. doi: 10.1175/1520-0493(1977)105<0270:ACPSUA>2.0.CO;2
- Aristarain, A., and Delmas, R. (1993). Firn-core study from the southern Patagonia ice cap, South America. *J. Glaciol.* 39, 249–254. doi: 10.1017/S0022143000015914
- Beck, H. E., Zimmermann, N. E., McVicar, T. R., Vergopolan, N., Berg, A., and Wood, E. F. (2018). Present and future Köppen-Geiger climate classification maps at 1-km resolution. *Sci. Data.* 5:180214 doi: 10.1038/sdata.2018.214
- Behrangi, A., Yin, X., Rajagopal, S., Stampoulis, D., and Ye, H. (2018). On distinguishing snowfall from rainfall using near-surface atmospheric information: comparative analysis, uncertainties, and hydrologic importance. *Quart. J. Roy. Meteor. Soc.* 144, 89–102. doi: 10.1002/qj.3240
- Boisier, J. P., Alvarez-Garreton, C. R., Cordero, R., Damiani, A., Gallardo, L., Garreaud, R., et al. (2019). Anthropogenic drying in central-southern Chile evidenced by long term observations and climate model simulations. *Elem Sci. Anth.* 6:74. doi: 10.1525/elementa.328
- Bolton, D. (1980). The computation of equivalent potential temperature. *Mon. Weather Rev.* 108, 1046–1053. doi: 10.1175/1520-0493(1980)108<1046:TCOEPT>2.0.CO;2
- Bozkurt, D., Rondanelli, R., Garreaud, R., and Arriagada, A. (2016). Impact of warmer eastern tropical Pacific SST on the March 2015 Atacama floods. *Mon. Wea. Rev.* 144, 4441–4460. doi: 10.1175/MWR-D-16-0041.1

- Bozkurt, D., Rondanelli, R., Marín, J., and Garreaud, R. (2018). Foehn event triggered by an atmospheric river underlies record-setting temperature along continental Antarctica. *J. Geophys. Res. Atmospheres* 128, 3871–3892. doi: 10.1002/2017JD027796
- Braun, M. H., Malz, P., Sommer, C., Farías-Barahona, D., Sauter, T., Casassa, G., et al. (2019). Constraining glacier elevation and mass changes in South America. *Nat. Clim. Change* 9, 130–136. doi: 10.1038/s41558-018-0375-7
- Carrasco, J., Casassa, G., and Rivera, A. (2002). “Meteorological and climatological aspects of the Southern Patagonia Icefields,” in *The Patagonian Icefields. A Unique Natural Laboratory for Environmental and Climate Change Studies*, eds G. Casassa, F. Sepulveda, and R. Sinclair (New York, NY: Kluwer Academic; Plenum Publishers), 29–41. doi: 10.1007/978-1-4615-0645-4_4
- CECs-DGA (2016). Línea de Base Glaciológica del Sector Norte de Campo de Hielo Sur: Glaciares Jorge Montt, Témpano y O'Higgins. SIT N° 404, DGA, Technical Report in Spanish.
- Cook, K., Yang, X., Carter, C., and Belcher, B. (2003). A modelling system for studying climate controls on mountain glaciers with application to the Patagonian Icefields. *Clim. Change* 56, 339–367. doi: 10.1023/A:1021772504938
- Davies, B. J., and Glasser, N. F. (2012). Accelerating shrinkage of Patagonian glaciers from the little ice Age (~AD 1870) to 2011. *J. Glaciol.* 58, 1063–1084. doi: 10.3189/2012JoG12J026
- De Angelis, H. (2014). Hypsometry and sensitivity of the mass balance to change in equilibrium-line altitude: the case of the Southern Patagonia Icefield. *J. Glaciol.* 60, 14–28. doi: 10.3189/2014JoG13J127.
- De Angelis, H., Rau, F., and Skvarca, P. (2007). Snow zonation on Hielo Patagonico Sur, Southern Patagonia, derived from Landsat 5 TM data. *Global Planet. Change* 59, 149–158. doi: 10.1016/j.gloplacha.2006.11.032
- Dickinson, R. E., Henderson-Sellers, A., and Kennedy, P. J. (1993). Biosphere-Atmosphere Transfer Scheme (BATS) Version 1e as Coupled to the NCAR Community Climate Model. NCAR Tech. Note NCAR/TN-387+STR, NCAR, Boulder.
- Ding, B., Yang, K., Qin, J., Wang, L., Chen, Y., and He, X. (2014). The dependence of precipitation types on surface elevation and meteorological

conditions and its parameterization. *J. Hydrol.* 513,154–163. doi: 10.1016/j.jhydrol.2014.03.038

Dussaillant, I., Berthier, E., and Brun, F. (2018). Geodetic mass balance of the Northern Patagonian Icefield from 2000 to 2012 using two independent methods. *Front. Earth Sci.* 6:8. doi: 10.3389/feart.2018.00008

Emanuel, K. A. (1991). A scheme for representing cumulus convection in large-scale models. *J. Atmos. Sci.* 48, 2313–2335. doi: 10.1175/1520-0469(1991)048<2313:ASFRCC>2.0.CO;2

Foresta, L., Gourmelen, N., Weissgerber, F., Nienow, P., Williams, J. J., Shepherd, A., et al. (2018). Heterogeneous and rapid ice loss over the Patagonian Ice Fields revealed by CryoSat-2 swath radar altimetry. *Remote Sens. Environ.* 211, 441–455. doi: 10.1016/j.rse.2018.03.041

Fritsch, J. M., and Chappell, C. F. (1980). Numerical prediction of convectively driven mesoscale pressure systems. Convective parameterization. *J. Geophys. Res.* 37, 1722–1733. doi: 10.1175/1520-0469(1980)037<1722:NPOCDM>2.0.CO;2

Gardner, A. S., Moholdt, G., Cogley, J. G., Wouters, B., Arendt, A. A., Wahr, J., et al. (2013). A reconciled estimate of glacier contributions to sea level rise: 2003 to 2009. *Science* 340, 852–857. doi: 10.1126/science.1234532

Garreaud, R., Lopez, P., Minvielle, M., and Rojas, M. (2013). Large-scale control on the patagonian climate. *J. Clim.* 26, 215–230. doi: 10.1175/JCLI-D-12-00001.1

Gillett, N. P., Kell, T. D., and Jones, P. D. (2006). Regional climate impacts of the Southern Annular Mode. *Geophys. Res. Lett.* 33:L23704. doi: 10.1029/2006GL027721

Giorgi, F., Coppola, E., Solmon, F., Mariotti, L., Sylla, M. B., Bi, X., et al. (2012). RegCM4: model description and preliminary tests over multiple CORDEX domains. *Clim. Res.* 52, 7– 29. doi: 10.3354/cr01018

Giorgi, F., Marinucci, M. R., and Bates, G. T. (1993a). Development of a second generation regional climate model (RegCM2). Part I: Boundary layer and radiative transfer processes. *Mon. Wea. Rev.* 121, 2794–2813. doi: 10.1175/1520-0493(1993)121<2794:DOASGR>2.0.CO;2

Giorgi, F., Marinucci, M. R., Bates, G. T., and DeCanio, G. (1993b). Development of a second generation regional climate model (RegCM2). Part II: convective processes and assimilation of lateral boundary conditions. *Mon.*

Wea. Rev. 121, 2814–2832. doi: 10.1175/1520-0493(1993)121<2814:DOASGR>2.0.CO;2

Giorgi, F., Torma, C., Coppola, E., Ban, N., Schar, C., and Somot, S. (2016). Enhanced summer convective rainfall at Alpine high elevations in response to climate warming. *Nat. Geosci.* 9, 584–589. doi: 10.1038/ngeo2761

Glasser, N. F., Holt, T. O., Enas, Z. D., Davies, B. J., Pelto, M., and Harrison, S. (2016). Recent spatial and temporal variations in debris cover on Patagonian glaciers. *Geomorphology* 273, 202–216. doi: 10.1016/j.geomorph.2016.07.036

Gourlet, P., Rignot, E., Rivera, A., and Casassa, G. (2016). Ice thickness of the northern half of the Patagonia Icefields of South America from high-resolution airborne gravity surveys. *Geophys. Res. Lett.* 43, 241–249. doi: 10.1002/2015GL066728

Grassi, B., Redaelli, G., and Visconti, G. (2013). Arctic sea ice reduction and extreme climate events over the Mediterranean region. *J. Clim.* 26, 10101–10110. doi: 10.1175/JCLI-D-12-00697.1

Grell, G. A. (1993). Prognostic evaluation of assumptions used by cumulus parameterizations. *Mon. Wea. Rev.* 121, 764–787. doi: 10.1175/1520-0493(1993)121<0764:PEOAUB>2.0.CO;2

Grell, G. A., Dudhia, J., and Stauffer, D. R. (1994). Description of the fifth generation Penn State/NCAR Mesoscale Model (MM5). NCAR Tech. Note NCAR/TN-398+STR, NCAR, Boulder.

Gupta, A. S., and England, M. H. (2006). Coupled ocean–atmosphere–ice response to variations in the Southern Annular Mode. *J. Clim.* 19, 4457–4486. doi: 10.1175/JCLI3843.1

Hall, A., and Visbeck, M. (2002). Synchronous variability in the southern hemisphere atmosphere, sea ice, and ocean resulting from the annular mode. *J. Clim.* 15, 3043–3057. doi: 10.1175/1520-0442(2002)015<3043:SVITSH>2.0.CO;2

Hammond, J. C., Saavedra, F. A., and Kampf, S. K. (2018). Global snow zone maps and trends in snow persistence 2001–2016. *Int. J. Climatol.* 38, 4369–4383. doi: 10.1002/joc.5674

Harpold, A. A., Kaplan, M. L., Klos, P. Z., Link, T., McNamara, J. P., Rajagopal, S., et al. (2017). Rain or snow: hydrologic processes, observations, prediction, and research needs. *Hydrol. Earth Syst. Sci.* 21, 1–22. doi: 10.5194/hess-21-1-2017

Hedstrom, N. R., and Pomeroy, J. W. (1998). Measurements and modeling of snow interception in the boreal forest. *Hydrol. Process.* 12, 1611–1625. doi: 10.1002/(SICI)1099-1085(199808/09)12:10/11<1611::AID-HYP684>3.0.CO;2-4

Holtzlag, A. A. M., de Bruijn, E. I. F., and Pan, H. L. (1990). A high resolution air mass transformation model for short-range weather forecasting. *Mon. Wea. Rev.* 118, 1561–1575. doi: 10.1175/1520-0493(1990)118<1561:AHRAMT>2.0.CO;2

Kapnick, S. B. T. L., Delworth, T. L., Ashfaq, M., Malyshev, S., and Milly, P. C. D. (2014). Snowfall less sensitive to warming in Karakoram than in Himalayas due to a unique seasonal cycle. *Nat. Geosci.* 7, 834–840. doi: 10.1038/ngeo2269

Kiehl, J. T., Hack, J. J., Bonan, G. B., Boville, B. A., Breigleb, B. P., Williamson, D., et al. (1996). Description of the NCAR Community Climate Model (CCM3). NCAR Tech. Note NCAR/TN-420+STR, NCAR, Boulder.

Kohshima, S., Takeuchi, N., Uetake, J., Shiraiwa, T., Uemura, R., Yoshida, N., et al. (2007). Estimation of net accumulation rate at a Patagonian glacier by ice core analyses using snow algae. *Global Planet. Change* 59, 236–244. doi: 10.1016/j.gloplacha.2006.11.014

Koppes, M., Conway, H., Rasmussen, L. A., and Chernos, M. (2011). Deriving mass balance variations and calving variations from reanalysis data and sparse observations, Glaciar San Rafael, northern Patagonia, 1950-2005. *Cryosphere* 5, 791–808. doi: 10.5194/tc-5-791-2011

Krogh, S., Pomeroy, J., and McPhee, J. (2015). Physically based mountain hydrological modeling using reanalysis data in Patagonia. *J. Hydrometeorol.* 16, 172–193. doi: 10.1175/JHM-D-13-0178.1

Lenaerts, J. T. M., van den Broeke, M. R., van Wessem, J. M., van de Berg, W. J., van Meijgaard, E., van Uft, L., et al. (2014). Extreme precipitations and climate gradients in patagonia revealed by high-resolution regional atmospheric climate modeling. *J. Clim.* 27, 4607–4621. doi: 10.1175/JCLI-D-13-00579.1

Lopez, P., Sirguey, P., Arnaud, Y., Pouyaud, B., and Chevallier, P. (2008). Snow cover monitoring in the Northern Patagonia Icefield using MODIS satellite images (2000–2006). *Global Planet. Change* 61, 103–116. doi: 10.1016/j.gloplacha.2007.07.005

- Loriaux, T., and Casassa, G. (2013). Evolution of glacial lakes from the Northern Patagonia Icefield and terrestrial water storage in a sea-level rise context. *Global Planet. Change* 102, 33–40. doi: 10.1016/j.gloplacha.2012.12.012
- Malz, P., Meier, W., Casassa, G., Ja-a, R., Skvarca, P., and Braun, M. H. (2018). Elevation and mass changes of the southern patagonia icefield derived from TanDEM-X and SRTM Data. *Remote Sens.* 10:188. doi: 10.3390/rs10020188
- Marshall, G. (2003). Trends in the southern annular mode from observations and reanalyses. *J. Clim.* 16, 4134–4143. doi: 10.1175/1520-0442(2003)016<4134:TITSAM>2.0.CO;2
- Masiokas, M., Rivera, A., Espizúa, L., Villalba, R., Delgado, S., and Aravena, J. C. (2009). Glacier fluctuations in extratropical South America during the past 1000 years. *Palaeogeogr. Palaeoec.* 281, 242–268. doi: 10.1016/j.palaeo.2009.08.006
- Matsuoka, K., and Naruse, R. (1999). Mass balance features derived from a firn core at Hielo Patagonico Norte, South America. *Arct. Antarct. Alp. Res.* 31, 333–340.
- Medley, B., and Thomas, E. R. (2019). Increased snowfall over the Antarctic Ice Sheet mitigated 20th century sea-level rise. *Nat. Clim. Change* 9, 34–39. doi: 10.1038/s41558-018-0356-x
- Meier, W. J. H., Griesinger, J., Hochreuther, P., and Braun, M. H. (2018). An updated multi-temporal glacier inventory for the Patagonian Andes with changes between the little ice age and 2016. *Front. Earth Sci.* 6:8. doi: 10.3389/feart.2018.00062
- Mernild, S. H., Liston, G. E., Hiemstra, C. A., Malmros, J. K., and McPhee, J. (2016a). The andes cordillera. part i: snow distribution, properties, and trends (1979–2014). *Int. J. Climatol.* 37, 1680–1980. doi: 10.1002/joc.4804
- Mernild, S. H., Liston, G. E., Hiemstra, C. A., and Wilson, R. (2016b). The andes cordillera. part III: glacier surface mass balance and contribution to sea level rise (1979–2014). *Int. J. Climatol.* 37, 3154–3174. doi: 10.1002/joc.4907
- Möller, M., Schneider, C., and Kilian, R. (2007). Glacier change and climate forcing in recent decades at Gran Campo Nevado, southernmost Patagonia. *Ann. Glaciol.* 46, 136–144. doi: 10.3189/172756407782871530

- Mouginot, J., and Rignot, E. (2015). Ice motion of the patagonian icefields of South America: 1984–2014. *Geophys. Res. Lett.* 42, 1441–1449. doi: 10.1002/2014GL062661
- Olivares-Contreras, V. A., Mattar, C., Gutierrez, A. G., and Jimenex, J. C. (2018). Warming trends in Patagonian subantarctic forest. In. *J. Appl. Earth Obs. Geoinform.* 76, 51–65. doi: 10.1016/j.jag.2018.10.015
- Ostrometzky, J., Cherkassky, D., and Messer, H. (2015). Accumulated mixed precipitation estimation using measurements from multiple microwave links. *Adv. Meteorol.* 2015:707646. doi: 10.1155/2015/707646
- Pal, J. S., Small, E. E., and Eltahir, E. A. B. (2000). Simulation of regional-scale water and energy budgets: Representation of surged cloud and precipitation processes within RegCM. *J. Geophys. Res.* 105, 29579–29594. doi: 10.1029/2000JD900415
- Pellicciotti, F., Ragettli, S., Carenzo, M., and McPhee, J. (2014). Changes of glaciers in the Andes of Chile and priorities for future work. *Sci. Total Environ.* 493, 1197–1210. doi: 10.1016/j.scitotenv.2013.10.055
- Pérez, T., Mattar, C., and Fuster, R. (2018). Decrease in snow cover over the Aysén River catchment in Patagonia, Chile. *Water* 10:619. doi: 10.3390/w10050619
- Rasmussen, L. A., Conway, H., and Raymond, C. F. (2007). Influence of upper air conditions on the Patagonia icefields. *Global Planet. Change* 59, 203–216. doi: 10.1016/j.gloplacha.2006.11.025
- RGI Consortium (2017). Randolph Glacier Inventory – A Dataset of Global Glacier Outlines: Version 6.0: Technical Report, Global Land Ice Measurements From Space. Digital Media.
- Rignot, E., Rivera, A., and Casassa, G. (2003). Contribution of the patagonia icefields of South America to sea level rise. *Science* 302, 434–436, 2003. doi: 10.1126/science.1087393
- Rivera, A. (2004). Mass Balance Investigations at Glaciar Chico, Southern Patagonia. Doctoral dissertation, University of Bristol, Icefield, Chile.
- Rivera, A., Benham, T., Casassa, G., Bamber, J., and Dowdeswell, J. A. (2007). Ice elevation and areal changes of glaciers from the Northern Patagonia icefield, Chile. *Global Planet. Change* 59, 126–137. doi: 10.1016/j.gloplacha.2006.11.037

Rivera, A., and Casassa, G. (1999). Volume changes on Glaciar Pío XI, Patagonia: 1975-1995. *Global Planet. Change* 22, 233–244. doi: 10.1016/S0921-8181(99)00040-5

Rivera, A., and Casassa, G. (2002). "Ice thickness measurements on the Southern Patagonia Icefield," in *The Patagonian Icefields. A Unique Natural Laboratory for Environmental and Climate Change Studies*, eds G. Casassa, F. Sepulveda, and R. Sinclair (New York, NY: Kluwer Academic; Plenum Publishers), 101–115. doi: 10.1007/978-1-4615-0645-4_10

Rojas-Zamorano, C., Maier, E., Arigony-Neto, J., de Almeida Espinoza, J. M., Jaa, R., and Gonzalez, I. (2017). Snow coverage mapping in Darwin Mountain Ranges through satellite images optical and its relationship with data climate (2005–2016) (in Portuguese). *Rev. Brasil. Cartogr.* 69, 743–758.

Sagredo, E., and Lowell, T. (2012), *Climatology of Andean glaciers: a framework to understand glacier response to climate change*. *Global Planet Change* 86–87, 101–109. doi: 10.1016/j.gloplacha.2012.02.010

Sakakibara, D., and Sugiyama, S. (2014). Ice-front variations and speed changes of calving glaciers in the Southern Patagonia Icefield from 1984 to 2011. *J. Geophys. Res. Earth* 119, 2541–2554. doi: 10.1002/2014JF003148

Salmi, T., Maatta, A., Anttila, P., Ruoho-Airola, T., and Amnell, T. (2002). *Detecting Trends of Annual Values of Atmospheric Pollutants by the Mann-Kendall Test and Sen's Slope Estimates—The Excel Template Application Makesens*. Helsinki: Finnish Meteorological Institute Publications on Air Quality No. 31.

Schaefer, M., Machguth, H., Falvey, M., and Casassa, G. (2013). Modeling past and future surface mass balance of the Northern Patagonian Icefield. *J. Geophys. Res. Earth* 118, 571–588. doi: 10.1002/jgrf.20038

Schaefer, M., Machguth, H., Falvey, M., Casassa, G., and Rignot, E. (2015). Quantifying mass balance processes on the Southern Patagonia Icefield. *Cryosphere* 9, 25–35. doi: 10.5194/tc-9-25-2015

Schneider, C., Glaser, M., Killian, R., Santana, A., Butorovic, N., and Casassa, G. (2003). Weather observations across the Southern Andes at 53°S. *Phys. Geogr.* 24, 97–119. doi: 10.2747/0272-3646.24.2.97

Schwikowski, M., Schläppi, M., Santiba-ez, P., Rivera, A., and Casassa, G. (2013). Net accumulation rates derived from ice core stable isotope records of Pío XI glacier, Southern Patagonia Icefield. *Cryosphere* 7, 1635–1644. doi: 10.5194/tc-7-1635-2013

- Shiraiwa, T., Kohshima, S., Uemura, R., Yoshida, N., Matoba, S., Uetake, J., et al. (2002). High net accumulation rates at Campo de Hielo Patagonico Sur, South America, revealed by analysis of a 45.97 m long ice core. *Ann. Glaciol.* 35, 84–90. doi: 10.3189/172756402781816942
- Smith, R., and Evans, J. (2007). Orographic precipitation and water vapor fractionation over the Southern Andes. *J. Hydrometeorol.* 8, 3–19. doi: 10.1175/JHM555.1
- Thomas, E. R., van Wessem, J. M., Roberts, J., Isaksson, E., Schlosser, E., Fudge, T. J., et al. (2017). Regional Antarctic snow accumulation over the past 1000 years. *Clim. Past* 13, 1491–1513. doi: 10.5194/cp-13-1491-2017
- Villarroel, C., Carrasco, J., Casassa, G., and Falvey, M. (2013). Modeling near-surface air temperature and precipitation using WRF with 5-km resolution in the Northern Patagonia Icefield: a pilot simulation. *Int. J. Geosci.* 4, 1193–1199. doi: 10.4236/ijg.2013.48113
- Weidemann, S., Sauter, T., Schneider, L., and Schneider, C. (2013). Impact of two conceptual precipitation downscaling schemes on mass-balance modeling of Gran Campo Nevado ice cap, Patagonia. *J. Glaciol.* 59, 1106–1116. doi: 10.3189/2013JoG13J046
- Weidemann, S. S., Sauter, T., Malz, P., Ja-a, R., Arigony-Neto, J., Casassa, G., et al. (2018). Glacier mass changes of lake-terminating Grey and Tyndall glaciers at the Southern Patagonia Icefield derived from geodetic observations and energy and mass balance modeling. *Front. Earth Sci.* 6:81. doi: 10.3389/feart.2018.00081
- White, A., and Copland, L. (2015). Decadal-scale variations in glacier area changes across the Southern Patagonian Icefield since the 1970s. *Arct. Antarct. Alp. Res.* 47, 147–167. doi: 10.1657/AAAR0013-102
- Whiteman, C. D., and Garibotti, R. (2013). Rime mushrooms on mountains: description, formation, and impacts on mountaineering. *Bull. Amer. Meteor. Soc.* 94, 1319–1327. doi: 10.1175/BAMS-D-12-00167.1
- Whiteman, D. (2000). *Mountain Meteorology*. New York, NY: Oxford University Press.
- Willis, M., Melkonian, A., Pritchard, M., and Rivera, A. (2012). Ice loss from the Southern Patagonian Ice Field, South America, between 2000 and 2012. *Geophys. Res. Lett.* 39:L17501. doi: 10.1029/2012GL053136
- Wilson, R., Carrión, D., and Rivera, A. (2016). Detailed dynamic, geometric and supraglacial moraine data for Glaciar Pío XI, the only surge-type glacier

of the Southern Patagonia Icefield. *Ann. Glaciol.* 57,119–130. doi: 10.1017/aog.2016.32

Yamada, T. (1987). Glaciological characteristics revealed by 37.6-m deep core drilled at the accumulation area of San Rafael Glacier, the Northern Patagonia Icefield. *Bull. Glac. Res.* 4, 59–67.

Zeng, X., Zhao, M., and Dickinson, R. E. (1998). Intercomparison of bulk aerodynamic algorithms for the computation of sea surface fluxes using TOGA COARE and TAO data. *J. Climate* 11, 2628– 2644. doi: 10.1175/1520-0442(1998)011<2628:IOBAAF>2.0.CO;2

Chapter 5
Drivers of surface ablation on the Southern Patagonian
Icefield

Claudio Bravo, Andrew N. Ross, Duncan J. Quincey, Sebastián Cisternas
and Andrés Rivera

5.1 Abstract

Glaciers in the Southern Patagonian Icefield (SPI) have been shrinking, but due to a lack of field observations, understanding of the drivers of ablation over long time scales is limited. Here, we present a distributed energy balance model, forced with meteorological observations from a west-east transect located to the north of the SPI. During our study period, humid and warm on-glacier conditions prevailed on the western side compared to dry and cold conditions on the eastern side. Energy available for melt reached a glacier-wide mean of 117 W m^{-2} (west) and 49 W m^{-2} (east). Sensible heat and net shortwave radiation provided the main source of energy reaching individual values between 52 W m^{-2} and 69 W m^{-2} . Net longwave radiation was an energy sink in the west (-33 W m^{-2}) and east (-48 W m^{-2}); while latent heat was an energy sink to the east (-7 W m^{-2}), but a source to the west (25 W m^{-2}). Over longer timescales, our results show that western glaciers were losing mass, while eastern glaciers were close to balanced conditions. These data provide new insights in the feedbacks related to ablation and in the discrepancy between modelled and geodetic mass balances in this region.

5.2 Introduction

In recent decades glaciers worldwide have been retreating and thinning and are widely considered as key icons of climate change. One of the regions with rapid ice loss is the Southern Andes (20° - 55° S), where glacier cumulative losses and specific negative mass changes have been determined since 1961 (Zemp and others, 2019). In this region, Patagonia (40° S- 55° S) comprises mostly large glaciers (>10 km in length), including the most extensive ice fields at mid-latitudes in the Southern Hemisphere: the Southern Patagonian Icefield (SPI) and the Northern Patagonian Icefield (NPI). Negative glacier area (Davies and Glasser, 2012; White and Copland, 2015) and volume changes in this region (Rignot and others, 2003; Willis and others, 2012; Foresta and others, 2018; Malz and others, 2018; Abdel Jaber and others, 2019) are a matter of concern due to their observed and potential contribution to sea-level rise (Gardner and others, 2013; Zemp and others, 2019) and their role in triggering hazardous natural events such as glacial-lake outburst floods (Wilson and others, 2018) and rock avalanche events associated with de-buttressing (Iribarren-Anacona and others, 2015).

The SPI is the largest continuous ice mass along the Andes with a total area of $12232 \pm 201 \text{ km}^2$ (Meier and others, 2018, Figure 5.1). Most of its glaciers are lacustrine-calving towards the east and marine-terminating to the west. This ice field has been the focus of several geodetic mass balance estimates

in recent years. Despite some differences in their magnitude and spatial variability, these geodetic mass balances agree in that most of the glaciers are shrinking, irrespective of the observation period (e.g. Rignot and others, 2003; Willis and others, 2012; Foresta and others, 2018; Malz and others, 2018; Abdel Jaber and others, 2019). Several mechanisms of glacier change have been discussed including changes in ice velocity and dynamics (Rivera and others, 2012; Muto and Furuya, 2013; Sakakibara and Sugiyama, 2014; Mouginot and Rignot 2015), frontal ablation (Bown and others, 2019) and surface mass balance and its components (Rasmussen and others, 2007; Monahan and Ramage, 2010; Schwikowski and others, 2013; Lenaerts and others, 2014; Schaefer and others, 2015; Mernild and others, 2016; Weidemann and others, 2018; Bravo and others, 2019a, 2019b). Dynamical adjustments on calving glacier have been invoked as a key control of the overall ice losses (Mouginot and Rignot, 2015, Braun and others, 2019) as land-terminating glaciers outside the Icefields show lower negative mass balance rates (e.g. Falaschi and others, 2017; 2019) despite being exposed to the same climatic forcing (Braun and others, 2019). Moreover, surface mass balance modelling forced with climate data, show positive mean values for the entire SPI (Schaefer and others, 2015; Mernild and others, 2016).

Empirically-based studies that characterise the fundamental glacier conditions needed for surface mass balance and energy balance models, as well as direct mass balance measurements using the glaciological method are, however, extremely limited in this region. The main reason is associated with the scarcity of in-situ long-term meteorological observations, especially on the plateau of the Icefields, where extreme weather conditions prevail throughout most of the year. This means that high uncertainty exists in earlier modelling efforts, as no on-glacier observations were available to validate the meteorological variables driving these models (e.g. Schaefer and others, 2015; Mernild and others, 2016). Additionally, efforts in estimating the sensitivity of these glaciers to climatic changes were made using coarse climate models and re-analysis (e.g. Cook and others, 2003; Rasmussen and others, 2007; Sagredo and Lowell, 2012) which did not capture the finer details and spatial differences of the drivers of the surface mass balance. Consequently, our understanding of how glaciers are responding to changes in climate over this important region of the Andes is limited (Pellicciotti and others, 2014).

In the SPI (Figure 5.1), the few meteorological observations and direct glaciological mass balance measurements that exist were acquired in the

ablation zones of glaciers at the eastern margin: the Perito Moreno Glacier (Takeuchi and others, 1995,1996, 1999; Stuefer and others, 2007), Upsala Glacier (Naruse and others, 1997), Tyndall Glacier (Koisumi and Naruse, 1992; Takeuchi and others, 1995,1999), De los Tres Glacier (Popovnin and others, 1999), Chico Glacier (Rivera, 2004) and Tyndall and Grey glaciers (Weidemann and others, 2018; Schaefer and others, 2020). These observations are scarce and most of them limited to ablation seasons only. Recently, Bravo and others (2019b) presented an analysis of the air temperature using data obtained during nine months by a network of five automatic weather stations (AWS) installed on rock surfaces and three on-glacier air temperature sensors. Data from this network were also used by Durand and others (2019) to assess snow accumulation and by Lo Vecchio and others (2019) to evaluate ice-surface temperature obtained by the processing of MODIS products. An important finding was that distinct lapse rates prevail between western and eastern glaciers which in turn has implications for the estimation of surface mass balance (Bravo and others, 2019b). The forcing of this distinct behaviour is related to the orographic effect which determines the meteorological conditions on both sides of the SPI, but how these differences impact the surface ablation rate remains unknown.

The orographic effect has been described at a regional scale in Patagonia, especially in terms of precipitation and water vapour. Due to the mechanical effect of the mountain chain, the air ascends in the western sector (windward) favouring conditions for the saturation and hence the occurrence of precipitation, while subsidence of the air and inhibition of the precipitation occurs in the eastern sector (leeward) (Schneider and others, 2003; Smith and Evans, 2007; Garreaud and others, 2013; Lenaerts and others, 2014). However, it seems that the orographic effect also has direct effects at the scale of the SPI. Indeed, Lo Vecchio and others (2019) found that more MODIS cloud-free images are available in the eastern side compared to the western side of the SPI. Snow accumulation also shows spatial variability and trends depending on which side of the ice divide the glaciers are located (Bravo and others, 2019a). Remote sensing observations suggest the influence of humid conditions is manifested in different snow facies between both sides (De Angelis and others, 2007) and also in differences in the timing of melt season onset, being earlier in the west compared to the east (Monahan and Ramage, 2010).

To assess how these meteorological differences impact the surface mass balance, we present a distributed energy balance model for glaciers located

in the northern section of the SPI (48°-49° S) and on both sides of the divide. The aim is to increase our understanding of the processes and fluxes controlling surface ablation. For this purpose, we used meteorological observations collected by Automatic Weather Stations (AWS) between October 2015 and June 2016 at several locations (Figure 5.1). We then estimate the role of surface ablation in the overall glacier shrinkage observed in the SPI in recent decades, using ERA5-Land re-analysis climate data to extend the time series to the period 1982-2019, using the observational period as calibration at a daily scale.

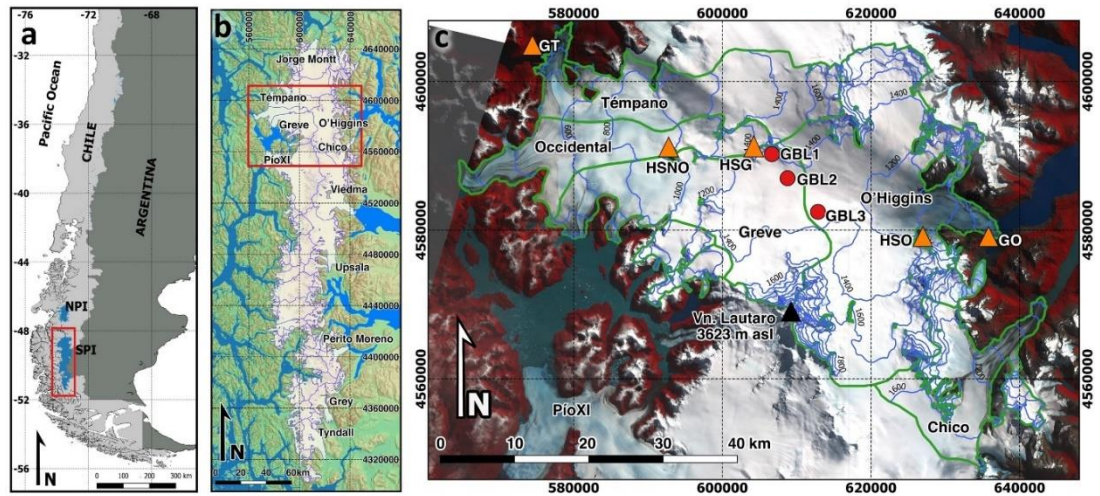


Figure 5.1 (a) Southern South America, NPI and SPI are the Northern and Southern Patagonian Icefields, respectively. (b) Southern Patagonian Icefield overlying a hillshade map of the region obtained from SRTM. (c) Study area and locations of the observational network in a Landsat 8 OLI acquired the 1 of April 2014. Symbols are Automatic Weather Stations (triangles) and on-glacier air temperature sensors (GBL, red circles). Image coordinates are UTM18-S, WGS-1984.

5.3 Materials and Methods

5.3.1 Energy balance model

A distributed energy balance (EB) model was applied using Automatic Weather Stations (AWS) data collected between 1 October 2015 and 31 June 2016 (Table 5.1). The distributed fields of meteorological variables used to force the energy balance is explained in the following sections.

The energy available for melting, Q_m ($W m^{-2}$) was determined following the equation:

$$Q_m = (1 - \alpha) S_{in} + L_{in} + L_{out} + Q_h + Q_l + Q_r, \quad (1)$$

where S_{in} and α are incoming shortwave radiation and the albedo, L_{in} and L_{out} are incoming and outgoing longwave radiation and Q_h and Q_l are the turbulent

fluxes of sensible and latent heat, respectively. Q_r is the sensible heat brought to the surface by rain. We quantified Q_r even though it is generally considered negligible, because in Patagonia higher precipitation rates occur during the year, with the westerlies showing their maximum intensity in summer around 50° S (Garreaud and others, 2013; Sauter, 2020) providing a potential source of energy available for melt and heating. The conductive heat flux was considered negligible due to the predominantly positive air temperatures and the temperate conditions of the glacier surface (e.g. Schneider and others, 2007; Gillet and Cullen, 2010). Net shortwave and longwave radiation were both estimated using standard approaches previously applied for energy balance calculations using the AWS observations to estimate transmissivity in the case of the shortwave radiation and cloud factor in the case of the longwave radiation. Turbulent sensible heat fluxes were calculated using the bulk approach (Cuffey and Paterson, 2010). The details of the estimation of the EB fluxes terms and other parametrizations are presented in the Supplementary Material A.3.

Melt was assumed to occur only when the glacier surface was at 0°C and Q_m was positive. The melt rate (M) was calculated using:

$$M = \frac{Q_m}{L_m \rho_w}, \quad (2)$$

where L_m is the latent heat of fusion and ρ_w is the water density (1000 kg m⁻³).

The sublimation rate (S) was calculated as (Cuffey and Paterson, 2010):

$$S = \frac{Q_l}{L_s \rho_w}, \quad (3)$$

where L_s is the latent heat of sublimation.

5.3.2 Automatic Weather Stations (AWSs).

The observational network consists of five AWS installed in proglacial zones and nunataks on the plateau of the SPI along a west-east transect around 48°S (Figure 5.1). Also, three air temperature sensors and ultrasonic depth gauges (UDGs) were installed over the glacier surface. This network allowed us to describe the spatial and temporal variability in meteorological conditions, as well as to calculate the components of the EB. Table 5.1 shows the details of each AWS, including the sensors and locations. Details of the characteristics of the locations of each AWS were given in Bravo and others (2019b).

Table 5.1 Locations and details of the sensors for each AWS. n/a are not available measurements.

| Automatic Weather Station Lat/ Lon/ Elevation SPI margin/surface type, height | Air temperature and relative humidity | Wind Speed | Atmospheric pressure | Incoming shortwave radiation | Incoming longwave radiation | Period |
|---|---|---------------------|-------------------------|------------------------------------|-----------------------------------|--|
| Glaciar Témpano (GT) 48°42'09"S/ 73°59'17"W/ 50 m asl West/ Rock, 2 m | Young 41382VC | RM Young 5103 | n/a | CMP3 | n/a | 1 October 2015 30 June 2016 |
| Hielo Sur Glaciar Greve, Nunatak Occidental (HSNO) 48°49'59"S/ 73°43'25"W/ 1040 m asl West, nunatak/ Rock, 2 m | Rotronic HC2-S3 | RM Young 5103 | Setra 278 | CMP3 | CGR3 | 1 October 2015 30 June 2016 |
| Hielo Sur Glaciar Greve (HSG) 48°49'55"S/ 73°34'53"W/ 1428 m asl Divide, nunatak / Rock, 2 m | Young 41382VC | RM Young 5103 | Vaisala PTB110 | CMP3 | n/a | 1 October 2015 30 June 2016 |
| Hielo Sur Glaciar O'Higgins (HSO) 48°55'28"S/ 73°16'26"W/ 1234 m asl East, nunatak/ Rock, 2 m | Rotronic HC2-S3 | RM Young 5103 | Vaisala PTB110 | CMP3 | CGR3 | 17 October 2015 30 June 2016 |
| Glaciar O'Higgins (GO) 48°55'47"S/ 73°08'21"W/ 310 m asl East/ Rock, 2 m | Young 41382VC | RM Young 5103 | Vaisala PTB110 | CMP3 | CGR3 | 1 October 2015 30 June 2016 |
| Glacier boundary layer station 1 (GBL1) 48°50'02"S/ 73°34'51"W/ 1415 m asl West, plateau/ glacier, 1.2 m | Thermistor 107-L | n/a | n/a | n/a | n/a | 17 October 2015 15 February 2016 |
| Glacier boundary layer station 2 (GBL2) 48°51'34"S/ 73°31'37"W/ 1294 m asl West, plateau/ glacier, 2 m | Thermistor 107-L | n/a | n/a | n/a | n/a | 25 October 2015 31 March 2016 |
| Glacier boundary layer station 3 (GBL3) 48°54'30"S/ 73°27'47"W/ 1378 m asl East, plateau/ glacier, 2 m | Thermistor 109-L | n/a | n/a | n/a | n/a | 10 April 2016 30 June 2016 |

5.3.3 Distribution of meteorological variables

The spatial coverage of the AWS network made it possible to distribute the meteorological variables that were needed to force the energy balance using the bulk-approach (Cuffey and Paterson, 2010). We used elevation gradients as the main method of spatial distribution of meteorological variables (Table 5.2).

TanDEM-X digital elevation data acquired by the German Aerospace Center (DLR) (Abdel-Jaber and others, 2019) and gridded at 200 m resolution, were used to distribute the meteorological variables and to estimate the radiation fluxes. The glacier outlines were obtained from the inventory of De Angelis (2014), but frontal positions and margins were manually updated on a cloud free Landsat 8 OLI satellite image acquired on the 1 of April 2014. Hence, the glacier outlines were representative of the years 2014-2015, a period that includes some of the AWS observations used in this work (Table 5.1).

The meteorological variables and factors related to cloud cover were taken from the AWS observations. We assumed that the AWS dataset installed on the west side (GT, HSNO) was representative of glaciers Témpano (327 km²), Occidental (218 km²), Greve (412 km²), HPS8 (34 km²), and one unnamed glacier (41 km²). AWSs installed on the east side (GO, HSO) were considered representative of glaciers O'Higgins (751 km²), Pirámide (27 km²), and Chico (229 km²). HSG AWS was considered as representative of the ice divide conditions; however, for some of the variables, this AWS seems to be most representative of the highest sections of the west side.

The air temperature was distributed using hourly lapse rates between each pair of AWS and a bias-correction was applied considering that the observations were taken on relatively small rock surfaces surrounded by ice (nunataks) which means that glacier cooling effect is not included directly on the air temperature observations. The details of the air temperature observations and bias-correction were given in Bravo and others (2019b).

The AWS network offered the possibility to distribute humidity, rather than assume a constant value (e.g. Braun and Hock, 2004; Fyffe and others, 2014). Considering the extreme meteorological gradients observed in the Patagonian region, an adequate representation of the humidity conditions at both sides of the SPI is critical to increasing our understanding of the meteorological factors controlling ablation. The distributed relative humidity was calculated using separate components; air vapour pressure (e_a) and air saturation vapour pressure (e_{sat}). For each AWS, we calculated the air vapour pressure, using the observed relative humidity (f) and air temperature, as:

$$e_a = e_{sat} \frac{f}{100}, \quad (4)$$

where e_{sat} according to the empirical formula of Clausius-Clapeyron (Bolton, 1980), is only a function of air temperature (T_a in °C):

$$e_{sat}(T) = 6.112 \exp\left(\frac{17.67T_a}{T_a + 243.5}\right), \quad (5)$$

Air vapour pressure was fitted against elevation (Shea and Moore, 2010) and hourly gradients were obtained. Mean gradient values of the air vapour pressure were -0.84 hPa km⁻¹ on the east side and -2.80 hPa km⁻¹ on the west side. Typical hourly gradients values observed in glaciers elsewhere were between -6 to -1 hPa km⁻¹ (Shea and Moore, 2010), hence our eastern gradient was slightly outside this typical range.

The atmospheric pressure was distributed using the hydrostatic equation (Wallace and Hobbs, 2006) that relates two geometric elevations and

pressure levels and allows correction of the atmospheric pressure to a reference level (e.g. sea level).

To estimate the surface temperature (T_s) we used as a proxy the dew point temperature (T_d) for the snow surface and the assumption of constant surface temperature (0°C) under melt conditions on glacier surfaces, namely when the air temperature is positive (Oerlemans and Klok, 2002). The T_d approach calculated at a standard height is a reasonable first-order approximation of daily T_s (Raleigh and others, 2013) and was calculated using the Magnus-Teten approach (Murray, 1967, Raleigh and others, 2013):

$$T_s = T_d = \frac{c \left[\ln(f) + \frac{bT_a}{c+T_a} \right]}{b - \ln(f) - \frac{bT_a}{c+T_a}}, \quad (6)$$

As the aim was to estimate snow surface temperature when $T_a < 0^\circ\text{C}$, the coefficients used were $b=22.587$ and $c=273.86^\circ\text{C}$ (Raleigh and others, 2013).

The surface vapour pressure (e_s) was calculated assuming that vapour in the atmospheric surface layer is well mixed (Collier and others, 2014), hence surface vapour pressure was given by:

$$e_s = \frac{e_a \cdot T_s}{T_a}, \quad (7)$$

When the air temperature was positive, the snow/ice surface temperature was fixed to 0°C and the surface vapour pressure was fixed to 6.11 hPa assuming saturation (Brock and Arnold, 2000).

Finally, the wind speed was distributed using the hourly observed gradients between pairs of AWS. On the west side the gradients were taken from GT and HSNO and on the eastern side from GO and HSO. This approach has been also used by Fyffe and others (2014) on alpine glaciers. However, due to the uncertainties of this approach (as wind speed is also related to local topographic characteristics), we used a constant wind speed to check the sensitivity of the EB model to this variable. Here, the mid-elevation AWSs HSNO and HSO (Table 5.1) were assumed representative of the west side and the east side, respectively. Table 5.2 shows a summary of the methods to distribute each meteorological variable including the time step and related references.

Table 5.2 Methods, assumptions and approach references used to distribute the meteorological data over the glaciers on the SPI.

| Variable | Symbol | Units | Method/Assumption | Time step | Approach reference |
|----------------------------|-----------|-------------------|--|-----------|---------------------------|
| Air temperature | T_a | °C | Observed lapse rate | Hourly | Bravo and others (2019b) |
| Surface temperature | T_s | °C | Dew point air temperature as proxy of snow surface temperature. Surface Temperature set to zero when $T_a > 0$ | Daily | Raleigh and others (2013) |
| Atmospheric pressure | P | Pa | Hydrostatic equation | Hourly | Wallace and Hobbs (2006) |
| Air vapour pressure | e_a | Pa | Observed gradient | Hourly | Shea and Moore (2010) |
| Saturation vapour pressure | e_{sat} | Pa | Function of air temperature | Hourly | Bolton (1980) |
| Surface vapour pressure | e_s | Pa | Water vapour in the atmospheric surface layer is well mixed. Set to 6.11 hPa when $T_s = 0$ | Hourly | Collier and others (2014) |
| Wind speed | u | m s ⁻¹ | Observed lapse rate | Hourly | Fyffe and others (2014) |

5.3.4 Extended ablation time series to hydrological years 1982/82-2018/19

To extend the ablation time series between hydrological years 1982/83 and 2018/19, we used data from ERA5-Land (~9 km) (Copernicus Climate Change Service, CS3, 2019) as input to the energy balance. ERA5-Land is the result of a single simulation driven by near-surface atmospheric fields from ERA5 atmospheric reanalysis, with precipitation and lapse-rate adjustments (Muñoz-Sabater, 2019). ERA5 is one of the latest state-of-the-art global land surface reanalysis datasets and shown to provide, for instance, a better representation of precipitation than previous re-analyses (e.g. Tetzner and others, 2019).

Instead of using a downscaling process, we used the outputs of ERA5-Land at daily time step in order to estimate how appropriate these data were for calculating ablation and accumulation at a mean glacier-wide scale. We maintained the resolution, intersecting the grid with the glacier outlines. Therefore, the ablation time series was representative of the 2015 area, i.e. the same area used to calculate the energy balance during the observational period. We used ERA5-Land fluxes output of surface solar radiation downwards and surface net thermal radiation as these fluxes showed a good correlation with the observations. Surface albedo was estimated using the

same data input (ERA5-Land total precipitation), the same phase partitioning method (PPM, Weidemann and others 2018) and the same model (Oerlemand and Knapp, 1998) as explained in Supplementary Material.

ERA5-Land sensible and latent heat flux were underestimated in comparison to those estimated using the observations. Consequently, to obtain a better representation of the turbulent fluxes, we used the bulk-approach model and ERA5-Land meteorological data as input: 2 m air temperature, 2 m dewpoint temperature (as a proxy to surface temperature), surface pressure, 10 m u and v wind components. The wind speed was corrected to 2 m height and bias-corrected as the ERA5-Land underestimated the wind speed in comparisons to the observations. Air and dewpoint temperature were also corrected to match the observational period. In this case, we used a bias correction as per Bravo and others (2019b). The snow/ice surface temperature was set to zero when the air temperature was positive. The rain heat flux was estimated using the same approach (data input and equation) as during the observational period. To close the surface mass balance, we used the snow accumulation that was calculated as input to the albedo parameterization (see Supplementary Material) using the ERA5-Land data. Since the uncertainty in snow accumulation over the SPI is high (depending greatly on the PPMs used as well on the input data), and a proper validation was impossible due to the lack of long-term observations (Masiokas and others, 2020), we also estimated snow accumulation using data from the RegCMv4 model as in Bravo and others (2019a). Consequently, we adopted a range of values in our calculations, to account for the differences in input datasets as well as for the differences brought about by using different PPMs.

5.4 Results

5.4.1 Meteorological conditions

As the meteorological spatial distribution approach had a strong observational basis (Figure 5.2), the distribution fields (Figure 5.3) show similar spatial patterns to the observations. At comparable elevations, off-glacier air temperatures were higher in the east compared to the west, as the mean value of HSO (1234 m asl.) was similar to HSNO (1040 m asl.), although the former was located at a higher elevation (Figure 5.2a). However, the mean value was higher in the west (4°C) compared to the east (1°C, Figure 5.3a). On-glacier air temperature and glacier surface temperature were lower on the east side compared to the west side due to a strong cooling effect (Bravo and others, 2019b). In the ablation zones, mean glacier surface temperatures were close to 0°C (and surface vapour pressure close to 6.11 hPa, Figures 5.3b and

5.3d). Western-facing glaciers comprised a larger elevational range area over the 0°C isotherm (Figure 5.3a).

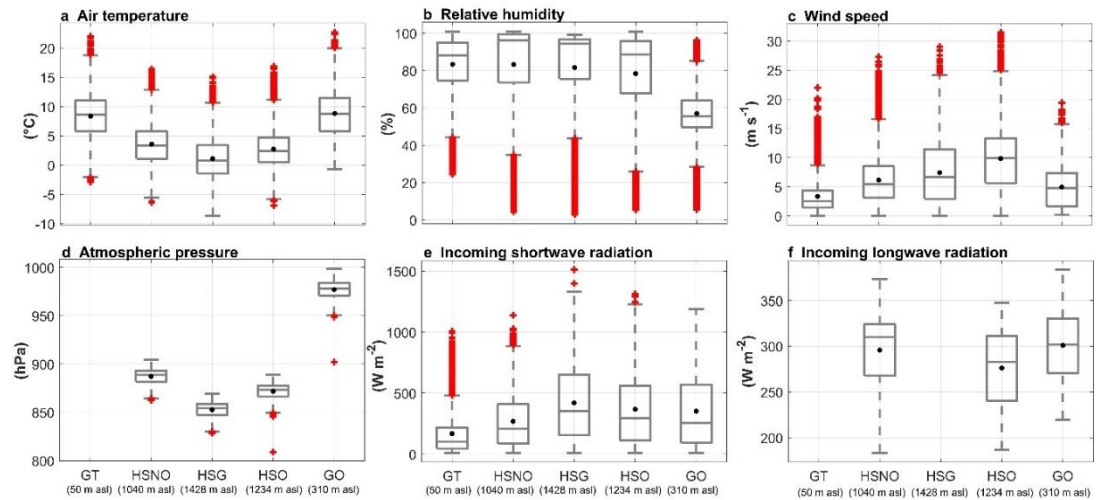


Figure 5.2 Boxplot summaries of the hourly observed meteorological variables in the SPI during the period October 2015 to June 2016. Data used in the incoming shortwave radiation boxplots (e) correspond to daytime hours.

Relative humidity shows different behaviour between each side of the SPI (Figure 5.2b and 5.3c). On the west side, the relative humidity tends to be stable irrespective of elevation. On the eastern side, lower mean values were observed (Figure 5.3c) and a strong gradient between HSO (mean 78%) and GO (mean 57%) was determined (Figure 5.2b). A sharp change was obtained on the plateau, in the ice divide zone defined for the humidity variables.

The wind speed (Figure 5.2c and 5.3f) increases with elevation on both sides. Lower mean values were observed at the lower elevations on the western side. The wind speed reached maximum values around 22 m s^{-1} at the highest elevation of the study area (Volcán Lautaro $\sim 3600 \text{ m asl}$). The wind speed we estimated here after using the observed gradient were comparable to those determined by Lenaerts and others (2014) using the regional atmospheric climate model RACMO2 at a level of 700 hPa, i.e. the free atmosphere. The AWSs (Figure 5.2c) shows that maximum values were observed at mid elevations of the eastern side (HSO), reaching a mean of 9 m s^{-1} but with observed local hourly maximum reaching $25\text{-}30 \text{ m s}^{-1}$.

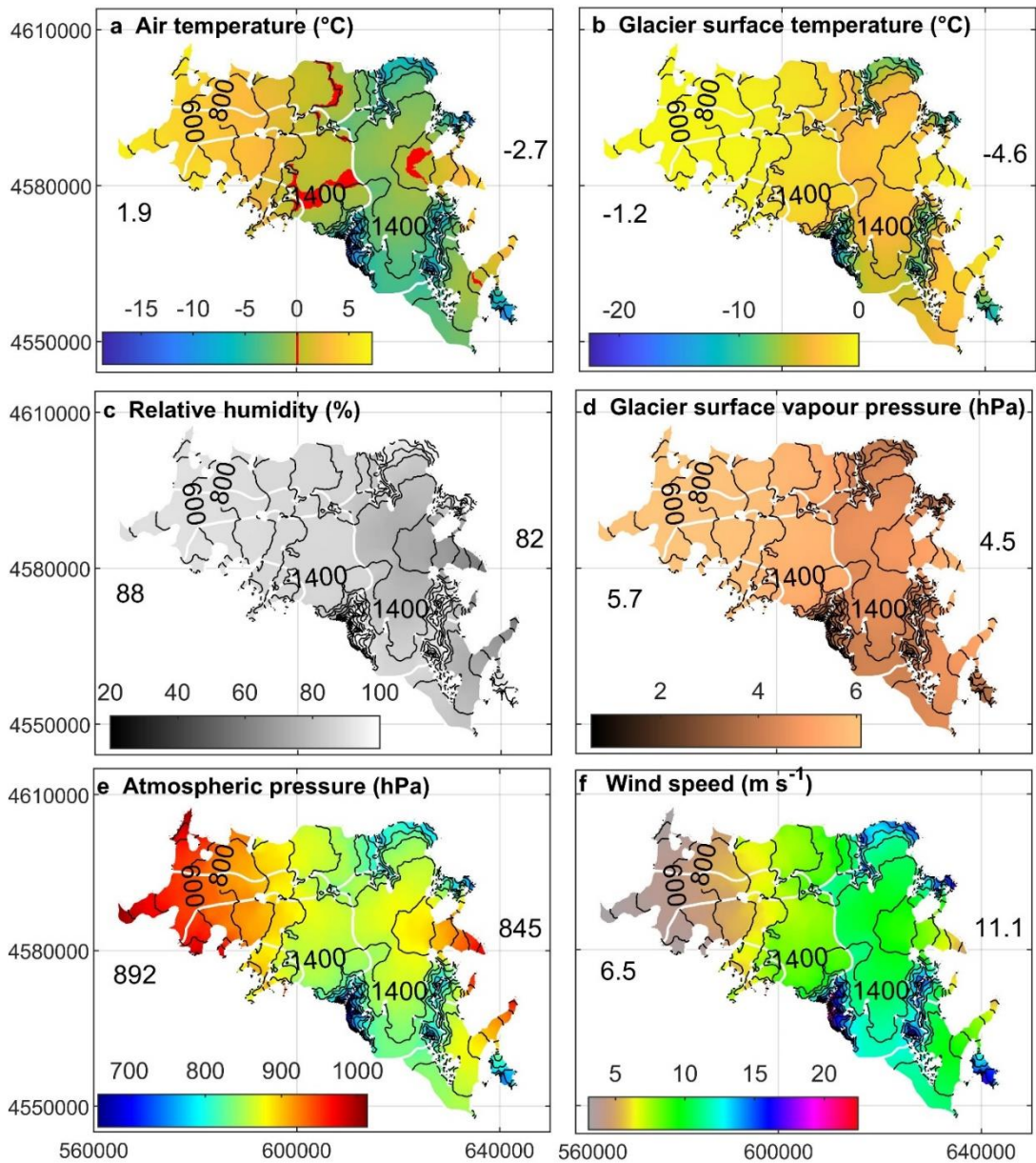


Figure 5.3 Spatially distributed mean values of the meteorological variables. Numbers shown in each variable map represent mean glacier-wide values for each side of the Icefield. White lines are the glacier divide and black lines are contour lines at an interval of 200 m. Coordinates are in m, UTM18-S, WGS-1984.

5.4.2 Energy balance fluxes and ablation

The observed incoming shortwave radiation showed differences between each side (Figure 5.2e). Lower values were observed on the western side of the divide, especially at GT and HSNO. On the ice divide (HSG) the incoming shortwave radiation showed the maximum values, followed by the eastern side AWSs (HSO, GO). Higher absolute values were due to the period between October 2015 and April 2016 being characterized by positive solar radiation anomalies increasing the insolation by around 20% compared to the

climatology (Garreaud, 2018). However, we cannot discard some outlier values due to erroneous measurements. The spatial differences in the incoming shortwave and longwave radiation were attributable to the differences in the cloud cover.

The cloud factor (F_{cl}) (Mölg and others, 2009; see Supplementary Material) quantifies the influence of the cloud cover on the incoming shortwave and longwave radiation fluxes (Figure 5.4). Under overcast conditions ($F_{cl} > 1.3$) a median reduction of -400 W m^{-2} was observed compared with potential shortwave radiation. For cloud factors between 1.1 and 1.3 the forcing was around -300 W m^{-2} and for clear sky conditions ($F_{cl} < 1.1$) it was around -100 W m^{-2} , which probably corresponds to the attenuation of the clear atmosphere. For the longwave radiation, the increase due to cloud cover compared to clear-sky conditions was in the order of 80, 60 and 5 W m^{-2} respectively. These forcings were similar between both sides, although more attenuation in the incoming shortwave radiation was determined under clear sky conditions on the western side (Figure 5.4) due to the greater water vapour content (Lenaerts and others, 2014). However, the greatest difference was in the number of cases. The F_{cl} histograms show a similar bimodal distribution on both sides, however, the overcast conditions ($F_{cl} > 1.3$) west of the divide exceeded those east of the divide by a factor of 2. In terms of the mean glacier-wide values, incoming shortwave radiation was 169 W m^{-2} on the west side and 226 W m^{-2} on the east side. For the incoming longwave radiation, the opposite effect occurs due to cloud cover, as the western side receives relatively higher values of incoming longwave radiation (mean of 283 W m^{-2}) relative to the eastern side (mean of 247 W m^{-2}).

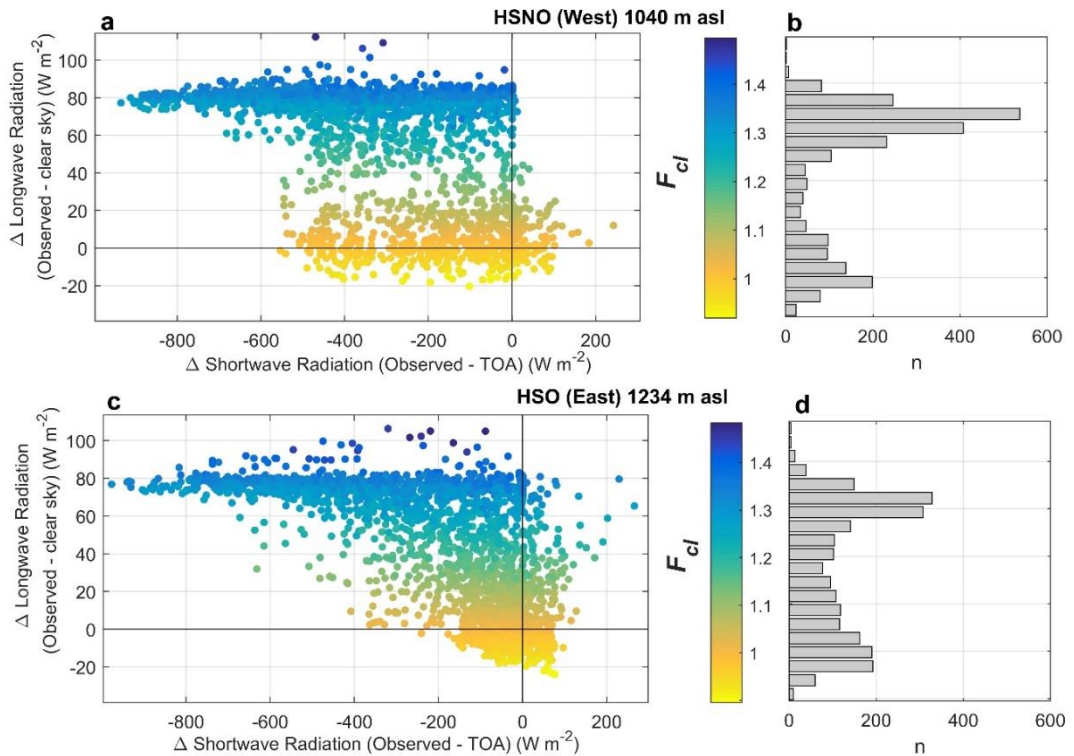


Figure 5.4 Comparative forcing of the cloud factor on the incoming shortwave and longwave radiation observed at HSNO (a) and HSO (c). Panels (b) and (d) show histograms of the cloud factor estimated at the same AWSs. TOA is top of atmosphere.

The mean EB fluxes modelled for the period between October 2015 and June 2016 are shown in Figure 5.5. Overall, across all the glacier surfaces, net shortwave radiation, sensible heat flux and rain heat flux were positive, which means that they were a source of energy available for surface melt and heating. Due to a relatively high albedo in the east (mean 0.77) compared to the west (0.67), the mean net shortwave radiation was almost identical between both sides; $54 W m^{-2}$ to the west and $52 W m^{-2}$ to the east. The net shortwave radiation showed a relative maximum in the supraglacial moraine area as a reduction in albedo occurs.

Net longwave radiation was negative across almost all the glacier surface, hence removing energy. The exception to this was in the lower elevations of the west side, where near-constant cloud cover and positive temperatures prevailed over the analysed period. The latent heat was the flux with the largest spatial variability, as positive values were estimated on the west side and negative values were estimated on the east side agreeing with the relatively dry conditions and strong wind speeds observed and distributed on the east side. The sensible heat flux showed the largest positive values on the lower elevations of the east side. This area was characterized by a strong temperature gradient between the glacier surface (fixed at $0^{\circ}C$ for most of the

period) and the air (4 to 5 °C), and relatively strong winds. However, the maximum values correspond to the supraglacial moraine areas; thus, the value depends on the fixed surface roughness. On the ice surface areas, the mean sensible heat flux reached a mean value of 190 W m^{-2} while on the supraglacial moraine surfaces it reached a mean value of 220 W m^{-2} . This 30 W m^{-2} of enhanced sensible heat corresponds to a difference in surface roughness of only 0.006 m (see Supplementary Table 5.1). Finally, the rain heat flux showed maximum values on the west side where more rainfall occurs, however, despite the larger rainfall amounts previously reported at the Patagonia west coast (Garreaud and others, 2013, Sauter, 2020) this flux reached a mean maximum of just 4-5 W m^{-2} with daily maxima in the order of 11 W m^{-2} .

As might be expected, the maximum values ($>300 \text{ W m}^{-2}$) of energy available for melt/heating were at lower elevations on each side, decreasing to values lower than 100 W m^{-2} in most of the plateau area. Glacier-wide mean values were considerably higher in the west (117 W m^{-2}) compared to the east (49 W m^{-2}).

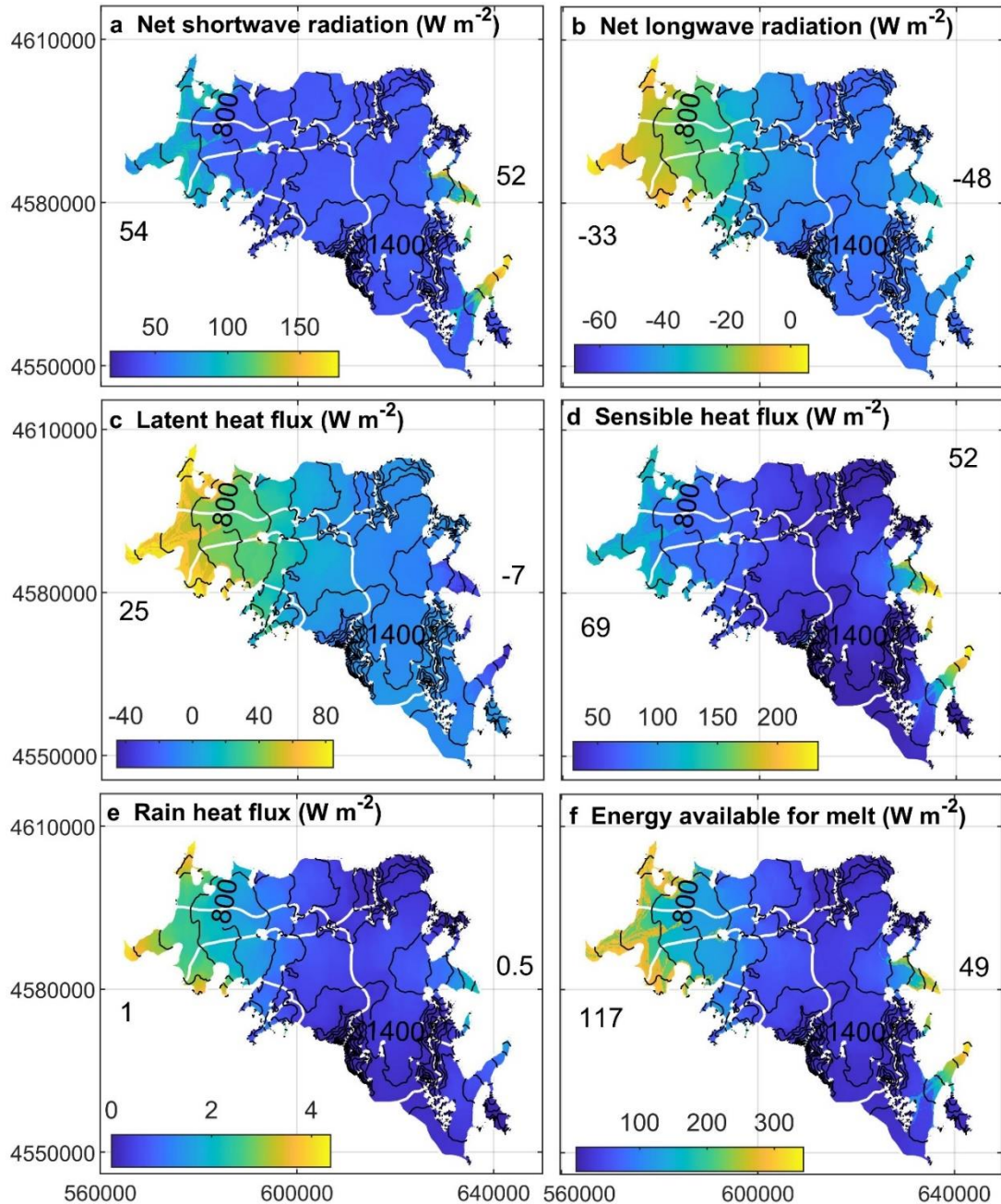


Figure 5.5 Distributed mean values of the energy balance fluxes estimated over the period October 2015 – June 2016. Values are the mean glacier-wide for each flux. White lines are the glacier divide and black lines are contour lines at an interval of 200 m. Coordinates are in m, UTM18-S, WGS-1984.

The mean values per elevation range (Figure 5.6) show some details that were not well represented on the distributed mean values maps (Figure 5.5). Figure 5.6 also shows the result of the calculations of the turbulent heat fluxes under the assumption of constant wind. Sensible heat flux was the dominant source of energy on both sides, even assuming constant wind speed. However, at elevations over 1500 m a.s.l., the magnitude was similar to the net shortwave and longwave radiation. The net shortwave radiation was the

second highest flux at the lower elevations (<1000 m a.s.l.), but the magnitude on the east side, where clear skies prevail, was higher. The cloud cover also influences the net longwave radiation, which over an elevation of 1000 m a.s.l. was the flux with the second highest absolute value as the cloud cover on the western side increases the amount of incoming longwave radiation. In the western lower elevations, incoming longwave radiation reached values comparable to the emitted longwave radiation, which most of the time was at 315 W m^{-2} as the glacier surface was at the melting point. Hence, the net longwave radiation was close to zero in this area. At the same elevation on the eastern side, the cloud cover was lower, and less water vapour was in the atmosphere, hence the incoming longwave radiation was predominantly lower than the emitted, as the glacier surface was still close to the melting point most of the time.

The latent heat was the only flux showing different patterns; on the eastern side it was a sink of energy at all elevations, whereas on the western side it was a source of energy up to around 2000 m a.s.l.

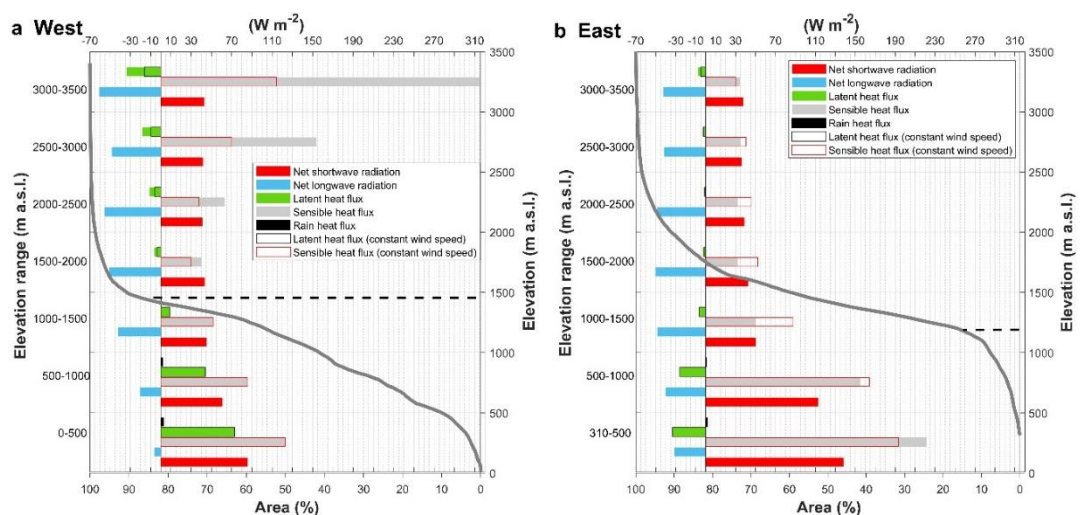


Figure 5.6 Mean values of the energy balance fluxes per elevation range and margin of the SPI during the period between October 2015 and June 2016, (a) West and (b) East. For reference, hypsometric curves (grey continuous line) estimated using the TanDEM-X with the accumulated area in the bottom axis are showed and the mean elevation of the isotherm 0°C (segmented line).

Assuming that melt occurs when the surface temperature was 0°C , we estimated the total melt for the period (Figure 5.7). The surface melt was the dominant ablation component on both sides over most of their respective areas. The magnitude was higher on the west at a lower elevation, especially in the range between 500-1500 m a.s.l. where differences were in the order of 3-4 m w.e. when compared to the east side. On the eastern side, between

1000 and 1500 m a.s.l., the melt was approximately half of the melt on the west side at the same elevation range. In this elevational range, the eastern side melt decreased sharply to less than 5 m w.e., above 1000 m a.s.l. hence, most of the melt on the eastern side glaciers was observed around the terminus section. On the western side, magnitudes greater than 10 m w.e. were observed up to an elevation of around 1000-1100 m a.s.l.

On both sides, the maximum melt occurred at supraglacial moraine areas on the lower sections (e.g. Chico Glacier, Figure 5.1) reaching values between 19-22 m w.e. The parameterization of the supraglacial moraine in the mid-lower sections on each side of the Icefield showed the importance of a thin debris layer in enhancing surface melt rates (Figure 5.7). Melt in supraglacial moraine areas was 2 to 5 m w.e. higher than melt in debris-free areas at the same elevations (Figure 5.7). To assess the impact of the supraglacial moraine on total melt, we estimated it with and without supraglacial moraine albedo parameterization. The total melt for the study period using the supraglacial moraine parameterization reached 8.2 m w.e. on the west side, while on the east it reached 2.1 m w.e. Without the parameterization, melt was 7.5 m w.e. and 1.8 m w.e. respectively. Hence, the impact was relatively higher on the eastern side as melt increased by 17%, while in the west, it increased by 9%.

The percentage of sublimation compared to net ablation in the west was 1.9% and in the east it was 5.4%. Spatial differences were observed when comparing both sides. On the western side, glacier sublimation was at a minimum at lower elevations and reached a relative maximum at the highest elevations, being the dominant component from 2000 m a.s.l. (Figure 5.7a). Meanwhile, eastern-facing glaciers showed maximum values on their lower sections. In this area, drier conditions were observed in the air in comparison to the glacier surface, which is mostly saturated reaching 6.11 hPa, the vapour pressure of a melting glacier surface. These conditions explain this relative maximum and contrasting behaviour in comparison to western side glaciers, which were under strong maritime climate conditions.

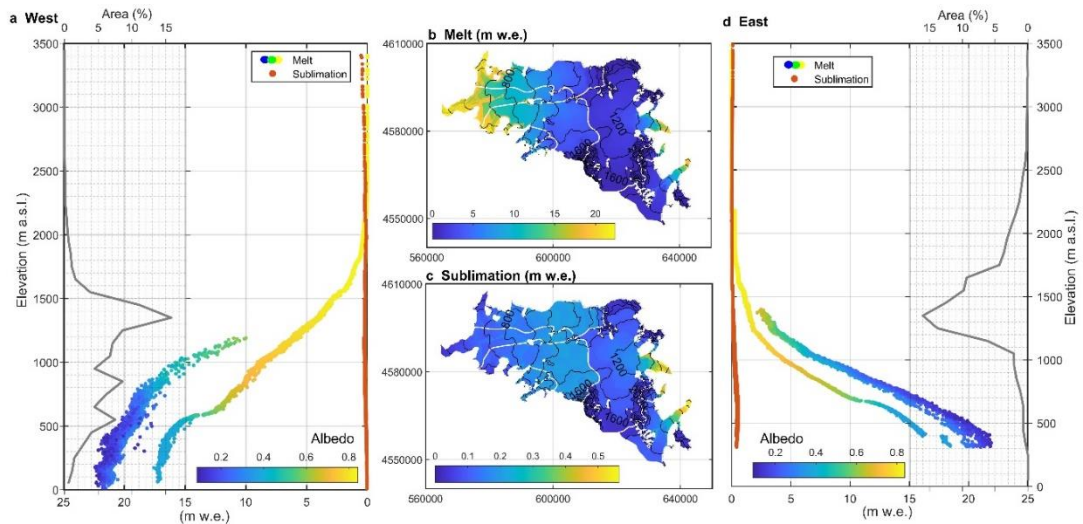


Figure 5.7 Total modelled melt and sublimation over the whole period. (a) West, melt and sublimation vs elevation. The colour of each melt point denotes the albedo used in the EB model and the grey line is the glacier hypsometry with the area (upper axis) per 100 m bin. (b) Map of the total melt, (c) Map of the total sublimation and (d) same as (a) but for the eastern margin glaciers.

5.4.3 Extended ablation time series and mass balance

Time series of daily ablation during the period October 2015 and June 2016 showed that EB model forcing with daily ERA5-Land data on the western (eastern) side explains 56% (69%) of the variance observed in the EB forced with the distributed field of meteorological variables. At daily time step, the root-mean square error is 0.02 m w.e. on the west side and 0.01 m w.e. on the east side. The larger differences were in the magnitude of some peaks where the EB forced with ERA5-Land model showed higher ablation rates compared to the EB forced with AWS observations, especially on the east side. The cumulative ablation for the 274 days in the EB forced with AWS observations reached 8.2 m w.e. to the west and 2.1 m w.e. to the east, while using the EB forced with ERA5-Land model the totals were 8.7 and 1.8 m w.e. respectively. This means that EB ERA5-Land model overestimates the ablation in the west (0.5 m w.e.) and underestimates the ablation in the east (0.3 m w.e.). We therefore assumed these values as the uncertainty in our long-term ablation estimation.

The extended time series of ablation, accumulation and surface mass balance between hydrological years 1982/83 and 2018/19 are presented in m w.e. in Figure 5.8. Higher rates of ablation were estimated on the west side in comparison to the east side, but the interannual variability is similar between both sides. The extended annual time series of ablation replicated the characteristics during the observational period, i.e. annual total ablation in the

west was three to four times ablation on the east. The accumulation showed the same interannual variability with a slightly greater rate on the west compared to the east (0.9 m w.e.). A negative mass balance over the whole 37 years period on the west was determined (mean of -6.6 ± 2.2 m w.e) while the east showed a positive mean mass balance (0.9 ± 1.3 m w.e.), with only a couple of years showing negative mass balance (Figure 5.8c). The mean values per glacier on the west side were noticeably high for Occidental Glacier, reaching -13.9 ± 2.2 m w.e., while Témpano and Greve glaciers reached -6.5 ± 2.2 m w.e. and -3.1 ± 2.2 m w.e. respectively. On the east side, mean values were 1.2 ± 1.3 m w.e for O'Higgins Glacier and -0.4 ± 1.3 m w.e for Chico Glacier.

The variance of the mass balance depends largely on the ablation ($R^2= 0.90$ to the west and 0.76 to the east). Trends in ablation were not evident, but snow accumulation trends were in the order of 0.13 m w.e. yr^{-1} on each side. Using Mann-Kendall, a statistically significant trend at the 95% level was found in the east (p -value = 0.0134) and at 90% in the west (p -value = 0.0732). As the trend in ablation was absent and mass balance depends largely on ablation, the trend in mass balance was minimal and not significant.

An important issue was that with the exception of the positive trends of snow accumulation, modelled mass balance shown here, as well as geodetic mass balances published elsewhere, do not show positive trends. Bravo and others (2019a) suggested that the significant increase in snow accumulation in recent decades impacted glacier mass balance only where the accumulation area-ratio (i.e. the ratio between a glacier's accumulation area and total area) was larger than 0.8. In these cases, the geodetic mass balance was close to neutral or positive as for instance, on Pio XI Glacier, which show positive surface elevation changes (Malz and others, 2018; Foresta and others, 2018; Abdel-Jaber and others, 2019; Dusallant and others, 2019).

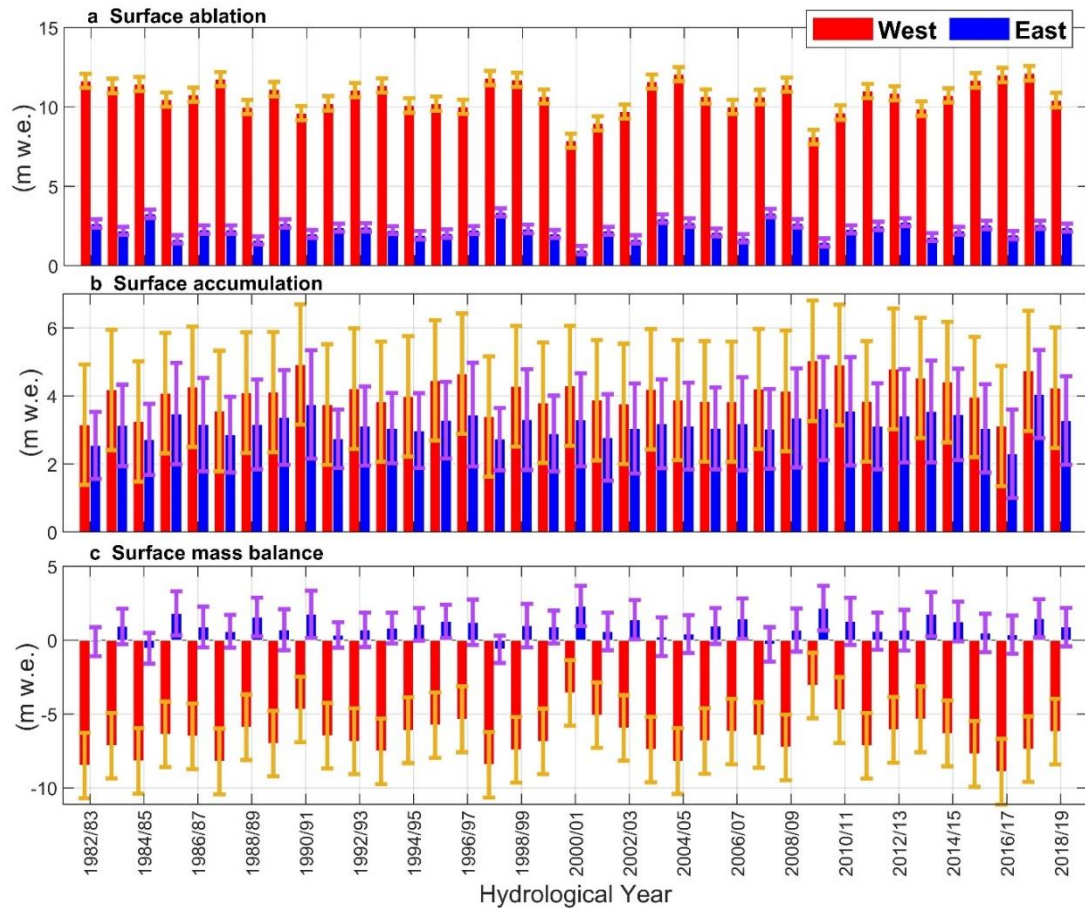


Figure 5.8 Extended time series of ablation (a), accumulation (b) and surface mass balance (c) calculated with data from re-analysis ERA5-Land and regional model RegCMv4 in the case of the accumulation. Error bars show the uncertainties in the estimations. These data are representative of the 2014 glacier area.

5.5 Discussion

5.5.1 Energy balance fluxes: Uncertainties and comparison with previous works

Inherent limitations and uncertainties exist in the EB model and meteorological distribution approach used in this work. One of them, which is impossible to quantify, is the uncertainty associated with the AWS sensors and their operation without regular maintenance. Bravo and others (2019b) discussed the possible limitations and representativeness of each AWS location in terms of air temperature. Similar consideration can be given here to the other observed meteorological variables, particularly those with greater spatial variability that depends, for instance, on cloud cover. For instance, bias in local cloud cover (e.g. topographic effects) could be extended to the whole glacier area. Additionally, limitations are also related to how representative a limited number of meteorological observations are for fully characterizing the

micrometeorological conditions (e.g. Sauter and Galos, 2016; Bonekamp and others, 2020). For instance, wind speed is known to be highly variable over glacierised surfaces (Sauter and Galos, 2016; Shaw and others, 2017) and bulk values are likely therefore to mask much of the detail. Indeed, this has great impact on sensible heat flux estimations on mountain glaciers (Sauter and Galos, 2016). Despite the limitation of our approach, the use of elevational gradients of meteorological variables is of interest for glacier mass balance modelling approaches at different spatial and temporal scales (Braun and Hock, 2004; Fyffe and others, 2014; Mölg and others, 2020).

In order to analyse the sensitivity of the EB modelled to wind speed, our results were presented using two wind speed parametrizations. In terms of sensible heat flux there were areas where the differences were larger than 100 W m^{-2} , however, in terms of melt, uncertainty related to wind speed was less as the highest differences in the magnitude of sensible heat flux were in areas where the surface air temperature was constantly below 0°C and/or represented a small fraction of the total area (Figure 5.6). In the former case, this means that the available energy was heating the snow surface and no melting occurred.

Previous quantification of EB fluxes for SPI glaciers at different spatial and temporal scales were limited to a few cases. Using short period and point-scale AWS observations (4 to 15 days), Takeuchi and others (1995, 1999) estimated EB fluxes for Moreno (50.5° S) and Tyndall (51.3° S) glaciers. For the latter glacier, Schaefer and others (2020) also estimated EB fluxes for the years 2015 and 2016. Glacier-wide mean EB fluxes during the period 2000-2016 were estimated by Weidemann and others (2018) for Tyndall and Grey (50.7° S) glaciers. A direct comparison of values is difficult, bearing in mind the inevitable differences in spatial and temporal scales of analysis. Nevertheless, as might be expected, net shortwave radiation is consistently shown to be a source of energy. In the case of net longwave radiation, all previous work agrees that it is a sink of energy as negative values prevail over respective glaciers (Weidemann and others, 2018; Schaefer and others, 2020). In our case, just a small areal fraction on the frontal section on the west side showed slightly positive values (Figure 5.5b).

Overall, most of the previous works agree on the importance of sensible heat flux on SPI glaciers. The dominance of the sensible heat flux is a common characteristic of glaciers under maritime conditions (e.g. Schneider and others, 2007). In Tyndall Glacier, Takeuchi and others (1999) estimated that sensible heat flux is around 45% of the total energy available for melt, while Schaefer and others (2020) recently estimated that sensible heat flux was the

second highest flux after net shortwave radiation. Our calculated values were higher than those previously estimated, at point-scale and at glacier-wide scale, meaning that it was the main source of energy in the study area.

For latent heat flux, disagreements exist in the literature around its magnitude and the role that it plays on the EB. Takeuchi and others (1999) and Schaefer and others (2020) both estimated positive values on Tyndall Glacier. Weidemann et al. (2018) estimated a mean glacier-wide negative value at Tyndall Glacier as well as over Grey Glacier. Our calculations show that latent heat was the most spatially variable flux in terms of its role in the EB. At lower elevations (0-1500 m a.s.l.) on the west side it is a source of energy, whilst above this elevation on the west side, as well as at all elevations on the east side, it was a sink of energy. This variability was also temporal, as during the austral autumn of 2016 the latent heat flux was mostly negative on the west side, meaning that the vapour pressure gradient was negative. This is a direct consequence of the severe drought detected in western Patagonia during this season (Garreaud, 2018) where anomalously lower moisture transport from the Pacific Ocean to the western flank of Patagonia led to the relative lower vapour pressure in the air compared to the glacier surface. Hence, the temporal and spatial variability of the latent heat flux observed in our study, as well in previous ones (e.g. Schneider and others, 2007), is explained by this flux depending on the air vapour pressure, which in turn depends on synoptic conditions that define the advection of water vapour over glacier areas.

The differences in turbulent fluxes can be related to the characteristics of each glacier. For instance, the fetch length of O'Higgins Glacier (~30 km) differs markedly when compared to Grey and Tyndall Glaciers (~20 km). This could strengthen the intensity of the katabatic wind (Ayala and others, 2015), increasing the cooling effect and the dryness of a descending air parcel over the glacier surface.

Although there are qualitative agreements and similar orders of magnitude in the EB fluxes estimated in this work and in previous ones, none of the previous studies show the elevational differences demonstrated herein, as most of them are either estimations at point-scale (Takeuchi and others, 1995, 1999; Schaefer and others, 2020) or in the case of the distributed EB, results are shown as monthly spatially mean values during the period 2000-2014 (Weidemann and others, 2018). The lack of spatial detail precludes a complete analysis of the sensitivities and controls on the ablation and their differences. Our EB modelling shows that turbulent fluxes depended largely on moisture conditions (latent heat flux) and wind speed (sensible and latent

heat flux), defining spatial and temporal variability on these fluxes which in turn exerts a high control on melt rates and their west-to-east differences.

5.5.2 Drivers of ablation

The relative importance of each EB flux depends primarily on aspect and elevation, varying in magnitude and even sign (positive vs negative) in the case of the latent heat flux (Figure 5.6). This pattern was related to the meteorological differences and contrasts between both sides, forced mainly by the orographic effect and its feedbacks.

Air vapour pressure and cloud cover were the meteorological variables showing clearest differences between both sides. In the case of the incoming shortwave radiation, larger differences between clear sky and overcast conditions exist especially on the west side, but due to bulk albedo differences, net values were similar between both sides. For incoming longwave radiation, there were also differences, but cloud cover forcing was lower in comparison to the effect on incoming shortwave radiation (Figure 5.4). Moreover, the differences in the magnitude of the incoming longwave radiation were lower comparing both sides, despite differences in cloud cover, probably as relatively warmer off-glacier conditions to the east increase the incoming longwave radiation (Figure 5.2). This, along with the near-constant surface glacier temperature that determine the emitted longwave radiation, leads to net longwave radiation being the most spatially homogeneous EB flux in our study area, showing values between -30 and -60 W m^{-2} , except below 1000 m a.s.l. on the west side, where values drop to values under -10 W m^{-2} .

Quantification of turbulent fluxes depends largely on vapour pressure gradients along with wind speed. Here, differences were evident in terms of magnitudes of the sensible heat flux, reaching maxima where wind speed was higher. On the western side the maxima have been suggested to be a result of exposure to the dominant westerlies (Takeuchi and others, 1999). Probably, the occurrence of katabatic winds as well as foehn events (e.g. Ohata and others, 1985; Takeuchi and others, 1995; Bravo and others, 2019b) determines a maximum relative wind speed at mid to lower elevations ($<1000 \text{ m a.s.l.}$) on the eastern side. Sensible heat flux mean values between 155 and 220 W m^{-2} were found here depending on the parameterization of wind speed. This range of values was similar to the values at a higher elevation of the west side, in a zone exposed to the dominant westerlies (Garreaud and others, 2013; Lenaerts and others, 2014; Damseux and others, 2020). The latent heat flux also showed relatively higher values on the mid-to-lower elevations to the east in response to a drier atmosphere as well as relatively

strong winds. Consequently, this elevation range in the eastern side also showed a relative maximum in sublimation.

A key element that drives the disparity in ablation rates between each side of the divide is the magnitude and role of the latent heat flux and net longwave radiation. On the west side, and below 1500 m a.s.l., was the only section in our study area where the latent heat flux was a source of energy, leaving the net longwave radiation as the only sink of energy, but reaching relatively lower values (-8 to -20 W m⁻² below the 1000 m a.s.l.). Meanwhile, to the east, net longwave radiation and latent heat flux were sinks of energy with magnitudes in the order of -30 to -40 W m⁻² compensating the higher sensible heat flux (Figure 5.6). As the on-glacier air temperature was warmer in the west and decreased at a relatively shallow lapse rate (Bravo and others, 2019b), at the same elevation, the melt over debris-free surface was 1 to 4 m w.e. higher in the west compared to the east.

At a glacier scale, along with previous characteristics, the hypsometry determined a larger area under melt in the west. High melt (values over 5 m w.e.) in the west occurred over 90% of the total area, while in the east this magnitude of melt was observed over just 10% of the total area.

Melt enhancement was found under supraglacial moraine areas on both sides, but with a higher relative impact at the glacier scale in the east. Ice here is covered by relatively thin debris, which is enough to lead to an albedo decrease in the order of 0.1 to 0.2 (Figure 5.7 and Supplementary Figure 5.2). In our EB model, these areas were parameterized in terms of their radiative properties, and except for the surface roughness, the turbulence properties between ice-free and supraglacial moraine were treated under the same assumptions.

According to Nicholson and Stiperski (2020), turbulent heat fluxes in both thinner debris and debris-free areas are positive and of similar magnitude, but larger differences in the fluxes between both surface-types occur under sunny conditions. For instance, sensible heat flux on a thin debris-covered glacier surface is a sink of energy, while in debris-free areas it is a source. This introduces some uncertainties in our estimations of turbulent fluxes, especially over supraglacial moraines in the east (e.g. Chico Glacier, Figure 5.1), where sunny conditions were more frequent. In order to better represent the influence of the debris on turbulent fluxes, surface temperature measurements on supraglacial debris will be needed. Another source of uncertainty is the percentage of debris cover; however, the rate of melt seems not to change considerably across a range of percentage debris cover per unit

area (30-80%) (Fyffe and others, 2020). The increase of melt under thinner debris-covered areas of the Patagonian glaciers is a potential positive feedback on glacier retreat due to the destabilization of adjacent slopes, increasing the flux of debris over the glacier surface as was reported by Glasser and others (2016) in the NPI between 1987 and 2015.

5.5.3 Long-term ablation and surface mass balance

Here, we discuss the implications of the surface mass balance and its components over the long-term. The differences in the EB fluxes noted above were replicated in the extended time series of ablation, i.e. greater ablation on the west compared to the east. This, in conjunction with the snow accumulation, leads to negative surface mass balance conditions prevailing in the west and balanced to slightly positive mass balance prevailing in the east. This could be one of the reasons for the lower mass loss determined on the glaciers in the east (O'Higgins, Chico) compared to the glaciers in the west (Occidental, Greve, Témpano) using geodetic methods.

Overall, Willis and others, (2012), Malz and others, (2018) and Abdel-Jaber and others (2018) estimate that the thinning rates on these glaciers between 2000-2012, 2000-2015/16 and 2000-2016 respectively, was 0.6 to 1.1 m yr⁻¹ higher on the west side, whilst on the east, the lower thinning rate is focused on the terminus of the O'Higgins Glacier, though more extended in the case of Chico Glacier (e.g. maps of Abdel-Jaber and others, 2019 and Dussailant and others, 2019). Between 1975 and 2000, a greater thinning was also determined for the west side glaciers when compared to the east, although in this case, the difference was lower (Rignot and others, 2003). These differences agree with our results, i.e. in that more favourable conditions for ablation prevail in the west glaciers, although in contrast our surface mass balance estimation was positive (O'Higgins Glacier) or nearly balanced (Chico Glacier) for the east. We also found qualitative agreement in our mass balances compared with previously published data. Earlier works show predominantly negative values on the western side when compared to the eastern side at these latitudes of the SPI (Schaefer et. al., 2015; Mernild and others, 2016).

In the case of O'Higgins Glacier, geodetic glacier mass balance has been shown to be negative (e.g. Malz and others, 2018) in contrast to the positive mass balance estimated in this work and in previous one (Schaefer et. al., 2015; Mernild and others, 2016). In this case, it seems that ice dynamics and/or calving dynamics play an important role in the observed negative surface changes. Indeed, O'Higgins Glacier, showed times of abrupt change

as well as times of stability, suggesting the control of calving processes and lake depth on frontal changes (Lopez and others, 2008). Ice dynamics adjustments of the tidewater and lake calving have been suggested as the main control of SPI glacier shrinkage (Schaefer and others, 2015; Mouginit and Rignot, 2015; Braun and others, 2019). However, this generalization to explain the response over glaciers of the entire SPI precludes a full understanding of the local conditions that define the glacier response, as for instance the characteristics of the glacier boundary layer (Bravo and others, 2019b) and the hypsometry (De Angelis, 2014).

The uncertainty in snow accumulation in our study was high however, depending to a great extent on the input dataset and on the phase-partitioning method (PPM) used to calculate it (e.g. Bravo and others, 2019a). Recent analysis indicated that the moisture flux over Patagonia is untenable to maintain precipitation rates exceeding $\sim 6 \text{ m yr}^{-1}$ (Sauter, 2020). This suggests that previous modelling studies overestimate precipitation and/or snow accumulation in their calculations (Weidemann and others, 2018).

Moreover, it seems that the apparent discrepancy between geodetic and modelling mass balance was also related to higher ablation rates estimated here than previously (Schaefer et. al., 2015; Mernild and others, 2016). An explanation could be the use of a simplified energy balance models, as turbulent fluxes and longwave radiation were estimated by a linear function in air temperature (e.g. Schaefer and others, 2015) and/or for the use of general parameterization as spatially invariant air temperature lapse rate for the SPI (e.g. Mernild and others, 2016). Our results, in accord with other EB studies in Patagonia (e.g. Schaefer and others, 2020; Weidemann and others, 2020) showed the importance of the turbulent fluxes in the estimation of the surface ablation as well as the spatial differences in meteorological conditions.

At the glacier scale, our surface mass balance data show a predominance of negative values, with the exception of O'Higgins Glacier. The extreme negative surface mass balance values shown for the Occidental Glacier seem to be somewhat unrealistic, and to a lesser degree the same can be said for T mpano Glacier. In these cases, in addition to the high uncertainty associated with the surface accumulation, these extremely negative values could be associated with a poor delineation of basin extent, as maps of ice motion by Mouginit and Rignot (2015) suggest. Also, the representativeness of ERA5-Land for glaciers with lower elevation areas seems to be poor as a consequence of the coarse resolution, which is most useful for estimate bulk values of surface mass balance. Nevertheless, extreme surface lowering

observed over west-side glaciers are thought to be triggered by events associated with the drainage of a proglacial lake in the frontal zone of Témpano Glacier in 2007 (Iribarren-Anaconda and others, 2015) and several ice and rock-bar dammed lakes associated with Occidental and Greve glaciers (Wilson and others, 2018).

Acknowledging the limitations of the modelling and the lack of glaciological observations of any kind on the surface and/or surroundings of SPI, a case by case analysis is recommended if the aim is to analyse the forcing of the observed changes, as in the case of Jorge Montt Glacier in the north of the SPI (Bown and others, 2019). Surface elevation changes in the SPI have been shown to be highly heterogeneous (e.g. Foresta and others, 2018; Abdel-Jaber and others, 2019) and as we have demonstrated herein, west to east differences exist in meteorological conditions as well as in EB fluxes, both of which are key factors in controlling ablation.

5.6 Conclusions

In this work, we have estimated and assessed the energy balance fluxes, the ablation rates, and their spatial differences in a west-east transect for glaciers of the Southern Patagonian Icefield. Using meteorological observations and remote sensing, we conducted a distributed EB model at daily time step for the period between October 2015 and June 2016. Our basic principle was that the meteorological variables needed for the model can be spatially distributed through elevation gradients and hence a network of five AWS and three on-glacier temperature sensors were representative of the meteorological conditions, including the glacier boundary layer. After that, using climate re-analysis data and validating the results with the observational period, we extended the application of the EB model, estimating the total ablation and the snow accumulation from 1982 to 2019. Uncertainties exist in our approach that needs to be addressed, but considering these unprecedented meteorological observations in the SPI, the main findings and conclusions based on our results and discussions were:

i) Based on the meteorological observations and its spatial distribution, we found that in the northern section of the SPI, west-east differences exist in terms of humidity, cloud cover, glacier cooling effect, air temperature lapse rate and wind speed. This defines humid and warm on-glacier conditions on the western side and dry and cold on-glacier conditions on the eastern side. All these differences are feedbacks forced by the orographic effect widely described in the literature for Patagonia.

ii) Throughout the study area, net longwave radiation was a sink of energy, whilst net shortwave radiation and sensible heat flux were sources of energy. The latent heat flux was both a source and a sink, depending on the location. The importance of each flux depends on the location and elevation range, but over most of the glacier surface, sensible heat flux was the main source of energy, followed by net shortwave radiation.

iii) The results of the EB model showed that in the study area, favourable conditions for ablation exist, especially in terms of melt on the lower sections at both sides of the study area. Comparatively, these conditions define stronger melt rates on the west side glaciers. Here, a key to understanding the comparatively strong melt on the west was that net longwave radiation, the only sink of energy, showed the lowest values through the study area and latent heat flux was a source of energy, while on the east, it is a sink. The spatial extent of the melt is controlled by the hypsometry on each side, showing that there were favourable conditions for a larger area under melt on the west side compared to the east.

iv) Over longer timescales, our surface mass balance estimates show that western glaciers were losing mass during the last 37 years, while eastern side glaciers were close to balanced conditions. Qualitatively, this agrees with geodetic estimations of ice loss in the west, but not in the east. Thus, in the west, negative surface mass balance is an important explanation of the ice loss observed; whilst in the east, other factors (e.g. ice dynamics) besides the surface mass balance seem to control the observed ice loss.

Overall, the heterogeneous response of the glaciers that comprise the SPI is determined partly by the meteorological and climatological spatial variability that exists over this region. Therefore, we understand the SPI as a complex system with a diversity of conditions that through feedbacks and relationships define the glacier response. We recommend avoiding analysis of the glacier response and sensitivities that treats the SPI as a whole.

We recognized that the complete picture is far from being resolved in attributing the glacier response in the SPI to simply climate and meteorological conditions. The results presented here, however, give new insights in the spatial variability of the forcing that exerts controls on the response of the glacier surface mass balance. This analysis of the EB fluxes and their spatial differences provides a foundation on which further feedbacks associated with future climate change in this region can be investigated.

Acknowledgments

We acknowledge the Dirección General de Aguas de Chile (DGA) for providing their data for analysis. The Centro de Estudios Científicos (CECs) installed the AWS and GBL stations and provided all the metadata of these stations. CB acknowledge support from the Agencia Nacional de Investigación y Desarrollo (ANID) Programa Becas de Doctorado en el Extranjero, Beca Chile for the doctoral scholarship. Andrés Rivera acknowledges FONDECYT 1171832

5.7 References

Abdel Jaber W, Rott H, Floricioiu D, Wuite J and Miranda N (2019) Heterogeneous spatial and temporal pattern of surface elevation change and mass balance of the Patagonian ice fields between 2000 and 2016. *The Cryosphere* 13(9), 2511–2535. doi: [org/105194/tc-13-2511-2019](https://doi.org/10.5194/tc-13-2511-2019).

Ayala A, Pellicciotti F and Shea JM (2015) Modelling 2 m air temperatures over mountain glaciers: Exploring the influence of katabatic cooling and external warming. *Journal of Geophysical Research: Atmospheres* 120, 1–19. doi: [org/101002/2015JD023137](https://doi.org/10.1002/2015JD023137).

Bolton D (1980) The computation of equivalent potential temperature. *Monthly Weather Review* 108, 1046–1053. doi: [org/10.1175/1520-0493\(1980\)108<1046:TCOEPT>2.0.CO;2](https://doi.org/10.1175/1520-0493(1980)108<1046:TCOEPT>2.0.CO;2).

Bonekamp PNJ, van Heerwaarden CC, Steiner JF and Immerzeel WW (2020) Using 3D turbulence-resolving simulations to understand the impact of surface properties on the energy balance of a debris-covered glacier. *The Cryosphere* 14(5), 1611–1632. doi: [org/105194/tc-14-1611-2020](https://doi.org/10.5194/tc-14-1611-2020).

Bown F, Rivera A, Pęćlicki M, Bravo C, Oberreuter J and Moffat C (2019) Recent ice dynamics and mass balance of Jorge Montt Glacier, Southern Patagonia Icefield. *Journal of Glaciology* 65(253), 732-744. doi: [org/101017/jog201947](https://doi.org/10.1017/jog201947)

Braun M and Hock R (2004) Spatially distributed surface energy balance and ablation modelling on the ice cap of King George Island (Antarctica). *Global and Planetary Change* 42(1-4), 45-58. doi: [101016/jgloplacha200311010](https://doi.org/10.1016/j.gloplacha.2003.11.010).

Braun MH and 8 others (2019) Constraining glacier elevation and mass changes in South America. *Nature Climate Change* 9, 130–136. doi: [org/101038/s41558-018-0375-7](https://doi.org/10.1038/s41558-018-0375-7).

Bravo C and 6 others (2019a) Assessing snow accumulation patterns and changes on the Patagonian Icefields. *Frontiers in Environmental Science* 7(1), 30. doi: [org/10.3389/fenvs.2019.00030](https://doi.org/10.3389/fenvs.2019.00030).

Bravo C and 6 others (2019b) Air temperature characteristics, distribution and impact on modeled ablation for the South Patagonia Icefield. *Journal of Geophysical Research: Atmospheres* 124(2), 907–925. doi: [org/10.1029/2018JD028857](https://doi.org/10.1029/2018JD028857).

Brock B and Arnold N (2000) A spreadsheet-based (Microsoft Excel) point surface energy balance model for glacier and snowmelt studies. *Earth Surface Processes and Landforms* 25(6), 649–658. doi: [org/10.1002/1096-9837\(200006\)25:6<649::AID-ESP97>3.0.CO;2-U](https://doi.org/10.1002/1096-9837(200006)25:6<649::AID-ESP97>3.0.CO;2-U).

Collier E, Nicholson LI, Brock BW, Maussion F, Essery R and Bush ABG (2014) Representing moisture fluxes and phase changes in glacier debris cover using a reservoir approach *The Cryosphere* 8(4), 1429–1444. doi: [org/10.5194/tc-8-1429-2014](https://doi.org/10.5194/tc-8-1429-2014).

Cook K, Yang X, Carter C and Belcher B (2003) A modelling system for studying climate controls on mountain glaciers with application to the Patagonian Icefields. *Climatic Change* 56, 339–367. doi: [org/10.1023/A:1021772504938](https://doi.org/10.1023/A:1021772504938)

Copernicus Climate Change Service (C3S) (2019) C3S ERA5-Land reanalysis Copernicus Climate Change Service, date of access <https://cdsclimatecopernicuseu/cdsapp#!/home>

Cuffey KM and Paterson WSB (2010) *The physics of glaciers*, 4th edn. Butterworth-Heinemann, Oxford

Davies BJ and Glasser NF (2012) Accelerating shrinkage of Patagonian glaciers from the Little Ice Age (~AD 1870) to 2011. *Journal of Glaciology* 58(212), 1063–1084. doi: [org/10.3189/2012JoG12J026](https://doi.org/10.3189/2012JoG12J026).

Damseaux A, Fettweis X, Lambert M and Cornet Y (2020) Representation of the rainshadow effect in Patagonia using an orographic-derived regional climate model. *International Journal of Climatology* 40(3), 1769–1783. doi: [org/10.1002/joc6300](https://doi.org/10.1002/joc6300).

De Angelis H, Rau F and Skvarca P (2007) Snow zonation on Hielo Patagónico Sur, southern Patagonia, derived from Landsat 5 TM data. *Global and Planetary Change* 59(1-4), 149–158. doi: [org/10.1016/j.gloplacha.2006.11.032](https://doi.org/10.1016/j.gloplacha.2006.11.032).

De Angelis H (2014) Hypsometry and sensitivity of the mass balance to change in equilibrium-line altitude: the case of the Southern Patagonia Icefield. *Journal of Glaciology* 60(219), 14–28. doi: org/10.3189/2014JoG13J127.

Durand M and 6 others (2019) GPS reflectometry study detecting snow height changes in the Southern Patagonia Icefield. *Cold Regions Science and Technology* 166, 102840. doi: 101016/jcoldregions2019102840.

Dussaillant, I and 8 others (2019) Two decades of glacier mass loss along the Andes. *Nature Geosciences* 12, 802–808. doi: org/10.1038/s41561-019-0432-5.

Falaschi, D and 6 others (2017) Mass changes of Alpine Glaciers at the Eastern Margin of the Northern and Southern Patagonian Icefields between 2000 and 2012. *Journal of Glaciology* 63(238), 258–272. doi: 101017/jog2016136.

Falaschi D, Lenzano MG, Villalba R, Bolch T, Rivera A and Lo Vecchio A (2019) Six Decades (1958–2018) of Geodetic Glacier Mass Balance in Monte San Lorenzo, Patagonian Andes. *Frontiers in Earth Scienc*, 7. doi: org/103389/feart201900326.

Foresta L and 7 others (2018) Heterogeneous and rapid ice loss over the Patagonian Ice Fields revealed by CryoSat-2 swath radar altimetry. *Remote Sensing of Environment* 211, 441-455. doi: org/101016/jrse201803041.

Fyffe, C and 6 others (2014) A distributed energy-balance melt model of an alpine debris-covered glacier. *Journal of Glaciology* 60(221), 587-602. doi:103189/2014JoG13J148.

Fyffe C, Woodget AS, Kirkbride M, Deline P, Westoby M and Brock B (2020) Processes at the margins of supraglacial debris cover: quantifying dirty ice ablation and debris redistribution. *Earth Surface Processes and Landforms*, doi: org/10.1002/esp.4879

Gardner AS and 15 others (2013), A reconciled estimate of glacier contributions to sea level rise: 2003 to 2009. *Science* 340 (6134), 852–857. doi: org/101126/science1234532.

Garreaud R (2018) Record-breaking climate anomalies lead to severe drought and environmental disruption in Western Patagonia in 2016. *Climate Research* 74, 217-229. doi: org/103354/cr01505.

Garreaud R, Lopez P, Minvielle M and Rojas M (2013) Large-Scale control on the Patagonian Climate. *Journal of Climate* 26(1), 215–230. doi: org/10.1175/JCLI-D-12-00001.1

Gillett S and Cullen NJ (2010) Atmospheric controls on summer ablation over Brewster Glacier, New Zealand. *International Journal of Climatology* 31(13), 2033–2048. doi: 101002/joc2216.

Glasser NF, Holt TO, Evans ZD, Davies BJ, Pelto M and Harrison S (2016) Recent spatial and temporal variations in debris cover on Patagonian glaciers. *Geomorphology* 273, 202–216. doi: org/10.1016/j.geomorph.2016.07.036.

Iribarren-Anacona P, Mackintosh A and Norton KP (2015) Hazardous processes and events from glacier and permafrost areas: Lessons from the Chilean and Argentinean Andes. *Earth Surf Processes Landforms* 40 (1), 2–21. doi: org/10.1002/esp.3524.

Koizumi K and Naruse R (1992) Measurements of meteorological conditions and ablation at Tyndall Glacier, Southern Patagonia, in December 1990. *Bulletin of Glacier Research* 10, 79-82.

Lenaerts, JTM and 6 others (2014) Extreme Precipitations and Climate Gradients in Patagonia Revealed by High-Resolution Regional Atmospheric Climate Modeling. *Journal of Climate* 27(12), 4607-4621. doi: org/10.1175/JCLI-D-13-00579.1.

Lo Vecchio A, Lannutti E, Lenzano MG, Mikkan R, Vacafior P and Lenzano L (2019) MODIS Image-derived ice surface temperature assessment in the Southern Patagonian Icefield. *Progress in Physical Geography: Earth and Environment* 43(6), 754-776. doi: org/10.1177/0309133319851022.

López P, Chevallier P, Favier V, Apoyad B, Ordenes F and Oerlemans J (2010) A regional view of fluctuations in glacier length in southern South America. *Global and Planetary Change* 71(1-2), 85–108. doi: org/10.1016/j.gloplacha.2009.12.009.

Malz P, Meier W, Casassa G, Jaña R, Skvarca P and Braun MH (2018) Elevation and Mass Changes of the Southern Patagonia Icefield Derived from TanDEM-X and SRTM Data. *Remote Sensing* 10(2), 188. doi: org/103390/rs10020188.

Masiokas M and 11 others (2020) Review of the Current State and Recent Changes of the Andean Cryosphere. *Frontiers in Earth Science* 8. doi: org/10.3389/feart.2020.00099

Meier WJH, Griebinger J, Hochreuther P and Braun MH (2018) An Updated Multi-Temporal Glacier Inventory for the Patagonian Andes With Changes Between the Little Ice Age and 2016. *Frontiers in Earth Science* 6. doi: org/10.3389/feart201800062.

Mernild SH, Liston GE, Hiemstra CA and Wilson R (2016) The Andes Cordillera Part III: Glacier Surface Mass Balance and Contribution to Sea Level Rise (1979–2014). *International Journal of Climatology* 37(7), 3154–3174. doi: org/10.1002/joc.4907.

Mölg T, Cullen NJ and Kaser G (2009) Solar radiation, cloudiness and longwave radiation over low-latitude glaciers: Implications for mass balance modelling *Journal of Glaciology* 55(190), 292-302. doi: org/10.3189/002214309788608822.

Mölg T and 8 others (2020) Mesoscale atmospheric circulation controls of local meteorological elevation gradients on Kersten Glacier near Kilimanjaro summit. *Earth System Dynamics* 11, 653-672. doi.org/10.5194/esd-11-653-2020

Monahan P and Ramage J (2010) AMSR-E Melt Patterns on the Southern Patagonian Icefield. *Journal of Glaciology* 56(198), 699-708. doi: org/10.3189/002214310793146197.

Mouginot, J and Rignot E (2015) Ice motion of the Patagonian icefields of South America: 1984–2014. *Geophysical Research Letters* 42(5), 1441–1449. doi: org/10.1002/2014GL062661.

Muñoz Sabater J (2019) First ERA5-Land dataset to be released this spring, ECMWF newsletter 159.

Murray FW (1967) On the computation of saturation vapor pressure, *Journal of Applied Meteorology* 6 (1), 203–204. doi: 10.1175/1520-0450(1967)006<0203:OTCOSV>2.0.CO;2

Muto M and Furuya M (2013) Surface velocities and ice-front positions of eight major glaciers in the southern Patagonian ice field, South America, from 2002 to 2011. *Remote Sensing of Environment* 139, 50–59. doi: org/10.1016/j.rse.2013.07.034.

Naruse R, Skvarca P and Takeuchi Y (1997) Thinning and retreat of Glaciar Upsala, and an estimate of annual ablation changes in Southern Patagonia. *Annals of Glaciology* 24, 38-42. doi: org/10.3189/S0260305500011903.

Nicholson L and Stiperski I (2020) Comparison of turbulent structures and energy fluxes over exposed and debris-covered glacier ice. *Journal of Glaciology* 1–13. doi: [org/10.1017/jog202023](https://doi.org/10.1017/jog202023).

Oerlemans J and Knap WH (1998) A one-year record of global radiation and albedo from the ablation zone of the Morteratschgletscher, Switzerland. *Journal of Glaciology* 44(147), 231-238. doi: [org/10.3189/S0022143000002574](https://doi.org/10.3189/S0022143000002574).

Oerlemans J and Klok EJ (2002) Energy balance of a glacier surface: analysis of Automatic Weather Station data from the Morteratschgletscher, Switzerland. *Arctic, Antarctic and Alpine Research* 34(4), 477-485. doi: [org/10.1080/15230430.2002.12003519](https://doi.org/10.1080/15230430.2002.12003519)

Ohata T, Kobayashi S, Enomoto H, Kondo H, Saito T and Nakajima C (1985) The east-west contrast in meteorological conditions and its effect on glacier ablation. *Bulletin of Glaciological Research* 3, 52–53.

Pellicciotti F, Ragetti S, Carenzo M and McPhee J (2014) Changes of glaciers in the Andes of Chile and priorities for future work. *Science of the Total Environment*, 493, 1197-1210. doi: [org/10.1016/j.scitotenv.2013.10.055](https://doi.org/10.1016/j.scitotenv.2013.10.055).

Popovnin V, Danilova T and Petrakov D (1999) A pioneer mass balance estimate for a Patagonian glacier: Glaciar De Los Tres, Argentina. *Global and Planetary Change* 22(1-4), 255–267. doi: [org/10.1016/S0921-8181\(99\)00042-9](https://doi.org/10.1016/S0921-8181(99)00042-9).

Raleigh MS, Landry CC, Hayashi M, Quinton WL and Lundquist JD (2013) Approximating snow surface temperature from standard temperature and humidity data: new possibilities for snow model and remote sensing evaluation. *Water Resources Research* 49(12), 8053–8069. doi: [org/10.1002/2013WR013958](https://doi.org/10.1002/2013WR013958).

Rasmussen LA, Conway H and Raymond CF (2007) Influence of upper air conditions on the Patagonia icefields. *Global Planet Change* 59(1-4), 203–216, doi: [org/10.1016/j.jgloplacha.2006.11.025](https://doi.org/10.1016/j.jgloplacha.2006.11.025).

Rignot E, Rivera A and Casassa G (2003) Contribution of the Patagonia Icefields of South America to Sea Level Rise. *Science* 302(5644), 434-436. doi: [0.1126/science.1087393](https://doi.org/10.1126/science.1087393).

Rivera A (2004) Mass balance investigations at Glaciar Chico, Southern Patagonia Icefield, Chile. (PhD thesis, University of Bristol).

Rivera A, Corripio J, Bravo C and Cisternas S (2012) Glaciar Jorge Montt (Chilean Patagonia) dynamics derived from photos obtained by fixed cameras

and satellite image feature tracking *Annals of Glaciology* 53(60), 147-155. doi: org/10.3189/2012AoG60A152.

Sagredo E and Lowell T (2012) Climatology of Andean glaciers: A framework to understand glacier response to climate change. *Global and Planetary Change* 86–87, 101–109. doi: org/10.1016/j.gloplacha.2012.02.010.

Sakakibara D and Sugiyama S (2014) Ice-front variations and speed changes of calving glaciers in the Southern Patagonia Icefield from 1984 to 2011. *Journal of Geophysical Research: Earth Surface* 119(11), 2541–2554. doi:org/101002/2014JF003148.

Sauter T and Galos SP (2016) Effects of local advection on the spatial sensible heat flux variation on a mountain glacier. *The Cryosphere* 10, 2887–2905. doi: org/105194/tc-10-2887-2016.

Sauter T (2020) Revisiting extreme precipitation amounts over southern South America and implications for the Patagonian Icefields. *Hydrological and Earth System Sciences* 24(4), 2003–2016. doi: org/105194/hess-24-2003-2020.

Schaefer M, Machguth H, Falvey M, Casassa G and Rignot E (2015) Quantifying mass balance processes on the Southern Patagonia Icefield. *The Cryosphere* 9(1), 25–35. doi: org/10.5194/tc-9-25-2015.

Schaefer M, Fonseca D, Farias-Barahona D and Casassa, G (2020) Surface energy fluxes on Chilean glaciers: measurements and models. *The Cryosphere* 14, 2545–2565, doi:org/10.5194/tc-14-2545-2020.

Schneider C, Glaser M, Killian R, Santana A, Butorovic N and Casassa G (2003) Weather observations across the Southern Andes at 53°S. *Physical Geography* 24(2), 97-119. doi: org/10.2747/0272-3646.24.2.97.

Schneider C, Kilian R and Glaser M (2007) Energy balance in the ablation zone during the summer season at the Gran Campo Nevado Ice Cap in the Southern Andes. *Global and Planetary Change*, 59, 175–188. doi: org/101016/j.gloplacha 200611033.

Schwikowski M, Schläppi M, Santibañez P, Rivera A and Casassa G (2013) Net accumulation rates derived from ice core stable isotope records of Pío XI glacier, Southern Patagonia Icefield. *The Cryosphere* 7, 1635-1644. doi: org/05194/tc-7-1635-2013

Shea JM and Moore RD (2010) Prediction of spatially distributed regional-scale fields of air temperature and vapour pressure over mountain glaciers. *Journal of Geophysical Research: Atmospheres* 115(D23). doi: org/101029/2010JD014351.

Smith R and Evans J (2007) Orographic precipitation and water vapor fractionation over the Southern Andes. *Journal of Hydrometeorology* 8(1), 3–19. doi: [org/10.1175/JHM555.1](https://doi.org/10.1175/JHM555.1).

Stuefer M, Rott H, and Skvarca P (2007) Glaciar Perito Moreno, Patagonia: climate sensitivities and glacier characteristics preceding the 2003/04 and 2005/06 damming events. *Journal of Glaciology* 53(180), 3–16. doi: [org/10.3189/172756507781833848](https://doi.org/10.3189/172756507781833848).

Takeuchi Y, Naruse R and Satow K (1995) Characteristics of heat balance and ablation on Moreno and Tyndall glaciers, Patagonia, in the summer 1993/94. *Bulletin of Glacier Research* 13, 45–56.

Takeuchi Y, Naruse R and Skvarca P (1996) Annual air-temperature measurement and ablation estimate at Moreno Glacier, Patagonia. *Bulletin of Glacier Research* 14, 23-28.

Takeuchi Y, Naruse R, Satow K and Ishikawa N (1999) Comparison of heat balance characteristics at five glaciers in the Southern Hemisphere. *Global Planet Change* 22, 201-208. doi: [org/10.1016/S0921-8181\(99\)00037-5](https://doi.org/10.1016/S0921-8181(99)00037-5).

Tetzner D, Thomas E and Allen C (2019) A validation of ERA5 reanalysis data in the southern Antarctic Peninsula Ellsworth land region, and its implications for ice core studies. *Geosciences* 9(7), 289. doi: [org/10.3390/geosciences9070289](https://doi.org/10.3390/geosciences9070289).

Wallace JM and Hobbs PV (2006) *Atmospheric science: an introductory survey*, 2nd Edition, Elsevier Academic Press, Amsterdam, Boston.

Weidemann, SS and 6 others (2018) Glacier mass changes of lake-terminating Grey and Tyndall glaciers at the Southern Patagonia Icefield derived from geodetic observations and energy and mass balance modeling. *Frontiers in Earth Science* 6. doi: [org/10.3389/feart201800081](https://doi.org/10.3389/feart201800081).

Weidemann, SS and 6 others (2020) Recent climatic mass balance of the Schiaparelli glacier at the Monte Sarmiento massif and reconstruction of Little Ice Age climate by simulating steady-state glacier conditions. *Geosciences* 10 (272). doi: [org/10.3390/geosciences10070272](https://doi.org/10.3390/geosciences10070272).

White A and Copland L (2015) Decadal-scale variations in glacier area changes across the Southern Patagonian Icefield since the 1970s. *Arctic, Antarctic, and Alpine Research* 47(1), 147–167. doi: [org/10.1657/AAAR0013-102](https://doi.org/10.1657/AAAR0013-102)

Willis M, Melkonian A, Pritchard M and Rivera A (2012) Ice loss from the Southern Patagonian Ice Field, South America, between 2000 and 2012.

Geophysical Research Letters, 39(17), L17501. doi:
org/10.1029/2012GL053136.

Wilson, R, and 6 others (2018) Glacial lakes of the Central and Patagonian Andes. Global and Planetary Change 162, 275-291. doi:
org/10.1016/j.gloplacha.2018.01.004.

Zemp M and 14 others (2019) Global glacier mass changes and their contributions to sea-level rise from 1961 to 2016. Nature 568, 382–386. doi:
org/101038/s41586-019-1071-0.

Chapter 6
Projected increases in surface melt and ice loss for the
Northern and Southern Patagonian Icefields

Claudio Bravo, Deniz Bozkurt, Andrew N. Ross and Duncan J. Quincey

6.1 Abstract

The North Patagonian Icefield (NPI) and the South Patagonian Icefield (SPI) increased their ice mass loss in recent decades. In view of the local, regional and worldwide impacts of glacier retreat in Patagonia, an assessment of the potential future surface mass balance (SMB) of the icefields is critical. In this work, we seek to provide this assessment by modelling the SMB between 1976 and 2050 for both icefields, using regional climate model data (RegCM4.6) and a range of emission scenarios. For the NPI, a reduction between 1.51 m w.e. (RCP2.6) and 1.88 m w.e. (RCP8.5) was projected, suggesting that negative SMB will prevail well into future decades. For the SPI the reduction in mass balance was within the range 1.12 m w.e. (RCP2.6) and 1.45 m w.e. (RCP8.5), which implies positive SMB will dominate, albeit at a lower rate than is currently observed. However, if it is assumed that frontal ablation rates of the recent past will continue, ice loss and sea-level rise will increase for both Icefields. A rise in equilibrium-line altitude indicates there will be areal reductions in the glaciers of the NPI as well as in some areas of the SPI, depending on individual topographic characteristics. The trend towards lower SMB overall is explained by an increase in melt, and to a lesser extent by a reduction in snow accumulation. Increase in meltwater availability could act as a positive feedback, triggering ice-speed acceleration and ice loss due to an increase in frontal ablation of calving glaciers.

6.2 Introduction

Meltwater generated by receding land ice is impacting global sea-levels at an accelerating rate¹. The glaciers of the Southern Andes represent one of the highest contributors, responsible for a total of 3.3 mm of sea-level rise between 1961 and 2016². This region includes larger temperate icefields: the Northern Patagonian Icefield (NPI) and the Southern Patagonian Icefield (SPI) (Figure 6.1). In recent years, both icefields have been the focus for studies of geodetic mass balance³⁻¹². These analyses are uniform in their assessment that overall ice mass loss has increased through time for both Patagonian Icefields, although patterns on the SPI are somewhat heterogeneous^{9,12}. Together, the Patagonian Icefields represent 83% of the total ice loss in the Southern Andes¹⁰ and over long time scales it has been estimated that the sea level contribution of Patagonian glaciers in the last 50 years is one order of magnitude larger than at the Little Ice Age (LIA) maximum, dated AD1650 in the SPI and AD1870 in the NPI¹³.

The primary conditions shaping the response of Patagonian glaciers are complex¹⁴, defined at a broad-scale by the interaction of the Andean

topography with the dominant westerlies and water vapour flux transported at these latitudes, which creates a strong climatic divide¹⁵ in terms of humidity and precipitation¹⁶. West-east spatial differences in local (glacier-scale) climate characteristics have been described in terms of cloud cover¹⁷, air temperature lapse rates, glacier cooling effect¹⁸, snow accumulation¹⁹ and the occurrence of föhn events²⁰. In turn, these characteristics define west-east differences over the glacier surface, for instance, in producing variable snow facies²¹ and leading to asynchronous melt seasons²².

In addition to the local climate differences of the Patagonian Icefields and its glaciers, other mechanisms exert an influence on ice loss rates. Most Patagonian Icefield glaciers terminate in lacustrine or marine calving settings. In the case of the NPI, the frontal areas mostly terminate in relatively small and shallow lakes, while SPI glaciers terminate in fjords on the west side and deep and large lakes on the east side. There is discrepancy between positively modelled surface mass balances using climate data²³⁻²⁶ and negative total mass balances derived by the geodetic approach, which can be explained by the importance of the frontal ablation mechanisms in calving glaciers. In turn, this mechanism is associated with adjustments to the ice dynamics of large glaciers¹⁰ and/or the lake/fjord characteristics of each glacier²⁷.

Climate conditions that define the broad-scale surface mass balance (SMB) also play a primary role in driving glacier-scale ablation. Fundamentally, climate conditions define the energy available for melt. Air temperature is important, but turbulent fluxes are high in Patagonia, which in turn depend on wind speed, humidity gradients and surface temperature, among others^{28,29}. Secondly, feedbacks between ice dynamics and SMB have been identified for the glaciers in this region. Patagonian glaciers comprise temperate ice^{30,31} leading to the presence of abundant meltwater, enhancing crevassing in the terminus areas and leading to flotation and increasing frontal ablation³¹. Additionally, a strong correlation between ice speed and air temperature fluctuations has been evidenced for the calving terminus of the Perito Moreno Glacier in the SPI^{32,33} suggesting that the meltwater infiltrating into the glacier increases basal water pressure, which in turn increases basal sliding and thus overall ice speed.

In view of the local, regional and worldwide impacts observed due to the ongoing glacier retreat of Patagonian glaciers, and the direct and indirect importance of the climate conditions that drive the total ice loss, an assessment of the potential future SMB is critical and timely. The aim of this

work is therefore to estimate the SMB and its components for both the NPI and the SPI (Figure 6.1). We used dynamically downscaled outputs of the MPI-ESM-MR Earth System Model³⁴ obtained with Regional Model RegCM4.6 at 10-km spatial resolutions for the historical period³⁵ (hydrological years between 1976/77 and 2004/05) and for two pathway scenarios (RCP2.6 and RCP8.5, between hydrological years 2005/06 and 2049/50). These pathway scenarios were chosen due to current emissions are following a path similar to RCP8.5³⁶, while, although insufficient, RCP2.6 is the closest scenario in to achieve the 2015 Paris Agreement in terms of temperature³⁷. Additionally, it is also important to show if important contrasts exist between under low (RCP2.6) and high (RCP8.5) emissions scenarios.

These products were used directly to estimate snow accumulation and its changes, and subsequently to feed an energy balance model (EBM) to estimate the ablation and its changes over both Patagonian Icefields. Changes in the equilibrium-line altitudes (ELA) obtained from the SMB were also analysed and a first-order estimation of the ice loss and its contribution to sea-level rise until 2050 was derived.

In the first section of this manuscript, we compare the results of the historical SMB run with previous estimations of modelled and geodetic mass balance, as well as the ELA, at the scale of the two Icefields. Then, we present the results of the future SMB and ELA under both scenarios and we quantify the changes in comparison to the historical period as well as estimating total ice loss. Finally, we discuss the implications of the results in terms of potential glacier response and feedbacks associated with changes in ELA, SMB and their components.

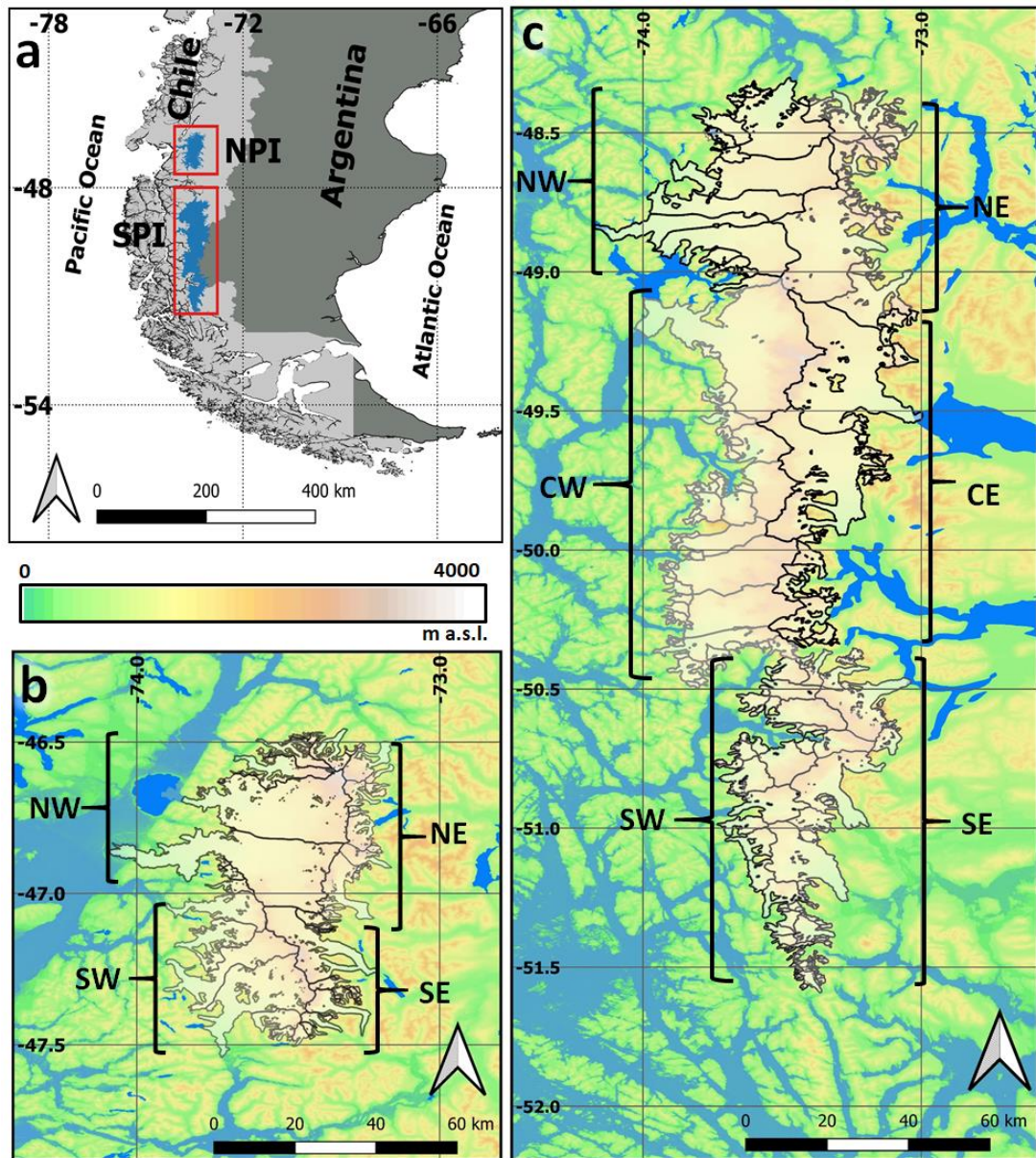


Figure 6.1 Location of the NPI and SPI in Southern South America (a). Details of the NPI (b) and the SPI (c). Colour shading is the topography from SRTM and blue tones are lakes and fjords. In the NPI the main glaciers per each sub-zone are: San Rafael and San Quintin (NW), Exploradores, Soler and Nef (NE), Steffen and Acodado (SW) and Colonia, Pared Norte and Pared Sur (SE). In the SPI: Jorge Montt, Témpano, Bernardo, Occidental and Greve (NW), O'Higgins and Chico (NE), Pio XI, HPS12, HPS13, Europa and Guilardi (CW), Viedma and Upsala(CE), Calvo, Asia and Amalia (SW) and Perito Moreno, Grey and Tyndall (SE).

6.3 Results

6.3.1 Historical SMB

For both the NPI and the SPI, we calculated the annual SMB between the hydrological years 1976/77 and 2005/06, defined as the historical period, and between the hydrological years 2006/07 and 2049/50 under two pathway scenarios (RCP2.6 and RCP8.5) (Figure 6.2).

For the historical period the mean SMB was negative in the NPI, reaching an annual mean value of -0.63 ± 2.14 m w.e., in agreement with previously published geodetic mass balances in the comparative periods^{3,4,6,8-12} (Figure 6.2a) and with previously modelled SMBs (e.g. mean of -0.16 ± 0.73 m w.e. for the period 1979/80-2009/10²³). On the other hand, the historical SMB was found to be in disagreement with the slightly positive modelled SMB of 0.15 ± 0.49 m w.e. for the period 1979/80-2013/14²⁶. Note, however, that the periods of analysis are not directly comparable in each case. For the common period between the hydrological years of 1979/80 and 2003/04 we obtained an annual mean of -0.71 ± 2.14 m w.e. while Mernild et al.²⁶ estimated 0.12 ± 0.50 m w.e. Additionally, we note that all previous values are in the uncertainty range estimated in our historical SMB, which is high and reflects the uncertainty mainly associated with snow accumulation and the parametrization of the glacier cooling effect.

In the SPI (Figure 6.2b), SMB was positive with a mean of 2.70 ± 1.61 m w.e., in general agreement with previous modelling, although our results slightly exceed those of 1.78 ± 0.36 m w.e.²⁶ and 2.30 ± 0.95 m w.e.²⁵ between 1979/80 and 2009/10. For the hydrological years between 1979/80 and 2003/04 we obtained 2.65 ± 1.61 m w.e. and Mernild et al.²⁶ derived a value of 1.72 ± 0.38 m w.e. Geodetic mass balances were all negative^{3,5,7,9-12} and outside of our uncertainty range (Figure 6.2b). There was a slight decreasing trend in SMB which was not significant, but which contradicts previous SMBs for a similar period that showed a positive trend^{24,25}.

Qualitatively, agreement between surface and geodetic mass balance in the NPI seems to be related to the frontal characteristics of the glaciers. Many of them are located on land and terminate in small lakes, reducing the effect of frontal ablation. Indeed, it has been estimated that calving flux was insignificant for the San Quintin Glacier, the largest glacier in the NPI, during the period 1975-2000²³. The exception is San Rafael Glacier, which terminates in a lake connected to a fjord, where previous estimations have defined the frontal ablation as being the most important ice loss mechanism³⁸

being one order of magnitude higher than for most of the NPI glaciers²³. Most glaciers in the SPI are tidewater-terminating in the west and freshwater-terminating in the east. Both fjords and lakes are of considerable depth, indicating frontal ablation plays an important role³¹, although we cannot account for this directly within the modelling.

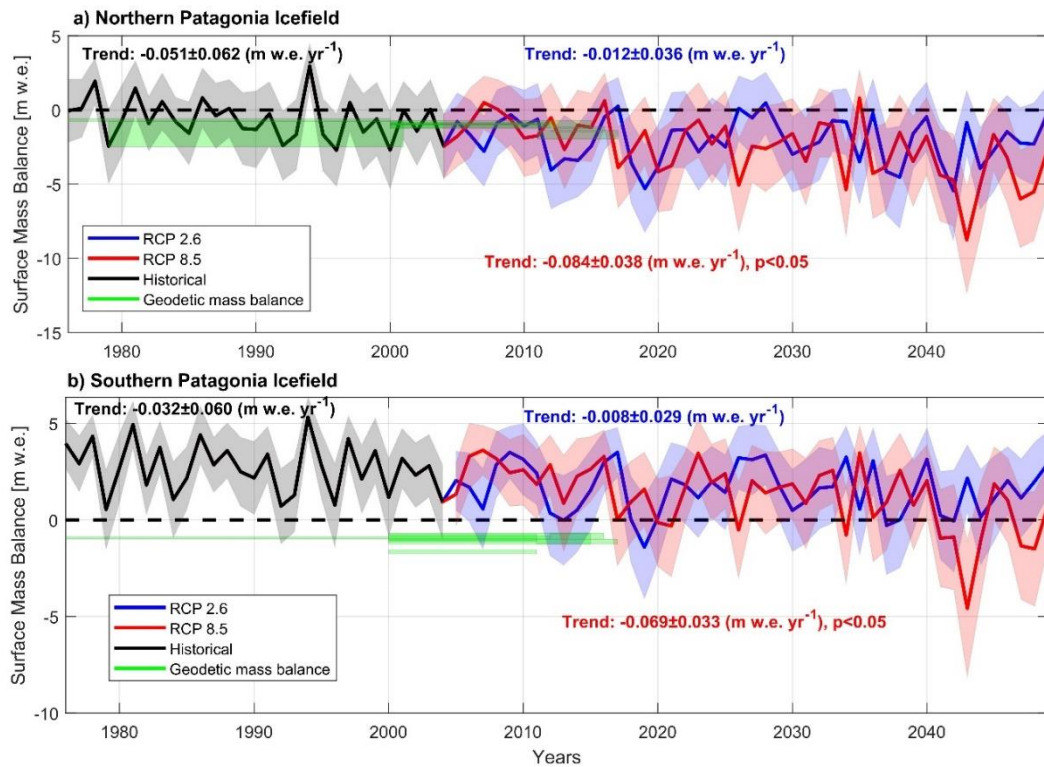


Figure 6.2 Time series of the modelled surface annual mass balance. (a) NPI and (b) SPI. Colour shadow represent the uncertainties in the modelled SMB for the historical period and the two scenarios. This is mainly due to the parametrization of the glacier cooling effect and the method used for the phase partitioning in the total precipitation to define the surface snow accumulation. Green coloured bars indicate previously derived geodetic mass balances and their error range previously estimated in NPI^{3,4,6,8-12} and in the SPI^{3,5,7,9-12}. Trends with the 95% confidence interval are shown. Significant trends are also indicated when $p < 0.05$.

6.3.2 Equilibrium-Line Altitudes

The mean long-term ELA was estimated for the historical period for each sub-zone defined in Figure 6.1. Overall, the west side showed a lower ELA in comparison to the east side glaciers for both icefields. Although there are no previous ELA estimations that can be directly compared with our ELA (as most of them are for specific years), observing the end-of-summer snowline using satellite images^{4,5,39-41} provides some form of validation (Table 6.1). Our modelled values correspond well, although a notable exception is found along the western margins, where our ELA was generally 100-300 m lower than

previous estimations (Table 6.1). The parameterisation of the cooling effect plays a key role in determining the ELA, and explains the range of values presented in Table 6.1. Our previous work¹⁸ has demonstrated that this cooling effect is more significant in the east compared to the west of the SPI, a fact that is also borne out by our modelled data here.

In the SW and NE of the NPI, our values were close to those obtained by Barcaza et al.⁴⁰, who estimated the mean ELA by measuring the end-of-summer snowline using five satellite images in the period between 1979 and 2003, and to Schaefer et al.²³ who estimated the ELA for the period 1975-2011, similar to our approach but reported just for a few glaciers. On the eastern side of the SPI, the long-term mean ELA was in the range of most of the previously observed and modelled ELAs (Table 6.1).

Disagreement between the end-of-summer snowline and the mean long-term ELA along the western margins is likely to reflect the high mass turnover observed in maritime glaciers. In addition, snow accumulation frequently occurs in summer months¹⁹, but a high 0°C isotherm means much of this snow is quickly lost to melt⁴⁰.

Table 6.1 Comparison of the ELA per sub-zone obtained in this work with those obtained by observations of the end of summer snowline using satellite images^{3-5,39-41} and by SMB modelling^{23,25}. Previous values are the mean of several glaciers observed. Number of glaciers are variable depending availability in the references. The lower limit in this work was obtained using a higher glacier cooling effect and the upper limit was obtained using lower glacier cooling. In bold are the closest ELA values of this work comparing with the previous observations and estimations.

| NPI | Aniya ³⁹ | Rivera et al. ⁴ | Barcaza et al. ⁴⁰ | Schaefer et al. ²³ | This work |
|-----|--------------------------|-------------------------------|------------------------------|-------------------------------|--------------------|
| NW | 1031 | 1096 | 1095 | 1185 | 624 - 862 |
| NE | 1217 | 1224 | 1371 | 1387 | 1250 - 1517 |
| SW | 1044 | 1026 | 924 | 1163 | 796 - 1081 |
| SE | 1075 | 1138 | 1124 | 1351 | 1264 - 1586 |
| SPI | De Angelis ⁴¹ | Schaefer et al. ²⁵ | Willis et al. ⁵ | This work | |
| NW | 928 | 1112 | 1015 | 612-827 | |
| NE | 1164 | 1282 | 1224 | 1166 -1392 | |
| CW | 1017 | 989 | 1032 | 520- 695 | |
| CE | 1248 | 1249 | 1268 | 1210 -1402 | |
| SW | 1042 | 900 | 856 | 540- 765 | |
| SE | 1018 | 1023 | 1045 | 812- 1139 | |

6.3.3 Projected changes in SMB and ELAs

Projected SMB results (which as stated do not account for frontal ablation mechanisms) indicate that the NPI will be characterized by a notable negative SMB until at least 2050. Solely by climate forcing, the SPI will continue to gain mass, but at a lower rate compared to the historical period (Figure 6.2). In the

NPI, the mean projected SMB values were -2.04 ± 2.49 m w.e. (RCP2.6) and -2.51 ± 2.61 m w.e. (RCP8.5), while in the SPI, the projected mean SMB values were 1.58 ± 1.96 m w.e. (RCP2.6) and 1.25 ± 2.07 m w.e. (RCP8.5). However, after the year 2040, a predominance of negative annual SMB in the SPI is projected. This finding is in agreement with projections by Schaefer et al.²³ for the NPI, although the magnitude of their projection is lower, reaching values around -2 m w.e. after 2070.

There are notable differences in the interannual variability in the SMB between scenario pathways. For instance, some particular years from the RCP2.6 scenario were lower in magnitude than those arising from the RCP8.5 SMB run, indicating that the EBM used here captured feedbacks related to other meteorological variables used to feed the model. This is important as it has been demonstrated that the surface ablation of Patagonian glacier depends to a large extent on turbulent fluxes, especially the sensible heat flux^{28,29,42}, which in turn also depends on the wind speed. However, the natural interdecadal variability also could play a role in this behaviour, especially over the first decades of the projection. After 2040, the differences between both scenarios are higher as the higher signal-to-noise ratio for the RCP8.5 scenario dominates as it has a more prominent temperature increase. As might be expected, long-term mean values show that RCP8.5 yielded the greatest reductions in SMB for both Icefields.

Figure 6.3 shows the projected mean SMB differences per elevation range (for each historical period) for the different sub-zones defined for both Icefields (Figure 6.1). The reductions in SMB were homogeneous within different regions, but with some differences in the magnitude between regions, being notably larger in the lower section of the south of the SPI (Figure 6.3i,j) and lower in the higher elevations (i.e. plateau zone) of the north-central section of the SPI (Figure 6.3e,f,g,h).

From the SMB profiles, we estimated a long-term ELA for each sub-zone and for the two pathway scenarios (2005/06-2949-50). Depending on the scenario and the SMB uncertainties the magnitude of the long-term ELA increase was between 72 and 450 m in the NPI, while in the SPI it was between 46 and 104 m (Table 6.2). Considering the glacier-cooling effect differences between the west side and the east margin glaciers¹⁸, the most probable range was a rise of 91 to 133 m in NPI and 38 to 108 m in the SPI (Table 6.2, values in bold).

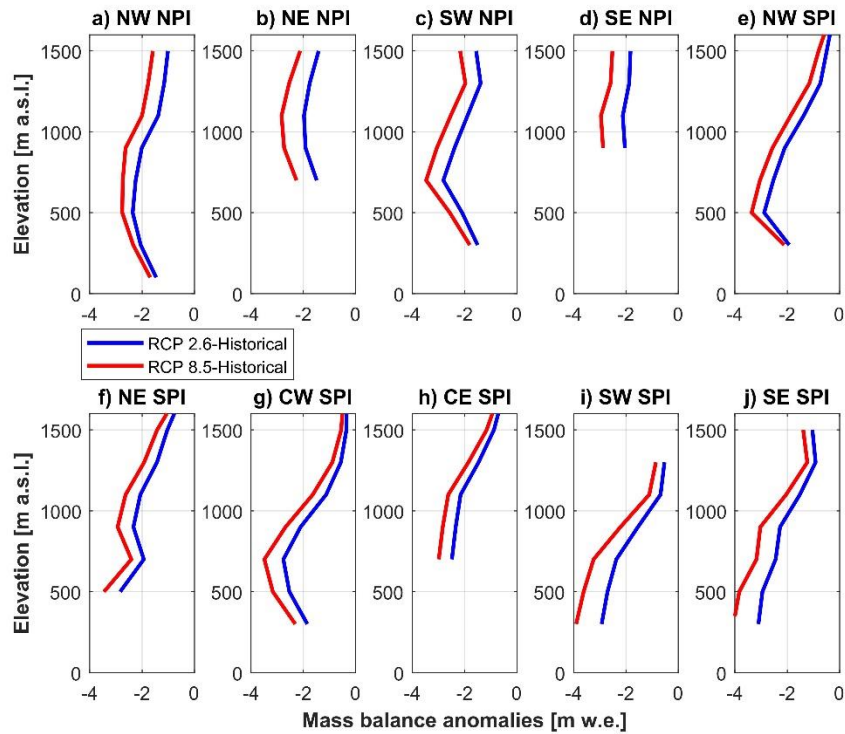


Figure 6.3 Surface mass balance differences per sub-zone (Figure 6.1) and elevation range in both Icefields. The differences were derived by comparing long-term SMBs between the historical period and each RCP scenario.

Table 6.2 Range of difference in the mean long-term ELA per sub-zone between historical period and each RCP scenario. ELA was obtained as the long-term mean of the elevation where the SMB reach 0 m w.e. The range of difference at each scenario is given by the runs using -1°C and -3°C of cooling effect as meteorological observations suggests¹⁸. Following Table 6.1, bold values denote values that most closely approach actual conditions observed in SPI in terms of glacier cooling effect and ELA.

| Sub-Zone | RCP2.6 (m) | RCP8.5 (m) |
|----------|---------------|---------------|
| NW NPI | 72-91 | 97-108 |
| NE NPI | 96-201 | 137-404 |
| SW NPI | 59-125 | 75-166 |
| SE NPI | 99-170 | 133-455 |
| NW SPI | 45-88 | 53-104 |
| NE SPI | 48-133 | 64-149 |
| CW SPI | 48-77 | 60-96 |
| CE SPI | 48-64 | 60-80 |
| SW SPI | 46-57 | 62-76 |
| SE SPI | 65-74 | 86-94 |

6.3.4 Annual time series and trends in accumulation, melt and sublimation

Annual time series of the components of the SMB are given in Figure 6.4. We found that the variance of the annual SMB depends largely on the ablation (R^2 0.88 and 0.94 for the NPI and SPI respectively) rather than accumulation (R^2 of 0.57 and 0.73).

Almost all the components in each scenario and during the historical period show trends that lead to negative SMB in the NPI and lower, but still positive, SMB in the SPI (Figure 6.2). Surface accumulation in the NPI (Figure 6.4a) showed an overall decrease for the historical period and both scenarios, being marginally statistically significant ($p < 0.05$) in the RCP8.5 scenario. SPI accumulation (Figure 6.4b) showed a slight decrease during the historical period and RCP8.5 scenario and a slight increase for RCP2.6. Previous estimations of the snow accumulation trend for both Icefields also showed a non-significant change at annual scale for the period 1980-2015; however a significant increase in snow accumulation during the autumn season was found for the same period¹⁹.

In the case of surface melt, an overall increase was determined over the historical period and both scenarios and for both Icefields. The projected melt increase was statistically significant ($p < 0.05$) during the historical period in NPI (Figure 6.4c) and for scenario RCP8.5 in both Icefields. The magnitude of the change was larger in the NPI compared to SPI (Figure 6.4d). Increased surface melt was projected for the hydrological year 2043/44, reaching 12 m w.e. in NPI and 9 m w.e. in SPI. When excluding this large value, the trends were still significant at 0.008 m w.e. yr^{-1} . Finally, sublimation showed an increase during the historical period and then plateaus during both future scenarios for both Icefields, although its contribution to overall ablation remained small.

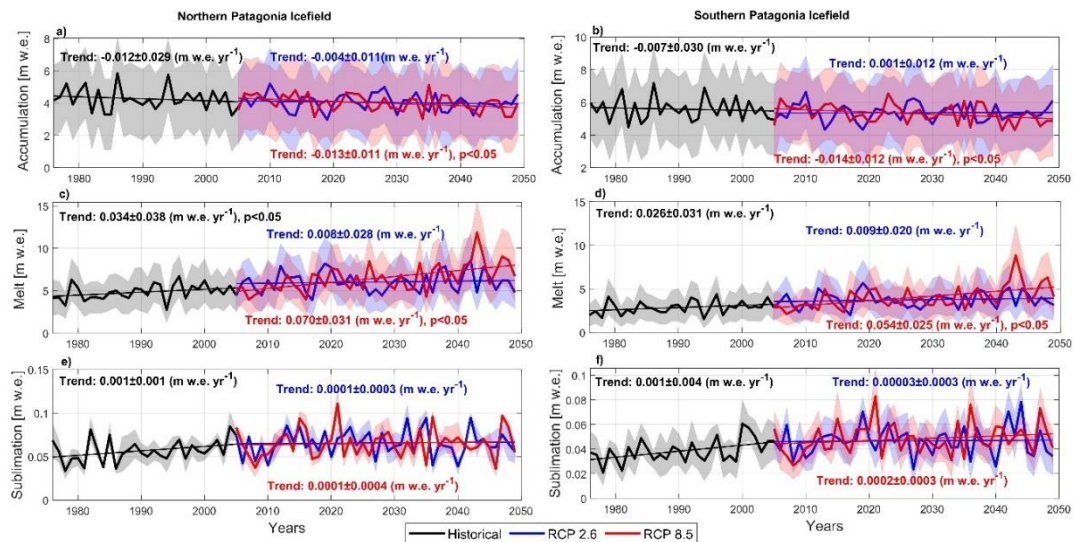


Figure 6.4 Annual values (hydrological years 1976/77-2049/50) and linear trends of the SMB components in m w.e. in NPI and SPI for the historical period and the two pathway scenarios. (a),(c) and (e) are accumulation, melt and sublimation in the NPI and (b),(d) and (f) are accumulation, melt and sublimation in the SPI. Trends with the 95% confidence interval are shown. Significant trends are also indicated when $p < 0.05$. Trends in melt for RCP2.6 are significant where estimated between 1976 and 2050, reaching 0.027 ± 0.012 m w.e. in NPI and 0.0204 ± 0.009 m w.e. in SPI.

6.3.5 Ice loss and contribution to sea-level rise

In this section, we estimate the ice loss and the contribution to sea-level rise to year 2050 for both Patagonian Icefields. We make a key assumption that future rates of frontal ablation will be unchanged from those estimated during past and present conditions, masking the interannual variability as has been estimated, for instance, in Jorge Montt Glacier³¹. We calculate these frontal ablation rates by differencing our modelled SMB and previously published geodetic mass balances. For the NPI, we derive a frontal ablation contribution of $0.2 \text{ m w.e. yr}^{-1}$ (Supplementary Table 6.1); for the SPI the mean difference was $3.28 \text{ m w.e. yr}^{-1}$ (Supplementary Table 6.2). This latter value is equivalent to a volume of $48.2 \text{ km}^3 \text{ yr}^{-1}$ of ice, which is larger than the 44.4 km^3 estimated between 1975 and 2000 but lower than the $61.3 \text{ km}^3 \text{ yr}^{-1}$ obtained between 2000 and 2011 for the SPI²⁵.

Estimation of total ice mass loss between 2012 and 2050 and total sea-level rise equivalent to year 2050 are shown in Figure 6.5. Both Icefields shown a clear ice loss trend, meaning that the climate conditions reflected in the positive SMB in the SPI are not enough to balance the loss by frontal ablation. Between 2012 and 2030 the greatest reduction in SMB is associated with the RCP2.6 scenario, after which the largest ice retreat is projected by RCP8.5, particularly after 2040. RCP8.5 results agree well with those of Abdel-Jaber

et al.¹² and Foresta et al.⁹ (Figure 6.5) between 2012 and 2016, particularly so in the NPI where frontal ablation (and specifically calving) plays only a minor role. Our ice loss estimations are in the lower range of those made by the GlacierMIP initiative⁴³ (Figure 6.5), but it is worth noting that their results incorporate the entire Southern Andes, and (with the exception of one model), neglect frontal ablation mechanisms entirely.

The total equivalent sea-level rise estimated here for both Icefields, accumulated to 2050 (Figure 6.5b) reaches 3.1 mm (RCP2.6) and 3.8 mm (RCP8.5). Within this, the SPI contributes the largest part with 2.3 and 2.8 mm, respectively. The uncertainty, however, is large mainly due to the lack of knowledge in define the actual range of the snow accumulation rate, which we introduce in our SMB modelling (Figures 6.4a and 6.4b).

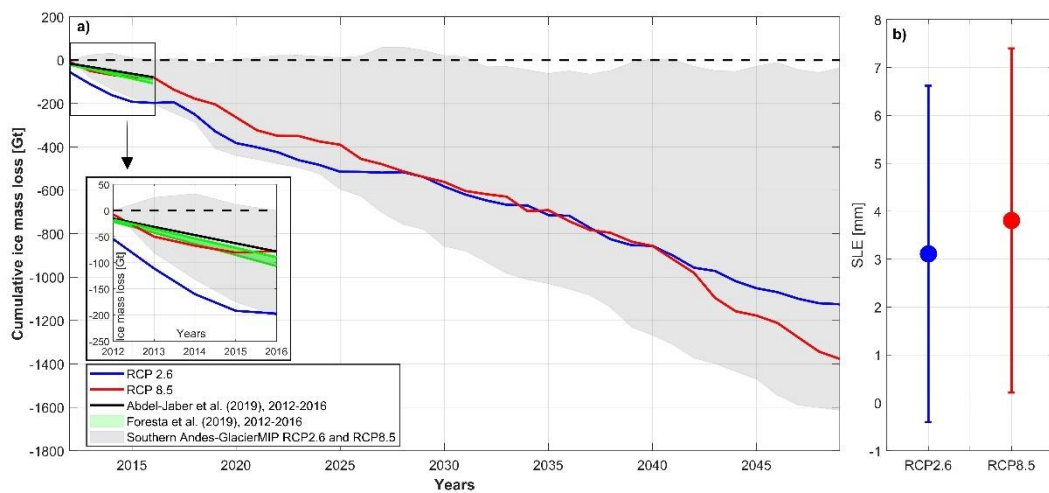


Figure 6.5 Cumulative ice loss estimated for both Icefields combined between 2012 and 2050 (a) and total equivalent sea-level contribution to year 2050 (b). For comparison purposes, data from GlacierMIP⁴³ is showed (grey area). GlacierMIP ice mass loss corresponds to all the models runs under scenarios RCP2.6 and 8.5 computed for the Southern Andes RGI region. Ice mass loss estimations by Abdel-Jaber et al.¹² and Foresta et al.⁹ for the four first years (2012-2016) are also shown. Inset, corresponds to a detailed view of this period.

6.4 Discussion

The results of our modelling showed that an increase in surface melt is the main driver that leads to negative SMB in the NPI and lower positive SMB in the SPI and a rise in the ELA throughout both Icefields. These changes are in agreement with a projected warming in the region (Supplementary Figure 6.1) and align with previous observations of the high sensitivity of Patagonian glaciers to ablation and air temperature variations¹⁴.

These changes will lead to a continuation or acceleration of the impacts associated with glacier shrinkage as has been observed in recent decades in the region, and also to an increase in the contribution to sea-level rise. Other than the positive SMB that is projected for the SPI, a rise in ELA was projected for the NPI. The extent to which this impacts on glacier length depends on several factors, including hypsometry⁴¹ and bed slope⁴⁴. Previous work has shown that glaciers with a lower bed slope (e.g. the Upsala Glacier, SPI, and San Quintin Glacier, NPI) could retreat between 50 to 60 m per each m of ELA rise⁴⁴. This means that even without accounting for dynamic changes and mass loss via calving, some glaciers could retreat between 4 and 5 km within the next 30 years. It should be noted, however, that the projected rise in ELA in areas of the SPI could occur under positive mass balance, meaning that glacier retreat in these zones solely associated with climate forcing will not occur.

Potential glacier retreat will introduce new changes in the landscape. For instance, subglacial topography estimates suggest that pro-glacial lakes will likely form in several new areas of both the SPI and NPI⁴⁵. These changes will in turn affect calving rates and subsequently glacier dynamics, making the prediction of future glacier evolution very complex²³. Our estimation in this sense is, therefore, best considered first order. Indeed, it is possible that in some areas frontal ablation rates could reduce as the glaciers thin, or even retreat out of their lacustrine environments and onto land²³. This scenario has already been proposed for the future evolution of Jorge Montt Glacier in the SPI; if the ongoing retreat continues, the glacier front will stabilise above the fjord level, reducing frontal ablation overall³¹.

Evidence found in the Patagonian Icefields, however, seems to suggest further positive feedbacks related to increases in surface melt, and associated dynamic adjustments in calving glaciers³² and the appearance of supraglacial melt ponds¹⁷, which would serve to increase the local surface albedo. Several studies^{32,38} have evidenced acceleration of glaciers in response to an increase of the basal sliding due to an input of meltwater percolating to the base. The temperate conditions of the ablation zones of Patagonian glaciers means that refreezing would be minimal, and the subglacial hydrological network will likely play an important role in determining future dynamic behaviour.

Since glacier dynamics are closely connected to the climate conditions that define the input of meltwater to the system^{32,33}, a qualitative projection and assessment of glacier response is possible with our results. The areas with greatest projected positive trends in surface melt, in addition to a strong

thinning due to surface processes, are most likely to be affected by ice acceleration and increases in the calving flux²⁷ and frontal ablation³³. These areas are primarily located in the NE of the NPI (e.g. Steffen Glacier), along the western margin of the SPI (Occidental, Témpano, HPS-29 glaciers) and in the south of the SPI (Tyndall, HPS-38 glaciers) (Figure 6.6). To a lesser extent, a future increase in surface melt was also estimated for the Upsala and Viedma glaciers in the SPI and San Quintin Glacier in the NPI (Figure 6.6). In accordance with our results, most of these Patagonian glaciers are already thinning rapidly^{7-9,12}. The only exception is Jorge Montt Glacier, located in the SPI. Here, along with other factors, glacier melt is also forced by warm water entering the fjord⁴⁶, explaining the strong retreat³¹ that is not suggested in our modelled increase in surface melt (Figure 6.6).

In terms of projected sea-level contribution, the annual rates projected for both Icefields are larger than those previously estimated from the LIA and most of the 20th century. For the 38 years period between 2012 and 2050, we estimated a mean annual rate of both scenarios of 0.067 mm yr⁻¹ for the SPI and 0.024 mm yr⁻¹ for the NPI, which in total represent 0.091 mm yr⁻¹ for both Icefields. These rates are larger than those estimated by Glasser et al.¹³ who estimated 0.0018 mm yr⁻¹ between 1870 and 2010 in NPI and 0.005 mm yr⁻¹ between 1750 and 2010 in SPI. Between 1945 and 1996⁴⁷, the contribution of both Icefields was estimated to be 0.032 mm yr⁻¹ and between 1968/75-2000³ it was estimated as 0.042 mm yr⁻¹. The rate of ice loss during most of the 20th century is one order of magnitude higher than in previous centuries¹³. Additionally, in the last six years of the 20th century, a new acceleration in ice mass loss was estimated³ reaching a sea-level contribution of 0.105 mm yr⁻¹, while between 2002 and 2006⁴⁸ the sea-level contribution of both Icefields was estimated as 0.078 mm yr⁻¹. Therefore, our projected sea-level contribution suggests that accelerated ice loss estimated for the end of 20th³ and beginning of the 21st⁴⁸ centuries, will continue under both scenarios.

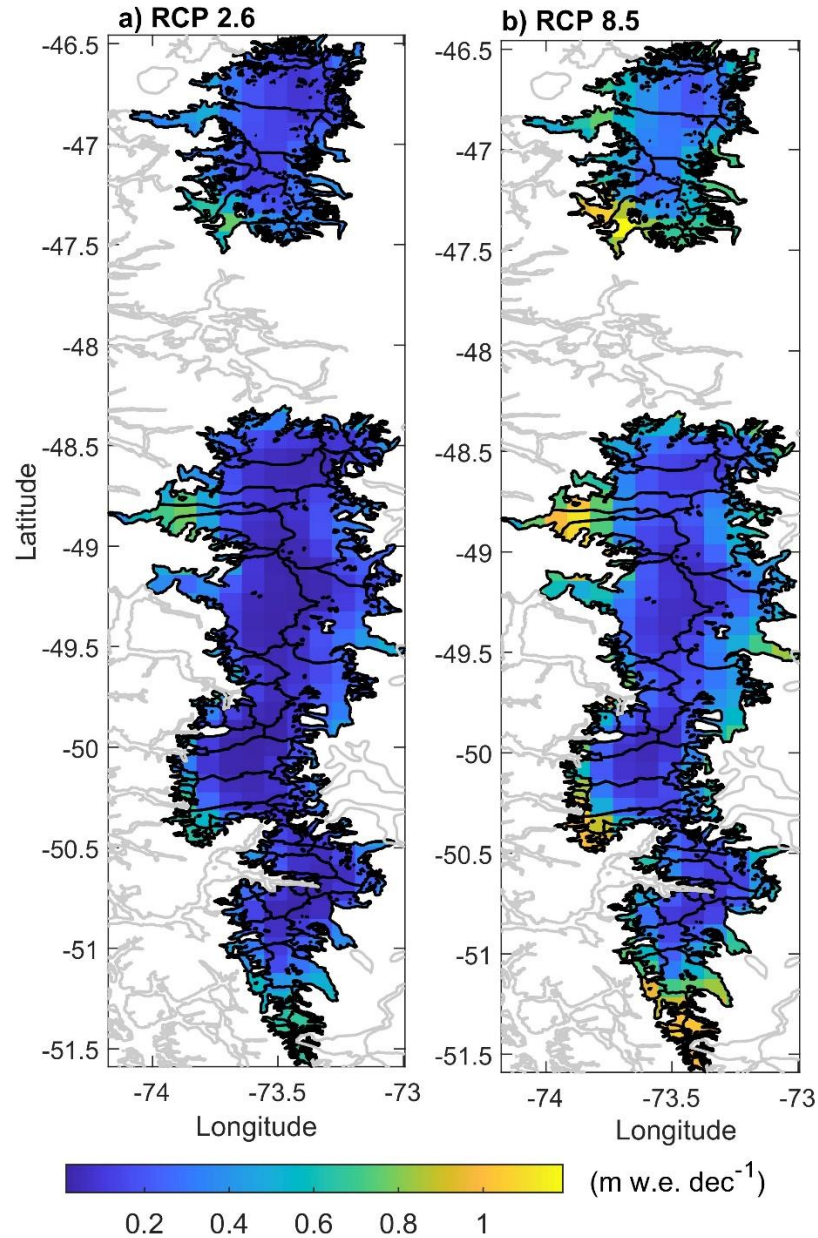


Figure 6.6 Spatially distributed melt trends over the Patagonian Icefields estimated with the EBM. Trends are from hydrological year 1976/77 to 2049/50, following after 2005 the pathway scenario RCP2.6 (a) and the pathway scenario RCP8.5 (b). Black lines are the glacier basins and grey lines are coast lines. All the grid points are significant ($p < 0.05$).

6.5 Conclusions

In this work, we have quantified the present and future SMB for both the NPI and SPI using historical data and two pathway scenarios (RCP2.6 and 8.5) obtained from the RegCM4.6 model. Snow accumulation and ablation using an EBM were estimated, as well as their changes throughout the years. We estimated a reduction in the SMB in both Icefields. For the NPI a reduction between 1.51 and 1.88 m w.e. was projected for the scenarios RCP2.6 and 8.5 respectively, while in SPI the reduction was within the range of 1.12 and

1.45 m w.e. Despite its reduction in the SPI, future SMB was still projected to be positive overall. With the assumption that the annual rate of frontal ablation will remain unchanged, we estimated the contribution of the ice loss of the Patagonian Icefields to sea-level rise between 2012 and 2050, reaching between 3.1 mm (RCP2.6) and 3.8 mm (RCP8.5). Projected ELA rise indicates potential area reductions in the glaciers of the NPI as well as in some areas of the SPI, but limited to those with projected negative surface mass balances such as in the SW and only under the RCP8.5 scenario. The magnitude of ELA rise is spatially variable (between 46 and 455 m) and the impact at each glacier would depend on its topographic characteristics. The trend towards lower SMB overall is explained by an increase in melt and to a lesser extent by a reduction in snow accumulation. The input of infiltrating meltwater could act as a positive feedback, triggering ice-speed acceleration and ice loss due to an increase in frontal ablation of calving glaciers.

Although a complete quantification of future response depends on factors not accounted for by our modelling (e.g. ice dynamics), this knowledge of changes climatic conditions gives new insights into recent trends of ice loss, their controls, and their likely impact on the future response of the Patagonian glaciers, and its variability through space and time.

6.6 Data and methods

6.6.1 RegCM4.6 simulations

Regional Climate Model, version 4 (RegCM4.6) is a primitive equation and limited area model developed by the International Centre for Theoretical Physics⁴⁹. The dynamical core of the RegCM4.6 is based on the hydrostatic version of the Penn State/NCAR mesoscale model MM5⁵⁰. RegCM4.6 was used to downscale lateral boundary conditions derived from MPI-ESM-MR Earth System Model³⁴ on a nested domain centralizing over Chile at 10-km spatial resolution for historical period (1976-2005) and projections (2006-2050) under the RCP2.6 and RCP8.5 scenarios³⁵. This study makes use of daily mean near-surface temperature, total precipitation, wind speed, surface pressure, near-surface relative humidity, incoming shortwave and longwave radiation obtained from the downscaled RegCM4.6 simulations. RegCM4.6 simulations used in the present study are based on the land surface model Biosphere-Atmosphere Transfer Scheme of Dickinson et al.⁵¹ and the radiative scheme of the NCAR Community Climate System Model Version 3 (CCSM3)⁵⁰. More information about the simulations, performance of the RegCM4.6 as well as added value analysis are detailed in Bozkurt et al.³⁵. Bozkurt et al.³⁵ showed that high resolution hindcast simulations (i.e.,

RegCM4.6 forced with reanalysis) robustly simulated the spatiotemporal variability of temperature and precipitation in southern Chile including the Patagonian Icefields, despite some discrepancies such as the overestimation of precipitation extremes. In addition, it was also highlighted that coarse resolution boundary conditions can miss important climate gradients imposed by complex topography in Chile. In this regard, downscaled simulations of RegCM4.6 forced with MPI-ESM-MR were found to exhibit added value for both temperature and precipitation by resolving local-scale features in a large part of Chile, including several grid points in the Patagonian Icefields.

6.6.2 Energy balance modelling

A distributed energy balance model (EBM) was applied using daily data obtained from the RegCM4.6 regional model between 1 April 1976 and 31 March 2050, the Southern hemisphere mid-latitudes hydrological year. The details of the equations are given in Bravo et al.⁵³ and correspond to the bulk method to estimate sensible, latent and rainfall fluxes including stability corrections in the first two fluxes. In addition to the meteorological data obtained from RegCM4.6 (previous section), we estimated additional variables necessary to feed the EBM. These are surface temperature, air and surface vapour pressure, outgoing longwave radiation, surface albedo and surface roughness. The first three variables, were estimated with standard equations and parametrization and using the data from RegCM4.6. Details of these equation and parametrization are given in Bravo et al.⁵³. Outgoing longwave radiation was in turn estimated using the distributed field of the surface temperature and assuming a surface emissivity equal to 1 in the Stefan-Boltzmann law. The surface albedo was estimated following Oerlemans and Knapp⁵⁴. Surface roughness was estimate using the surface albedo values as proxy. Here, albedo values between 0.35 to 0.60 were associated with ice and firn (higher surface roughness) and between 0.60 to 0.80 to different snow ages (lower surface roughness). From the EBM we obtained the melt and the sublimation at daily scale, which is then calculated at annual scale. The use of daily data allows a better representation of the inter-daily variability of the albedo and the impact in the reflected shortwave radiation. In order to quantify the uncertainty in one of the parametrizations, we run two experiments using different magnitude of the glacier cooling effect assuming -1°C and -3°C , respectively. These values were taken from the analysis of air temperature data observed on-glacier and compared with data measured off-glacier at both sides of the SPI¹⁸. Although there are others inherent uncertainties in the modelling that are hard to quantify, such as the

parametrization of the surface roughness, the use of an EBM makes it possible to integrate more meteorological variables than a temperature-index model allowing a more complete evaluation of the impacts of the projected climate change over glaciated areas.

6.6.3 Snow accumulation

We estimated the snow accumulation over the glacier surface following the method of Weidemann et al.²⁸ and Schaefer et al.^{23,25} previously applied at single glaciers and at the Patagonian Icefield scale, respectively. This method showed the best magnitude representation compared with short-term snow accumulation in the SPI¹⁹. However, as the uncertainty in precipitation is high¹⁵ and hence also in the snow accumulation, we quantify the uncertainty based on different methods to estimate the partitioning between rain and snow. These methods are described in full in Bravo et al.¹⁹. The input for these estimations were total precipitation, air temperature and relative humidity to estimate dew point temperature for one of the methods¹⁹. The daily snow accumulation was then used to estimate annual accumulation at each hydrological year.

6.6.4 Ice loss estimation and contribution to sea-level rise

The ice loss and contribution to sea-level rise was estimated using previous area and volume data. For the first case, we assume as initial condition the area estimated for the 2011 year by Davies and Glasser⁵⁵ and the total volume estimated by Millan et al.⁵⁶ which was computed using airborne gravity and radar measurements taken between 2012 and 2016 and complemented with ice thickness, modelled by Carrivick et al.⁴⁵. The areas used were 13219 km² for the SPI and 3976 km² for the NPI. Volumes were 3632 km³ in the SPI and 1124 km³ in the NPI. Using these data we estimated the factors for a bulk volume-area scaling at each Icefield. For glacier area S the volume V was estimated as $V=cS^\gamma$ ⁵⁷. The empirical factor c was estimated, finding that the best adjustment was obtained with c equal to 0.01264 in NPI and 0.007825 in SPI. Exponent parameter γ is constant and its value is 1.375. The main assumption to estimate total ice loss in the future was that the annual rate of frontal ablation in the SPI is equal than present conditions. The rate of present frontal ablation was estimated following Schaefer et al.²⁵ and assumed that the differences between geodetic mass balance and modelled SMB correspond to the frontal ablation. In our case, we estimate a mean of the differences showed in Supplementary Tables 6.1 and 6.2.

Using the initial conditions, the modelled SMB plus frontal ablation (in the case of the SPI) and the volume-area scaling parameters, the volume loss at year time step was estimated (ΔV_y) and is consecutively added to the volume of the previous year (V_y). The new volume, and using the defined parameters (c and γ) in turn is used to estimate the new area for the following year (A_{y+1}), which is then multiplied with the SMB. This relationship take the following form⁵⁷:

$$A_{y+1} = \left(\frac{V_y + \Delta V_y}{c} \right)^{\frac{1}{\gamma}}$$

The volume loss is then adjusted by the area in each time step. Finally, volume is converted to mass using an ice density of 900 kg m^{-3} , and the resulting ice loss (Gt) is converted to sea-level equivalent.

6.7 References

- 1 Bamber, J. L., Westaway, R. M., Marzeion, B. & Wouters, B. The land ice contribution to sea level during the satellite era. *Environ. Res. Lett.* **13**, 063008 (2018).
- 2 Zemp, M. *et al.* Global glacier mass changes and their contributions to sea-level rise from 1961 to 2016. *Nature* **568**, 382–386 (2019).
- 3 Rignot, E., Rivera, A. & Casassa, G. Contribution of the Patagonia Icefields of South America to Sea Level Rise. *Science* **302**(5644), 434-436 (2003).
- 4 Rivera, A., Benham, T., Casassa, G., Bamber, J. & Dowdeswell, J. Ice elevation and areal changes of glaciers from the Northern Patagonia Icefield, Chile. *Global Planet. Change* **59**, 126-137 (2007).
- 5 Willis, M. J., Melkonian, A. K., Pritchard, M. E. & Rivera, A. Ice loss from the Southern Patagonian Ice Field, South America, between 2000 and 2012. *Geophys. Res. Lett.* **39**(17), L17501; 10.1029/2012GL053136 (2012).
- 6 Willis, M. J., Melkonian, A. K., Pritchard, M. E. & Ramage, J. M. Ice loss rates at the Northern Patagonian Ice Field derived using a decade of satellite remote sensing. *Remote Sens. Environ.* **117**, 184–198 (2012).
- 7 Malz, P. *et al.* Elevation and Mass Changes of the Southern Patagonia Icefield Derived from TanDEM-X and SRTM Data. *Remote Sens.* **10**(2), 188 (2018).
- 8 Dussaillant, I., Berthier, E. & Brun, F. Geodetic mass balance of the Northern Patagonian Icefield from 2000 to 2012 using two independent methods. *Front. Earth Sci.* **6**, 8. 10.3389/feart.2018.00008 (2018).

- 9 Foresta, L. *et al.* Heterogeneous and rapid ice loss over the Patagonian Ice Fields revealed by CryoSat-2 swath radar altimetry. *Remote Sens. Environ.* **211**, 441-455 (2018).
- 10 Braun, M. H. *et al.* Constraining glacier elevation and mass changes in South America. *Nat. Clim. Change* **9**, 130–136 (2019).
- 11 Dussailant, I. *et al.* Two decades of glacier mass loss along the Andes. *Nat. Geosci.* **12**, 802–808 (2019).
- 12 Abdel-Jaber, W., Rott, H., Floricioiu, D., Wuite, J. & Miranda, N. Heterogeneous spatial and temporal pattern of surface elevation change and mass balance of the Patagonian ice fields between 2000 and 2016. *Cryosphere* **13**(9), 2511–2535 (2019).
- 13 Glasser, N. F., Harrison, S., Jansson, K. N., Anderson, K. & Cowley A. Global sea-level contribution from the Patagonian Icefields since the Little Ice Age maximum. *Nature Geosci.* **4**, 303–307 (2011).
- 14 Sagredo, E. & Lowell, T. Climatology of Andean glaciers: A framework to understand glacier response to climate change. *Global Planet. Change* **86–87**, 101–109 (2012).
- 15 Sauter, T. Revisiting extreme precipitation amounts over southern South America and implications for the Patagonian Icefields. *Hydrol. Earth Syst. Sci.*, **24**, 2003–2016 (2020).
- 16 Garreaud, R., Lopez, P., Minvielle, M. & Rojas, M. Large-Scale control on the Patagonian Climate. *J. Clim.* **26**(1), 215–230 (2013).
- 17 Lo Vecchio, A., Lannutti, E., Lenzano, M. G., Mikkan, R., Vacafior, P. & Lenzano, L. MODIS Image-derived ice surface temperature assessment in the Southern Patagonian Icefield. *Prog. Phys. Geogr.* **43**(6), 754-776 (2019).
- 18 Bravo, C. *et al.* Air temperature characteristics, distribution and impact on modeled ablation for the South Patagonia Icefield. *J. Geophys. Res. Atmos.* **124**(2), 907–925 (2019).
- 19 Bravo, C. *et al.* Assessing snow accumulation patterns and changes on the Patagonian Icefields. *Front. Environ. Sci.* **7**, 30; 10.3389/fenvs.2019.00030 (2019).
- 20 Temme, F., Turton, J.V., Mölg, T. & Sauter, T. Flow Regimes and Föhn Types Characterize the Local Climate of Southern Patagonia. *Atmosphere* **11**, 899 (2020).

- 21 De Angelis, H., Rau, F. & Skvarca, P. Snow zonation on Hielo Patagónico Sur, southern Patagonia, derived from Landsat 5 TM data. *Global Planet. Change* **59**, 149–158 (2007).
- 22 Monahan, P. & Ramage, J. AMSR-E Melt Patterns on the Southern Patagonian Icefield. *J. Glaciol.* **56**(198), 699-708 (2010).
- 23 Schaefer, M., Machguth, H., Falvey, M. & Casassa, G. (2013). Modeling past and future surface mass balance of the Northern Patagonian Icefield. *J. Geophys. Res. Earth* **118**, 571–588. (2013).
- 24 Lenaerts, J. T. M. *et al.* Extreme Precipitations and Climate Gradients in Patagonia Revealed by High-Resolution Regional Atmospheric Climate Modeling. *J. Climate* **27**(12), 4607-4621 (2014).
- 25 Schaefer, M., Machguth, H., Falvey, M., Casassa, G. & Rignot, E. Quantifying mass balance processes on the Southern Patagonia Icefield. *Cryosphere* **9**(1), 25–35 (2015).
- 26 Mernild, S. H., Liston, G. E., Hiemstra, C. A. & Wilson, R. The Andes Cordillera Part III: Glacier Surface Mass Balance and Contribution to Sea Level Rise (1979–2014). *Int. J. Climatol.* **37**(7), 3154–317 (2016).
- 27 Muto, M. & Furuya, M. Surface velocities and ice-front positions of eight major glaciers in the southern Patagonian ice field, South America, from 2002 to 2011. *Remote Sens. Environ.* **139**, 50–59 (2013).
- 28 Weidemann, S.S. *et al.* Glacier mass changes of lake-terminating Grey and Tyndall glaciers at the Southern Patagonia Icefield derived from geodetic observations and energy and mass balance modeling. *Front. Earth Sci.* **6**, 81 10.3389/feart2018.00081 (2018).
- 29 Schaefer, M., Fonseca, D., Farias-Barahona, D. & Casassa, G. Surface energy fluxes on Chilean glaciers: measurements and models. *Cryosphere* **14**, 2545–2565 (2020).
- 30 Warren, C.R. & Sugden, D.E. The Patagonian Icefields: a Glaciological Review. *Arct. Alp. Res.* **25**(4), 316–331 (1993).
- 31 Bown, F. *et al.* Recent ice dynamics and mass balance of Jorge Montt Glacier, Southern Patagonia Icefield. *J. Glaciol.* **65**(253), 732-744 (2019).
- 32 Sugiyama, S., *et al.* Ice speed of a calving glacier modulated by small fluctuations in basal water pressure. *Nat. Geosci.* **4**, 597–600 (2011).
- 33 Minowa, M., Sugiyama, S., Sakakibara, D. & Skvarca, P. Seasonal Variations in Ice-Front Position Controlled by Frontal Ablation at Glaciar Perito

Moreno, the Southern Patagonia Icefield. *Front. Earth Sci.* **5**, 1. 10.3389/feart.2017.00001 (2017).

34 Giorgetta, M. A., *et al.* Climate and carbon cycle changes from 1850 to 2100 in MPI-ESM simulations for the Coupled Model Intercomparison Project phase 5. *J. Adv. Model Earth Syst.* **5**(3), 572–597 (2013).

35 Bozkurt, D. *et al.* Dynamical downscaling over the complex terrain of southwest South America: present climate conditions and added value analysis. *Clim. Dyn.* **53**, 6745-6767 (2019).

36 Schwalm, C. R. , Glendon, S., & Duffy, P. B. RCP8.5 tracks cumulative CO2 emissions. *Proc. Natl. Acad. Sci. U.S.A.* **117**, 19656–19657 (2020)

37 Sanderson B., Tebaldi, C., & O'Neill, B. What would it take to achieve the Paris temperature targets? *Geophys. Res. Lett.* **43**, 7133–7142 (2016).

38 Collao-Barrios, G., Gilliet-Chaulet, F., Favier, V., Casassa, G., & Berthier, E. Ice flow modelling to constrain the surface mass balance and ice discharge of San Rafael Glacier, Northern Patagonia Icefield. *J. Glaciol.* **64** (246), 568–582 (2018).

39 Aniya, M. Glacier Inventory for the Northern Patagonia Icefield, Chile, and Variations 1944/45 to 1985/86. *Arct. Alp. Res.* **20**, 179–187 (1988).

40 Barcaza, G., Aniya, M., Matsumoto, T., & Aoki, T. Satellite-derived equilibrium lines in Northern Patagonia Icefield, Chile, and their implications to glacier variations. *Arct. Antarct. Alp. Res.* **41**, 174–182 (2009).

41 De Angelis, H. Hypsometry and sensitivity of the mass balance to change in equilibrium-line altitude: the case of the Southern Patagonia Icefield. *J. Glaciol.* **60**(219), 14–28 (2014).

42 Schneider, C., Kilian, R. & Glaser, M. Energy balance in the ablation zone during the summer season at the Gran Campo Nevado Ice Cap in the Southern Andes. *Global Planet. Change* **59**, 175–188 (2007).

43 Hock, R. *et al.* GlacierMIP – A model intercomparison of global-scale glacier mass-balance models and projections. *J. Glaciol.* **65**(251), 453–467 (2019).

44 Oerlemans, J. Linear modeling of glacier fluctuations. *Geografiska Ann. Ser. A Phys. Geography* **94**(2), 183-194 (2012).

45 Carrivick, J. L., Davies, B. J., James, W. H. M., Quincey, D. J. & Glasser, N.F. Distributed ice thickness and glacier volume in southern South America. *Global Planet. Change* **146**, 122-132 (2016)

- 46 Moffat, C. *et al.* Seasonal evolution of ocean heat supply and freshwater discharge from a rapidly retreating tidewater glacier: Jorge Montt, Patagonia. *J. Geophys. Res. Oceans* **123**, 4200–4223 (2018).
- 47 Rivera, A. Acuna, C., Casassa, G. & Bown, F. Use of remotely sensed and field data to estimate the contribution of Chilean glaciers to eustatic sea-level rise. *Ann. Glaciol.* **34**, 367-372 (2002).
- 48 Chen, J. L., Wilson, C. R., Tapley, B. D., Blankenship, D. D. & Ivins, E. R.. Patagonia Icefield melting observed by Gravity Recovery and Climate Experiment (GRACE). *Geophys. Res. Lett.* **34**, L22501 (2007).
- 49 Giorgi, F. *et al.* RegCM4: Model description and preliminary tests over multiple CORDEX domains. *Clim. Res.* **52**, 7–29 (2012).
- 50 Grell, G. A., Dudhia, J., & Stauffer, D. R. Description of the fifth generation Penn State/NCAR Mesoscale Model (MM5) (NCAR Tech. Note NCAR/TN-398+STR). Boulder, CO: NCAR (1994).
- 51 Dickinson, R. E., Henderson-Sellers, A., & Kennedy, P. J. Biosphere-Atmosphere Transfer Scheme (BATS) Version 1e as Coupled to the NCAR Community Climate Model. NCAR Tech. Note NCAR/TN-387+STR, NCAR, Boulder (1993).
- 52 Kiehl, J. T. *et al.* Description of the NCAR Community Climate Model (CCM3) (NCAR Tech. Note NCAR/TN-420+STR). Boulder, CO: NCAR (1996).
- 53 Bravo, C., Ross, A.N., Quincey, D. J., Cisternas, S. & Rivera, A. (In preparation). Drivers of surface ablation on the Southern Patagonia Icefield.
- 54 Oerlemans, J. & Knap, W. H. A one-year record of global radiation and albedo from the ablation zone of the Morteratschgletscher, Switzerland. *J. Glaciol.* **44**(147), 231-238 (1998).
- 55 Davies, B.J. & Glasser, N.F. Accelerating shrinkage of Patagonian glaciers from the Little Ice Age (~AD 1870) to 2011. *J. Glaciol.* **58**(212), 1063–1084 (2012).
- 56 Millan, R. *et al.* Ice thickness and bed elevation of the Northern and Southern Patagonian Icefields. *Geophys. Res. Lett.* **46**(12), 6626-6635 (2019).
- 57 Moller, M. & Schneider, C. Calibration of glacier volume–area relations from surface extent fluctuations and application to future glacier change. *J. Glaciol.* **56**(195), 33–40 (2010).

Chapter 7

Discussion and Conclusions

Using nine months of meteorological observations, gridded-climate products and glacier modelling in a multi-scale approach, this thesis was focused to answer two main research questions. First, do the glaciers located on either side of the Icefields show different sensitivities and surface mass balance controls due to different meteorological conditions? and secondly, how are these glaciers responding to ongoing climate change and how differently will these glaciers respond to climate change scenarios? To answer these questions and to achieve the main aim of this work, the thesis was structured following four objectives (section 1.4). The following sections comprise an integrated discussion of the key findings presented in each of the earlier chapters, concentrating on the spatial differences found in terms of meteorological and glaciological conditions and their implications in terms of past, present and future surface mass balance modelling. Results obtained for the glaciers of the northern sector of the SPI are also discussed within the context of the Icefield scale analyses and compared with the results of previous studies.

7.1 West-east ablation spatial differences

For the glaciers in the northern SPI, large differences were found in the rates of ablation, being notably high on the glaciers of the western margin compared to the glaciers of the eastern margin. The glacier-wide differences reached ~6 m w.e. in both the short-term (9 months) and the long-term (1982-2019) ablation estimations. This figure qualitatively agrees with ice mass loss differences detected by geodetic methods for the glaciers of the northern part of the SPI (Table 1.4).

At the local-scale, and at comparable elevations, the west-east difference in melt is reduced to a mean difference of 0.7 m w.e. with the largest differences being detected between 800 and 1600 m a.s.l. (Figure 7.1a). Sublimation also shows spatial differences, reaching larger values at higher elevations on the west and lower elevations on the east (Figure 7.1b).

These differences correspond to the meteorological conditions that prevail on each side of the Icefield divide. Figure 7.2 schematically represents the differences between the west and east showing the mean values of key meteorological variables, energy balance fluxes and ablation components for every 100 m elevation bin. As a primary control, these spatial differences are strongly related to the orographic effect as a consequence of the interaction

between the Andes and the predominant westerly winds at these latitudes, defining both wind speed and humidity which in turn define the air temperature lapse rate and the magnitude of the glacier cooling effect.

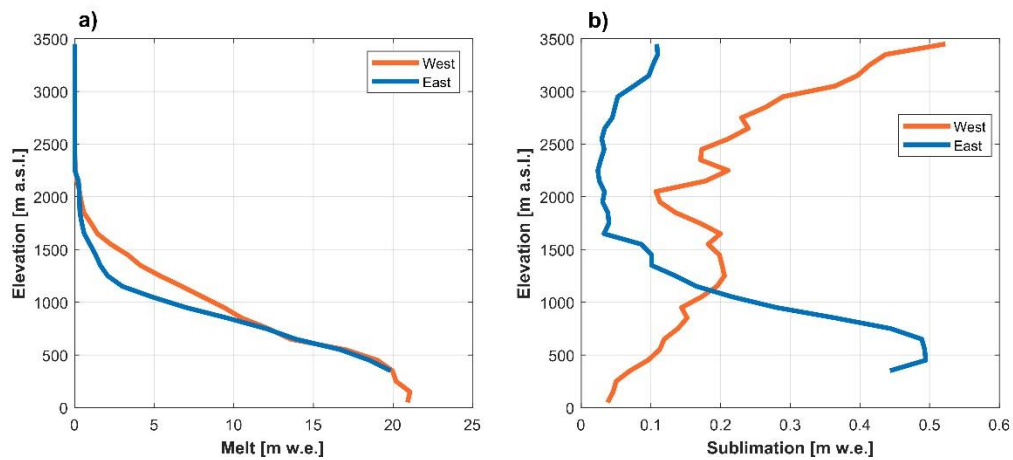


Figure 7.1 Profile of the mean melt (a) and sublimation (b) per 100 m elevation bin, obtained for the northern glaciers of the SPI during the period between October 2015 and June 2016.

Chapter 3 demonstrated that air temperatures decrease at a steeper lapse rate (LR) on the east side compared to the west side of the topographic divide (Figure 7.2). Additionally, the eastern on-glacier data suggest a strong glacier cooling effect. The comparison of the mean melt calculated with degree-day modelling showed that the west side responded faster to a change in air temperature compared to the east (Figure 7.3). As the glacier cooling effect is higher on the east and the LRs are steeper, it is expected that these glaciers are less sensitive to air temperature compared to the west. In accordance, Sagredo et al. (2014) found that glacier equilibrium-line altitude sensitivity to temperature will often be lower in drier regions than in humid regions. This could suggest a relatively lower climate-sensitivity of the eastern side glaciers in NPI and SPI. Indeed, the rates of surface elevation thinning and area loss observed in the study area were overall greater for the west side glaciers (Table 1.4; e.g. Malz et al., 2017; White & Copland, 2015; Willis et al., 2012).

Nevertheless, this spatial pattern is not observed along the whole SPI, indicating that several factors (climatic and non-climatic) play a role in the ice mass changes. At the regional scale, however, Falaschi et al. (2016) found that glaciers situated on the eastern side of the Andes, but outside the greater Icefield extent, showed lower negative mass balance than previously reported for those glaciers situated within the Icefields. The relative dryness that characterizes eastern Patagonia, could therefore help to explain this regional difference, assuming that a similar forcing in the air temperature increase was detected in Patagonia (e.g. Braun et al., 2019).

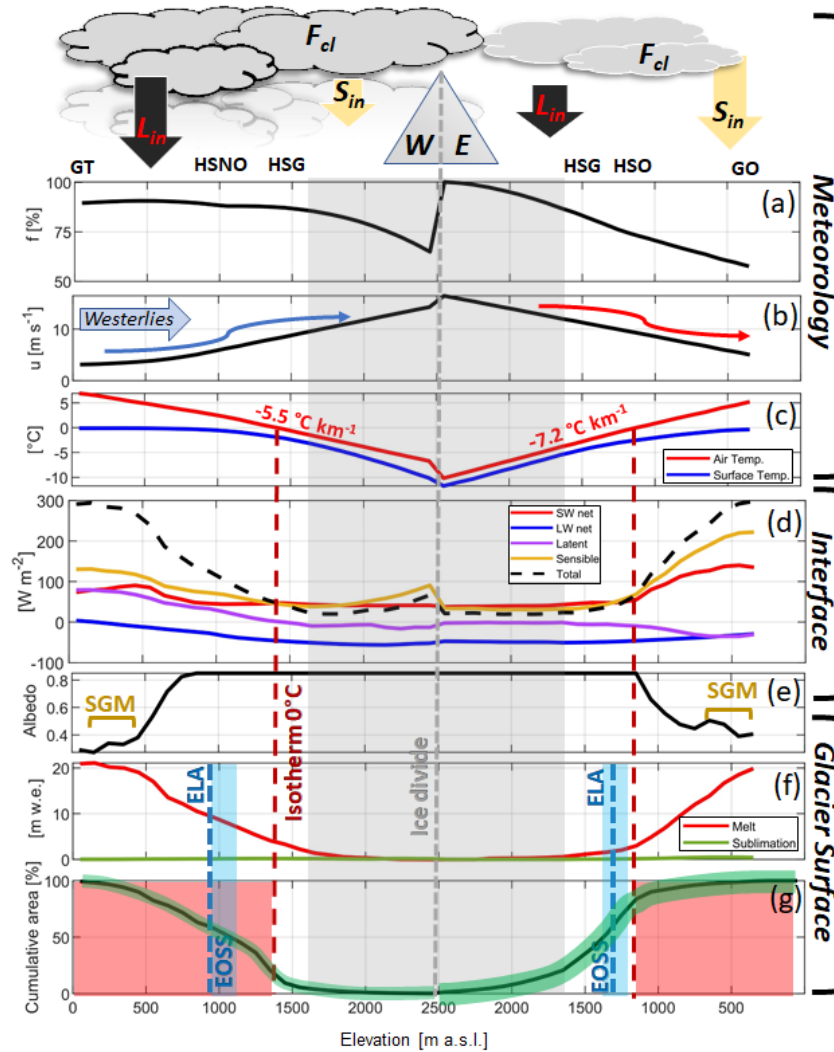


Figure 7.2 Semi-quantitative schematic representation of the meteorological and glaciological conditions along the west-east transect on the northern SPI during the period between October 2015 and June 2016. Mean values were obtained per 100 m elevation bin, for the northern glaciers of the SPI. Panel (a) shows the relative humidity and the location of the AWS. Panel (b) shows the wind speed. Arrows represent the predominant observed wind direction. Panel (c) is the surface and air temperature. Mean air temperature lapse rates at each margin are indicated. Panel (d) shows the energy fluxes obtained with the energy balance modelling. Panel (e) is the modelled albedo. SGM corresponds to the surface area where the supra-glacial moraine influence albedo. Panel (f) is the melt and sublimation. Panel (g) is the hypsometry, showing the accumulated area versus elevation. The red area corresponds to the zone under predominant melt and the green area is a qualitative representation of the glacier cooling effect. EOSS corresponds to the end-of-summer snowline observed with a satellite image acquired on 12th March 2016 and the ELA is the mean value of several previous studies. The grey area corresponds to those elevations of the Icefields where the meteorological variables were extrapolated based on the lower elevations observations.

Of course, ablation depends on more than just air temperature (Figure 7.2). In the process of spatially distributing the meteorological variables needed for the energy balance, other fluxes were also found to be spatially variable. In this respect, cloud cover has an important role to play, particularly at the point-scale. When considered at the glacier-scale, however, net shortwave radiation values were similar between both sides (Figure 5.5), as a consequence of the darker surface appearance (and low albedo) of ice surfaces in the west (Figure 7.2).

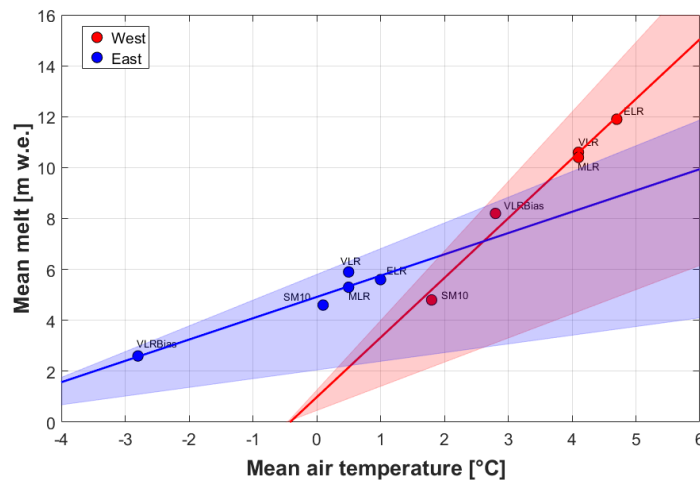


Figure 7.3 Comparison between glacier-wide mean air temperature and glacier-wide mean melt using a Distributed-Degree Day model. Each point represents the mean values for ELR, MLR, VLR, VLRBias and SM10 (Chapter 3) and the lines the regression using a Degree-Day Factor (DDF) of $8.5 \text{ mm w.e. } ^\circ\text{C}^{-1} \text{ d}^{-1}$. Shadow area represents the boundary of the linear regression of the melt using a DDF between $10 \text{ mm w.e. } ^\circ\text{C}^{-1} \text{ d}^{-1}$ (upper limit) and $3.5 \text{ mm w.e. } ^\circ\text{C}^{-1} \text{ d}^{-1}$ (lower limit).

The spatial differences in humidity and wind speed also determine the turbulent fluxes. Sensible heat flux represents a high percentage of the energy available for melt and one of the main controls is the wind speed. Interestingly, strong winds at the higher elevations facing the synoptic westerlies cause maxima in sensible heat flux above 2500 m a.s.l. (Figure 5.6), while relatively strong winds due to föhn and/or katabatic events cause a maxima of sensible heat flux below 1000 m a.s.l. on the eastern side. In terms of ablation, the control of strong winds is more important on the eastern side considering the larger area influenced by these winds (Figure 7.2). Additionally, air temperature in the high western elevations is constantly below 0°C , meaning that the energy available to warm the surface is minimal and no melt occurs. However, under certain atmospheric conditions, e.g. temperature inversion,

and as has been observed elsewhere (Table 3.2 and Supplementary Figure 3.2), melt events can occur at elevations over 2000 m a.s.l.

After calculating the energy balance fluxes, it was found that melt was strong and comprised the main component of ablation on both sides, but the drivers of the melt showed spatial differences between west and east as well as at different elevations (Figure 7.2). This means that the similar melt rates at comparative elevations between west and east were for a different balance in the energy fluxes.

As stated, the finding that at same elevations the mean ablation is 0.7 m w.e. higher in the west compared to the east, with a maximum of 3.7 m w.e. between 1100 and 1200 m a.s.l. (Figure 7.1), indicates that glaciers in the west are more sensitive than those in the east to the same forcing. However, at the scale of the Icefields, this expected west-east spatial difference is not evident in the geodetically-derived elevation changes (dh/dt) presented by previous studies (e.g. Abdel-Jaber et al., 2019; Malz et al., 2018). If a simple comparison of the elevation change rate (e.g. Abdel-Jaber et al., 2019) and the accumulation-area ratio (AAR) (e.g. Rivera et al., 2007; De Angelis, 2014) of the main glaciers is conducted, it can be seen that for the same AAR, western-facing glaciers tend to show higher thinning than eastern-facing glaciers (Figure 7.4). The relationship is of course clearer in the NPI than in the SPI given that frontal ablation plays a more significant role in the total ablation of the SPI (Schaefer et al., 2015). The surface mass balance of historical times (modelled in Chapter 6) showed that the values obtained for the NPI were close to those estimated by the geodetic method, indicating a relatively stronger climate signal in this Icefield compared to the SPI.

At the glacier-scale, the magnitude of ablation is largely controlled by the hypsometry. Local differences in melt are amplified by the characteristics of the AAR as shown by the linear relationship in Figure 7.4. O'Higgins and Chico glaciers (to the east) have AARs of 0.84 and 0.67 respectively, while for Témpano, Occidental and Greve glaciers (to the west) it is 0.69, 0.26 and 0.75, respectively (De Angelis, 2014). Considering the areas, this implies that ~200 km² of ice on the east side is exposed to strong melt rates (>10 m w.e.) while in the west this area is ~385 km². The overall areas of these glaciers are comparable as glacier area on both sides of the divide totals around 1000 km².

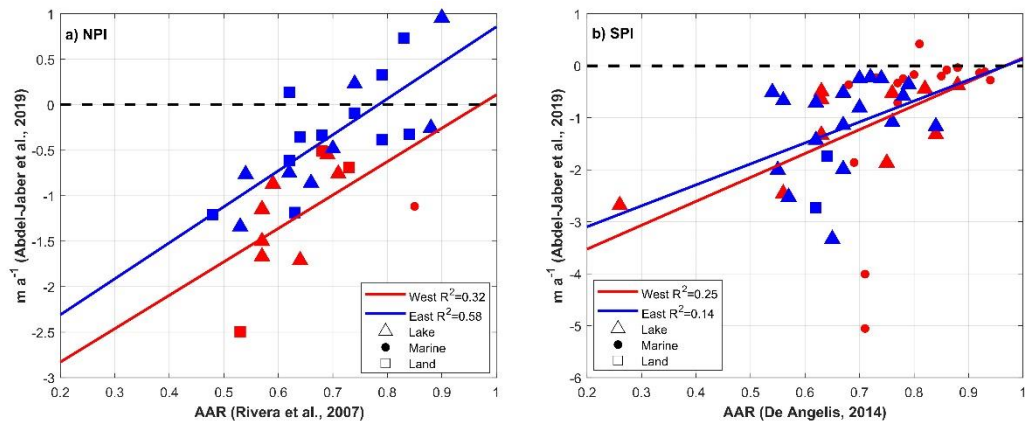


Figure 7.4 Relationship between geodetic mass balance and AAR for glaciers in the NPI (a) and in the SPI (b). Symbols indicated the front characteristic of each glacier. Glaciers of the western side of the NPI are Acodado, Andree, Benito, Fraenkel, Gualas, HPN1, Reichert, San Quintin, San Rafael, Strindberg and Steffen. Glaciers of the eastern side of the NPI are Arco, Cachet, Cachet Norte, Colonia, Cristal, Fiero, Hyades, Leones, Mocho, Nef, Soler, U-4, U-5, U-6, U-7, Exploradores, Grosse, Pared Norte and Pared Sur. Glaciers of the western side of the SPI are Amalia, Asia, Bernardo, Calvo, Europa, Greve, Guilardi HPS8, HPS9, HPS10, HPS12, HPS13, HPS15, HPS19, HPS28, HPS29, HPS31, HPS34, HPS38, HPS41, Jorge Montt, Occidental, Ofhidro, Penguin, Pio XI and Témpano. Glaciers of the eastern side of the SPI are Agassiz, Ameghino, Balmaceda, Bravo, Chico, Frias, Grey, Dickson, Lucia, Mayo, Mellizo Sur, O’Higgins, Onelli, Oriental, Pascua, Perito Moreno, Pingo, Spegazzini, Tyndall, Upsala and Viedma.

Invoking the AAR as a control of glacier-wide ablation rates also seems to offer an explanation for other glaciers where the ice mass changes were negative. Assuming the EB fluxes present at Viedma and Upsala glaciers, both of which are lake-terminating and located 60-100 km to the south, are similar to those on the eastern side of our study area, there is a clear disparity between the rates of ice loss reported in the literature for those southern glaciers when compared to those reported in the present study (Foresta et al., 2018; Malz et al., 2018; Abdel-Jaber et al., 2019; Braun et al., 2019; Dusallant et al., 2019). Part of this difference could well be associated with hypsometry characteristics, as O’Higgins glacier has an AAR of 0.84, while in Viedma and Upsala it is 0.67 and 0.65, respectively (De Angelis, 2014). Therefore, a greater area is consistently being exposed to strong melt in the latter two glaciers.

7.2 West-east accumulation spatial differences

To analyse the approach for estimating accumulation, both climate data and short-term field-based observations were used. Although significant advances

have been made in recent years, uncertainty on accumulation patterns in the region is still very high, and a wide range of precipitation and snow accumulation estimations are reported in the literature (Sauter, 2020). Chapter 4 showed that the choice of the precipitation Phase Partitioning Method (PPM) has a significant impact on the derived rate of snow accumulation. Although the short-term accumulation observations showed that some PPMs represent the accumulation quite well, this was a point-scale comparison for just a couple of months. Additionally, the derived rates also depend on the quality of the input data, as differences between the RegCM4.6 and ERA5-Land were also highlighted.

Overall, it was found that the accumulation rate to the west was larger than that to the east. This was observed throughout both Icefields using RegCM4.6 (Chapter 4) and in the northern sector of the SPI using ERA5-Land (Chapter 5 and Figure 7.5). The RegCM4.6 data showed a significantly positive (negative) trend in snow accumulation in the western (eastern) side of the SPI during austral autumn. During the rest of the year, an increase in snow accumulation was detected, but it was not statistically significant. However, the highest annual increase in snow accumulation was concentrated on the western side, south of 49°S. For glaciers at this latitude, the geodetic mass balance showed stable and even positive elevation change. The impact of the snow accumulation, however, seems to depend also on the AAR. Those glaciers with an AAR above 0.8 and an increase in snow accumulation seem to counter-balance the mass loss due to regional warming (e.g. Braun et al., 2019). Perhaps the clearest example of this relates to Pio XI Glacier (AAR = 0.81), which showed positive surface elevation changes in most of its area between 2012 and 2016 (Abdel-Jaber et al., 2019).

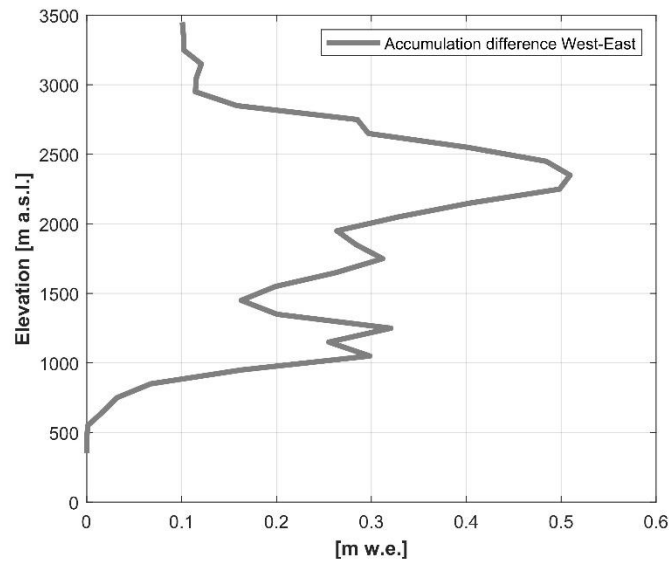


Figure 7.5 Profile of the differences of the total snow accumulation per 100 m elevation bin, obtained for the northern glaciers of the SPI during the period between October 2015 and March 2016 using ERA5-Land reanalysis.

The spatially heterogeneous glacier response that can be observed over both Icefields (Foresta et al., 2018; Abdel-Jaber et al., 2019) could be also associated with the Southern Annual Mode (SAM), especially on the SPI. The SPI is located at the limit of where a positive SAM exerts the opposite influence, i.e. an increase (decrease) of precipitation south (north) of $\sim 50^{\circ}\text{S}$ (Garreaud et al., 2013). It also induces differences in snow accumulation, being significantly positive in autumn over the western side glaciers (Chapter 4). This could explain the predominance of stable elevation changes estimated for glaciers south of 49°S (e.g. maps of Foresta et al., 2018; Abdel-Jaber et al., 2019; Dusallant et al., 2019), especially at the western margin.

7.3 Implications for glacier modelling

Findings related to the meteorological observations have the potential to be used as parameters for glacier modelling in this region and/or to validate and compare different approaches to quantifying mass balance. For instance, the fact that there are differences in the air temperature lapse rates (Chapter 3) between the west and the east side in the northern glaciers of the SPI was accounted for by Abdel-Jaber et al. (2019), who used this information to estimate balance gradients in validating their results.

In general, the spatial distribution of temperatures in Patagonia has been described to be linear with respect to elevation. Distinct air temperature lapse rates, however, have been estimated for the region based upon direct measurements and available temperature records outside the Patagonian

Icefields. For example, at Benito Glacier located on the western side of the North Patagonia Icefield (NPI), Sessions (1975) measured a lapse rate - $0.0050 \text{ }^{\circ}\text{C m}^{-1}$. Peña and Gutiérrez (1992) estimated a slightly higher value of $-0.0053 \text{ }^{\circ}\text{C m}^{-1}$ for Torres del Paine located on the eastern side of the southern SPI. Also on the eastern side of the SPI, Takeuchi et al. (1996) and Stuefer et al. (2007) derived a lapse rate of $-0.0080 \text{ }^{\circ}\text{C m}^{-1}$ at the lower end of Perito Moreno Glacier. All these observations, in addition to the results in Chapter 3, demonstrate the high spatial variability in air temperature, and hence that the use of a single value to distribute air temperature (e.g. Schaefer et al., 2015) does not capture the diverse conditions along the Patagonian Icefields. The use of an appropriate air temperature lapse rate is key in terms of incoming longwave radiation and in the definition of the location of the threshold to define the partitioning between rain and snow.

Spatial variability in glacier cooling is also a key parameter used to model the glacier response. Including this parameter is an important part of physical models, especially for the calculation of turbulent fluxes. Here, spatial differences in the magnitude of the glacier cooling effect were detected, however, these comparisons were at point-scale and more observations are needed. Still, the on-glacier observations, as well as previous remote sensing studies (e.g. De Angelis et al., 2007; Monahan and Ramage, 2010) suggest colder conditions over glaciers to the east when compared to the west. In line with this, surface mass balance modelling outputs (Chapter 6) suggest that for matching previous estimations of equilibrium-line altitude, the cooling effect must indeed be higher on the eastern-facing glaciers.

7.4 Surface mass balance feedbacks

A number of other sources, not accounted for above, are also influencing the response of Patagonian glaciers. In particular, results in Chapter 5 showed that the presence of a continuous supraglacial moraine could increase melt, locally by around 4-5 m w.e., and at glacier-wide scale by between 9-15%. A similar finding was presented by Fukima and Naruse (1987) who used stake measurements to estimate that debris covered areas, from very thin to about 3 cm thick, showed twice the melt rate compared to bare ice areas at the same elevation, on the eastern Soler Glacier in NPI. This will become increasingly relevant at the Icefield scale as debris-covered areas increase (Glasser et al., 2016), although only up to a point beyond which areas under a thick layer would become insulated from atmospheric forcing, as has been shown elsewhere (Scherler et al., 2011).

Chapter 6 specifically discussed the importance of meltwater input into the glacier system, with the possibility of it enhancing ice dynamics and hence increasing frontal ablation (e.g. Sugiyama et al., 2011). A thorough assessment of this ablation feedback is beyond the scope of this thesis, and therefore remains unquantified, but it should be considered as a key driver of future short- and long-term ice loss, as increases in melt are projected for coming decades (Chapter 6), as are increases in air temperature (Huss et al., 2017; Pabón-Caicedo et al., 2020).

7.5 Future Work

There are several key questions that are necessary to address before projections of Patagonian glacier change can be considered robust. Efforts must be made to better constrain snow accumulation on both Icefields in order to estimate the surface mass balance with higher confidence. Measurements using different techniques and the use of multi-sensors will be necessary to capture the actual rates of snow accumulation on the plateau zones, considering the harsh weather conditions and the high probability of malfunctioning due to riming and strong winds. Until then, any quantification of surface mass balance must incorporate a high uncertainty to account for poorly defined accumulation rates.

Following the work presented here, the logical next step is to integrate the surface mass balance with an ice flux model in order to estimate the real volume and area loss (Chapter 6). New research in this direction has appeared in recent years relating to present conditions (e.g. Collao-Barrios et al., 2018; Bown et al., 2019) but is still limited to only a couple of glaciers. However, ice thickness estimations based on modelling approaches (e.g. Carrivick et al., 2016), airborne gravity surveys and radar measurements (Gourlet et al., 2015; Millan et al., 2019) along with ice speed estimations (e.g. Mougnot and Rignot, 2015) have become increasingly available for both Icefields. These datasets represent a remarkable advance towards increasing the understanding of ice flux dynamics on the Patagonian Icefields.

Data from the weather stations analysed herein can also be used to parameterise glaciological modelling efforts and will allow validation and downscaling of coarse climate models to feed glaciological models to estimate current and future mass balance of the Patagonia Icefields. However, it should be reinforced that more long-term on-glacier meteorological observations are necessary to investigate air temperature characteristics at the glacier boundary-layer, for example relating to the spatially variable glacier cooling effect discussed in Chapter 3. The aim is to obtain more accurate modelling

of the variables that control the surface mass balance and hence yield more robust assessments of the likely future response of these glaciers, considering the ongoing and projected air temperature increase in the region.

7.6 Conclusions

In this thesis, through the use of unprecedented in-situ meteorological observations on the plateau of the Southern Patagonian Icefield and gridded-climate data over both Patagonian Icefields, the meteorological and climatological characteristics and their influence on the glacier surface mass balance has been described, quantified and analysed at different spatial and temporal scales. Observational and gridded-climate data were used as input to physical models that quantified the components of the surface mass balance i.e. an energy balance for ablation and precipitation phase partitioning methods for accumulation. In the case of ablation and during the observation period, the approach estimated spatially distributed fluxes and their magnitude; meteorological inputs were therefore spatially distributed using elevation gradients obtained from the meteorological observations.

The results presented here provide a dual purpose; first to increase the knowledge of the meteorological and glaciological characteristics of Patagonian glaciers, and second to quantify the response of the glaciers to atmospheric changes.

First, notable spatial differences at the scale of the Icefields in both meteorological and glaciological variables were estimated. Secondly, the quantification of surface mass balance at longer time-scales demonstrated the importance of the atmospheric controls in the heterogeneous mass changes during the last decades over the Patagonian Icefields and gives insight in their future response.

Recognising these spatial differences represents a major step forward in our knowledge of the characteristics of the glaciers in Patagonia and their interaction with the atmosphere, which in turn determines the surface mass balance. In view of this meteorological and glaciological heterogeneity, a clear recommendation arising from this work is to avoid glacier sensitivity analyses that consider the Southern Patagonian Icefield and/or the Northern Patagonian Icefield as a whole. The distinct characteristics of each glacier, and the west-to-east gradients exhibited by meteorological variables, must be considered in modelling the surface mass balance. As the knowledge of these characteristics increases and the actual rate of accumulation is better constrained, confidence in future surface mass balance estimates for

Patagonian glaciers will increase. To reach this scientific community goal, and to summarize the findings herein, this thesis has contributed with several findings listed below by objective.

To address Objective 1, this thesis has contributed with:

- Characterising air temperature patterns on both sides of the north Southern Patagonia Icefield using in-situ observations, revealing that temperature lapse rates and glacier cooling effects are different in magnitude depending on the Icefield margin (east vs west).
- Quantifying the impact on melt and ablation estimations depending on the method used for air temperature distribution.

To address Objective 2, this thesis has contributed with:

- Determining that the controls in ablation i.e. the balance of radiative and turbulent fluxes, differs in the west-east transect of the northern Southern Patagonian Icefield . The melt is, however, strong at both sides of the Southern Patagonian Icefield, but locally i.e. at comparative elevations, is larger on the western side.
- Exploring the role of the accumulation-area ratio in amplifying the ablation rate at glacier-wide scale, being larger on west side glaciers of the northern Southern Patagonian Icefield.
- Examining potential positive feedbacks that increase glacier mass loss, quantifying the impact in ablation rates due to the albedo reduction of the supraglacial moraine, which increases the melt rate relative to bare ice.

To address Objective 3, this thesis has contributed with:

- Demonstrating that snow accumulation rates are higher on the west side compared to the eastern side and quantifying the impact on accumulation estimations depending on the method used to define the rain/snow ratio.
- Exploring the role of the estimated snow accumulation increases for those glaciers with stable and positive elevation changes determined by previous studies.

To address Objective 4, this thesis has contributed with:

- Modelling the future surface mass balance and showing that glacier mass loss could increase in the Northern Patagonian Icefield only due to atmospheric forcing, while in the Southern Patagonian Icefield, the surface mass balance could be close to balanced conditions. The main reason for the decrease in surface mass balance, particularly for the Northern Patagonian

Icefield, is related to projected increases in meltwater, which in turn could trigger other mechanisms of glacier mass loss associated with ice dynamics and frontal ablation for glaciers with calving fronts.

- Demonstrating that the atmospheric signal in the overall glacier mass loss is more evident in the Northern Patagonia Icefield (negative geodetic and surface mass balance) than in the Southern Patagonian Icefield (negative geodetic mass balance and positive surface mass balance).

List of References (Chapters 1, 2 and 7)

- Abdel-Jaber W, Rott H, Floricioiu D, Wuite J and Miranda N (2019). Heterogeneous spatial and temporal pattern of surface elevation change and mass balance of the Patagonian ice fields between 2000 and 2016. *The Cryosphere* 13(9), 2511–2535. doi: org/105194/tc-13-2511-2019.
- Aniya M (1988). Glacier Inventory for the Northern Patagonia Icefield, Chile, and Variations 1944/45 to 1985/86. *Arctic and Alpine Research* 20, 179–187.
- Aniya M, Sato H, Naruse R, Skvarca P and Casassa G (1996). The use of satellite and airborne imagery to inventory outlet glaciers of the Southern Patagonia Icefield, South America. *Photogrammetric Engineering and Remote Sensing* 62(12), 1361–1369.
- Aniya M, Sato H, Naruse R, Skvarca P and Casassa G (1997). Recent glacier variations in the Southern Patagonia Icefield, South America. *Arctic Antarctic and Alpine Research* 29 (1), 1–12.
- Barcaza G, Nussbaumer S, Tapia G, Valdes J, Garcia JL, Videla Y, Albornoz A and Arias V (2017). Glacier inventory and recent glacier variations in the Andes of Chile, South America. *Annals of Glaciology* 58 (75pt2), 166–180. doi: 10.1017/aog.2017.28.
- Bown F and Rivera A (2007). Climate changes and glacier responses during recent decades in the Chilean Lake District. *Global and Planetary Change* 59, 79-86.
- Bown F, Rivera A, Zenteno P, Bravo C, Cawkwell F (2014). First Glacier Inventory and Recent Glacier Variation on Isla Grande de Tierra Del Fuego and Adjacent Islands in Southern Chile. In *Global Land Ice Measurements from Space*, Kargel J, Leonard G, Bishop M, Käab A and Raup B. (Eds.). Springer, Berlin, pp. 661–674.
- Bown F, Rivera A, Pętllicki M, Bravo C, Oberreuter J, Moffat C (2019). Recent ice dynamics and mass balance of Jorge Montt Glacier, Southern Patagonia Icefield. *Journal of Glaciology* 65(253), 732-744. doi: 10.1017/jog.2019.47.
- Bozkurt D, Rojas M, Boisier JP, Rondanelli R, Garreaud R and Gallardo L. (2019). Dynamical downscaling over the complex terrain of southwest South America: present climate conditions and added value analysis. *Climate Dynamics* 53, 6745-6767. doi: 10.1007/s00382-019-04959-y.
- Braun MH, Malz P, Sommer C, Farias-Barahona D, Sauter T, Casassa G, Soruco A, Skvarca P and Seehaus T (2019). Constraining glacier elevation

and mass changes in South America. *Nature Climate Change* 9, 130–136. doi: [org/101038/s41558-018-0375-7](https://doi.org/10.1038/s41558-018-0375-7).

Carrasco J, Casassa G and Rivera A (2002). Meteorological and Climatological aspects of the Southern Patagonia Icefields. In *The Patagonian Icefields. A unique natural laboratory for environmental and climate change studies*, Casassa G, Sepulveda F and Sinclair R (Eds.). Kluwer Academic/Plenum Publishers, New York, pp 29-41.

Carrivick JL, Davies BJ, James WHM, Quincey DJ and Glasser NF (2016). Distributed ice thickness and glacier volume in southern South America. *Global and Planetary Change* 146, 122–132.

Casassa G, Smith K, Rivera A, Araos J, Schnirch M and Schneider C (2002). Inventory of glaciers in Isla Riesco, Patagonia, Chile, based on aerial photography and satellite imagery. *Annals of Glaciology* 34, 373-378.

Casassa G, Rodríguez JL and Loriaux T (2014) A new glacier inventory for the Southern Patagonia Icefield and areal changes 1986-2000. In *Global Land Ice Measurements from Space*, Kargel J, Leonard G, Bishop M, Kääb A and Raup B. (Eds.). Springer, Berlin, pp 639-660.

CECs-DGA (2016). Línea de base glaciológica del sector norte de Campo de Hielo Sur: Glaciares Jorge Montt, Témpano y O'Higgins. SIT N° 404, DGA, Technical Report in Spanish.

Cook K, Yang X, Carter C and Belcher B (2003). A modelling system for studying climate controls on mountain glaciers with application to the Patagonian Icefields. *Climatic Change* 56, 339–367.

Collao-Barrios G, Gilliet-Chaulet F, Favier V, Casassa G and Berthier E (2018). Ice flow modelling to constrain the surface mass balance and ice discharge of San Rafael Glacier, Northern Patagonia Icefield. *Journal of Glaciology* 64(246), 568–582. doi: [10.1017/jog.2018.46](https://doi.org/10.1017/jog.2018.46).

Copernicus Climate Change Service (C3S) (2019) C3S ERA5-Land reanalysis Copernicus Climate Change Service, <https://cdsclimatecopernicuseu/cdsapp#!/home>

Cuffey KM and Paterson WSB (2010). *The Physics of Glaciers*, 4th Edn., Elsevier, Oxford, UK.

Davies BJ and Glasser NF (2012). Accelerating shrinkage of Patagonian glaciers from the Little Ice Age (~AD 1870) to 2011. *Journal of Glaciology* 58(212), 1063–1084. doi: [10.3189/2012JoG12J026](https://doi.org/10.3189/2012JoG12J026).

Davies BJ, Darvill ChM, Lovell H, Bendle JM, Dowdeswell JA, Fabel D, García JL, Geiger A, Glasser NF, Gheorghiu DM, Harrison S, Hein AS, Kaplan, MR, Martin JRV, Mendelova M, Palmer A, Pelto M, Rodés Á, Sagredo EA, Smedley RK, Smellie JL and Thorndycraft VR (2020). The evolution of the Patagonian Ice Sheet from 35 ka to the present day (PATICE). *Earth Sciences Review* 204, 103152.

De Angelis H, Rau F and Skvarca P (2007). Snow zonation on Hielo Patagónico Sur, southern Patagonia, derived from Landsat 5 TM data. *Global and Planetary Change* 59(1-4), 149–158. doi: 10.1016/j.gloplacha.2006.11.032.

De Angelis H (2014). Hypsometry and sensitivity of the mass balance to change in equilibrium-line altitude: the case of the Southern Patagonia Icefield. *Journal of Glaciology* 60(219), 14–28. doi: 10.3189/2014JoG13J127.

Dussaillant A, Benito G, Buytaert W, Carling P, Meier C and Espinoza F (2010). Repeated glacial lake outburst floods in Patagonia; an increasing hazard? *Natural Hazards* 54 (2), 469–481. doi: 10.1007/s11069-009-9479-8.

Dussaillant I, Berthier E and Brun F (2018). Geodetic mass balance of the Northern Patagonian Icefield from 2000 to 2012 using two independent methods. *Frontiers in Earth Science* 6:8. doi: 10.3389/feart.2018.00008.

Dussaillant I, Berthier E, Brun F, Masiokas, M, Hugonnet R, Favier V, Rabatel A, Pitte P and Ruiz L (2019). Two decades of glacier mass loss along the Andes. *Nature Geosciences* 12, 802–808. doi: 10.1038/s41561-019-0432-5.

Falaschi D, Bravo C, Masiokas M, Villalba R and Rivera A (2013). First Glacier Inventory and Recent Changes in Glacier Area in the Monte San Lorenzo Region (47°S), Southern Patagonian Andes, South America. *Arctic, Antarctic, and Alpine Research* 45(1), 19-28.

Falaschi D, Bolch T, Rastner P, Lenzano MG, Lenzano L, Vecchio AL and Moragues S (2016). Mass changes of alpine glaciers at the eastern margin of the Northern and Southern Patagonian Icefields between 2000 and 2012. *Journal of Glaciology* 63, 258–272. doi: 10.1017/jog.2016.136.

Fernández A and Mark BG (2016). Modeling modern glacier response to climate changes along the Andes Cordillera: A multi-scale review. *Journal of Advances in Modeling Earth Systems* 8, 467–495. doi: 10.1002/2015MS000482.

Foresta L, Gourmelen N, Weissgerber F, Nienow P, Williams JJ, Shepherd A, Drinkwater MR and Plummer S (2018). Heterogeneous and rapid ice loss over

the Patagonian Ice Fields revealed by CryoSat-2 swath radar altimetry. *Remote Sensing of Environment* 211, 441-455. doi: [org/10.1016/j.rse.2018.03.041](https://doi.org/10.1016/j.rse.2018.03.041).

Fukami H and Naruse R (1987). Ablation of ice and heat balance on Soler Glacier, Patagonia. *Bulletin of Glacier Research* 4, 37-42.

Garreaud R, Lopez P, Minvielle M and Rojas M (2013). Large-Scale control on the Patagonian Climate. *Journal of Climate* 26(1), 215–230. doi: [org/10.1175/JCLI-D-12-00001.1](https://doi.org/10.1175/JCLI-D-12-00001.1).

Gillet N, Kell T and Jones P (2006). Regional climate impacts of the Southern Annular Mode. *Geophysical Research Letters* 33, L23704. doi: [10.1029/2006GL027721](https://doi.org/10.1029/2006GL027721).

Giorgetta MA, Jungclaus J, Reick CH et al. (2013). Climate and carbon cycle changes from 1850 to 2100 in MPI-ESM simulations for the Coupled Model Intercomparison Project phase 5. *Journal of Advances in Modeling Earth Systems* 5(3), 572–597. doi: [10.1002/jame.20038](https://doi.org/10.1002/jame.20038).

Glasser NF, Holt TO, Evans ZD, Davies BJ, Pelto M and Harrison S (2016) Recent spatial and temporal variations in debris cover on Patagonian glaciers. *Geomorphology* 273, 202–216. doi: [10.1016/j.geomorph.2016.07.036](https://doi.org/10.1016/j.geomorph.2016.07.036).

Gourlet P, Rignot E, Rivera A and Casassa G (2016). Ice thickness of the northern half of the Patagonia Icefields of South America from high-resolution airborne gravity surveys. *Geophysical Research Letters* 43, 241-249. doi: [10.1002/2015GL066728](https://doi.org/10.1002/2015GL066728).

Gutierrez MH, Galand PE, Moffat C and Pantoja S (2015). Melting glacier impacts community structure of Bacteria, Archaea and Fungi in a Chilean Patagonia fjord. *Environmental Microbiology* 17(10), 3882–3897.

Hall A and Visbeck M (2002). Synchronous Variability in the Southern Hemisphere Atmosphere, Sea Ice, and Ocean Resulting from the Annular Mode. *Journal of Climatology* 15, 3043-3057.

Hock R and Holmgren B (2005). A distributed energy balance model for complex topography and its application to Storglaciären, Sweden. *Journal of Glaciology* 51(172), 25-36. doi: [10.3189/172756505781829566](https://doi.org/10.3189/172756505781829566).

Huss M, Bookhagen B, Huggel C, Jacobsen D, Bradley R, Clague J, Vuille M, Buytaert W, Cayan D, Greenwood G, Mark B, Milner A, Weingartner R and Winder M (2017). Towards mountains without permanent snow and ice. *Earth's Future* 5, doi: [10.1002/2016EF00514](https://doi.org/10.1002/2016EF00514).

Immerzeel WW, Lutz AF, Andrade, M, et al. (2020). Importance and vulnerability of the world's water towers. *Nature* 577, 364–369. doi: [org/10.1038/s41586-019-1822-y](https://doi.org/10.1038/s41586-019-1822-y)

Iribarren-Anacona P, Mackintosh A and Norton KP (2015). Hazardous processes and events from glacier and permafrost areas: Lessons from the Chilean and Argentinean Andes. *Earth Surf Processes Landforms* 40 (1), 2–21. doi: [org/10.1002/esp.3524](https://doi.org/10.1002/esp.3524).

Kobayashi S and Saito T. (1985). Heat balance on Soler Glacier. *Glaciological studies in Patagonia, Northern Icefield, 1983– 1984*. Data Center for Glacier Res., JSSI, Report 7, 46–51.

Koizumi K and Naruse R (1992). Measurements of Meteorological Conditions and Ablation at Tyndall Glacier, Southern Patagonia, in December 1990. *Bulletin of Glacier Research* 10, 79–82.

Kondo H and Inoue J (1988). Heat balance on the icefield of San Rafael Glacier, the Northern Patagonia Icefield. *Bulletin of Glacier Research* 6, 1–8.

Konya K and Matsumoto T (2010). Influence of weather conditions and spatial variability on glacier surface melt in Chilean Patagonia. *Theoretical and Applied Climatology* 102, 139–149.

Koppes M, Conway H, Rasmussen LA and Chernos M (2011). Deriving mass balance and calving variations from reanalysis data and sparse observations, Glacier San Rafael, northern Patagonia, 1950–2005. *The Cryosphere* 5(3), 791–808. doi: [10.5194/tc-5-791-2011](https://doi.org/10.5194/tc-5-791-2011).

Lenaerts JTM, van den Broeke MR, van Wessem JM, van de Ber, WJ, van Meijgaard E, van Uft LH and Schaefer M (2014). Extreme Precipitations and Climate Gradients in Patagonia Revealed by High-Resolution Regional Atmospheric Climate Modeling. *Journal of Climate* 27(12), 4607-4621. doi: [10.1175/JCLI-D-13-00579.1](https://doi.org/10.1175/JCLI-D-13-00579.1).

Li J, Chen J, Ni S, Tang L and Hu X (2019) Long-term and inter-annual mass changes of Patagonia Ice Field from GRACE. *Geodesy and Geodynamics* 10, 100-109. doi: [org/10.1016/j.geog.2018.06.001](https://doi.org/10.1016/j.geog.2018.06.001).

López P, Chevallier P, Favier V, Apoyad B, Ordenes F and Oerlemans J (2010). A regional view of fluctuations in glacier length in southern South America. *Global and Planetary Change* 71(1-2), 85–108. doi: [10.1016/j.gloplacha.2009.12.009](https://doi.org/10.1016/j.gloplacha.2009.12.009).

Loriaux T and Casassa G (2013). Evolution of glacial lakes from the Northern Patagonia Icefield and terrestrial water storage in a sea-level rise context.

Global and Planetary Change 102, 33–40. doi: 10.1016/j.gloplacha.2012.12.012.

Lo Vecchio A, Lannutti E, Lenzano MG, Mikkan R, Vacaflor P and Lenzano L (2019) MODIS Image-derived ice surface temperature assessment in the Southern Patagonian Icefield. *Progress in Physical Geography: Earth and Environment* 43(6), 754-776. doi: 10.1177/0309133319851022.

Mackintosh AN, Anderson BM and Pierrehumbert RT (2017). Reconstructing climate from glaciers. *Annual Review of Earth and Planetary Sciences* 45, 649-680. doi:10.1146/annurev-earth-063016-020643.

Malz P, Meier W, Casassa G, Jaña R, Skvarca P and Braun MH (2018). Elevation and Mass Changes of the Southern Patagonia Icefield Derived from TanDEM-X and SRTM Data. *Remote Sensing* 10(2), 188. doi: 103390/rs10020188.

Marshall G (2003). Trends in the Southern Annular Mode from observations and reanalyses. *Journal of Climatology* 16, 4134 – 4143, 2003.

Masiokas MH, Delgado S, Pitte P, Berthier E, Villalba R, Skvarca P, Ruiz L, Ukita J, Yamanokuchi T, Tadono T, Marinsek S, Couvreur F and Zalazar L (2015). Inventory and recent changes of small glaciers on the northeast margin of the southern Patagonia icefield, Argentina. *Journal of Glaciology* 61(227), 511–523. doi: 10.3189/2015JoG14J094.

Masiokas MH, Rabatel A, Rivera A, Ruiz L, Pitte P, Ceballos JL, Barcaza G, Soruco A, Bown F, Berthier E, Dussaillant I and MacDonell S (2020). A Review of the Current State and Recent Changes of the Andean Cryosphere. *Frontiers in Earth Sciences* 8. doi: 10.3389/feart.2020.00099.

Meier WJH, Gießinger J, Hochreuther P and Braun MH (2018). An Updated Multi-Temporal Glacier Inventory for the Patagonian Andes With Changes Between the Little Ice Age and 2016. *Frontiers in Earth Science* 6. doi: org103389/feart201800062.

Mernild SH, Liston GE, Hiemstra CA and Wilson R (2016). The Andes Cordillera Part III: Glacier Surface Mass Balance and Contribution to Sea Level Rise (1979–2014). *International Journal of Climatology* 37(7), 3154–3174. doi: org/10.1002/joc.4907.

Millan R, Rignot E, Rivera A, Martineau V, Mougnot J, Zamora R, Uribe J, Lenzano G, De Fleurian B, Li X, Gim Y and Kirchner D(2019). Ice thickness and bed elevation of the Northern and Southern Patagonian Icefields. *Geophysical Research Letters* 46. doi: 10.1029/2019GL082485

Mölg T, Hardy D, Collier E, Kropac E, Schmid C, Cullen N, Kaser G, Prinz R and Winkler M (2020). Mesoscale atmospheric circulation controls of local meteorological elevation gradients on Kersten Glacier near Kilimanjaro summit. *Earth System Dynamics* 11, 653-672. doi: [org/10.5194/esd-11-653-2020](https://doi.org/10.5194/esd-11-653-2020).

Monahan P and Ramage J (2010). AMSR-E Melt Patterns on the Southern Patagonian Icefield. *Journal of Glaciology* 56(198), 699-708. doi: [10.3189/002214310793146197](https://doi.org/10.3189/002214310793146197).

Mouginot J and Rignot E (2015). Ice motion of the Patagonian Icefields of South America: 1984–2014. *Geophysical Research Letters* 42, 1441–1449. doi: [10.1002/2014GL062661](https://doi.org/10.1002/2014GL062661)

Muto M and Furuya M (2013). Surface velocities and ice-front positions of eight major glaciers in the southern Patagonian ice field, South America, from 2002 to 2011. *Remote Sensing of Environment* 139, 50–59. doi: [101016/jrse.201307034](https://doi.org/10.1016/j.rse.2013.07.034).

Naruse R, Skvarca P and Takeuchi Y (1997). Thinning and retreat of Glaciar Upsala, and an estimate of annual ablation changes in Southern Patagonia. *Annals of Glaciology* 24, 38-42. doi: [10.3189/S0260305500011903](https://doi.org/10.3189/S0260305500011903).

Oerlemans J and Knap WH (1998). A one-year record of global radiation and albedo from the ablation zone of the Morteratschgletscher, Switzerland. *Journal of Glaciology* 44(147), 231-238. doi: [10.3189/S0022143000002574](https://doi.org/10.3189/S0022143000002574).

Ohata T, Enomoto H and Kondo H (1985a). Characteristics of ablation at San Rafael Glacier. *Glaciological Studies in Patagonia, Northern Icefield, 1983–1984*. Data Center for Glacier Res., JSSI, Report 6, 37–45.

Ohata T, Kobayashi S, Enomoto H, Kondo H, Saito T and Nakajima C (1985b). The east-west contrast in meteorological conditions and its effect on glacier ablation. *Bulletin of Glaciological Research* 3, 52–53.

Pabón-Caicedo JD, Arias PA, Carril AF, Espinoza JC, Borrel LF, Goubanova K, Lavado-Casimiro W, Masiokas M, Solman S and Villalba R (2020). Observed and Projected Hydroclimate Changes in the Andes. *Frontiers in Earth Sciences* 8:61. doi: [10.3389/feart.2020.00061](https://doi.org/10.3389/feart.2020.00061)

Pellicciotti F, Ragetti S, Carenzo M and McPhee J (2014). Changes of glaciers in the Andes of Chile and priorities for future work. *Science of the Total Environment* 493, 1197-1210. doi: [10.1016/j.scitotenv.2013.10.055](https://doi.org/10.1016/j.scitotenv.2013.10.055).

Peña H and Gutiérrez R (1992). Statistical analysis of precipitation and air temperature in the Southern Patagonia Icefield. In R. Naruse and M. Aniya

(Eds.) *Glaciological Researches in Patagonia*, 1990, Japanese Society of Snow and Ice, p. 95-107.

Quincey D, Smith M, Rounce D, Ross A, King O and Watson C (2017). Evaluating morphological estimates of the aerodynamic roughness of debris covered glacier ice. *Earth Surface Process and Landforms* 42(15), 2541-2553. doi: 10.1002/esp.4198.

Quintana J and Aceituno P (2012). Changes in the rainfall regime along the extratropical west coast of South America (Chile): 30-43° S. *Atmósfera* 25(1), 1-22.

Quiroga E, Ortiz P, Gonzalez-Saldias R, Reid B, Tapia FJ, Perez-Santos I, Rebolledo L, Mansilla R, Pineda C, Cari I, Salinas N, Montiel A and Gerdes D (2016). Seasonal benthic patterns in a glacial Patagonian fjord: The role of suspended sediment and terrestrial organic matter. *Marine Ecology Progress Series*, 561, 31–50. doi: 10.3354/meps11903.

Rasmussen LA, Conway H and Raymond CF (2007). Influence of upper air conditions on the Patagonia icefields. *Global and Planetary Change* 59, 203–216. doi: 10.1016/j.gloplacha.2006.11.025.

Rignot E, Rivera A and Casassa G (2003). Contribution of the Patagonia Icefields of South America to Sea Level Rise. *Science* 302(5644), 434-436. doi: 10.1126/science.1087393.

Rivera A and Casassa G (2002). Ice Thickness measurements on the Southern Patagonia Icefield. In *The Patagonian Icefields. A unique natural laboratory for environmental and climate change studies*, Casassa G, Sepulveda F and Sinclair R. (Eds.). Kluwer Academic/Plenum Publishers, New York, pp 101-115.

Rivera A (2004). Mass balance investigations at Glaciar Chico, Southern Patagonia Icefield, Chile. (PhD thesis, University of Bristol).

Rivera A, Benham T, Casassa G, Bamber J and Dowdeswell J (2007). Ice elevation and areal changes of glaciers from the Northern Patagonia Icefield, Chile. *Global and Planetary Change* 59, 126-137.

Rivera A, Koppes M, Bravo C and Aravena JC (2012). Little Ice Age advance and retreat of Glaciar Jorge Montt, Chilean Patagonia. *Climate of the Past* 8, 403-414.

Rodbell D, Smith J and Mark B (2009). Glaciation in the Andes during Lateglacial and Holocene. *Quaternary Sciences Review* 28, 2165 – 2212.

Rott H, Stuefer M, Siegel A, Skvarca P and Eckstaller A (1998). Mass fluxes and dynamics of Moreno Glacier, Southern Patagonia Icefield. *Geophysical Research Letters* 25(9), 1407–1410.

Sagredo E and Lowell T (2012). Climatology of Andean glaciers: A framework to understand glacier response to climate change. *Global and Planetary Change* 86–87, 101–109. doi: 10.1016/j.gloplacha.2012.02.010.

Sagredo E, Lowell T and Rupper S (2014). Sensitivities of the equilibrium line altitude to temperature and precipitation changes along the Andes. *Quaternary Research* 81, 355-366.

Sakakibara D and Sugiyama S (2014). Ice-front variations and speed changes of calving glaciers in the Southern Patagonia Icefield from 1984 to 2011. *Journal of Geophysical Research Earth Surface* 119(11), 2541–2554. doi: org/101002/2014JF003148.

Sauter T (2020). Revisiting extreme precipitation amounts over southern South America and implications for the Patagonian Icefields. *Hydrological and Earth System Sciences* 24(4), 2003–2016. doi: 105194/hess-24-2003-2020.

Schaefer M, Machguth H, Falvey M and Casassa G (2013). Modeling past and future surface mass balance of the Northern Patagonian Icefield. *Journal of Geophysical Research Earth Surface* 118, 571–588. doi: 10.1002/jgrf.20038.

Schaefer M, Machguth H, Falvey M, Casassa G and Rignot E (2015). Quantifying mass balance processes on the Southern Patagonia Icefield. *The Cryosphere* 9(1), 25–35. doi: 10.5194/tc-9-25-2015.

Schaefer M, Fonseca D, Farias-Barahona D and Casassa, G (2020) Surface energy fluxes on Chilean glaciers: measurements and models. *The Cryosphere* 14, 2545–2565, doi: 10.5194/tc-14-2545-2020.

Scherler D, Bookhagen B and Strecker, M (2011) Spatially variable response of Himalayan glaciers to climate change affected by debris cover. *Nature Geoscience* 4, 156–159, doi: 10.1038/ngeo1068.

Schneider C, Glaser M, Killian R, Santana A, Butorovic N and Casassa G (2003). Weather observations across the Southern Andes at 53°S. *Physical Geography* 24(2), 97-119. doi: 10.2747/0272-3646.24.2.97.

Schneider C, Schnirch M, Acuña C, Casassa G and Kilian R (2007a). Glacier inventory of the Gran Campo Nevado Ice Cap in the Southern Andes and glacier changes observed during recent decades. *Global and Planetary Change* 59, 87-100.

Schneider C, Kilian R and Glaser M (2007b). Energy balance in the ablation zone during the summer season at the Gran Campo Nevado Ice Cap in the Southern Andes. *Global and Planetary Change* 59, 175–188. doi: 10.1016/j.gloplacha.2006.11.033.

Schoolmeester T, Johansen KS, Alfthan B, Baker E, Hespings M and Verbist K (2018). *The Andean Glacier and Water Atlas –The Impact of Glacier Retreat on Water Resources*. UNESCO and GRID-Arendal.

Schwikowski M, Schläppi M, Santibañez P, Rivera A and Casassa G (2013). Net accumulation rates derived from ice core stable isotope records of Pío XI glacier, Southern Patagonia Icefield. *The Cryosphere* 7, 1635-1644. doi: 05194/tc-7-1635-2013.

Sessions M (1975). *The meteorological report*. Unpublished report of the Joint Services expedition to Chilean Patagonia 1972-1973. Royal Geographical Society, London, 82 p.

Shugar DH, Burr A, Haritashya UK, Kargel J, Watson CS, Kennedy MC, Bevington AR, Betts RA, Harrison S and Strattman (2020). Rapid worldwide growth of glacial lakes since 1990. *Nature Climate Change* 10, 939-945. doi: 10.1038/s41558-020-0855-4.

Smith MW, Quincey DJ, Dixon T, Bingham RG, Carrivick JL, Irvine-Fynn TD and Rippin DM (2016). Aerodynamic roughness of glacial ice surfaces derived from high resolution topographic data. *Journal of Geophysical Research Earth Surface* 121(4), 748-766. doi: 10.1002/2015JF003759.

Smith R and Evans J (2007). Orographic precipitation and water vapor fractionation over the Southern Andes. *Journal of Hydrometeorology* 8(1), 3–19. doi: 10.1175/JHM555.1.

Stuefer M, Rott H and Skvarca P (2007). Glaciar Perito Moreno, Patagonia: climate sensitivities and glacier characteristics preceding the 2003/04 and 2005/06 damming events. *Journal of Glaciology* 53, 3–16.

Sugiyama S, Skvarca P, Naito N, Enomoto H, Tsutaki S, Tone K, Marinsek S and Aniya M (2011). Ice speed of a calving glacier modulated by small fluctuations in basal water pressure. *Nature Geosciences* 4, 597–600. doi: 10.1038/ngeo1218.

Takeuchi Y, Naruse R and Satow K (1995). Characteristics of heat balance and ablation on Moreno and Tyndall glaciers, Patagonia, in the summer 1993/94. *Bulletin of Glacier Research* 13, 45–56.

Takeuchi Y, Naruse R and Skvarca P (1996). Annual air-temperature measurement and ablation estimate at Moreno Glacier, Patagonia. *Bulletin of Glacier Research* 14, 23-28.

Takeuchi Y, Naruse R, Satow K and Ishikawa N (1999). Comparison of heat balance characteristics at five glaciers in the Southern Hemisphere. *Global Planet Change* 22, 201-208. doi: 10.1016/S0921-8181(99)00037-5.

Wang G, Cai W, Gan B, Wu L, Santoso A, Lin X, Chen Z and McPhaden MJ (2017). Continued increase of extreme El Niño frequency long after 1.5 °C warming stabilization. *Nature Climate Change* 7, 568–572. doi:org/10.1038/nclimate3351.

Weidemann SS, Sauter T, Malz P, Jaña R, Arigony-Neto J, Casassa G and Schneider C (2018). Glacier mass changes of lake-terminating Grey and Tyndall glaciers at the Southern Patagonia Icefield derived from geodetic observations and energy and mass balance modeling. *Frontiers in Earth Science* 6. doi: 10.3389/feart201800081.

Weidemann SS, Arigony-Neto J, Jaña R, Netto G, Gonzalez I, Casassa G and Schneider C (2020). Recent climatic mass balance of the Schiaparelli glacier at the Monte Sarmiento massif and reconstruction of Little Ice Age climate by simulating steady-state glacier conditions. *Geosciences* 10 (272). doi: 10.3390/geosciences10070272.

White A and Copland L (2015). Decadal-scale variations in glacier area changes across the Southern Patagonian Icefield since the 1970s. *Arctic, Antarctic, and Alpine Research* 47(1), 147–167. doi: 10.1657/AAAR0013-102.

Willis M, Melkonian A, Pritchard M and Rivera A (2012). Ice loss from the Southern Patagonian Ice Field, South America, between 2000 and 2012. *Geophysical Research Letters*, 39(17), L17501. doi: 10.1029/2012GL053136.

Wilson R, Glasser N, Reynolds J, Harrison S, Iribarren-Anacona, Schaefer M and Shannon S (2018). Glacial lakes of the Central and Patagonian Andes. *Global and Planetary Change* 162, 275-291. doi: 10.1016/j.gloplacha.2018.01.004.

Wilson R, Harrison S, Reynolds J, Hubbard A, Glasser N, Wünderlich O, Iribarren-Anacona P, Mao L and Shannon S (2019). The 2015 Chileno Valley glacial lake outburst flood, Patagonia. *Geomorphology* 332, 51-65. doi: 10.1016/j.geomorph.2019.01.015.

Zalazar L, Ferri L, Castro M, Gargantini H, Gimenez M, Pitte P, Ruiz L, Masiokas M, Costa G and Villalba R (2020). Spatial distribution and

characteristics of Andean ice masses in Argentina: results from the first National Glacier Inventory. *Journal of Glaciology*. doi: 10.1017/jog.2020.55.

Zemp M, Huss M, Thibert E, Eckert N, McNabb R, Huber J, Barandun M, Machguth H, Nussbaumer SU, Gärtner-Roer I, Thomson L, Paul F, Maussion F, Kutuzov S and Cogley JG (2019). Global glacier mass changes and their contributions to sea-level rise from 1961 to 2016. *Nature* 568, 382–386. doi: 10.1038/s41586-019-1071-0.

Appendix Supplementary Information

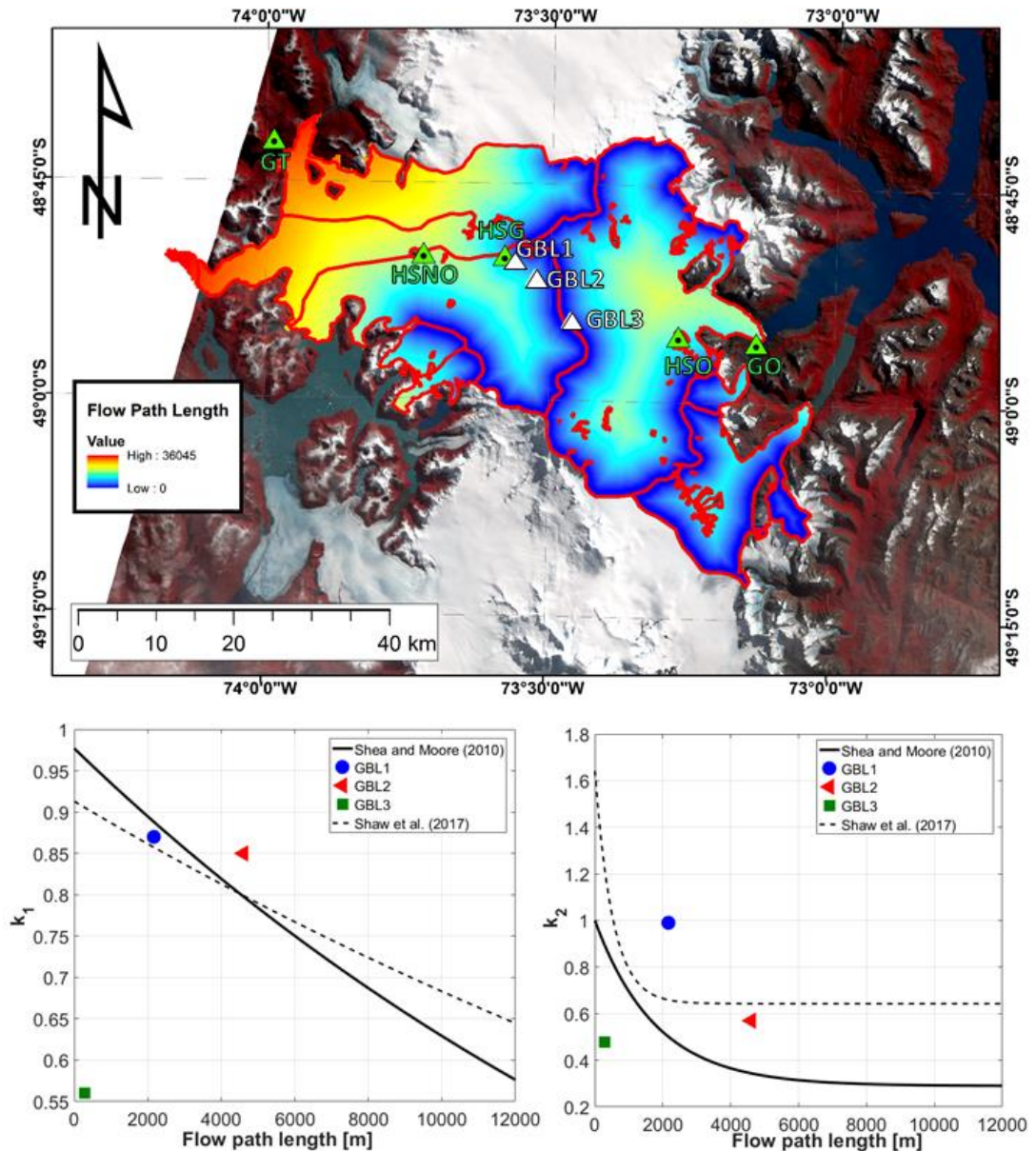
A.1 Chapter 3. Air Temperature Characteristics, Distribution and Impact on Modeled Ablation for the South Patagonia Icefield

Introduction

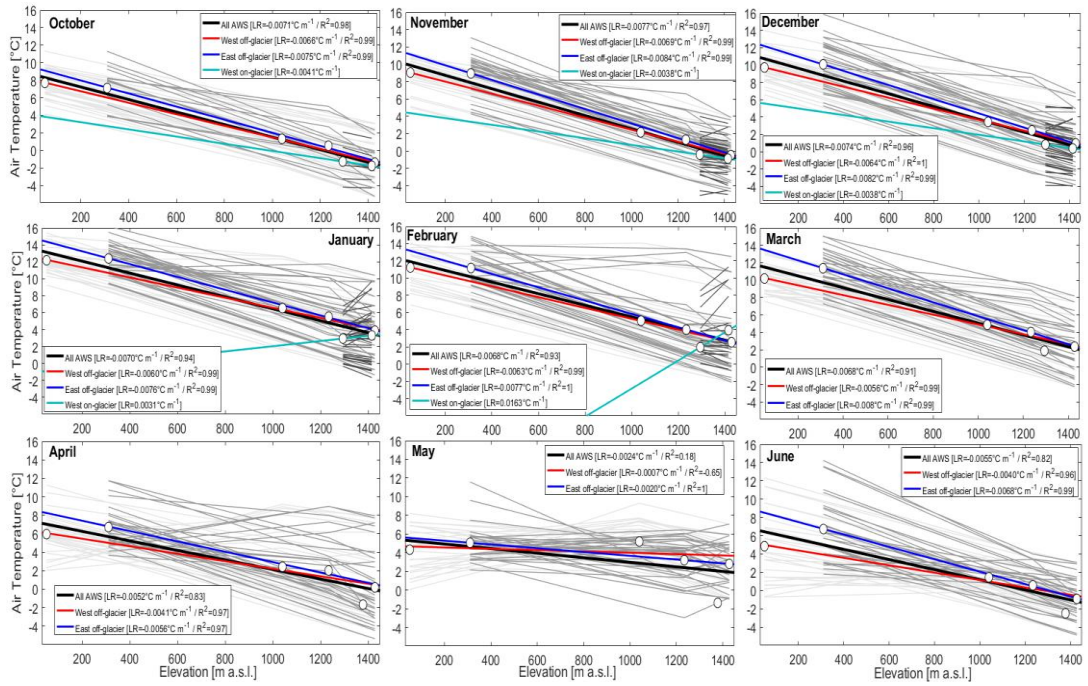
This supporting information provides more data (Figures and Tables) that complete our analysis on the South Patagonia Icefield (SPI) air temperature conditions. We show meteorological data to demonstrate the relationship (wind speed and relative humidity) with the observed lapse rate (Figure S3). Also, we show the correlation matrix between each air temperature time series demonstrating the generally good correlation between the time series (Table S1) that allow us to interpolate the air temperature using the observed lapse rates. The temporal (at monthly scale) and spatial variability (West-East) of the lapse rate is in Figure S2.

To complement the description of the method section we shown the flow path length of the glaciers, which are the input to model the air temperature using the Shea and Moore (2010) model (Figure S1) and also with comparative purpose the factors k_1 and k_2 determine with the data of the SPI and comparing with previous applications.

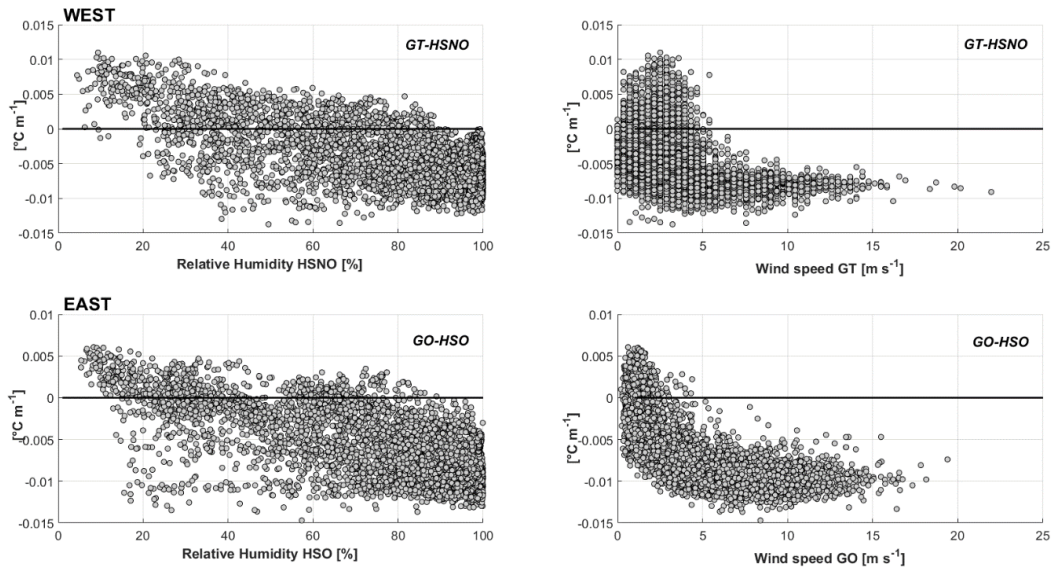
Table S2 shows the comparison of the Ultrasonic Depth Gauge (UDG) observations at GBL1 and GBL2 locations and the point-scale melt using a degree-day model with DDF of 8.5 mm w.e. °C-1 d-1.



Supplementary Figure 3.1 Estimated distance flow path length (upper). Below, parameters used by Shea and Moore (2010) and Shaw et al. (2017) to distribute the air temperature. Also as comparison purposes, the parameters observed at GBL1, GBL2 and GBL3 are included. The flow path length is defined as “the average flow distance to a given point starting from an upslope limit or ridge” (Carturan et al., 2015). In our estimation we first define the ridges. As shows in Figure, not all the ice divide was considered as a ridge. The ice divide between east and west was considered and also those ridge with a higher slope (e.g. Pirámide and Chico glaciers in the east, Unnamed and HPS8 in the west). The northern ice divide of Témpano glacier was not considered as this area is almost flat and is difficult to define the exact point of the ice divide. The same situation was assumed between the ice divide of Témpano-Occidental and Occidental-Greve. After we define the “ridge” zone we calculate the distance using the SRTM DEM and the “Path Distance” tool in ArcMap® 10.4.



Supplementary Figure 3.2. Mean monthly air temperature compared with elevation for all the AWS and GBL (black line) and mean monthly lapse rate for different spatial configurations (color line). Light grey, grey and dark grey lines are the mean daily air temperatures at the west, east and on-glacier, respectively.



Supplementary Figure 3.3 Relation between observed relative humidity and wind speed in the tongues of each side in the South Patagonia Icefield.

Supplementary Table 3.1 Correlation (Pearson r) matrix of the hourly time series of air temperature for the five AWS and three snow sensor. Time series of GBL3 with GBL1 and GBL2 do not coincide. All the values are significant ($p < 0.01$).

| | GT | HSNO | HSG | GBL1 | GBL2 | GBL3 | HSO | GO |
|------|------|------|------|------|------|------|------|----|
| GT | | | | | | | | |
| HSNO | 0.44 | | | | | | | |
| HSG | 0.37 | 0.96 | | | | | | |
| GBL1 | 0.62 | 0.93 | 0.96 | | | | | |
| GBL2 | 0.71 | 0.90 | 0.91 | 0.91 | | | | |
| GBL3 | 0.53 | 0.61 | 0.58 | -- | -- | | | |
| HSO | 0.42 | 0.90 | 0.92 | 0.93 | 0.88 | 0.60 | | |
| GO | 0.77 | 0.52 | 0.46 | 0.67 | 0.74 | 0.54 | 0.47 | |

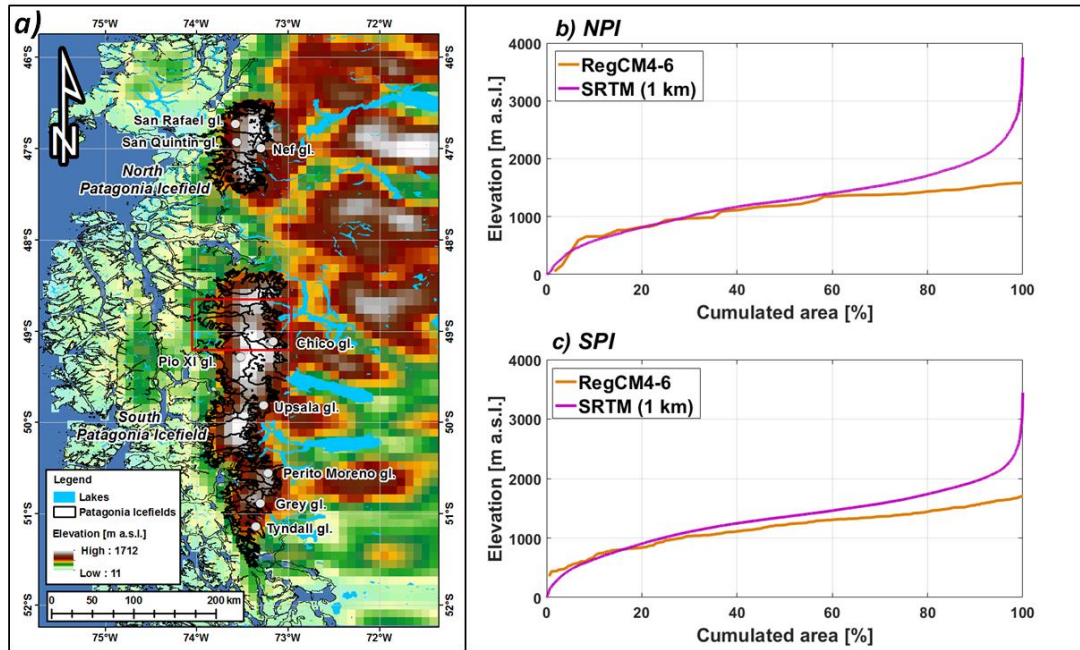
Supplementary Table 3.2. Comparison of the observed and estimated melt at GBL1 and GBL2 locations. Estimated melt is using the DDM.

| Location / Dates | Observed Ablation (UDG) [m w.e.] | Calculated melt using observed air temperature [8.5 mm w.e. °C ⁻¹ d ⁻¹] [m w.e.] | Calculated melt different methods for air temperature distribution [DDF: 8.5 mm w.e. °C ⁻¹ d ⁻¹] | | | | |
|--|----------------------------------|---|---|--------------|--------------|------------------|---------------|
| | | | ELR [m w.e.] | MLR [m w.e.] | VLR [m w.e.] | VLRBias [m w.e.] | SM10 [m w.e.] |
| GBL1 [1415 m a.s.l.], 1 Nov. 2015 - 10 Feb. 2016 | 1.8 | 1.8 | 2.2 | 2.3 | 2.3 | 1.6 | 1.8 |
| GBL2 [1294 m a.s.l.], 1 Nov. 2015 - 31 Mar. 2016 | 2.6 | 2.5 | 3.9 | 3.9 | 3.9 | 2.8 | 2.9 |

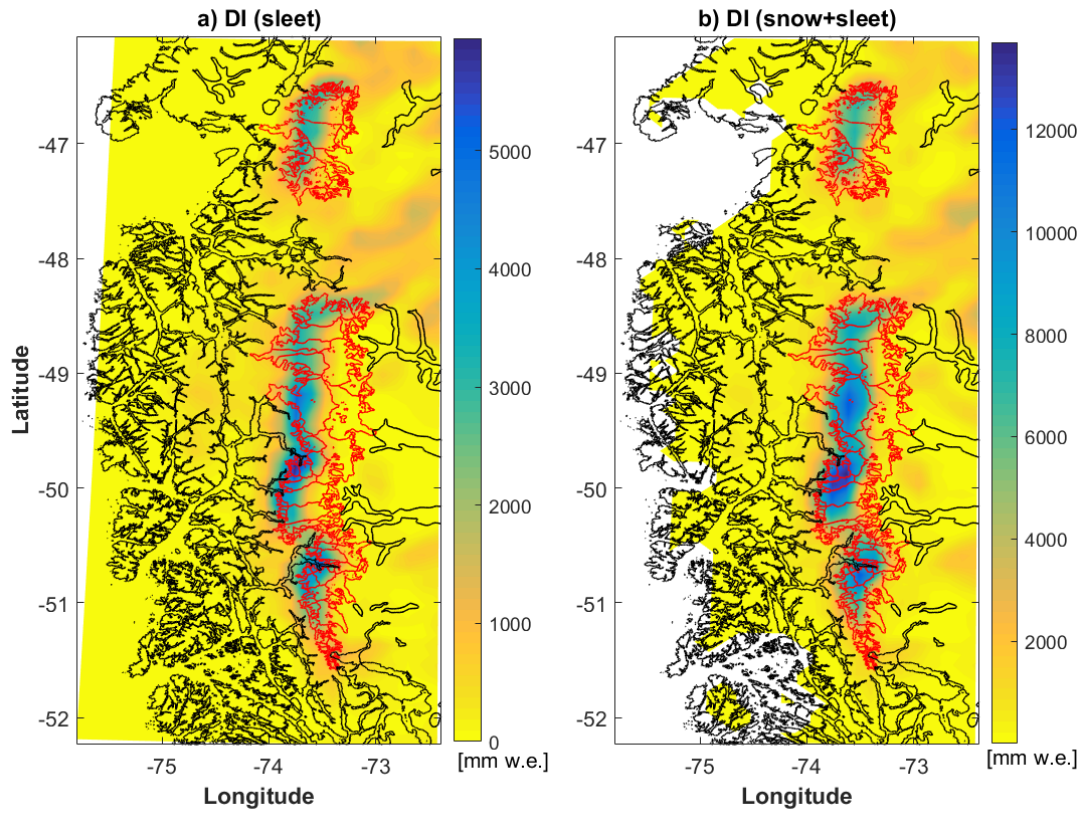
A.2 Chapter 4. Assessing Snow Accumulation Patterns and Changes on the Patagonian Icefields

Supplementary Figures and Tables

Supplementary Figures

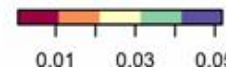
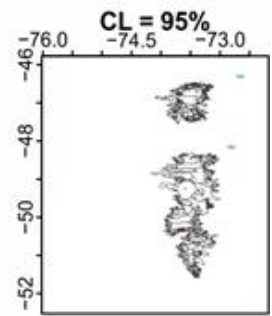
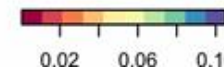
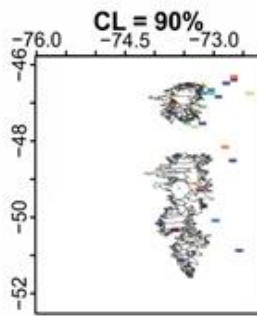
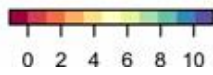
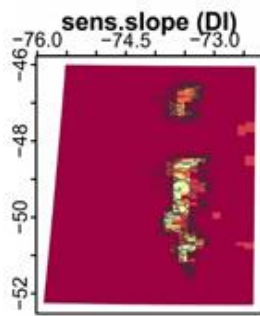
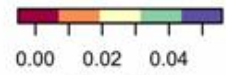
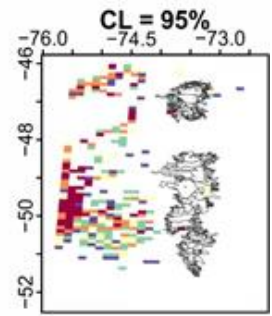
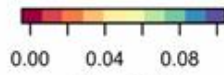
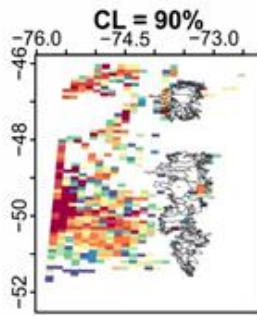
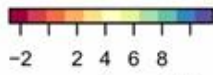
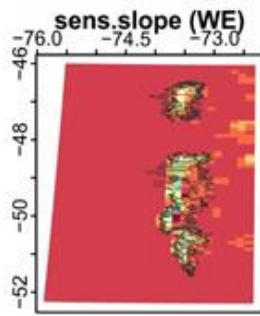
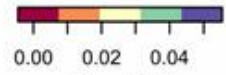
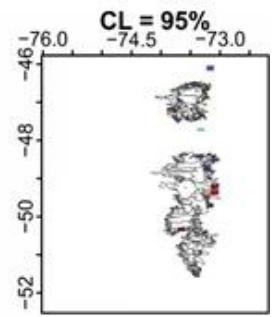
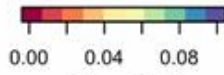
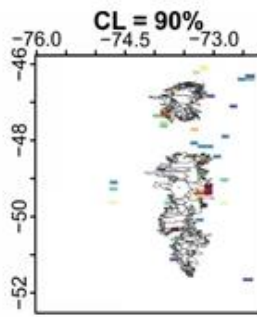
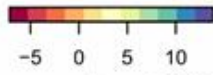
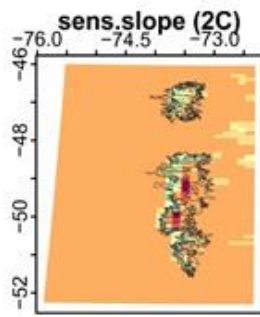


Supplementary Figure 4.1 a) RegCM4.6 topography at 10 km resolution, b) and c) comparative hypsometric curves of the icefields using 1 km SRTM topographic data and data from a).

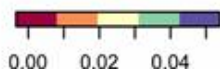
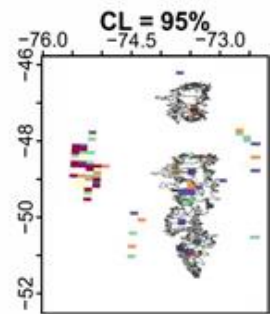
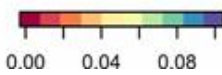
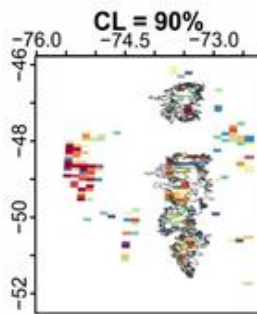
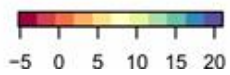
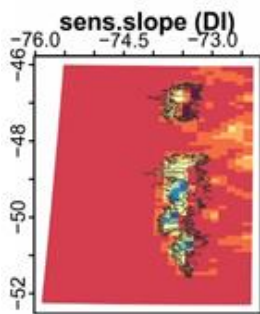
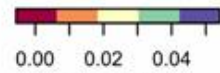
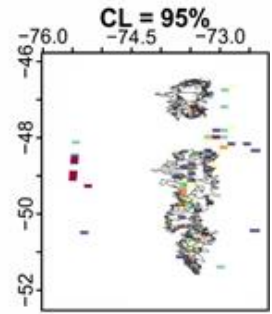
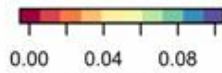
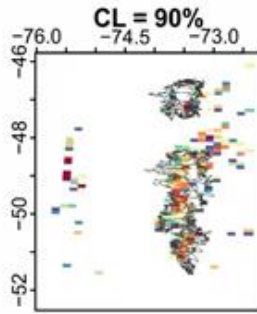
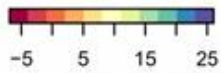
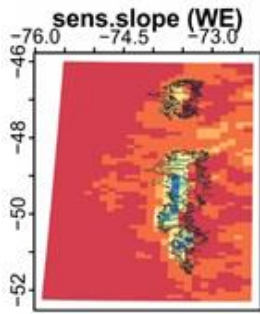
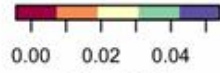
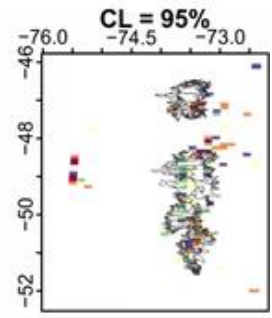
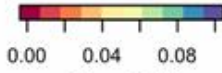
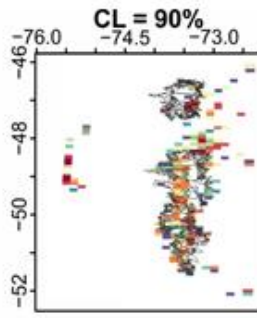
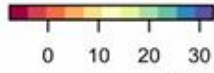
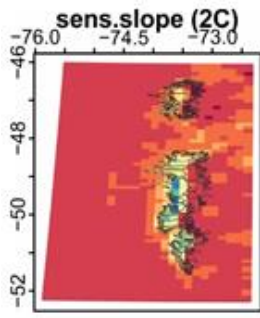


Supplementary Figure 4.2 1980-2015 annual mean value of accumulation type for DI PPM. a) sleet and b) snow plus sleet. Red line corresponds to the Icefields limits and glaciers.

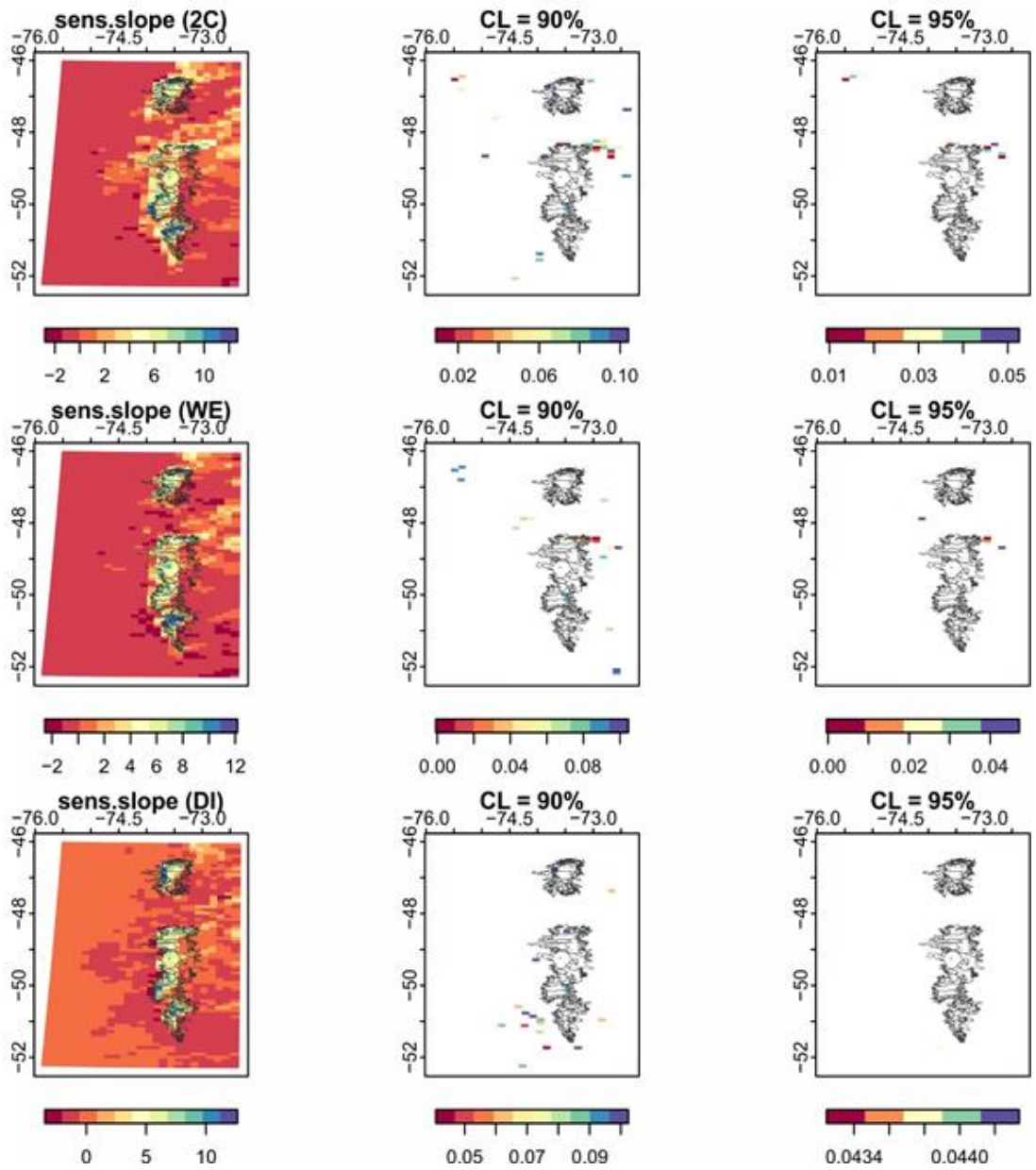
a) Summer

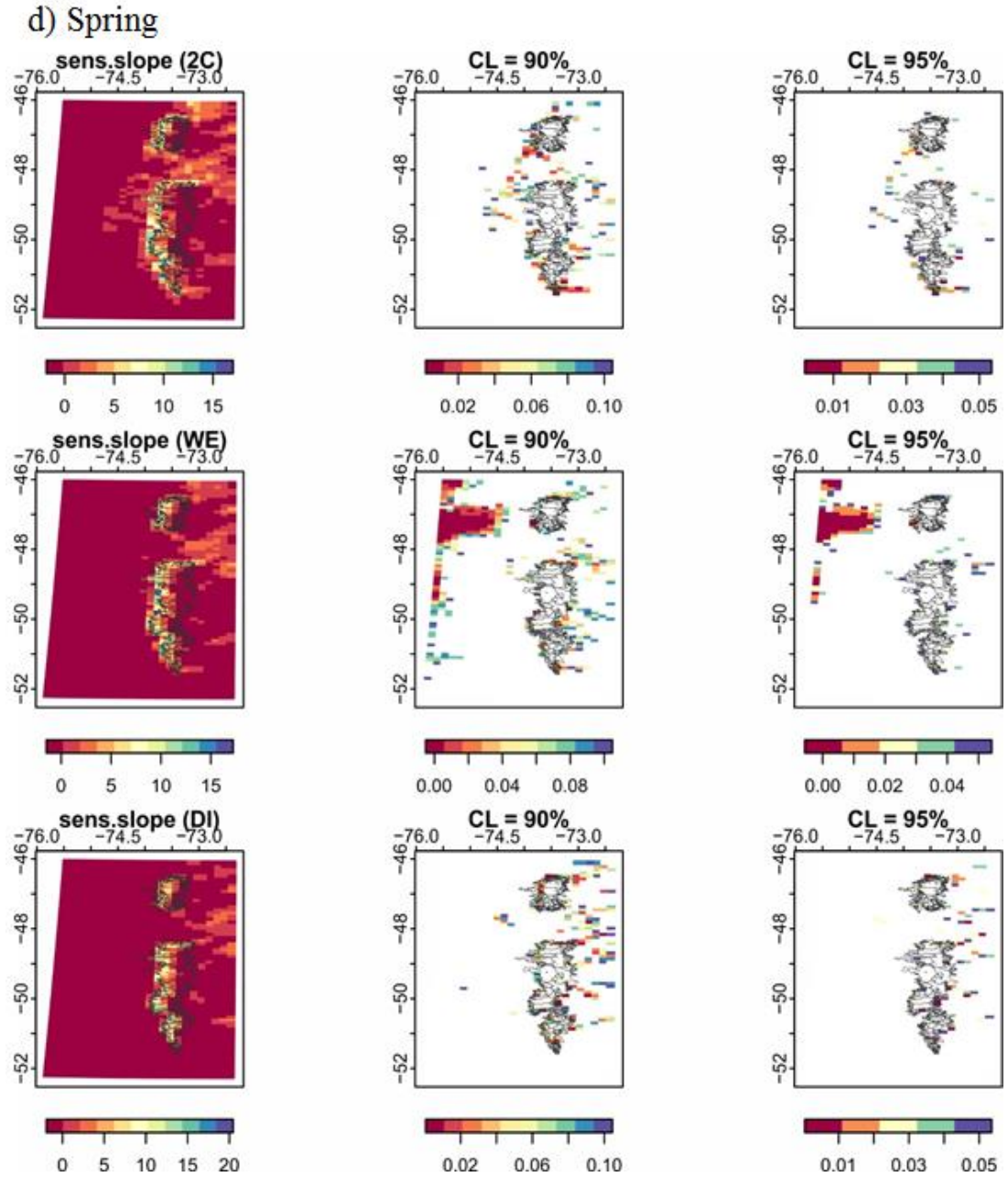


b) Autumn

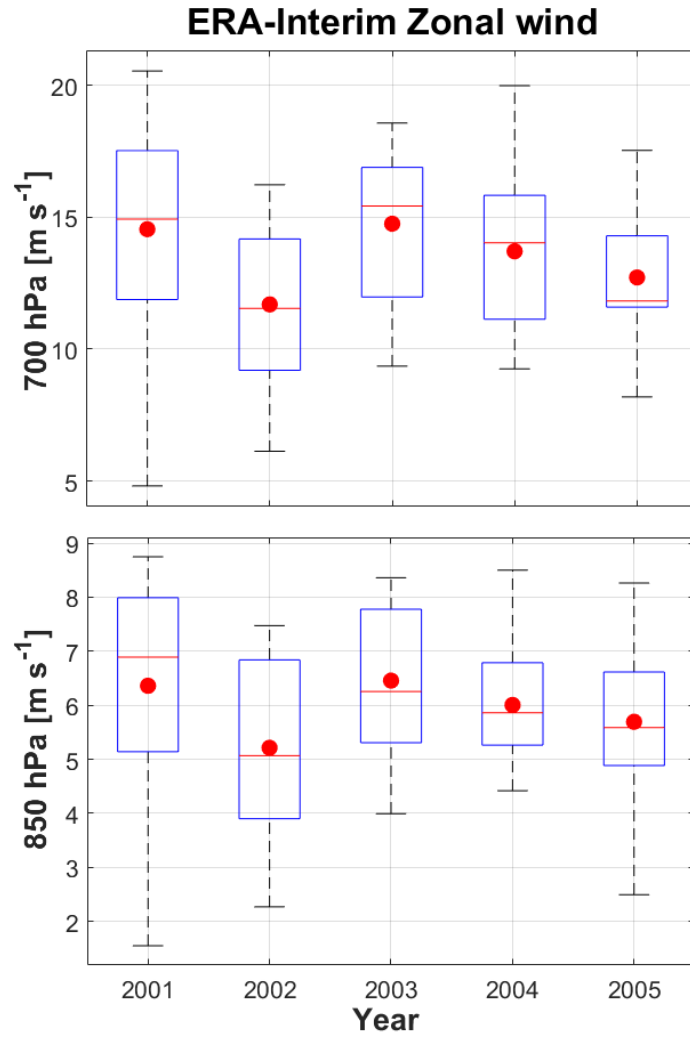


c) Winter

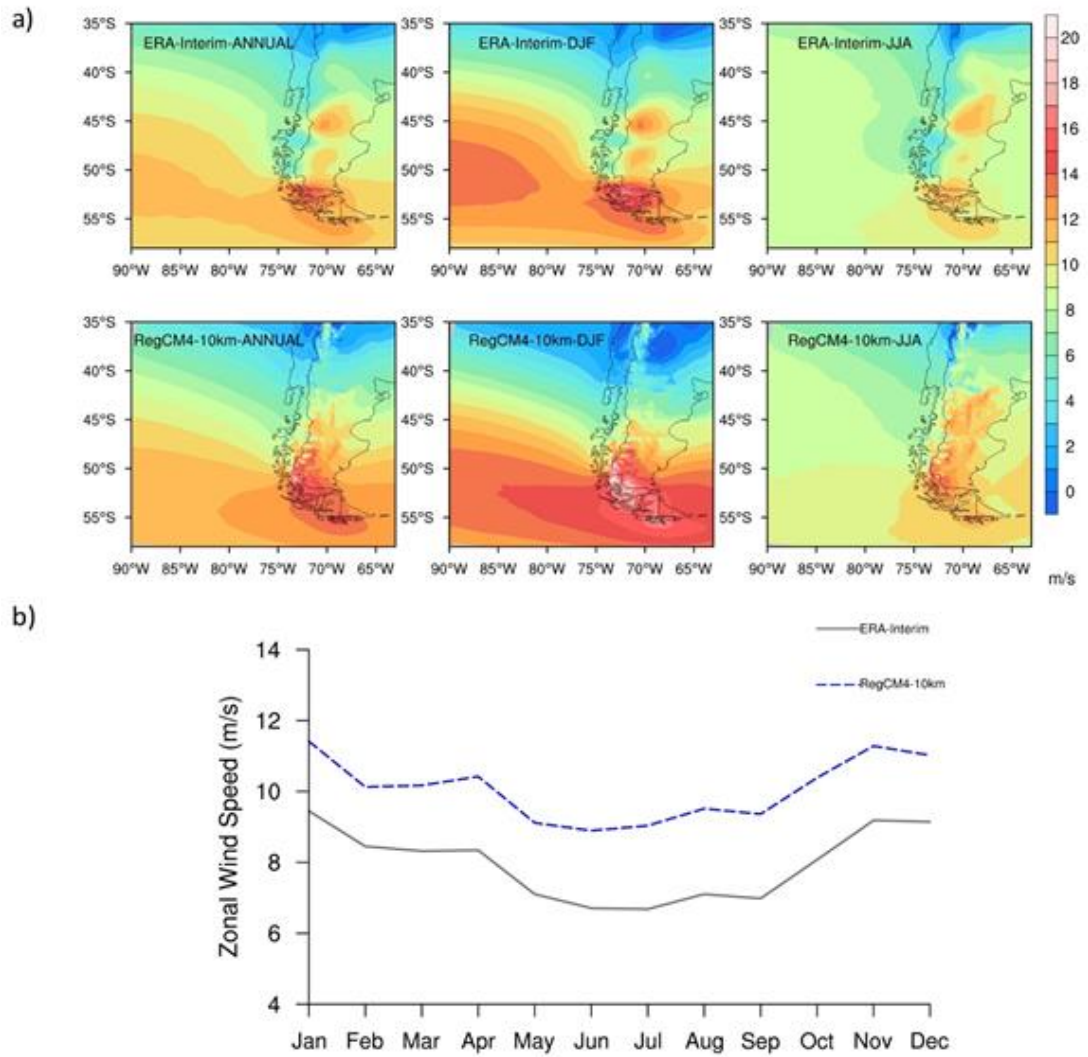




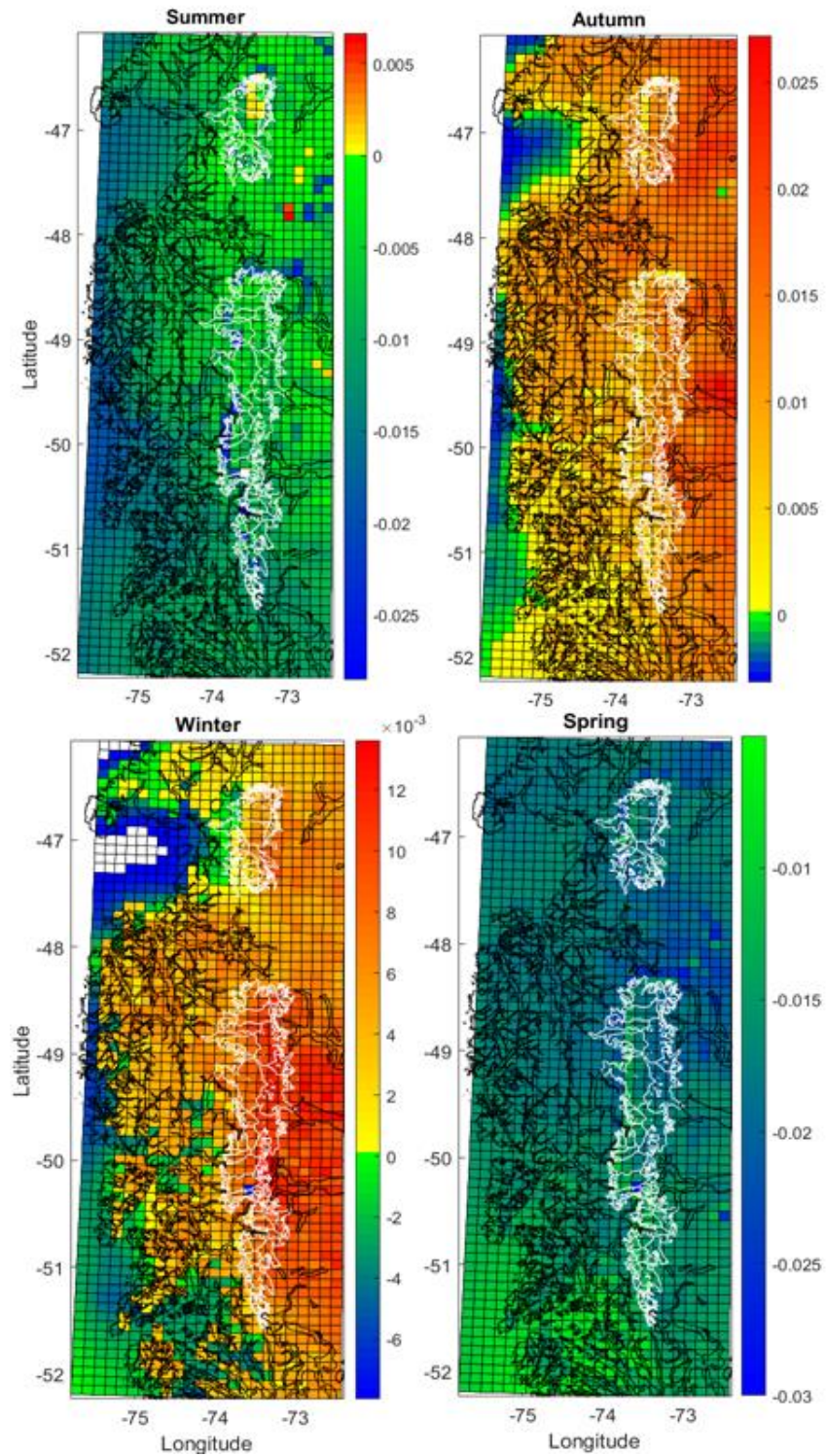
Supplementary Figure 4.3 Seasonal trends 1980-2015 in mm w.e. yr-1 for three PPMs using Sen's slope method. (a) Summer, (b) Autumn, (c) Winter and (d) Spring. Statistically significant trend ($p < 0.1$ and $p < 0.05$) are also shown. Icefields contours in black.



Supplementary Figure 4.4 Boxplot of the ERA-Interim zonal wind for a region covering the Icefields for calendar years 2001 to 2005 at two pressure levels of 700 hPa and 850 hPa.



Supplementary Figure 4.5 (a) Spatial distribution of 36-year (1980-2015) mean annual, DJF and JJA average of 850hPa zonal wind speed (m/s) from ERA-Interim and RegCM4. (b) 36-year (1980-2015) mean annual cycle of 850hPa zonal wind speed (m/s) from ERA-Interim and RegCM4 for a region covering the Icefields.



Supplementary Figure 4.6 Seasonal trends 1980-2015 for the near surface air temperature obtained from RegCM4.6. Colorbar in in $^{\circ}\text{C yr}^{-1}$. Note that each season show a different scale in the trends. Icefields limits in white and coastlines in black.

Supplementary Tables

Supplementary Table 4.1 Mean and standard deviation (inter-annual variability) of the snow accumulation values by season, zone and PPM in the period 1980-2015.

| Zone | Season | PPM / RegCM4.6 [mm w.e.] | | | | | | | | | | |
|------------|-----------|--------------------------|---------|------|---------|------|---------|------|---------|-----------------|---------|-----|
| | | 2C | | WE | | SC | | DI | | DI (snow+sleet) | | |
| | | Mean | Std Dev | Mean | Std Dev | Mean | Std Dev | Mean | Std Dev | Mean | Std Dev | |
| NPI | Summer | 711 | 235 | 492 | 203 | 491 | 203 | 250 | 144 | 694 | 234 | |
| | W | Autumn | 1,396 | 245 | 1,198 | 227 | 1,199 | 227 | 896 | 206 | 1,378 | 244 |
| | | Winter | 1,601 | 327 | 1,525 | 302 | 1,526 | 302 | 1,331 | 250 | 1,597 | 325 |
| | | Spring | 1,232 | 256 | 1,098 | 248 | 1,099 | 248 | 838 | 225 | 1,223 | 254 |
| | | Annual | 4,941 | 463 | 4,313 | 416 | 4,314 | 416 | 3,315 | 381 | 4,892 | 459 |
| NPI | Summer | 90 | 38 | 55 | 28 | 56 | 28 | 31 | 18 | 90 | 38 | |
| | E | Autumn | 332 | 71 | 274 | 69 | 274 | 69 | 204 | 65 | 330 | 71 |
| | | Winter | 429 | 53 | 396 | 50 | 396 | 50 | 337 | 50 | 429 | 53 |
| | | Spring | 233 | 62 | 188 | 57 | 189 | 57 | 138 | 47 | 234 | 62 |
| | | Annual | 1,084 | 107 | 913 | 98 | 914 | 99 | 710 | 92 | 1,084 | 107 |
| SPI | Summer | 1,274 | 344 | 820 | 279 | 819 | 279 | 378 | 175 | 1,229 | 339 | |
| | NW | Autumn | 2,051 | 456 | 1,640 | 373 | 1,640 | 373 | 1,103 | 274 | 2,015 | 446 |
| | | Winter | 2,452 | 612 | 2,227 | 548 | 2,227 | 548 | 1,782 | 443 | 2,440 | 606 |
| | | Spring | 2,233 | 413 | 1,813 | 367 | 1,813 | 368 | 1,204 | 292 | 2,199 | 408 |
| | | Annual | 8,010 | 908 | 6,500 | 796 | 6,500 | 796 | 4,467 | 641 | 7,883 | 891 |
| SPI | Summer | 852 | 160 | 715 | 155 | 715 | 156 | 513 | 149 | 841 | 159 | |
| | NE | Autumn | 1,104 | 200 | 1,027 | 195 | 1,027 | 195 | 894 | 176 | 1,099 | 200 |
| | | Winter | 1,172 | 264 | 1,133 | 255 | 1,133 | 255 | 1,066 | 239 | 1,170 | 263 |
| | | Spring | 1,058 | 175 | 999 | 169 | 999 | 169 | 890 | 159 | 1,055 | 175 |
| | | Annual | 4,186 | 381 | 3,873 | 358 | 3,874 | 358 | 3,363 | 326 | 4,166 | 380 |
| SPI | Summer | 1,031 | 213 | 698 | 200 | 697 | 200 | 330 | 143 | 999 | 210 | |
| | SW | Autumn | 1,387 | 292 | 1,182 | 248 | 1,182 | 248 | 867 | 187 | 1,374 | 289 |
| | | Winter | 1,532 | 345 | 1,469 | 320 | 1,470 | 321 | 1,291 | 281 | 1,529 | 343 |
| | | Spring | 1,520 | 242 | 1,332 | 233 | 1,332 | 232 | 967 | 206 | 1,507 | 240 |
| | | Annual | 5,471 | 532 | 4,680 | 492 | 4,680 | 491 | 3,455 | 436 | 5,408 | 527 |
| SPI | Summer | 636 | 94 | 519 | 93 | 519 | 93 | 340 | 99 | 630 | 94 | |
| | SE | Autumn | 780 | 129 | 723 | 126 | 723 | 126 | 616 | 109 | 780 | 129 |
| | | Winter | 833 | 149 | 815 | 146 | 815 | 146 | 775 | 136 | 833 | 148 |
| | | Spring | 785 | 97 | 743 | 97 | 744 | 97 | 656 | 96 | 784 | 98 |
| | | Annual | 3,033 | 226 | 2,801 | 215 | 2,801 | 216 | 2,388 | 201 | 3,027 | 224 |

Supplementary Table 4.2 Maximum and minimum values of the mean snow accumulation values (1980-2015) by season, zone and PPMs.

| Zone | Season | PPM / RegCM4.6 [mm w.e.] | | | | | | | | | |
|-----------|---------------|--------------------------|-------|--------|-------|--------|-------|--------|-----|--------------------|-------|
| | | 2C | | WE | | SC | | DI | | DI (snow+sleet) | |
| | | Max | Min | Max | Min | Max | Min | Max | Min | Max | Min |
| NPI W | Summer | 1,187 | 93 | 876 | 65 | 875 | 65 | 506 | 15 | 1,156 | 94 |
| | Autumn | 2,132 | 229 | 1,755 | 209 | 1,756 | 209 | 1,449 | 175 | 2,104 | 229 |
| | Winter | 2,558 | 269 | 2,334 | 266 | 2,335 | 266 | 1,936 | 251 | 2,545 | 269 |
| | Spring | 1,921 | 175 | 1,685 | 160 | 1,684 | 160 | 1,369 | 130 | 1,906 | 175 |
| | Annual | 7,556 | 767 | 6,389 | 701 | 6,391 | 701 | 5,170 | 594 | 7,458 | 767 |
| NPI E | Summer | 354 | 8 | 243 | 2 | 243 | 2 | 166 | 1 | 339 | 10 |
| | Autumn | 1,127 | 121 | 830 | 95 | 831 | 95 | 526 | 72 | 1,099 | 124 |
| | Winter | 1,472 | 167 | 1,343 | 150 | 1,343 | 150 | 1,012 | 139 | 1,469 | 170 |
| | Spring | 986 | 58 | 756 | 40 | 757 | 40 | 423 | 36 | 974 | 63 |
| | Annual | 3,942 | 358 | 3,094 | 290 | 3,096 | 290 | 1,959 | 257 | 3,884 | 368 |
| SPI NW | Summer | 3,430 | 30 | 2,889 | 7 | 2,889 | 7 | 1,977 | 0 | 3,397 | 29 |
| | Autumn | 3,454 | 480 | 3,305 | 260 | 3,304 | 260 | 2,912 | 83 | 3,445 | 470 |
| | Winter | 3,552 | 1,149 | 3,391 | 752 | 3,391 | 751 | 3,252 | 314 | 3,547 | 1,122 |
| | Spring | 3,653 | 574 | 3,593 | 261 | 3,593 | 261 | 3,350 | 56 | 3,648 | 550 |
| | Annual | 13,821 | 2,235 | 13,069 | 1,281 | 13,069 | 1,278 | 11,503 | 454 | 13,774 | 2,171 |
| SPI NE | Summer | 2,210 | 4 | 1,993 | 0 | 1,993 | 0 | 1,620 | 0 | 2,196 | 4 |
| | Autumn | 2,375 | 181 | 2,329 | 142 | 2,330 | 141 | 2,193 | 46 | 2,375 | 181 |
| | Winter | 2,262 | 214 | 2,262 | 210 | 2,262 | 210 | 2,261 | 163 | 2,262 | 214 |
| | Spring | 2,315 | 133 | 2,305 | 97 | 2,306 | 97 | 2,239 | 14 | 2,315 | 133 |
| | Annual | 9,170 | 620 | 8,898 | 559 | 8,899 | 558 | 8,321 | 222 | 9,156 | 626 |
| SPI SW | Summer | 2,740 | 16 | 2,107 | 2 | 2,105 | 2 | 1,325 | 0 | 2,646 | 17 |
| | Autumn | 3,105 | 274 | 2,735 | 188 | 2,732 | 188 | 2,255 | 69 | 3,070 | 275 |
| | Winter | 3,020 | 313 | 2,999 | 312 | 3,000 | 312 | 2,873 | 225 | 3,020 | 313 |
| | Spring | 3,365 | 235 | 3,158 | 144 | 3,159 | 143 | 2,556 | 24 | 3,352 | 237 |
| | Annual | 12,240 | 988 | 10,814 | 870 | 10,812 | 870 | 8,839 | 319 | 12,099 | 993 |
| SPI SE | Summer | 2,482 | 32 | 2,103 | 17 | 2,103 | 17 | 1,534 | 0 | 2,430 | 35 |
| | Autumn | 2,351 | 123 | 2,196 | 102 | 2,197 | 102 | 1,960 | 93 | 2,347 | 126 |
| | Winter | 2,239 | 154 | 2,235 | 147 | 2,235 | 147 | 2,185 | 144 | 2,239 | 155 |
| | Spring | 2,678 | 80 | 2,603 | 60 | 2,605 | 60 | 2,324 | 54 | 2,676 | 83 |
| | Annual | 9,751 | 388 | 9,010 | 326 | 9,013 | 326 | 7,934 | 305 | 9,693 | 399 |

A.3 Chapter 5. Drivers of surface ablation on the Southern Patagonian Icefield

Supplementary Material

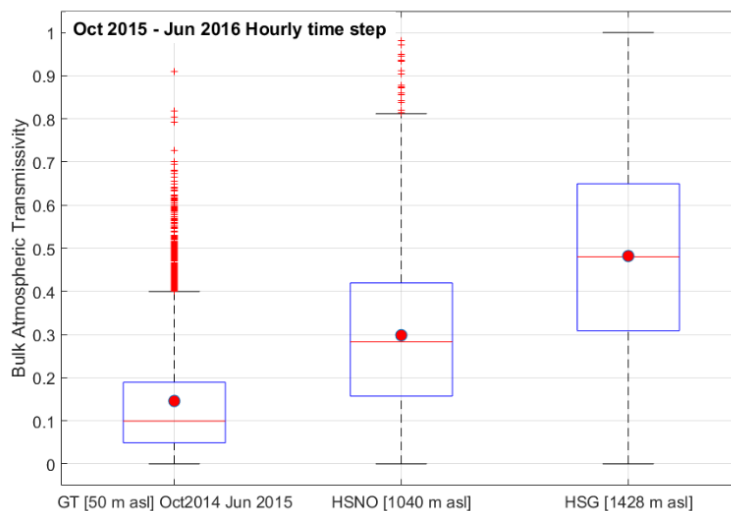
a) Energy Balance Components

Shortwave and longwave radiation fluxes

Shortwave and longwave radiation were both estimated using standard approaches previously applied for energy balance calculations.

Using the DEM, the distributed global radiation was derived using a radiation model in a Geographic Information System (GIS) environment (Fu and Rich, 2000, 2002). Global radiation comprises direct solar radiation and diffuse radiation and was computed under a clear sky assumption with atmospheric transmissivity equal to 1, to represent the potential shortwave radiation $S_{in,pot}$ at each grid point. The potential shortwave radiation was corrected using the bulk atmospheric transmissivity (τ_{atm}) derived from the relationship between the potential and the observed shortwave radiation at the location of each AWS (Sicart and others, 2010; MacDonnell and others, 2013). The bulk atmospheric transmissivity was spatially distributed ($\tau_{atm,dis}$) as a linear relationship was found for each side of the SPI (e.g. see west side data presented in Supplementary Figure 5.1). Hence the incoming shortwave radiation at the glacier surface is ($S_{in,gla}$):

$$S_{in,gla} = \tau_{atm,dis} \cdot S_{in,pot}$$



Supplementary Figure 5.1 Bulk atmospheric transmissivity on the west side of the Southern Patagonian Icefield.

The albedo of the glacier surface was estimated using the model of Oerlemans and Knapp (1998). This model assumes that albedo depends on

the age of the snow surface. To estimate the snow accumulation on the glacier surface we used the total precipitation data from ERA5-Land (9 km) resized to 200 m. The snow accumulation was estimated using the phase partitioning methods (PPM) proposed by Weidemann and others (2018) which showed a close fit between modelled and observed accumulation rates, with observations coming from ultrasonic depth gauges (UDGs) within the study area and presented in Bravo and others (2019a). The air temperature used to define the partitioning was not bias-corrected as we assumed that the contributing snow mass is formed entirely outside the glacier boundary layer. Then the albedo is estimated using the relationship:

$$\alpha_s^t = \alpha_{fi} + (\alpha_{fr} - \alpha_{fi}) \cdot e^{-\Delta t/t^*},$$

$$\alpha^t = \alpha_s^t + (\alpha_{ice} - \alpha_s^t) \cdot e^{-d/d^*},$$

where α^t corresponds to the global albedo at the surface on a specific t day. α_s^t corresponds to the snow albedo at the surface on a t day. The α_{fr} and α_{fi} parameters are related to fresh snow albedo (0.85) and firn or old snow albedo (0.53), respectively. α_{ice} represents a specific glacier ice albedo (0.35), while t^* corresponds to the time scales that represent the transition of fresh snow albedo to firn (3 days). The Δt term refers to days since the last snowfall event. The d and d^* parameters correspond to the snow depth (in meters), and scale coefficient of snow depth (0.032 m), respectively.

To validate the surface albedo output estimated by the model, we used albedo values derived from Landsat 8 satellite images during the same period. Processing of the Landsat 8 OLI is described and explained in section S2. Overall, the modelled albedo replicated the elevational gradient of the observed albedo (Supplementary Figure 5.2), but without some of the finer details. The greatest differences were concentrated on the glaciers at mid-elevation on each side of the SPI, probably related to the exact snow line altitude definition. The albedo from Landsat was also used to define the albedo of the supraglacial moraines observed on the glacier ablation zone of the study area. Hence, the albedo of the supraglacial moraine was obtained from the Landsat 8 images acquired on 8th March 2016 and was prescribed for each day depending on the snow line elevation.

The incoming longwave radiation ($L_{in, gla}$) was estimated using the Stefan Boltzmann law (Molg and others, 2009):

$$L_{in, gla} = \varepsilon_{atm} \cdot \sigma T^4 \cdot S_{vf},$$

where σ is the Stefan-Boltzmann constant and S_{vf} is the sky-view factor calculated with the DEM. Atmospheric emissivity for all-sky conditions (ε_{atm}) was calculated as the product of clear-sky emissivity ($\varepsilon_{atm,clear}$) and the cloud factor (F_{cl}). The cloud factor was obtained as the ratio of the observed and the clear sky incoming longwave radiation at the location of two representative mid-elevation AWSs, HSNO on the west side and HSO on the east side. In this case, it was assumed that the cloud factor is representative of the total area of the glaciers. Meanwhile, the clear-sky emissivity was estimated using the spatially distributed fields of air temperature (K) and the water vapour pressure (hPa) using the Brutsaert (1975) expression:

$$\varepsilon_{atm,clear} = P_1 (e/T_a)^{1/P_2},$$

where $P_1 = 1.24$ and $P_2 = 7$.

The outgoing longwave radiation was calculated using the distributed field of the surface temperature and assuming a surface emissivity equal to 1 in the Stefan-Boltzmann law.

Sensible, latent and rainfall heat fluxes

The turbulent sensible heat fluxes were calculated using the bulk approach (Cuffey and Paterson, 2010). In the case of the sensible heat flux;

$$Q_h = \rho_a c_a C^* u [T_a - T_s] (\Phi_m \Phi_h)^{-1},$$

where u is wind speed in m s^{-1} , T_a is air temperature in K and T_s is glacier surface temperature. C^* is a dimensionless transfer coefficient, which is a function of the surface aerodynamic roughness (z_o):

$$C^* = \frac{k^2}{\ln^2\left(\frac{z}{z_o}\right)},$$

where z is the height above the surface of the T and u measurements (2 m) and k is the von Kármán's constant (0.4). Due to the absence of microtopographic measurements, z_o was prescribed according to the albedo using values taken from Brock and others, (2006) (Supplementary Table 5.1). This is a general approximation to estimate the surface roughness as, for instance, wind speed is not considered, while in the aerodynamic method it is used for fitting the wind profile to determine z_o (Chambers and others, 2020). However, it has been suggested that surface roughness also affects surface albedo, especially on snow surfaces (Manninen and others, 2016). ρ_a is the density of air, which depends on atmospheric pressure P (in Pa):

$$\rho_a = \rho_a^0 \frac{P}{P_0},$$

where ρ_a^o (1.29 kg m⁻³) is the density at standard pressure P_0 (101300 Pa). Finally, c_a is the specific heat of air at a constant pressure (J kg⁻¹ K⁻¹) calculated as (Brock and Arnold, 2000):

$$c_a = 1004.67 \left(1 + 0.84 \left(0.622 \left(\frac{e}{P} \right) \right) \right),$$

Supplementary Table 5.1 Fixed surface roughness for albedo range depending on the surface type.

| Surface type | Albedo | Roughness (m) |
|----------------------|-----------|---------------|
| Supraglacial Moraine | <0.35 | 0.016 |
| Ice | 0.35-0.45 | 0.01 |
| Firn | 0.45-0.60 | 0.007 |
| Old snow | 0.60-0.70 | 0.005 |
| Glacier snow | 0.70-0.80 | 0.001 |
| Fresh snow | >0.80 | 0.0002 |

The latent heat flux Q_l is:

$$Q_l = \frac{0.622\rho_a L_{v/s} C^* u [e_a - e_s]}{P} (\Phi_m \Phi_h)^{-1},$$

where e_a is air vapour pressure, e_s is the vapour pressure at the glacier surface (Brock & Arnold, 2000) and both were estimated using the methods explained in previous sections. $L_{v/s}$ is the latent heat of vaporization or sublimation, depending on whether the surface temperature is at melting point (0°C) or below the melting point (<0°C), respectively.

Stability corrections were applied to turbulent fluxes using the bulk Richardson number (Ri_b), which is used to describe the stability of the surface layer (Oke, 1987):

$$\text{for } Ri_b \text{ positive (stable): } (\Phi_m \Phi_h)^{-1} = (\Phi_m \Phi_v)^{-1}$$

$$= (1 - 5Ri_b)^2,$$

$$\text{for } Ri_b \text{ negative (unstable): } (\Phi_m \Phi_h)^{-1} = (\Phi_m \Phi_v)^{-1}$$

$$= (1 - 16Ri_b)^{0.75}.$$

Ri_b is used to describe the stability of the surface layer:

$$Ri_b = \frac{g(T - T_s)(z - z_0)}{Tu^2},$$

where g is the acceleration due to gravity.

The rain heat flux (Q_r) is a function of the rainfall rate intensity (R , m s^{-1}) and the rain temperature (T_r) is assumed to be equal to the air temperature (Hock and Holmren, 2005; Gillet and Cullen, 2010):

$$Q_r = \rho_w c_w R [T_r - T_s],$$

where ρ_w is the density of water and c_w is the specific heat of water ($4180 \text{ J kg}^{-1} \text{ K}^{-1}$). The rainfall intensity was obtained from the total precipitation ERA5-Land dataset at a daily time step. The rainfall was obtained from the total precipitation using the Phase Partitioning Method (PPM) explained in the next section.

b) Landsat-8 Albedo

In order to compare and assess the limitation of the albedo model used in our energy balance model and to estimate the albedo on supraglacial moraine surfaces to prescribe it, we calculated the albedo from selected Landsat-8 images as follows.

The top of atmosphere (TOA) reflectance for each band is calculated by the conversion of the digital number of each image pixel (DN) to radiance and then to reflectance (Department of the Interior U.S. Geological Survey, 2015) using the equation:

$$\rho\lambda' = M_p DN + A_p$$

where $\rho\lambda'$ is the reflectance without correction for solar angle, M_p is a reflectance multiplicative scaling factor for the band, DN is the digital number of each pixel in the spectral band and A_p is the reflectance additive scaling factor for the band. The apparent reflectance is corrected by the solar zenith angle (θ) to calculate the true TOA reflectance ($\rho\lambda$):

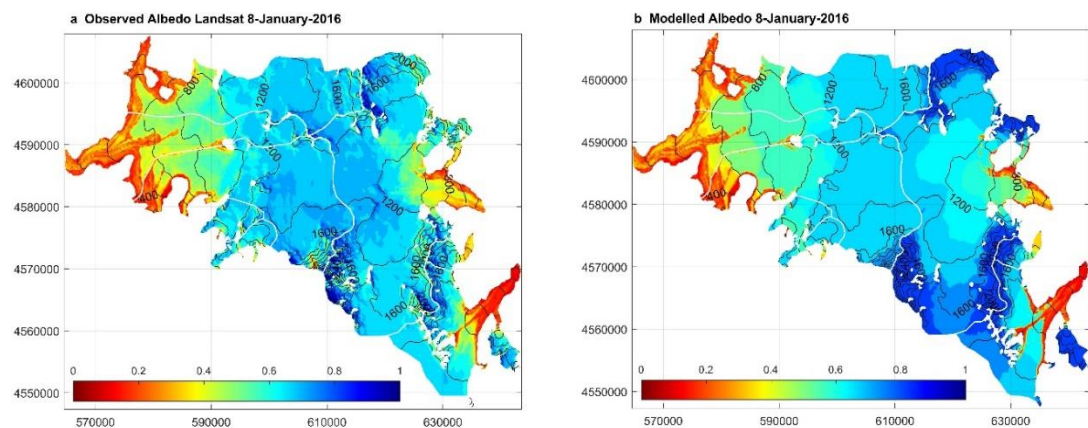
$$\rho\lambda = \frac{\rho\lambda'}{\cos(\theta)}$$

The transformation is carried out using the scaling factors M_p and A_p values included on the image metadata for each band, which are related to the radiometric calibration of the sensors and the satellite position at the acquisition time (Department of the Interior U.S. Geological Survey, 2015).

Albedo on Landsat 8 images was estimated using the method proposed by Wang and others (2016). Here, spectral bands 2 to 7 are used for snow areas. The narrowband albedo is thus transformed to broadband albedo using the conversion coefficients (C_i) from Wang and others (2016) in the next equation 3.

$$\alpha = \sum_{i=2}^{i=7} C_i \rho \lambda_i$$

We compared the results of the albedo model of Oerlemans and Knapp (1998) with the estimations using Landsat-8 for some specific dates, i.e. dates where the images are cloud free. For instance, the comparison for 8 January 2016 is presented on Supplementary Figure 5.2. In the results of the Oerlemans and Knapp (1998) model, the albedo on supraglacial moraine was already prescribed.



Supplementary Figure 5.2 Comparison of the observed albedo using Landsat-8 satellite images (a) and modelled albedo using Oerlemans and Knapp (1998) approach (b). Albedo values on supraglacial moraine is prescribed.

c) References

Bravo C, Bozkurt D, Gonzalez-Reyes A, Quincey DJ, Ross AN, Farías-Barahona D and Rojas M (2019a) Assessing snow accumulation patterns and changes on the Patagonian Icefields. *Frontiers in Environmental Science* 7(1), 30. doi: [org/10.3389/fenvs.2019.00030](https://doi.org/10.3389/fenvs.2019.00030).

Brock BW, Willis IC and Sharp M J (2006) Measurement and parameterization of aerodynamic roughness length variations at Haut Glacier D'Arolla, Switzerland. *Annals of Glaciology* 52(177), 281–297. doi: [org/10.3189/172756506781828746](https://doi.org/10.3189/172756506781828746).

Brutsaert, W (1975) On a derivable formula for long-wave radiation from clear skies. *Water Resources Research* 11(5), 742–744. doi: [org/10.1029/WR011i005p00742](https://doi.org/10.1029/WR011i005p00742)

Chambers JR, Smith MW, Quincey DJ, Carrivick JL, Ross AN and James MR (2020) Glacial aerodynamic roughness estimates: uncertainty, sensitivity and

precision in field measurements. *Journal of Geophysical Research: Earth Surface* 125(2). doi: org/10.1029/2019JF005167.

Department of the Interior U.S. Geological Survey (2019) Landsat 8 (L8) Data Users Handbook, version 5.0.

Fu P, and Rich PM (2002) A Geometric Solar Radiation Model with Applications in Agriculture and Forestry. *Computers and Electronics in Agriculture* 37, 25–35. doi: org/10.1016/S0168-1699(02)00115-1.

Gillett S, and Cullen NJ (2010) Atmospheric controls on summer ablation over Brewster Glacier, New Zealand. *International Journal of Climatology* 31(13), 2033–2048. doi: org.10.1002/joc.2216.

Hock R and Holmgren B (2005) A distributed energy balance model for complex topography and its application to Storglaciären, Sweden. *Journal of Glaciology* 51(172), 25-36. doi:org/10.3189/172756505781829566.

MacDonell S, Kinnard C, Mölg T, Nicholson L and Abermann J (2013) Meteorological drivers of ablation processes on a cold glacier in the semiarid Andes of Chile. *The Cryosphere* 7(5), 1513-1526. doi: org/10.5194/tc-7-1513-2013.

Manninen T, Lahtinen P, Anttila K and Riihelä A (2016) Detection of snow surface roughness and hoar at Summit, Greenland, using RADARSAT data. *International Journal of Remote Sensing* 37(12), 2860-2880. doi: org.10.1080/01431161.2015.1131873.

Mölg T, Cullen NJ and Kaser G (2009) Solar radiation, cloudiness and longwave radiation over low-latitude glaciers: Implications for mass balance modeling. *Journal of Glaciology* 55(190), 292-302. doi: org/10.3189/002214309788608822.

Oerlemans J and Knap WH (1998) A one-year record of global radiation and albedo from the ablation zone of the Morteratschgletscher, Switzerland. *Journal of Glaciology* 44(147), 231-238. doi: org/10.3189/S0022143000002574.

Oke TR (1987) *Boundary Layer Climate*, 2nd ed., London, Methuen.

Sicart JE, Hock R, Ribstein P and Chazarin JP (2010) Sky long-wave radiation on tropical Andean glaciers: parameterization and sensitivity to atmospheric

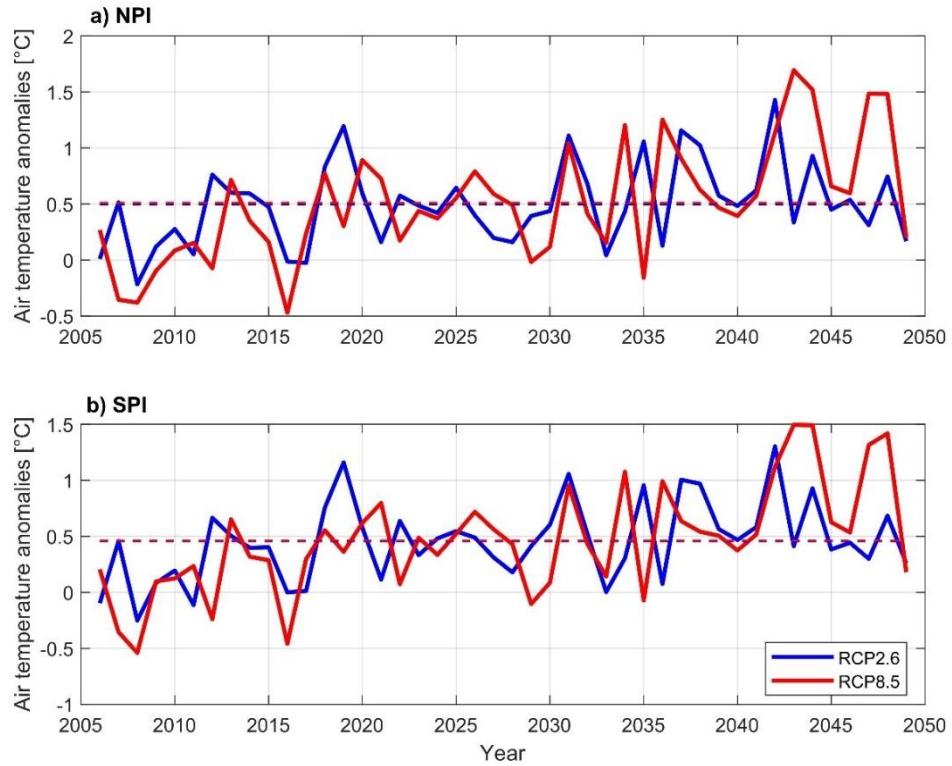
variables. *Journal of Glaciology* 56(199), 854-860. doi: org/10.3189/002214310794457182.

Wang Z and 8 others (2016) Early spring post-fire snow albedo dynamics in high latitude boreal forests using Landsat-8 OLI data. *Remote Sensing of Environment* 185, 71–83. doi: org.10.1016/j.rse.2016.02.059.

A.4 Chapter 6. Projected increases in surface melt will drive future changes in the Patagonian Icefields

Supplementary Material

Supplementary Figure 6.1 . Annual air temperature anomalies over NPI (a) and SPI (b) for both scenarios (RCP2.6 and 8.5) estimated with respect to the mean of the historical period (1976-2004).



Supplementary Table 6.1 Comparison of geodetic mass balance and modelled surface mass balance estimated in this work in the NPI. For those period started in 2000/01, we used values of the historical period until 2004 and then to complete the comparison period, we used the values for each scenario.

| Period | Reference | Geodetic mass balance (m w.e.) | This work (m w.e.) | |
|-----------|----------------------------------|--------------------------------|--------------------|------------|
| 1975-2000 | Rignot et al. ³ | -0.69±0.09 | -0.49±2.13 | |
| 1980-2002 | Rivera et al. ⁴ | -1.53±0.82 | -0.71±2.17 | |
| | | | RCP 2.6 | RCP 8.5 |
| 2001-2011 | Willis et al. ⁶ | -0.96±0.04 | -1.14±2.17 | -0.84±2.14 |
| 2000-2012 | Dusaillant et al. ⁸ | -1.06±0.15 | -1.22±2.23 | -1.07±2.21 |
| 2000-2014 | Abdel-Jaber et al. ¹² | -0.91±0.04 | -1.57±2.30 | -1.14±2.25 |
| 2000-2014 | Braun et al. ¹⁰ | -0.85±0.07 | | |
| 2000-2015 | Dusaillant et al. ¹¹ | -0.98±0.27 | -1.70±2.31 | -1.14±2.25 |
| 2012-2016 | Abdel-Jaber et al. ¹² | -1.22±0.16 | -3.29±2.64 | -1.35±2.40 |
| 2011-2016 | Foresta et al. ⁹ | -1.58±0.27 | -2.38±2.53 | -1.08±2.33 |

Supplementary Table 6.2 Comparison of geodetic mass balance and modelled surface mass balance estimated in this work in the SPI. For those period started in 2000/01, we used values of the historical period until 2004 and then to complete the comparison period, we used the values for each scenario.

| Period | Reference | Geodetic mass balance (m w.e.) | This work (m w.e.) | |
|-----------|----------------------------------|--------------------------------|--------------------|-----------|
| 1975-2000 | Rignot et al. ³ | -0.88±0.05 | 2.83±1.57 | |
| 1995-2000 | Rignot et al. ³ | -2.21±0.29 | 2.70±1.68 | |
| | | | RCP2.6 | RCP8.5 |
| 2000-2012 | Willis et al. ⁵ | -1.49±0.09 | 2.22±1.72 | 2.39±1.68 |
| 2000-2012 | Braun et al. ¹⁰ | -0.86±0.08 | | |
| 2000-2012 | Abdel-Jaber et al. ¹² | -0.97±0.03 | | |
| 2000-2015 | Malz et al. ⁷ | -0.89±0.24 | 1.83±1.82 | 2.31±1.74 |
| 2000-2015 | Dusaillant et al. ¹¹ | -0.96±0.29 | | |
| 2012-2016 | Abdel-Jaber et al. ¹² | -0.79±0.13 | 0.59±2.18 | 2.15±1.91 |
| 2011-2016 | Foresta et al. ⁹ | -0.98±0.11 | 0.96±2.07 | 2.09±1.89 |